AN EXPERIMENTAL INVESTIGATION OF STEADY AND PULSATILE FLOW THROUGH PARTIAL OCCLUSIONS IN A RIGID TUBE

A THESIS

Presented to

The Faculty of the Division of Graduate Studies

By

Robert A. Cassanova

In Partial Fulfillment

of the Requirements for the Degree

Doctor of Philosophy in the

School of Aerospace Engineering

Georgia Institute of Technology

August, 1975

AN EXPERIMENTAL INVESTIGATION OF STEADY AND PULSATILE FLOW THROUGH PARTIAL OCCLUSIONS IN A RIGID TUBE

Approved:

D. P. Giddens, Chairman

W. C. Strahle

R. F. Mabon

Date approved by Chairman: 8/4/75

ACKNOWLEDGMENTS

I wish to thank my advisor, Dr. D. P. Giddens, for his technical advice and continued encouragement throughout the time devoted to my thesis research. His willingness to contribute guidance in an open-minded fashion has made my research work a pleasureable undertaking.

I also thank Dr. Warren C. Strahle and Dr. Robert F. Mabon for their guidance in the presentation of the manuscript.

The financial support of the National Science Foundation and the National Institutes of Health is gratefully acknowledged.

Most importantly, I am eternally grateful to my wife, Alice, whose patience, understanding and encouragement have been most instrumental in the attainment of my academic goals.

TABLE OF CONTENTS

LIST OF ILLUSTRATIONS

Figure Page

Figure | Page

Figure Page

Figure Page

Figure

Figure Page

Figure Page

Figure Page

Page missing from thesis

SUMMARY

An experimental study of steady and pulsatile water flow through axisymmetric constrictions in a rigid tube was conducted. The study was motivated by the problem of subtotal vascular stenosis occurring with atherosclerosis. The steady flow experiments covered a Reynolds number range of 635 to 2540 based on the unrestricted tube flow and the pulsatile flow experiments were conducted at frequency parameters of 15,31.8 and 45 with corresponding peak Reynolds numbers of 2540, 5080 and 15,200. Both sharp-edged and contoured axisymmetric occlusions were investigated to determine the effect of occlusion geometry on the downstream flow field. Sharp-edged occlusions with 25 percent, 50 percent, 75 percent and 90 percent area reduction and contoured occlusions with 25 percent, 50 percent and 75 percent area reduction were tested.

Dye tracers were employed to visualize the flow field structure in both steady and pulsatile flow. Vortex shedding in the near distal region, the break-up of the vortices into random turbulence and wall interactions were observed and photographed. The sharp-edged occlusions produced flow instabilities at a lower Reynolds number than did the contoured occlusions.

The flow velocity was measured at numerous radial and axial locations with a conical hot film probe. Mean velocity profiles, pulsatile velocity waveforms and velocity fluctuation energy spectra were measured.

In general, the turbulent energy spectra obtained in both steady and pulsatile flows show an increase in the overall energy level and a relative increase in the high frequency content of the velocity fluctuations as the constriction blockage increases for the same proximal flow conditions.

For steady flow through the occlusions, the region immediately downstream of the constriction is dominated by vortex rings which produce velocity fluctuations in a narrow frequency band. These vortex rings break-up into more randomly distributed fluctuations farther downstream. Correlation of the vortex shedding frequency and energy spectra with nondimensional parameters is presented.

The pulsatile flow through the constrictions is characterized by the lack of a continuous recirculation zone in the immediately distal region. During the acceleration phase of the velocity pulse a vortex ring swirls into this region. The energy spectra show more radial homogeneity than did the corresponding steady flow spectra. Discrete vortex shedding frequencies could only be seen in the spectra obtained with the 75 percent occlusions in the lowest pulse rate flow. Nondimensional correlations were applied to the energy spectra and demonstrated that the lowest frequency parameter data obtained at several downstream axial locations with different sized sharp-edged occlusions scaled with the nondimensional energy and Strouhal number based on the local mean velocity and jet streamtube diameter. However, energy spectra obtained with the higher frequency parameter flows indicated that in the region dominated by the occlusive jet flow, the velocity fluctuations could be correlated with the degree of constriction by using the Strouhal number

based on the constriction flow conditions.

The presence of highly turbulent flow fields distal to the modelled stenoses implies that turbulence can be a factor in the development of poststenotic dilatation. Slight degrees of stenosis produced detectable turbulence in pulsatile flow. This fact suggests that the initial formation of occlusions could be detected long before audible turbulence is produced if more sensitive diagnostic instruments could be utilized in clinical practice.

CHAPTER I

INTRODUCTION

1.1 Background

Cardiovascular diseases result in more than half of all deaths in the United States and are the largest single cause of death on a world wide scale[1]. Disability due to cardiovascular disease in this country creates an estimated $19.7 million annual loss in income and payments for medical care and 52 million man-days of lost production.[2] Numerous studies have documented the interplay of heredity, personality, diet, occupation, smoking, alcohol, etc. on the likelihood of developing some form of heart disease. Diagnosis and treatment of cardiovascular problems have occupied a large segment of the medical profession for decades, but only in relatively recent times has there been a multi-disciplinary effort by researchers to understand the synergistic biochemical and fluid mechanical influences on the development of pathologic conditions. While not intending to pass over the importance of the biological and biochemical aspects, this work will concentrate on one particular problem related to fluid mechanics; i.e., the characterization of the turbulent flow distal to modelled arterial stenoses.

1.2 Turbulence in Blood Flow

Abnormal blood flow patterns, such as decreased flow rate and turbulence, are frequently associated with certain forms of cardiovascular disease. These patterns can result in a decrease in the supply

of oxygen and nutrients to the heart or other organs, eventually resulting in degeneration of the affected region.

Often occurring with the development of the pathologic conditions is the formation of turbulence as the blood flows past obstructions protruding from vessel walls. The extent to which the flow is disturbed depends upon, among other factors, (1) the flow conditions proximal to the obstruction and (2) the degree and geometry of the blockage. When the blood passes through a partial occlusion in larger vessels, separation may occur; and the flow may then degenerate into relatively intense turbulence distal to the stenosis. The velocity fluctuations produce pressure variations which are propagated through the vessel wall and surrounding tissues. These can frequently be heard as sounds at the body surface. The sounds produced by flow through the heart valves, for example, can be associated with certain of the normal heart sounds and have been thoroughly documented.[3] Turbulent flow which sometimes occurs in normal blood flow in large vessels is of a very low intensity and usually cannot be heard.

Cardiographic techniques evolved from an effort to transform the art of listening to the sounds into a clinical method yielding quantitative information. Investigators such as Lees and Dewey[4], Sachs, et al.[5] and Yellin[6] have attempted to relate the observed sound fields to the occlusion size and to flow parameters in occlusive vascular disease. However, the capability of quantitative diagnosis of subtotal vascular stenosis from analysis of the measured sound field is not yet fully realized. This is apparently due to two factors. First, the sounds

which are finally measured at the body surface have been modified considerably during their transmission through vessel walls and various body tissues. Thus, they represent a rather "non-focal" measure of the vascular obstructions which triggered the flow instability. Second, attenuation prevents sounds from being detected until the occlusive disease has progressed to an advanced stage. This limits the usefulness of sound field measurement as a tool for early diagnosis of vascular stenosis.

Turbulence distal to subtotal stenosis has also been implicated as a factor in poststenotic dilatation.[7] However, detailed clinical measurements of the turbulent energy spectra or sound power spectra are not presently available in the literature. An investigation of the somewhat simpler case of steady flow through simulated stenoses in rigid tubes has been reported by Kim and Corcoran.[8] In this study the high frequency content of the turbulence downstream of the constriction increased as the degree of the constriction increased.

1.3 Purpose of the Present Investigation

The present research was undertaken to investigate in detail the production of turbulence by flow through subtotal stenoses. Initial measurements of the velocity field distal to artifically produced stenoses in the thoracic aorta of mongrel dogs have been reported by Giddens, et al.[9] In these experiments the turbulent velocity flucuations and resulting sound fields were demonstrated to be sensitive indicators of stenosis in large arteries. A complementary set of *in vitro* experiments are reported here which model the principal characteristics of the *in vivo*

situation but under conditions which afford more rigorous control than that obtainable in the animal studies. Of particular interest is the frequency content of the velocity fluctuations, the axial and radial extent of turbulence, the relationship of the periodic nature of the pulsatile flow to the randomness of turbulence, and the possible existence of similarity parameters which might relate the energy spectra to degree of stenosis.

While the rationale of the present investigation is based on the need to provide specific data related to stenotic fluid dynamics, the information derived from this study is applicable to the broader field of the fluid dynamics of enclosed jets, or jets situated in pipes.

1.4 Review of Literature

The flow phenomena associated with constrictions in tubular vessels are not entirely unique to the physiological situation. The flow through pipe orifices and free jets has attracted the interest of researchers in the fields of hydraulics and acoustics for many years. A brief discussion of representative publications in these fields is appropriate here to illustrate the observed fluid dynamics phenomena. Only recently has attention been given to the flow phenomena associated with these flows by workers in the medical and bioengineering fields.

1.4.1 Free Jet and Pipe Orifice Flows

As early as 1929, Johansen[10] demonstrated the existence of a vortex ring system and a turbulent field in the downstream region of sharp-edged orifices situated within pipes at orifice Reynolds numbers of 30 to 2000. He also showed that the Strouhal number, which is a

nondimensional frequency, based on the orifice conditions and the vortex shedding frequency from the orifice lip was about 0.6. Discharge coefficients were also studied.

Anderson[11,12] used shadowgraph techniques to visualize free jets of carbon dioxide exhausting into still air at orifice Reynolds numbers up to about 5000. Measurements of audible tones, or frequencies, were made with a microphone. Vortex ring coalescence and propagation velocities were discussed in some detail.

Becker and Messaro[13] studied the free jet instabilities in air emerging from a pipe terminated by a smoothly contoured converging nozzle. Smoke photography, stroboscopic observation, and light-scattering were used to observe the formation of vortex rings, the coalescence of ring vortex pairs, and the disintegration into turbulent eddies at Reynolds numbers up to 10,000. Their results showed that the shedding frequency Strouhal number, S, was a direct function of the square root of nozzle Reynolds number, R_{e_N},

$$S = \text{constant } R_{e_N}^{\frac{1}{2}} \tag{1.1}$$

Also investigated by Becker and Messaro[13] was the effect of acoustical tone and broad band noise excitation on the selective amplification of the jet instabilities. Crow and Champagne[14] and Chan[15] studied extensively the orderly structure of turbulent free jets and the effects of introducing a periodic surging with a certain frequency into the jet flow. Crow and Champagne[14] used hot wire anemometry and schlieren photography and found that the saturation amplitude of the resulting disturbance

depends on the Strouhal number of the imposed surging and the maximum amplification occurs for a Strouhal number of 0.3 based on the surge frequency, exit diameter and jet exit centerline velocity. Chan[15] used microphones to scan the centerline and shear layers of similar free jets and reported that the most amplified mode in shear layer was at a Strouhal number of 0.5 and that for the centerline was 0.35.

Data by Iribarne, et al.[16] obtained in a laminar pipe jet at Reynolds numbers up to 1166 showed a similar $R_{e_N}^{\frac{1}{2}}$ trend for the shedding frequency Strouhal number. However, data reported by Beavers and Wilson[17] for jets issuing from sharp-edged orifices showed the Strouhal number to have a constant value of about 0.63 for a Reynolds number range of 500 to 2800. As pointed out by Beavers and Wilson[17], the boundary layer thickness and the resulting velocity profile has a significant effect on the shedding frequency, and hence on the Strouhal number, at a given nozzle Reynolds number. Therefore, at the same nozzle Reynolds number based on flowrate and exit diameter, different results would be expected for jets emerging from straight pipes, pipes terminated by a particular nozzle contour and pipes terminated by an orifice. For the results reported in the literature, no significant difference could be seen in comparing free jet with pipe, or bounded, jet results of the Strouhal number relationship. This agreement is not unexpected since the pipe jet results are for diameter changes of about 1 to 2 and the downstream wall is not sufficiently close to the vortex ring pattern to affect the initial formation. Of course, subsequent interactions of the vortex ring pattern with the pipe wall would be expected to yield different

turbulence development as compared with the free jet turbulence. As yet, such a comparison has not been reported.

Ko and Davies[18] made extensive measurements of velocity and pressure fluctuations inside and in the near surrounding field of a subsonic circular turbulent jet. Both radial and axial variations of the power and energy spectra were reported along with nozzle Strouhal number correlations. Their results showed that the Strouhal number based on the nozzle exit velocity and diameter and the most intense frequency at a specific axial station decreased in an approximately linear fashion with increasing distance from the nozzle exit. However, the Strouhal number of the most intense frequency in the entire field appeared to be about 0.6.

Teyssandier and Wilson[19] applied an integral type of analysis to the flow through sudden enlargements in pipes to predict reattachment lengths, axial wall pressure profiles and recirculation zone flow velocities. Their predictions showed good agreement with the measured results reported by Chaturvedi[20] and others. Chaturvedi also reported measurements of axial and radial variations of turbulence intensities.

1.4.2 Subtotal Stenotic Flow

It has been suggested by numerous investigators such as Fry[21] and Caro[22], that abnormal pressure patterns, wall shear stress distributions and static flow zones in the arterial system may be related to the formation and growth of atherosclerotic plaques. Many of the recent studies have approached the fluid mechanics of the problem by first presenting a steady flow model of stenotic flow which is analyti-

cally tractable. The prediction of a low energy recirculation zone, separation and reattachment phenomena has received particular attention. While obvious similarities with the pipe orifice flows do exist, the stenotic flow studies have included various constriction contours, both axisymmetric and antisymmetric. These contours are usually chosen for mathematical or experimental simplicity and bear little resemblance to the irregularly shaped arterial stenoses. However, these simple shapes do yield flow fields for which parametric studies can be made. Other aspects of stenotic flow which have received little or no attention include vessel wall elasticity and the relatively complex pulsatile nature of the flow.

Forrester and Young[23,24] studied both analytically and experimentally the steady flow through a mild axisymmetric, smoothly contoured stenosis in a rigid tube with a parabolic proximal velocity profile. Distal velocity profiles, pressures and wall shear stress were predicted analytically. Separation and reattachment as a function of Reynolds number were studied experimentally up to a Reynolds number of 1000. The flow field was reported to be completely laminar and no mention was made of the occurrence of flow instabilities.

Young and Tsai[25,26] have investigated experimentally the pressure drop, separation and turbulence formation distal to axisymmetric and nonsymmetric smoothly contoured constrictions in rigid tubes for both steady and unsteady flow. Data was obtained for the Reynolds number range of 100 to 5000. The critical Reynolds number for transition to turbulence was obtained using hot-film probes, but turbulence intensities

and energy spectra were not reported. However, Tsai and Young[27] did report in a later publication on measurements of the centerline turbulence intensities and general spectral trends for steady flow through an axisymmetric constriction.

More detailed measurements of turbulence spectra distal to simulated stenoses in a rigid tube have been reported recently. Kim and Corcoran[8] used a hot film probe to measure the turbulent field distal to the constrictions in steady flow with a parabolic upstream velocity profile. The constrictions were axisymmetric but had a rectangular cross-section in the axial plane as compared to the smoothly contoured cross-section used by the previously discussed authors. The sensor was a platinum film applied to the wedge-shaped end of a 0.06 inch diameter quartz rod. The rod was inserted radially through the tube wall into the center of the flow tube. Turbulence spectra were reported in the range of 10 to 1000 Hz for Reynolds numbers of 800 to 2000. The data shows that as the flow becomes more constricted, the overall turbulence intensity increased and the spectral distribution showed elevated high frequency content. However, very little indication of discrete vortex shedding was seen. The absence of discrete frequencies could have been caused by the constriction shape or possibly the probe support interfering with the flow patterns sensed by the hot film probe.

Yellin[6] reported on measurements of the pressure fluctuations made by inserting a phonocatheter radially into the turbulent field downstream of their orifice plates in a rigid tube. Relative increases

in turbulent intensity and high frequency content with increasing Reynolds number were observed. However, no correlation with Aeolian tone theory (discrete vortex shedding) could be seen. As with the Kim and Corcoran data[8], the radial positioning of the phonocatheter presents a good possibility of the probe interfering with the local fluctuations.

1.4.3 Relationship of Present Investigation to Published Results

In summary, there exists a large collection of information on the development of the orderly vortex growth and the random structure of turbulence in free jets issuing from pipes, orifices and contoured converging nozzles. The development of discrete vortices, or Aeolian tones, downstream of orifices contained in a pipe (or bounded jet flow) has also been investigated extensively. However, the development of a more random turbulence downstream from the large scale vortices has not been thoroughly documented and the effects of other constriction shapes or the degree of the constriction have not been considered.

The stenotic flow calculations have considered only idealized cases with no flow instabilities present. Very meager data (and often contradictory with pipe orifice flow data) are available on the development of instabilities and turbulence in steady flow and no detailed measurements are presently available on the radial and axial variations of turbulent energy spectra in steady or pulsatile flow.

The experiments reported in this thesis are designed to explore the spatial distribution and energy content of turbulent fields distal to simulated stenosis in both steady and pulsatile flow over a range

of flow conditions approximating physiological values. Axisymmetric occlusions, rather than asymmetric or irregularly shaped occlusions, are used so that the basic vortex shedding and turbulence formation phenomena can be studied in detail with simply defined shapes. However, both sharp-edged and smoothly contoured constrictions are employed to demonstrate the effects of protuberance shape on the resulting turbulent field. The effects of tube wall elasticity are likewise eliminated from generating additional complications by using rigid tubes.

CHAPTER II

DESCRIPTION OF THE PHYSICS OF FLOW THROUGH SUBTOTAL STENOSIS

As a basis for discussing the experimental results, a general, unified description is presented here of the flow field through an axisymmetric occlusion for both steady and pulsatile flows as related to applicable similarity parameters. This physical description of the flow phenomena has been drawn from the references cited in Chapter I and from the flow visualization results which are presented in detail in Chapter III.

2.1 Similarity Parameters

The fluid mechanics of blood flow through the normal cardiovascular system has been studied theoretically and experimentally by numerous investigators.[28,29,30,31,32] A description of the flow through the arterial system is complicated by the following physiological factors:[33]

1. the ejection of blood from the heart is complex
2. blood is a non-Newtonian fluid
3. the elastic properties of the vessel walls are non-uniform and non-linear.

Furthermore, the blood flow in the arterial system is pulsatile with the pulse shape changing as the wave propagates through the elastic and tapered vessels.

Two parameters which arise from similarity considerations of pulsatile flow are the Reynolds number and the frequency parameter. The Reynolds number, R_e, is defined as:

$$R_e = \frac{\rho V D}{\mu}$$

where ρ = density

V = velocity

D = diameter of the tube

μ = viscosity

which is the ratio of the inertial and viscous forces. Phenomena in viscous steady flow such as entrance lengths, velocity profiles, transition to turbulence and separation are dependent on the Reynolds number. The frequency parameter, α, is defined as:

$$\alpha = R \sqrt{\frac{w\rho}{\mu}}$$

where R = radius of tube

w = frequency, radians/sec

which is the ratio of inertial forces due to oscillatory flow and viscous forces. The frequency parameter arises in the solution of the equations of motion for a viscous flow driven by a pressure gradient

which varies periodically. Characteristics such as flow resistance, phase velocity, velocity profiles, velocity wave damping and wave reflection have been shown to be functions of α[32,34]. The normal ranges for these similarity parameters in the human aorta are $5{,}000 < R_e < 12{,}000$ (based on peak velocity) and $13 < \alpha < 16$[32]. For this range of Reynolds numbers, turbulent flow might be expected for part of the velocity pulse. Turbulence in the aorta of dogs has been investigated by Nerem, et al.,[35] who showed that both R_e and α must be considered in predicting the onset of disturbed flow.

The particular values of α and R_e used in the present study are defined as follows:

$$\alpha = R \sqrt{\frac{2\pi F \rho}{\mu}}$$

where F = fundamental pulse rate,

$$R_{eD} = R_e \text{ in unoccluded steady flow}$$

$$= \frac{UD}{\mu}$$

where U = mean velocity in unoccluded flow

D = diameter of unoccluded tube,

$$R_{ed} = R_e \text{ at occlusion minimum area in steady flow}$$

$$= \frac{U_o d}{\mu}$$

where U_o = mean velocity at occlusion minimum area

d = diameter at occlusion minimum area

R_{eDP} = R_e in unoccluded pulsatile flow based on peak pulse velocity

$$= \frac{\rho U_p D}{\mu}$$

where U_p = peak velocity of pulse

and R_{edP} = R_e at occlusion minimum area in pulsatile flow

$$= \frac{\rho U_{op} D}{\mu}$$

where U_{op} = peak velocity at occlusion minimum area

2.2 Steady Flow Through an Axisymmetric Stenosis

Figure 1 shows a model of the flow through an axisymmetric constriction in a tube. Up is the flow velocity in the unoccluded tube and U_o is the flow through the minimum area. As the flow emerges from the minimum area of the constriction, the effective area of the jet continues to decrease in the axial direction and the velocity to increase due to the vena contracta effect. The degree to which the velocity increases and the axial location of the maximum velocity in the vena contracta will be influenced by the proximal constriction contour, the proximal velocity profile and the severity of the constriction. In the region immediately distal to the minimum area and in proximity to the tube wall is a recirculation region continuing relatively low energy flow. The actual flow separation point defining the beginning of this region depends on the wall pressure gradient, which of course is a function of the Reynolds number and the constriction shape. In the near-centerline region past the point of maximum velocity in the vena contracta, a system of vortex rings is formed. The eddy

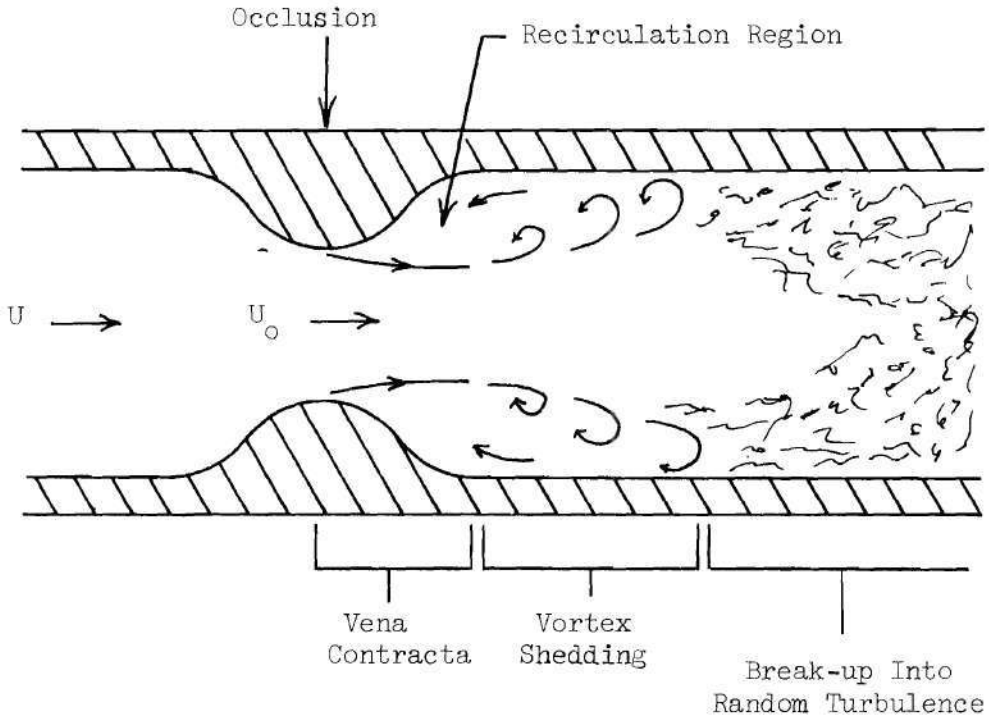

Figure 1. Steady Flow Through an Axisymmetric Occlusion

size of the vortex rings is governed primarily by the Reynolds number, $R_{e_d} = \rho U_o d/\mu$, with the eddy size decreasing with increasing Reynolds number. As a vortex ring travels downstream, the tendency is for adjacent ring pairs to coalesce to form a larger ring-like structure. This causes the observed shedding frequency to decrease with increasing axial distance from the constriction. For high enough Reynolds numbers, this vortex ring system breaks up into a more random distribution of eddy sizes characteristic of turbulence. This break-up of the more ordered structure can occur simply because; (1) the flow velocity is high enough in the jet to initiate the transfer of energy to eddies of smaller and larger sizes, and/or (2) the vortex rings interact with the tube wall. The interplay of these two factors will, of course, depend on the size of the constriction relative to the unoccluded area. For very low Reynolds numbers, the vortex ring break-up produces few smaller eddies and the ring-like disturbance quickly dissipate upon contact with the wall. If turbulence does result from the breakup, it may (depending on Reynolds number) gradually dissipate at more distal positions or it may reach an energy distribution among the eddies which is characteristic of fully developed turbulent pipe flow.

2.3 Pulsatile Flow Through Axisymmetric Stenosis

The behavior of pulsatile flow through constrictions in tubes is more complex than the steady flow case. The velocity pulse waveform typical of those found in a physiological situation is relatively complex in that it is composed of a number of harmonics of the funda-

mental pulse rate, and may have a reverse flow component. For the purpose of illustrating the basic phenomena present in post stenotic flow, a simpler sinusoidal-like waveform is employed. Following this somewhat simplified model is a brief discussion of other physically significant perturbations.

A pulsatile velocity waveform proximal to the partial occlusion is represented by the solid line shown in Figure 2. The resulting velocity pulse through the minimum area of the occlusion is depicted by the dashed curve. The peak pulse velocity proximal to the occlusion is denoted by U_p, and U_{op} is the peak pulse velocity at the minimum area of the occlusion. The difference between U_{op} and U_p depends not only on the geometrical area change, but also on the shape of the occlusion upstream of the minimum area. This shape influences the vena contracta, or effective minimum area, of the occlusion. At time (a) the mean velocity is zero and some turbulence generated in the previous pulsation lingers in the region distal to the occlusion. At time (b) the velocity through the occlusion has not yet reached that required for separation and the turbulent field from the previous pulse is being moved downstream. At time (c) the separation velocity U_s, is reached in the minimum area and vortices are shed which dissipate to form a turbulent field as they move downstream. From the times (c) through (d) and (e), vortices are continually shed to form random turbulence downstream. At time (d) the velocity through the minimum area reaches a maximum, U_{op}. The shedding frequency of the vortices at a given time is dependent on the instantaneous Reynolds number based on the conditions at the minimum area of the occlusion. For low peak Reynolds numbers,

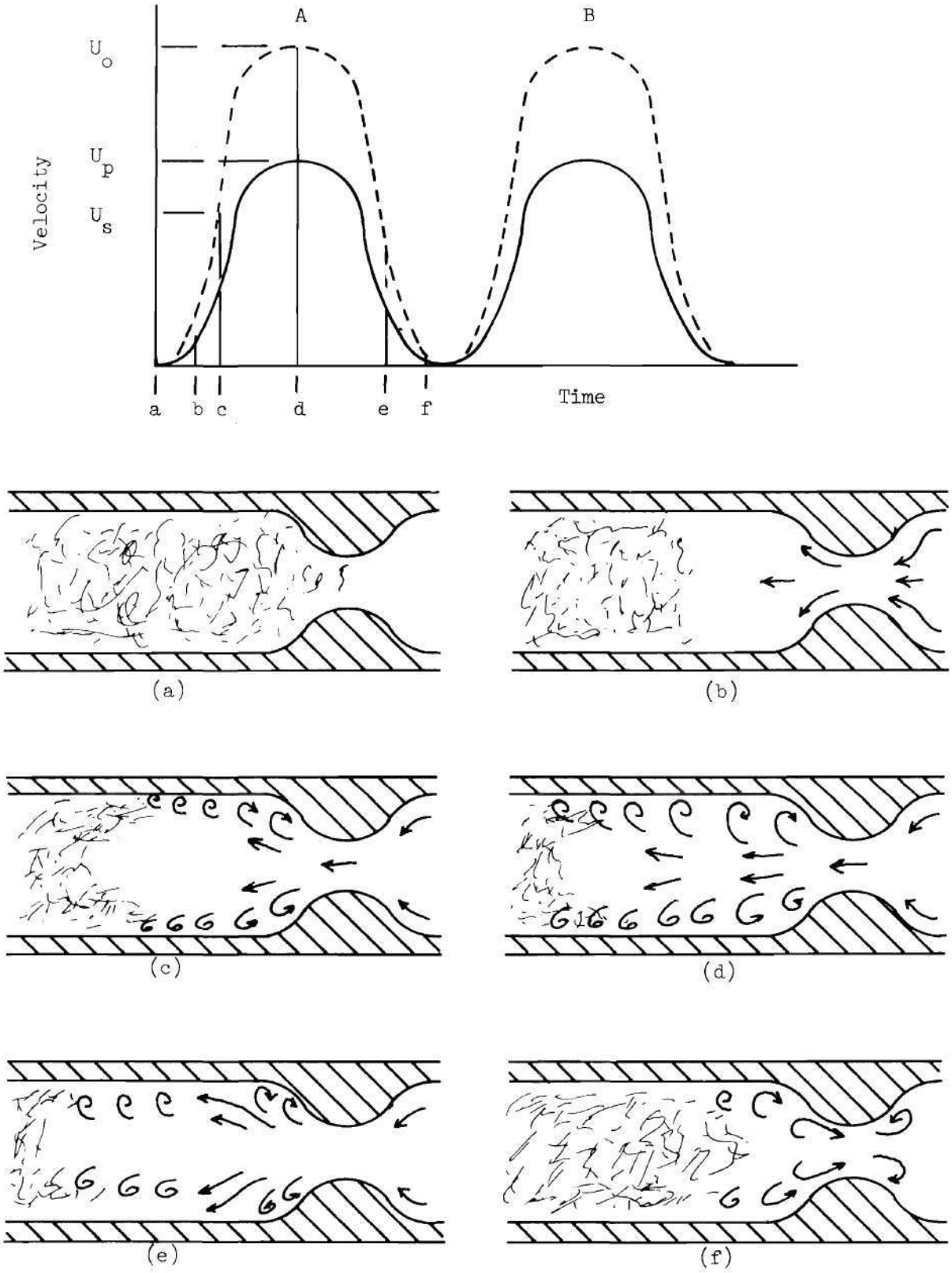

Figure 2. Pulsatile Flow Through Partial Occlusions

a large vortex ring can form downstream of the minimum area and swirl toward the center of the tube. The size of the vortex ring depends on the pulsation rate of the main flow and the degree of occlusion. It is emphasized that, contrary to a steady flow case where the separation region can be filled with a low velocity, low turbulence flow, the pulsatile "separation region" can be filled with a relatively violent, swirling vortex ring for an axisymmetric occlusion. The shape of the occlusion (sharp versus rounded) will probably influence the shedding frequency but this factor has not been investigated extensively. As the velocity decreases from (e) to (f) the flow reattaches to the surface and the turbulent eddies and vortices are carried downstream. At time (f) when the mean velocity is essentially zero, the remaining vortices and turbulent eddies can actually recirculate flow upstream of the minimum area. These eddies are then moved downstream as the mean velocity begins to increase in the next pulse and the process repeats. The length of time and distance that the turbulent eddies persist in the following pulsation is dependent on the fluid viscosity, the degree of occlusion and the waveform of the driving velocity pulse. The degree of occlusion, and to some extent the occlusion shape, influence the point at which the relatively large vortices of the turbulent jet interact with the wall and dissipate into smaller scale turbulence.

Among the fluid mechanical factors which may have a noticeable effect on the turbulent flow are:

1. velocity waveform and harmonic content; i.e., the acceleration and deceleration in the pulse can have stabilizing or destabilizing

effects on the development of instabilities, and the harmonic content may cause some frequencies to prevail more than others.

2. funadmental pulse rate and frequency parameter; i.e., for low pulse rates and frequency parameters the turbulence could possibly dissipate within the first pulse length; whereas for high pulse rates and frequency parameter, the dissipation times could be comparable to the pulse duration and the turbulence would linger into the second or third distal pulse lengths.

Factors which are related to the vessel geometry and construction are:

1. vessel elasticity; this variable would have an effect on the selective damping or possibly amplification of frequencies present in the flow. Since the stress-strain relationship for blood vessels is nonlinear, the blood pressure level might also be a synergistic factor.

2. occlusion shape; realistic shapes for stenoses are not axisymmetric, smoothly contoured, or sharp-edged but usually found to be non-symmetric, irregularly shaped and may have several localized minimum areas. These shapes would tend to break-up the orderly formation of vortices and produce a more randomized turbulent structure.

CHAPTER III

EXPERIMENTAL APPARATUS

3.1 Water Flow System

All of the experiments were conducted in the same basic flow system shown in Figure 3. The components consist of a pump and flowmeter, flow straightening inlet, test section tubing, occlusion couplings, occlusion, probe mounting station, constant head return tank, return flow piping and control valves. The pump and flowmeter configurations were different for the steady flow and three different pulsatile flows. All cases utilized a 1 inch I.D. x 1/8 inch wall plexiglas tubing for the test section. Also common to all the experiments were the probe mounting station and the occlusion couplings shown in Figure 4 and the occlusion shapes which are detailed in Figure 5.

3.1.1 Steady Flow Pumping System

The pump and flowmeter system for the steady flow cases is shown schematically in Figure 6. The pump was a Teel Model 1P677 centrifugal pump. The flow control valve and the float type flowmeter (Fischer and Porter) were used to set the proper flowrate. The occlusion site was located approximately 4D downstream from the tube entrance. This short entrance length yielded a laminar flow with a relatively flat velocity profile upstream of the occlusion for all the Reynolds numbers used.

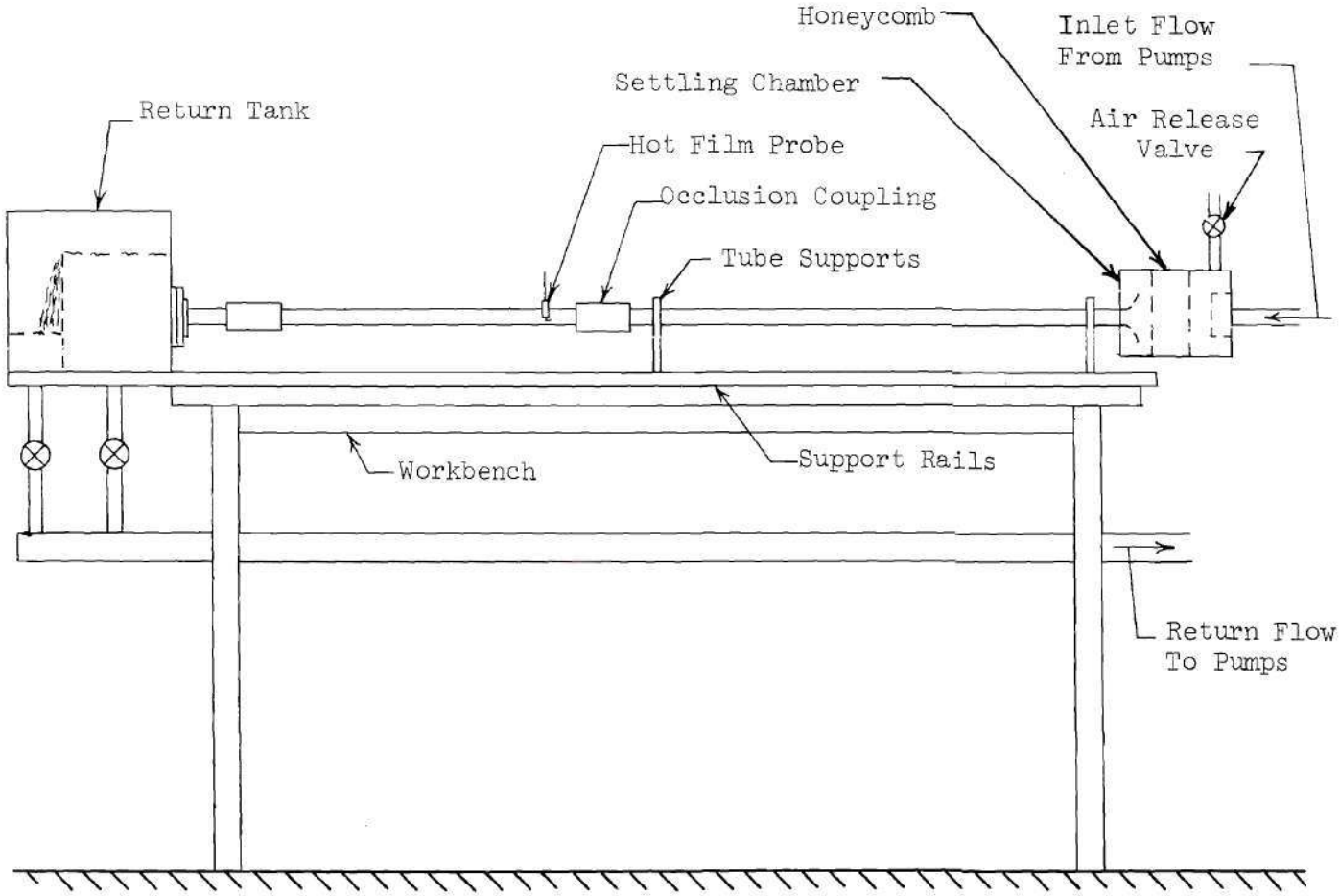

Figure 3. Water Flow System

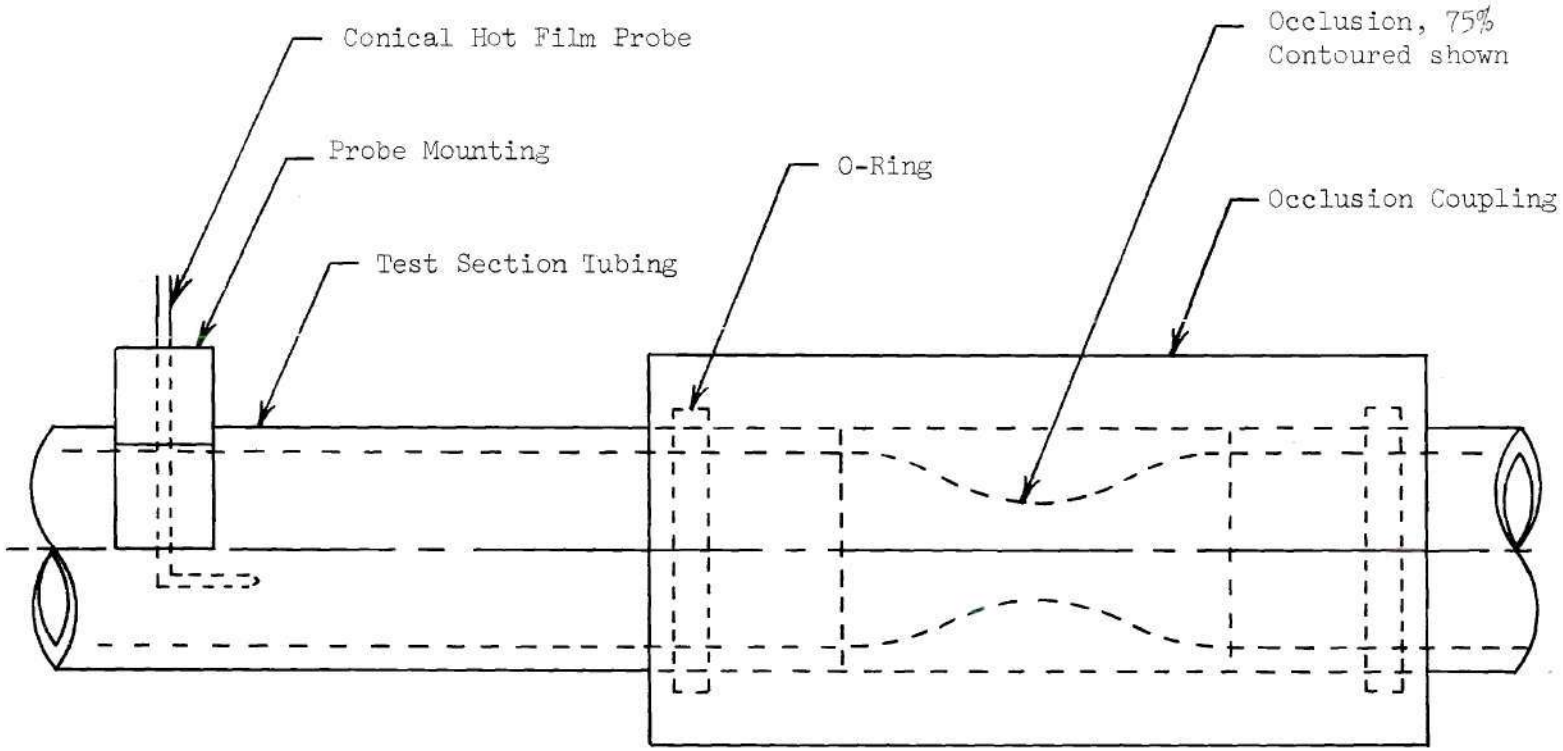

Figure 4. Occlusion Coupling and Hot Film Probe Mounting

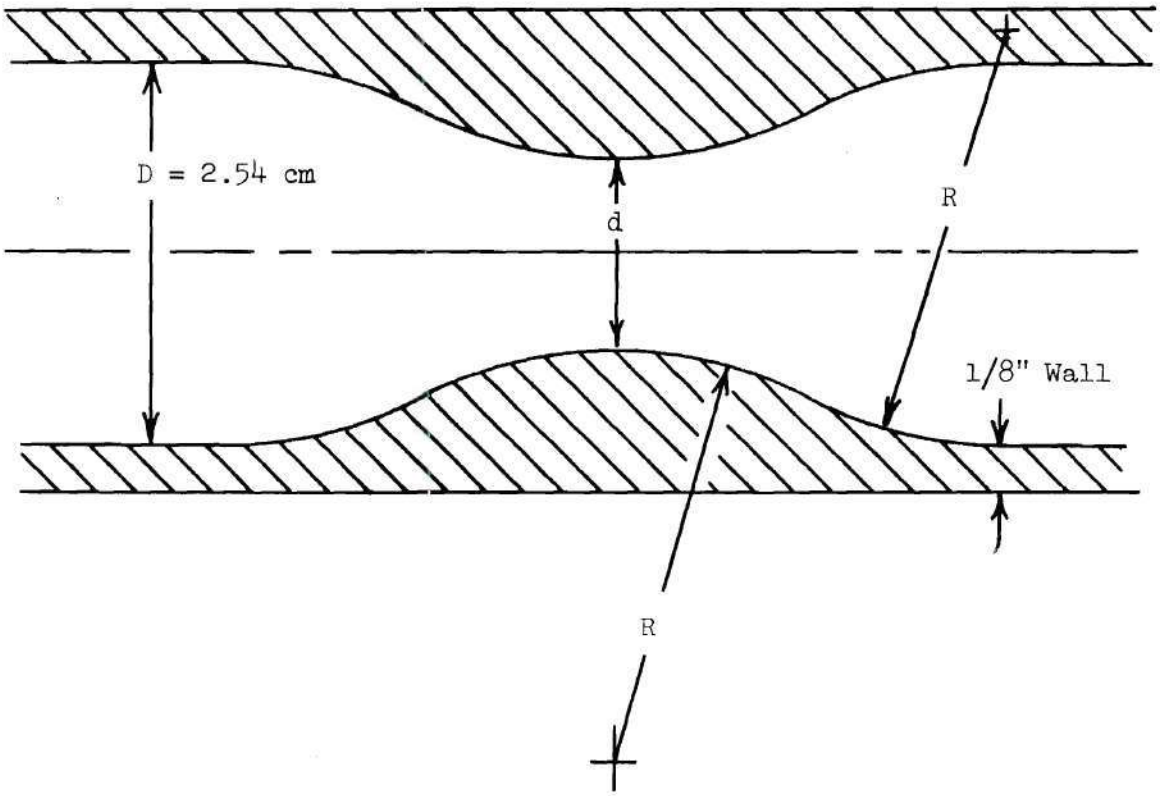

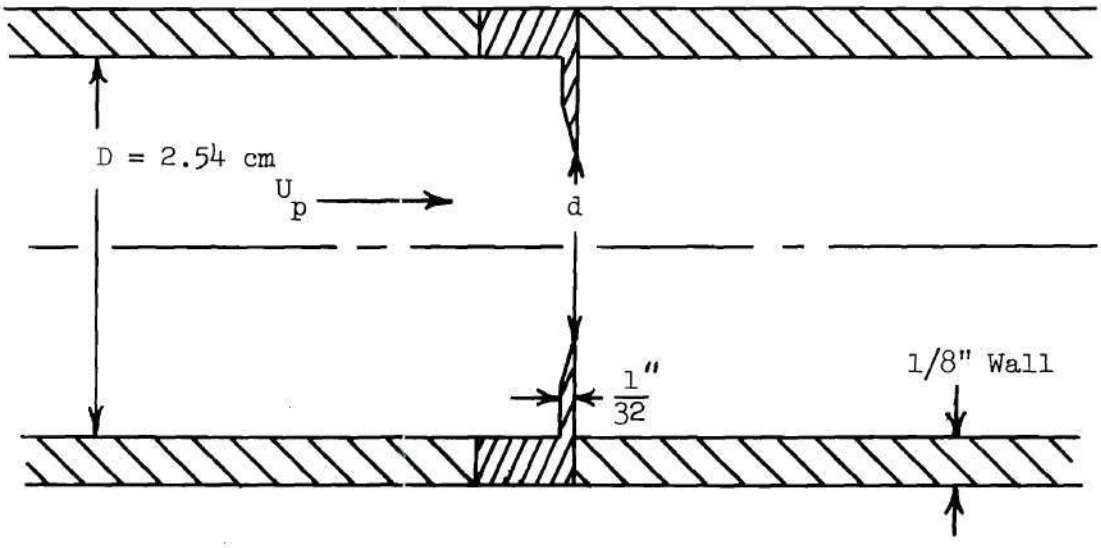

Figure 5. Occlusion Geometries

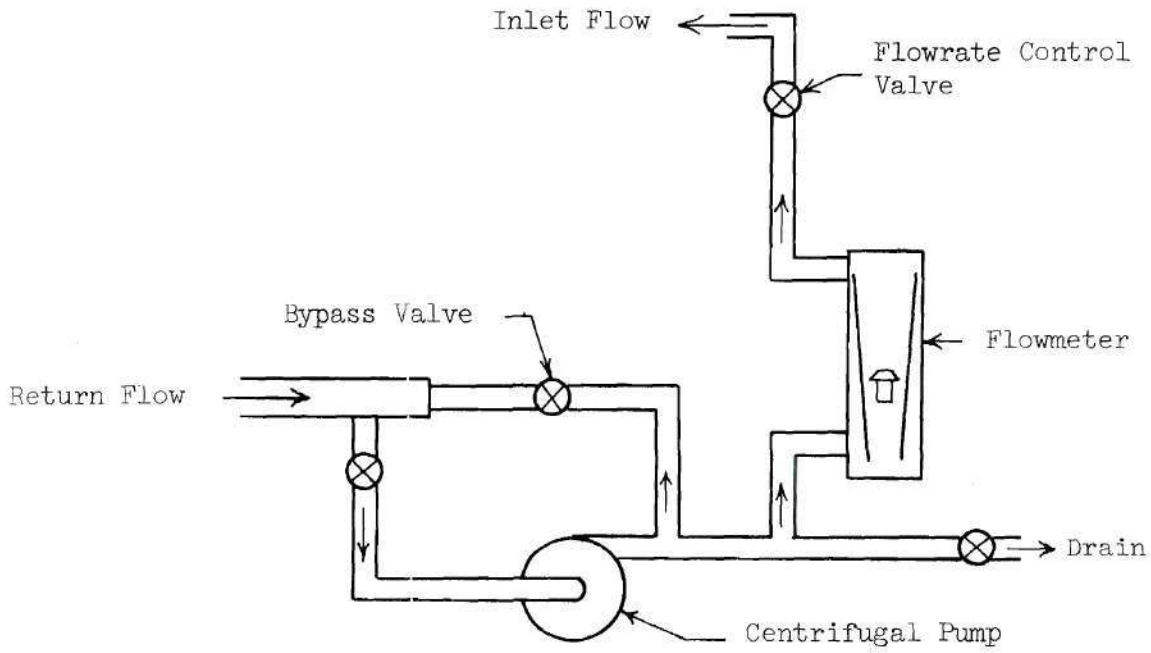

Figure 6. Steady Flow Pumping System

3.1.2 Pulsatile Flow Pumping Systems

Three different pulsatile pump systems were used in the course of these experiments. Each system was adjusted by trail and error until the desired waveform was achieved. However, none of the systems were capable of producing an approximation of a physiologically realistic waveform. Also, none of the pumping configurations could produce the same waveform over a wide range of peak Reynolds numbers and frequency parameters. The occlusion site was located approximately 36 D from the test section entrance to eliminate any entrance effects on the pulse proximal to the occlusion.

The piston pump was a Milton Ray Company Model H20 which incorporated dual pistons driven by a variable speed gear reduction drive motor. The piston travel and phasing could be adjusted mechanically. The plumbing arrangement of the control valves, check valves, and Latex tubing shown in Figure 7 permitted the velocity pulse height and shape to be adjusted. By trial and error adjustment of the valves and flexible tubing length, the elasticity of the tubing was utilized to yield smoother pulses. The adjustment of the valves was checked by measuring the velocity waveform and energy spectra upstream of each occlusion before each data run.

The roller pump was part of a Cardiovascular Electrodynamics Incorporated heart-lung machine. The pump casing was modified so that the roller was in contact with the flexible tubing for only 180° of the roller revolution. Valving and lengths of flexible tubing similar to those employed with the piston pump were also used here to allow adjustment of the pulse shape. Pulse waveform and energy spectra

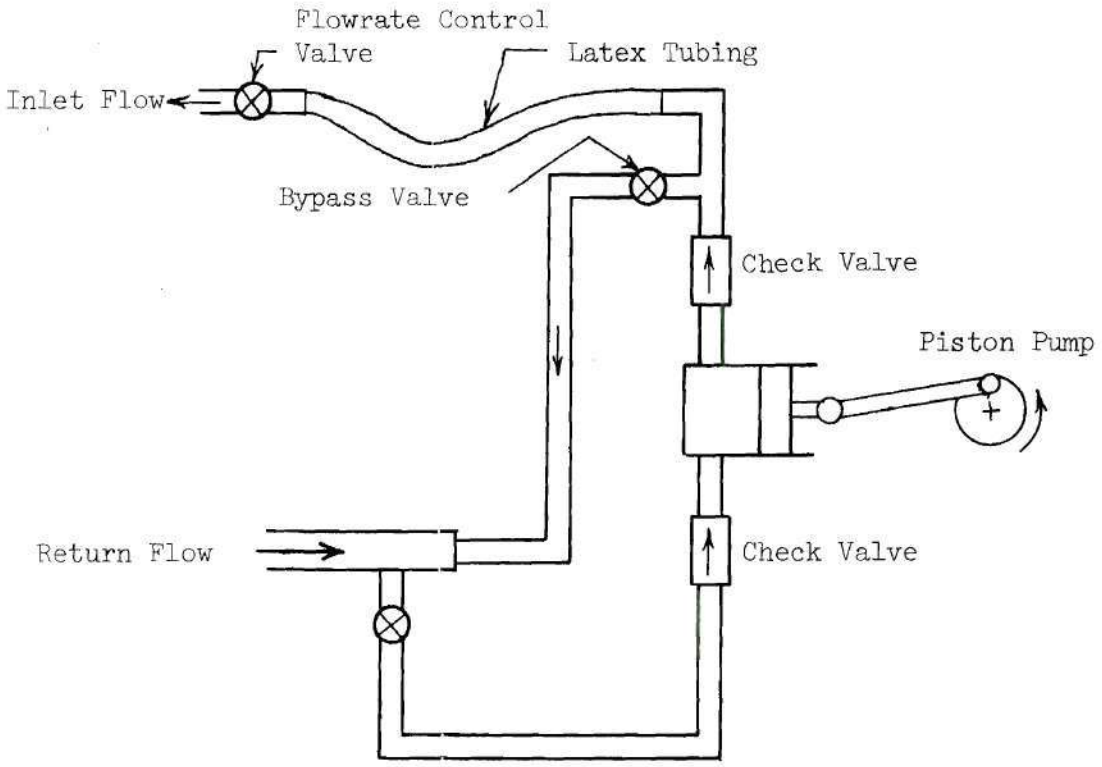

Figure 7. Pulsatile Flow Pumping System, $\alpha = 45$, $R_{e_D} = 15{,}200$

repeatability were also checked before each data run.

Neither the piston pump alone nor the roller pump discussed in the previous paragraphs were capable of satisfactory operation at low Reynolds numbers and frequency parameters, so the configuration shown in Figure 8 was assembled. The centrifugal pump furnishes a steady flow upon which is superimposed an sinusoidally varying pulse by the piston pump with the check valves removed. The pulse rate was controlled by the variable speed drive on the piston pump and the mean flowrate from the centrifugal pump was set with the flowmeter and control valves. An electromagnetic flowmeter (Carolina Medical Model 501) was used in the initial set up of the system to check the pulse rate and flowrate. After experience was gained with the system, it was found to be unnecessary to monitor the electromagnetic flowmeter at all times. However, it was required to leave the air release valve on the settling section partially open to damp out very noticeable flow oscillations in the test section.

3.2 Instrumentation

All of the instruments which were used in the experiments are briefly described in the following sections. The complete data acquisition system for the velocity and energy spectra measurements is illustrated in Figure 9.

3.2.1 Hot Film Anemometer System

The velocity measurements were performed using a commercially available minature conical hot film probe, anemometer, and linearizer. The conical probe geometry simplifies insertion into the artery in the

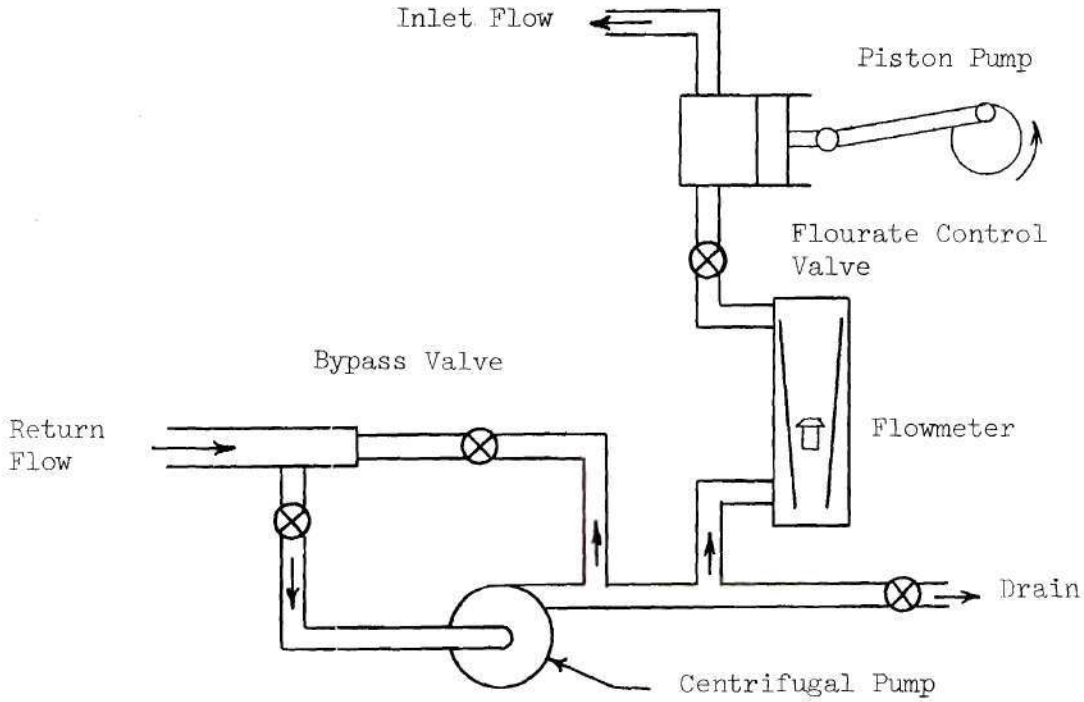

Figure 8. Pulsatile Flow Pumping System, $\alpha = 15$, $R_{e_D} = 2540$

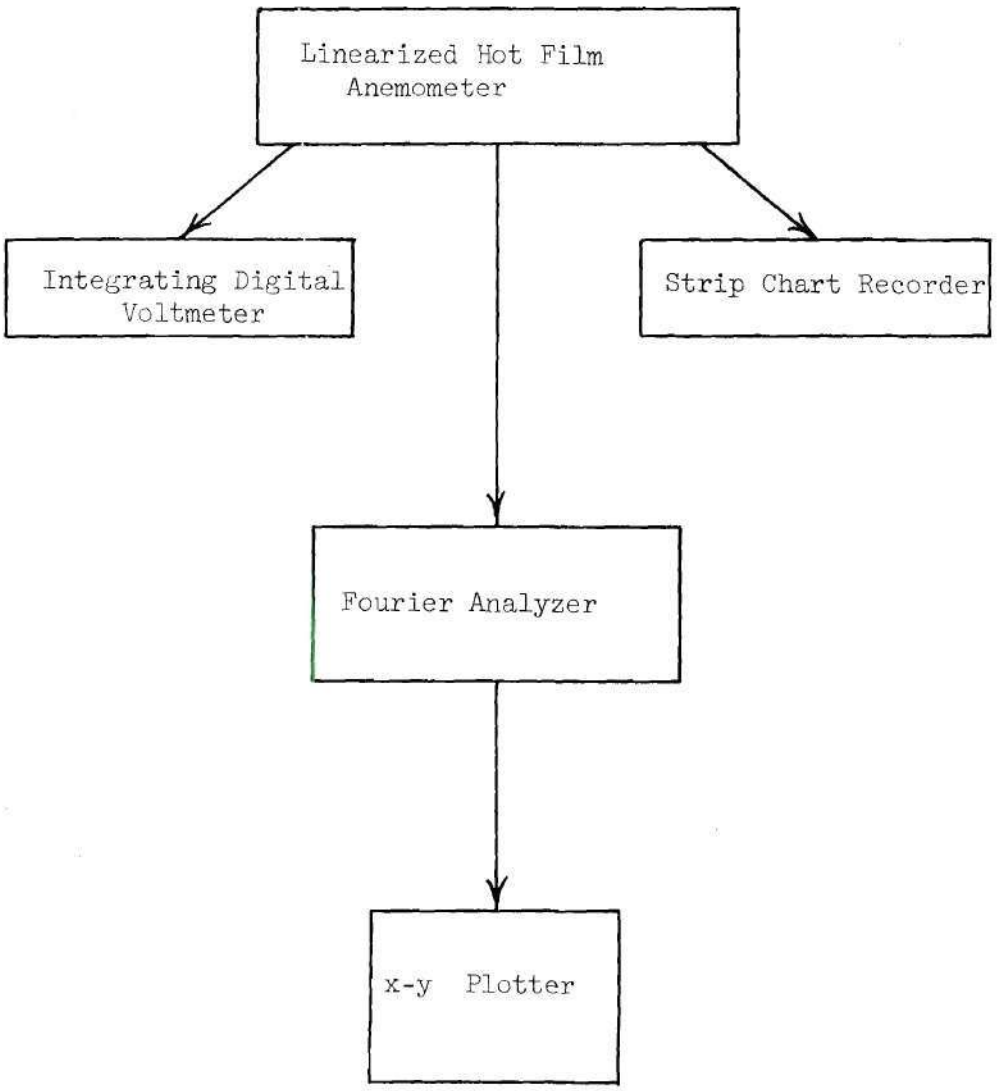

Figure 9. Data Acquisition System

in vivo experiments and was used here so that a direct comparison could be made with the in vivo data trends. A more complete description of the anemometer system and operating procedure is presented in the Appendix.

3.2.2 Strip Chart Recorder

The strip chart recorder was an HP Model 7702B two channel recorder with HP Model 8802A preamplifiers and has a frequency response of 20 Hz. It was used for recording the analog velocity output from the anemometer linearizer.

3.2.3 Digital Voltmeters

A digital voltmeter (Fluke Model 8000A) was used for visually monitoring the linearizer output and for setting the linearizer to fit a particular calibration. An integrating digital voltmeter (HP Model 2401C) was employed to monitor the anemometer output during the experiment and to measure the mean velocity in steady flow by integrating for 50 seconds and then taking the average.

3.2.4 Fourier Analyzer

The turbulent energy spectra were obtained by subjecting the entire linearized velocity waveform signal, in both steady and pulsatile flow, to Fourier analysis using an HP Model 5452A Fourier Analyzer. The frequency range to be analyzed, frequency resolution, sample time, and number of samples could be quickly adjusted to desired values. For all the steady flow data, the α = 31.8, 45, R_{eD} = 5080 data and the α = 45, R_{eD} = 15,200 data, the frequency range was DC to 512 Hz with a frequency resolution of 1 Hz. Fifty samples of one second duration were taken from the analog signal. Each one second sample was digitized,

the Fourier transform and power spectral programs performed and then the averaged result was plotted on an x-y plotter. The entire operation for one plot with these settings takes approximately three minutes. For the $\alpha = 15$, $R_e = 2540$ data, the frequency range was DC to 204.8 Hz with a frequency resolution of 0.2 Hz.

The energy axis output of the Fourier analyzer is of a form:

$$\overline{E} = \frac{u'^2_f}{U^2_{ref}\,\Delta f} \tag{3.1}$$

where Δf = frequency resolution

u'_f = velocity flucuation component at frequency f in bandwidth of about f

U_{ref} = reference velocity

3.2.3 Cameras

The camera used for the flow visualization photographs in the steady flow experiments was a 35 mm Nikon F with a 50 mm lens. Tri-X film was used with a shutter speed of 1/250 sec. at F 11. The movie camera employed for the pulsatile flow visualization was a Bolex Model H16 whose frame speed could be varied from 16 to 64 frames per sec. Tri-X film was also used for the movies. Portable flood lamps were used to back-light by reflecting the light from white cardboard which was positioned behind the plexiglas flow tube.

CHAPTER IV

FLOW VISUALIZATION RESULTS AND DISCUSSION

This chapter presents the photographic results of the dye tracer studies of the steady flow through the occlusions. It should be noted that the dye is usually seen flowing along only the bottom portion of the flow or along the bottom separation streamline. Hence, it is not immediately obvious from the photographs alone that a three dimensional flow structure, such as a vortex ring, is present. However, three dimensional structures can be visualized during the conduct of the tracer study and are noted in the following descriptions. Movies of the pulsatile flow through the occlusions for the $\alpha = 15$, $R_{eD} = 2540$ case are available through the School of Aerospace Engineering, Georgia Tech, but are not discussed in detail here. The pulsatile flow dye tracer results served as a basis for the discussion presented in Section 2.3.

4.1 Comparison of Flow Through Sharp Versus Contoured Occlusions

4.1.1 50% Occlusion, $R_{ed} = 449$, $R_{eD} = 318$, Figures 10 and 11

A slight flow instability can be seen florming near the wall downstream of the recirculation zone for the sharp occlusion case. However, the contoured occlusion case does not show any indication of an instability forming and only a small recirculation zone can be distinguished.

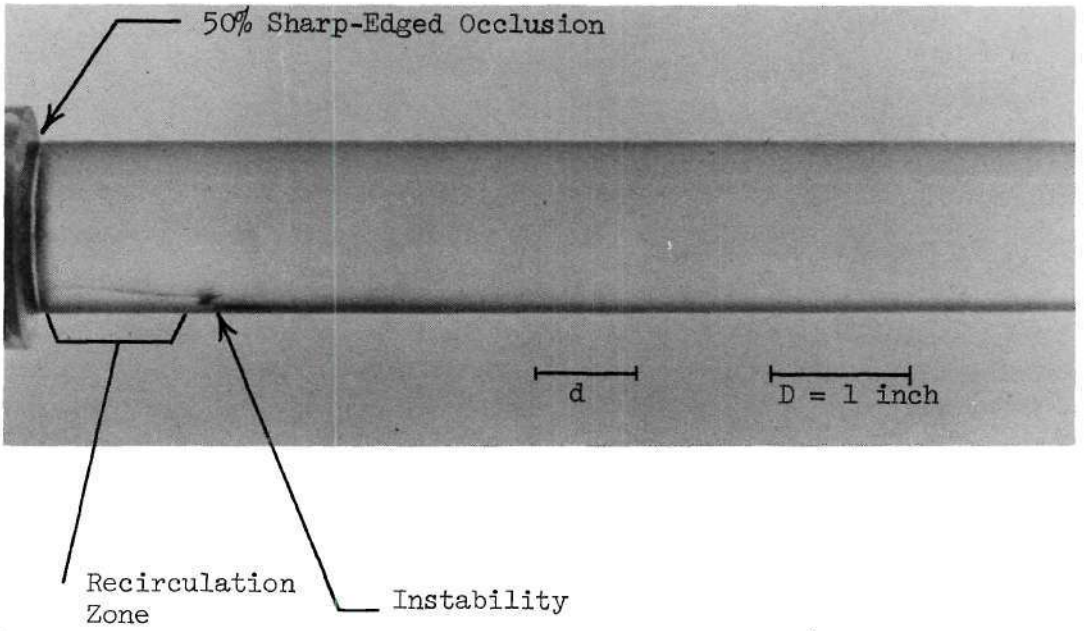

Figure 10. 50 Percent Sharp-Edged Occlusion, R_{e_d} = 499, R_{e_D} = 318

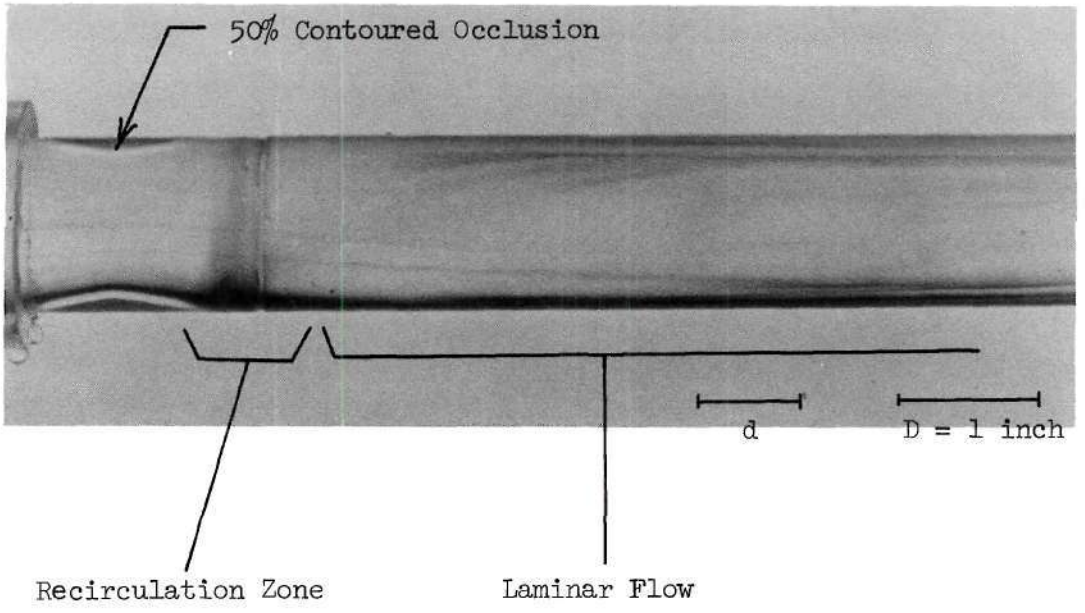

Figure 11. 50 Percent Contoured Occlusion, R_{e_d} = 449, R_{e_D} = 318

4.1.2 50 Percent Occlusion, R_{ed} = 893, R_{eD} = 635, Figures 12 and 13

The shape occlusion case shows a vortex ring, or instability ring, pattern which is broken up downstream of the large recirculation zone by contact with the wall. The contoured occlusion case does not have any flow disturbances present and only a small recirculation zone can be seen.

4.1.3 50 Percent Occlusion, R_{ed} = 1796, R_{eD} = 1270, Figures 14 and 15

The sharp occlusive flow has a definite vortex ring pattern and recirculation zone with the rings breaking up into smaller scale turbulence downstream of the recirculation region. Completely laminar flow with no visible instabilities still dominates the contoured occlusion case.

4.1.4 50 Percent Occlusion, R_{ed} = 3592, R_{eD} = 2540, Figures 16 and 17

The sharp occlusion results again show the vortex ring pattern which degenerates into smaller scale turbulence in a manner similar to the R_{ed} = 1796 case (Figure 14). However, the random turbulent eddies appear to be smaller than the R_{ed} = 1795 case. A large recirculation zone and large vortex ring structure now characterizes the contoured case. The vortex rings appear to break up by interacting with the wall to form relatively large scale random turbulent eddies.

4.1.5 75 Percent Occlusion, R_{ed} = 635, R_{eD} = 318, Figures 18 and 19

The flow through the sharp occlusion has a definite vortex ring pattern away from the wall which appears to coalesce and break up into more random turbulence. This picture is in contrast to the 50 percent sharp occlusion results for R_{ed} = 449 (Figure 10) and R_{ed} = 898 (Figure

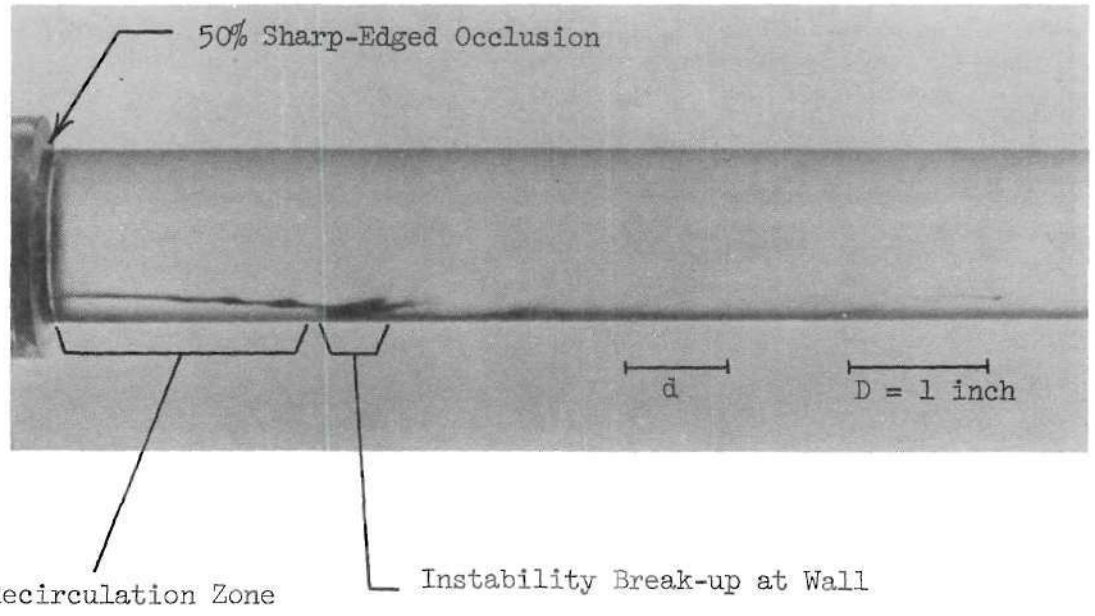

Figure 12. 50 Percent Sharp-Edged Occlusion, $R_{e_d} = 898$, $R_{e_D} = 635$

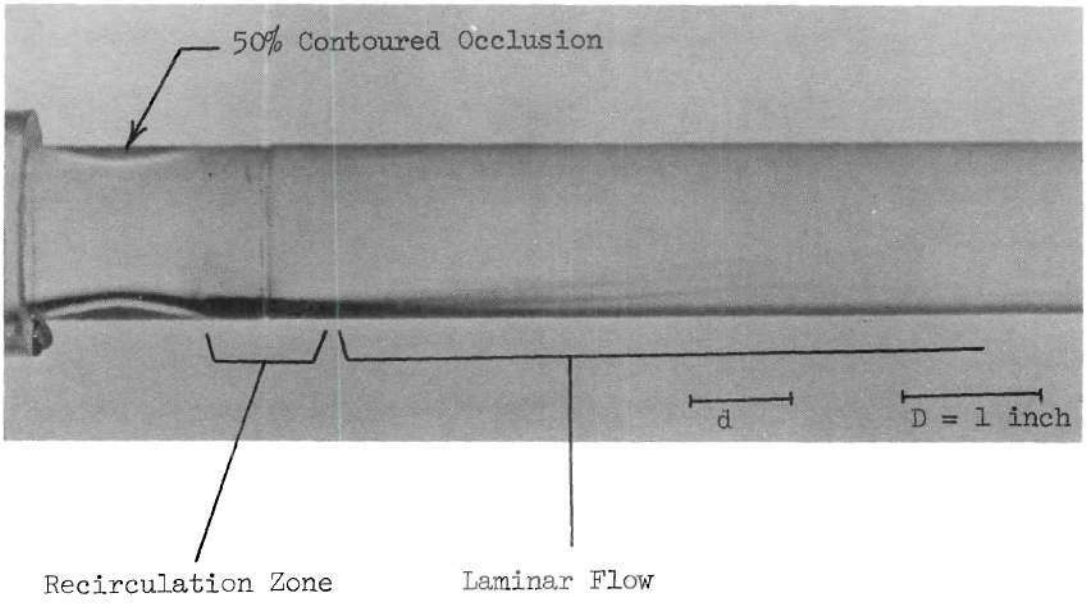

Figure 13. 50 Percent Contoured Occlusion, $R_{e_d} = 898$, $R_{e_D} = 635$

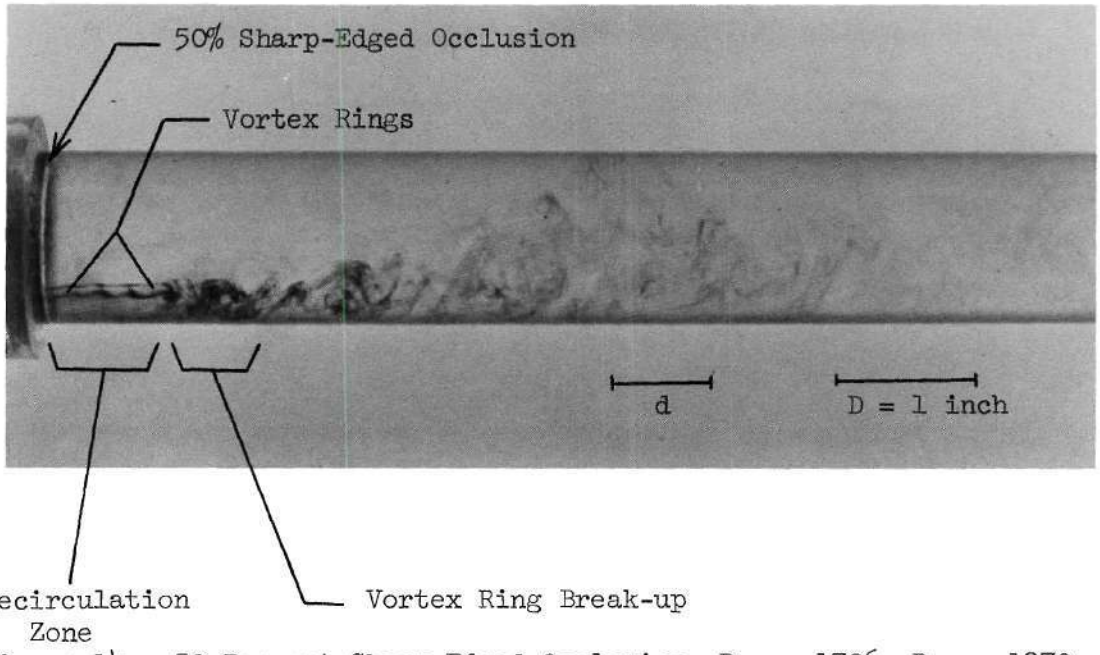

Figure 14. 50 Percent Sharp-Edged Occlusion, R_{e_d} = 1796, R_{e_D} = 1270

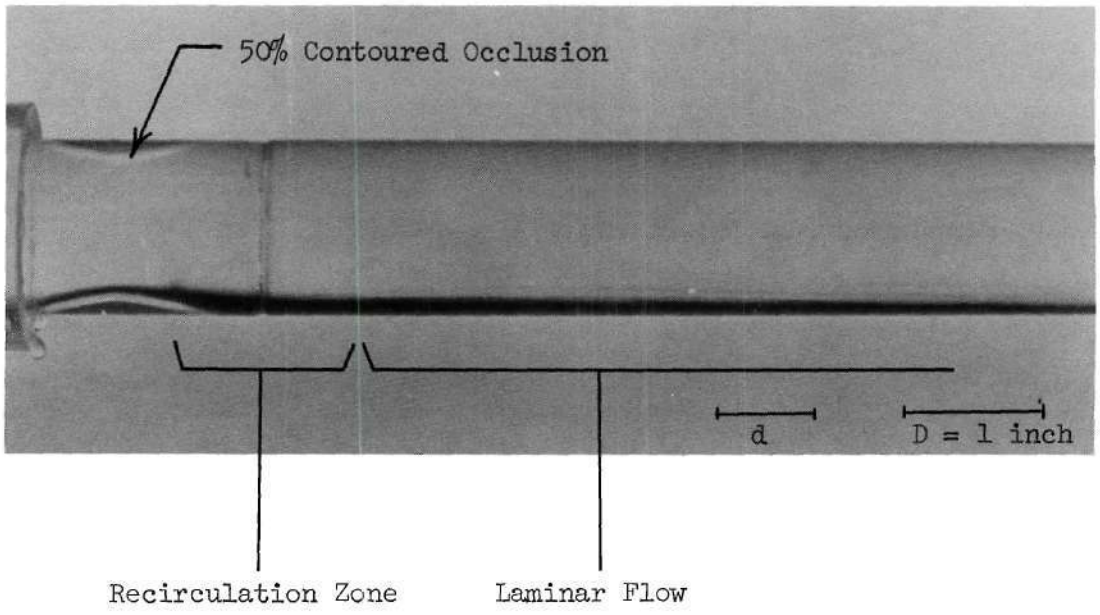

Figure 15. 50 Percent Contoured Occlusion, R_{e_d} = 1796, R_{e_D} = 1270

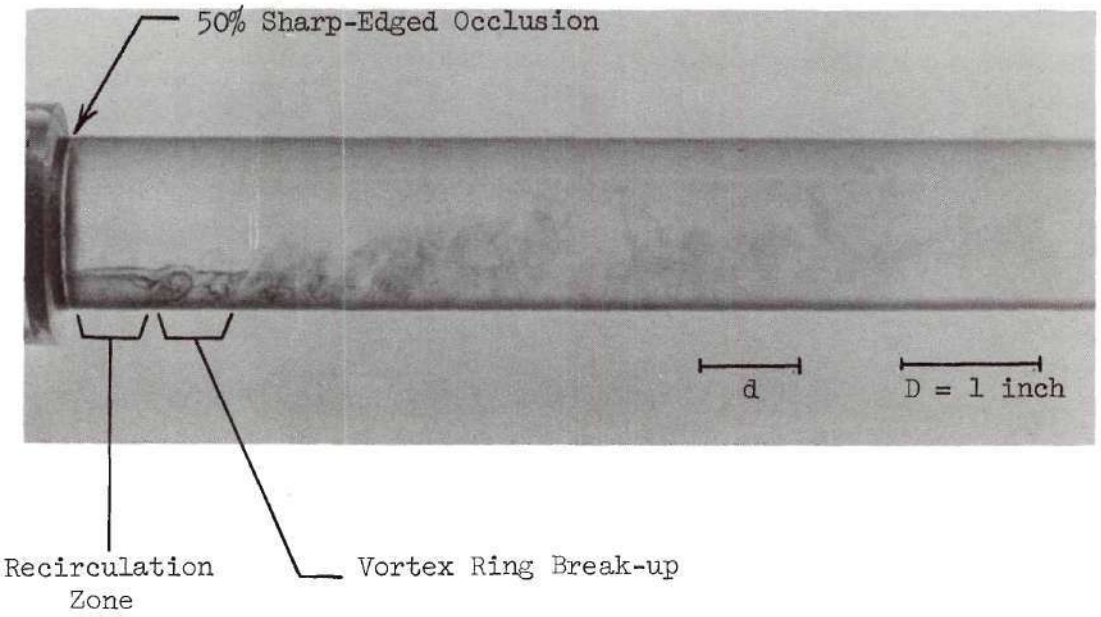

Figure 16. 50 Percent Sharp-Edged Occlusion, $R_{e_d} = 3592$, $R_{e_D} = 2540$

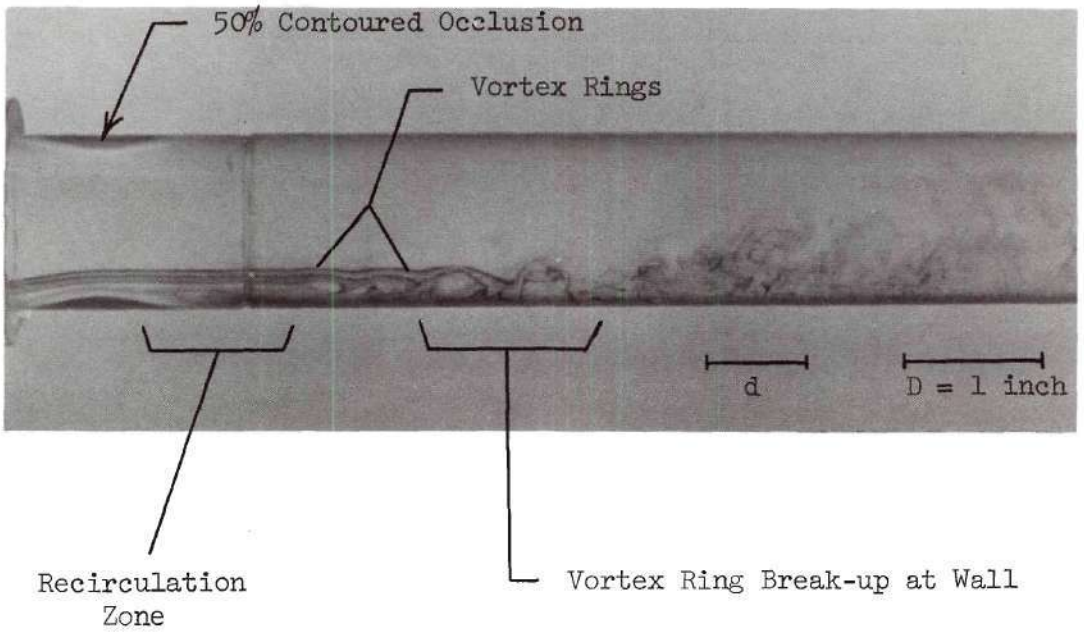

Figure 17. 50 Percent Contoured Occlusion, $R_{e_d} = 3592$, $R_{e_D} = 2540$

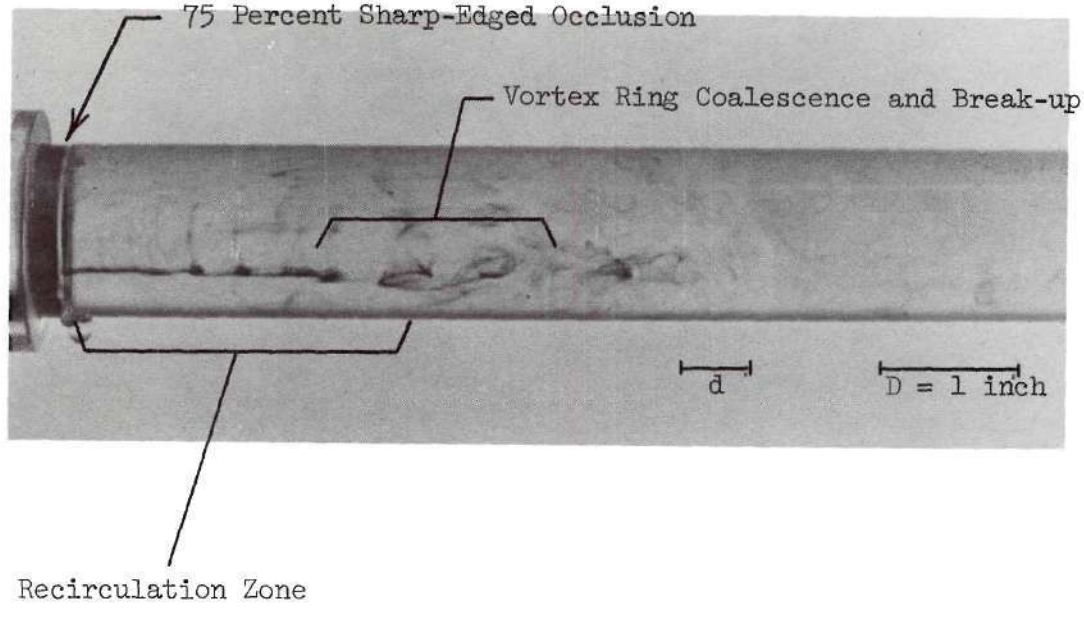

Figure 18. 75 Percent Sharp-Edged Occlusion, $R_{e_d} = 635$, $R_{e_D} = 318$

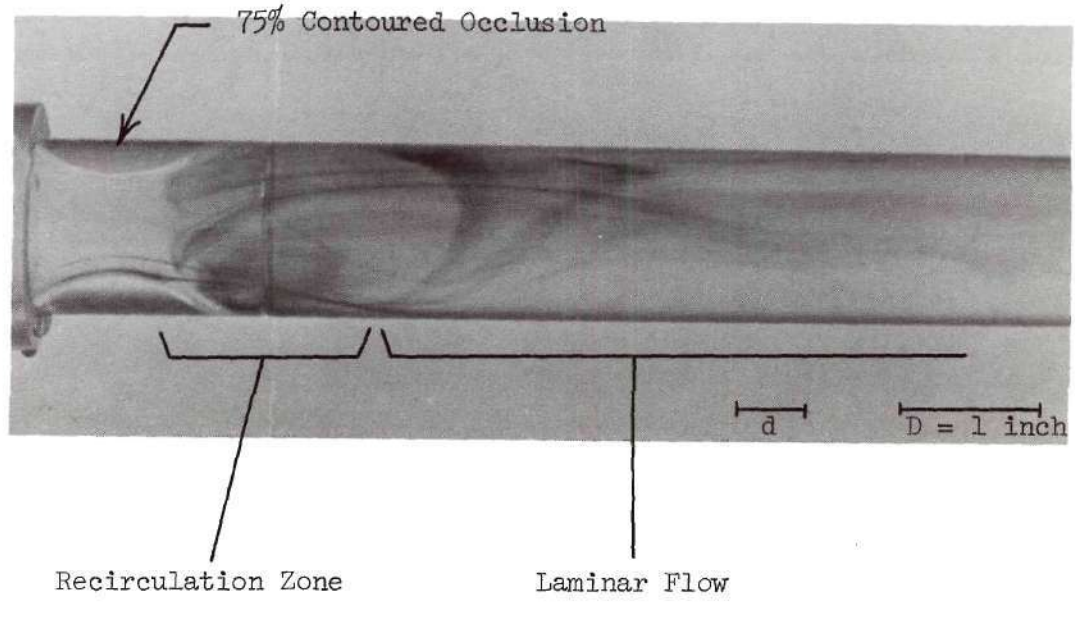

Figure 19. 75 Percent Contoured Occlusion, $R_{e_d} = 635$, $R_{e_D} = 318$

12) which do not show as extensive a vortex ring pattern development. The interaction of the 50 percent occlusive flow with the wall clearly retards the instability development. The contoured occlusion flow field shows the separation streamline and a laminar recirculation zone. No flow instabilities are visible in this case.

4.1.6 75 Percent Occlusion, $R_{ed} = 1270$, $R_{eD} = 635$, Figures 20 and 21

The vortex ring eddy size in the sharp occlusion case is smaller than the $R_{ed} = 635$ results (Figure 18) and the vortex structure breaks up away from the wall. An extremely large recirculation zone can be seen in the contoured occlusion case and a large scale flow instability appears which seems to interact with the wall and break up.

4.1.7 75 Percent Occlusion, $R_{ed} = 2540$, $R_{eD} = 1270$, Figures 22 and 23

The vortex ring structure in the sharp occlusion case breaks up into small random eddies without any obvious wall interaction. The vortex ring eddies in the contoured occlusion results are somewhat larger and form at a greater x/d than in the sharp occlusive flow. These eddies break up into turbulence but it is uncertain if this is spontaneous or a wall interaction phenomena.

4.1.8 75 Percent Occlusion, $R_{ed} = 5080$, $R_{eD} = 2540$, Figures 24 and 25

Both the sharp and contoured occlusion cases show a vortex ring formation and break-up, although the vortex rings in the contoured case form at a greater x/d than the sharp case.

4.2 Comparison of Flow Through 75 Percent and 90 Percent Sharp Occlusions

These comparisons are made for the same R_{ed} for both 75 percent

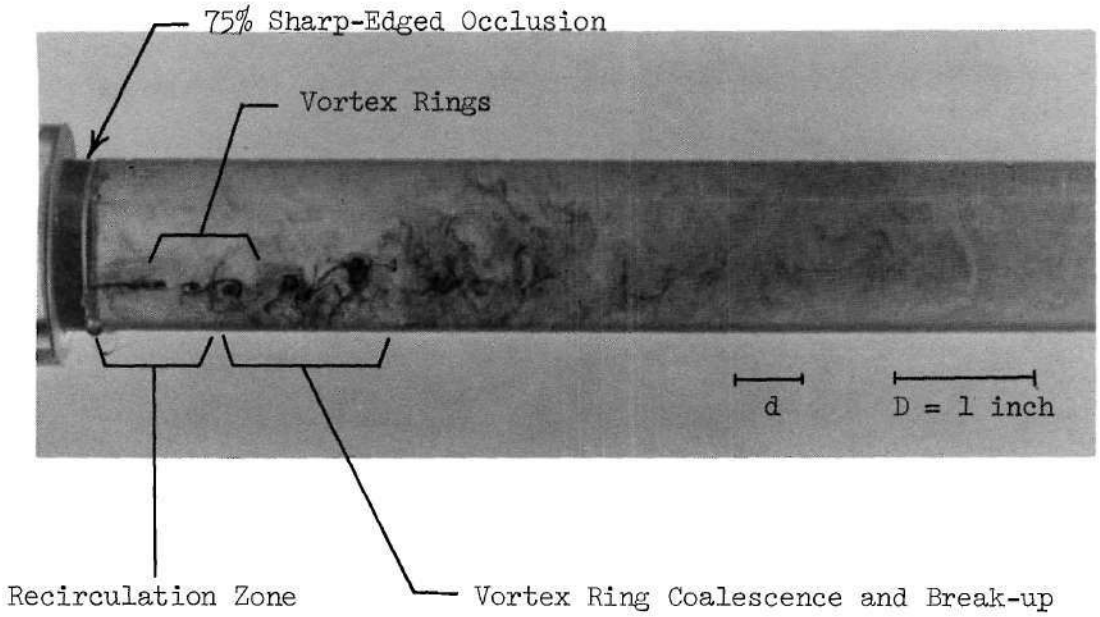

Figure 20. 75 Percent Sharp-Edged Occlusion, R_{e_d} = 1270, R_{e_D} = 635

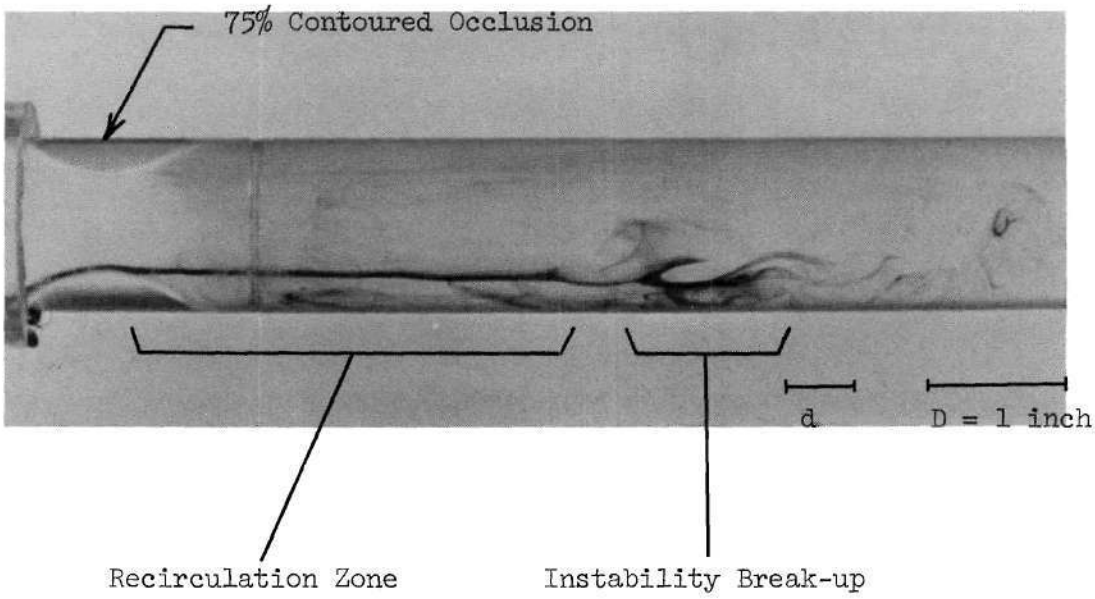

Figure 21. 75 Percent Contoured Occlusion, R_{e_d} = 1270, R_{e_D} = 635

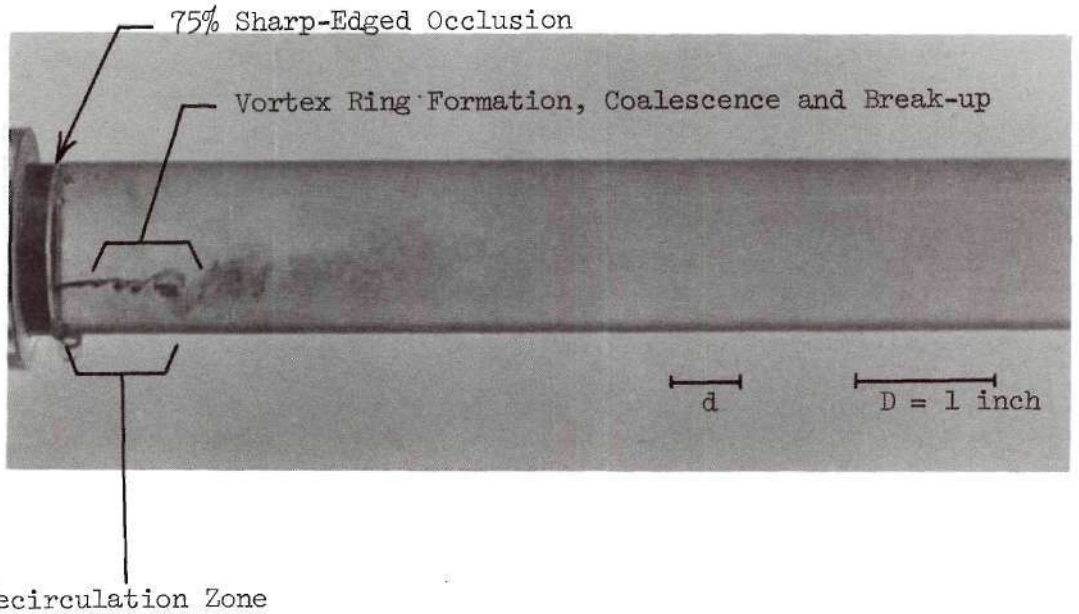

Figure 22. 75 Percent Sharp-Edged Occlusion, R_{e_d} = 2540, R_{e_D} = 1270

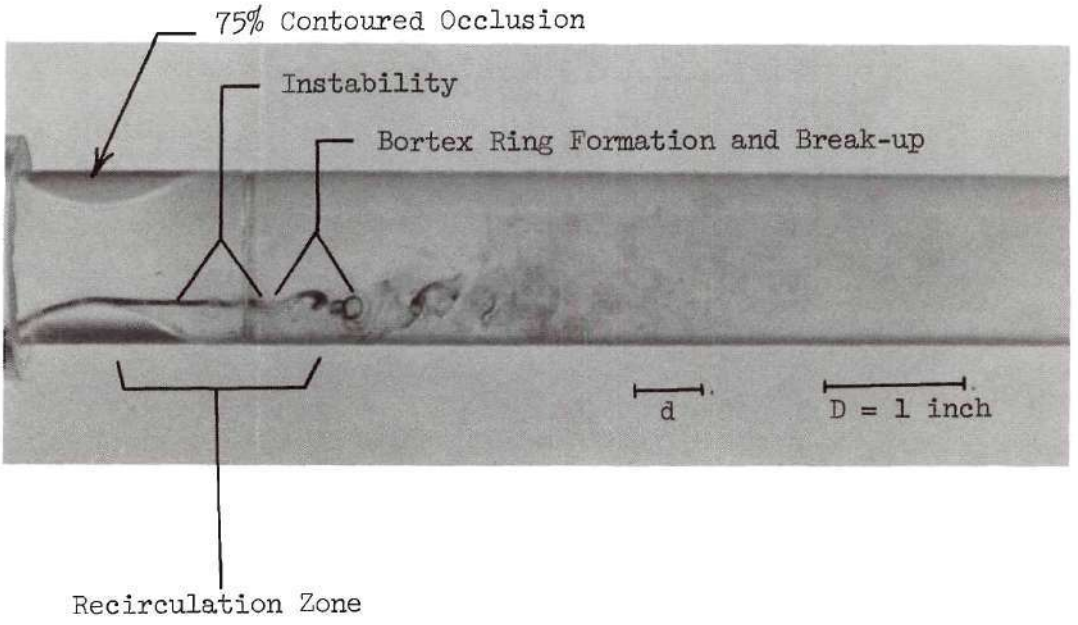

Figure 23. 75 Percent Contoured Occlusion, R_{e_d} = 2540, R_{e_D} = 1270

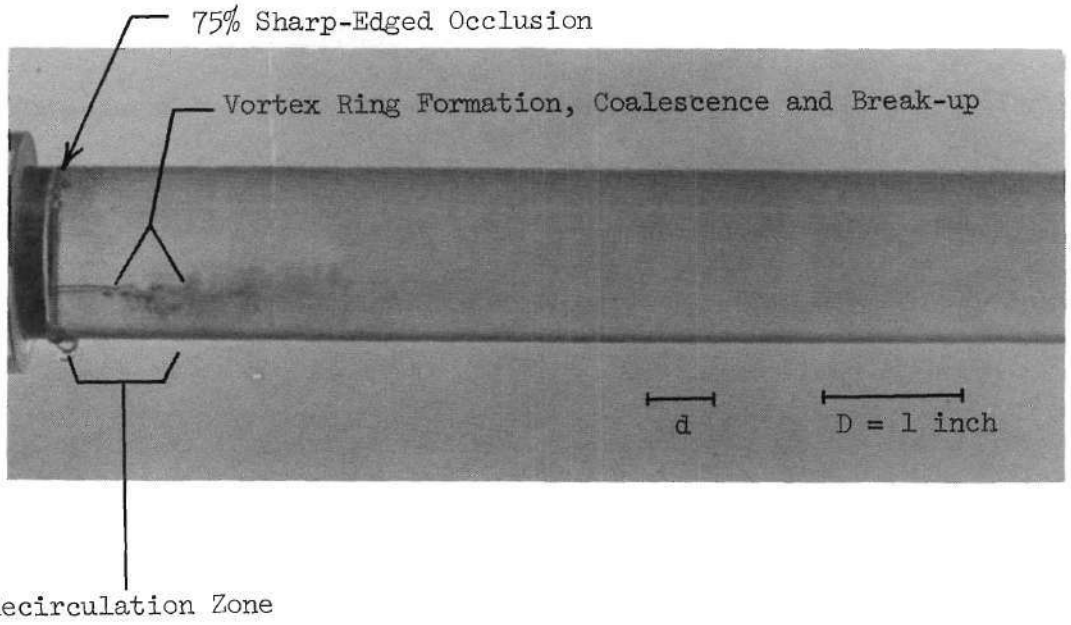

Figure 24. 75 Percent Sharp-Edged Occlusion, R_{e_d} = 5080, R_{e_D} = 2540

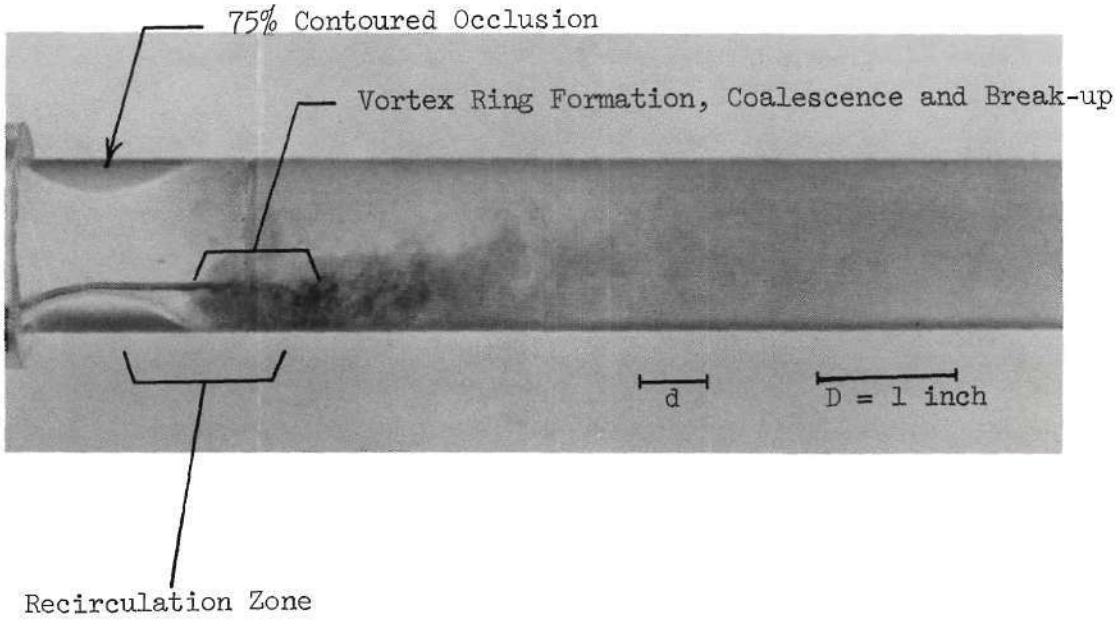

Figure 25. 75 Percent Contoured Occlusion, R_{e_d} = 5080, R_{e_D} = 2540

and 90 percent sharp occlusions, but for different R_{eD} and d/D ratio so that any wall interactions can be more clearly demonstrated.

4.2.1 R_{ed} = 635, Figures 26 and 18

The results for both cases show a distinct vortex ring pattern development, but the vortex eddies in the 90 percent case appear to be more of a rounded shape while the 75 percent case seems to have a more axially elongated shape. This elongation could be caused by the closer proximity of the vortex rings to the wall. Thr break-up of the vortex rings into turbulence occurs at about the same x/d of approximately 4 for each case.

4.2.2 R_{ed} = 1270, R_{ed} = 2540 and R_{ed} = 5080, Figures 27 through 29

The photos for the higher R_{ed} cases do not show any clear indication of differences in the wall interaction for either occlusion. An interesting feature which is noticeable for R_{ed} = 5080 in Figures 29 and 25 is the streamline contraction in the vena contracta for both cases. The vortex ring system forms at the point, or just downstream, of the vena contracta minimum area. This indicates that the flow instabilities begin to form in the deceleration region of the jet, as expected.

4.3 Comments on Confined Jet Flow

The wall interaction that was discussed thus far has been in reference to the vortex rings actually appearing to make contact with the wall and break up. In contrast to the situation arising for the free jet, all of the confined jet cases are affected by the presence of the wall to some extent. This is due to the change in the recirculation

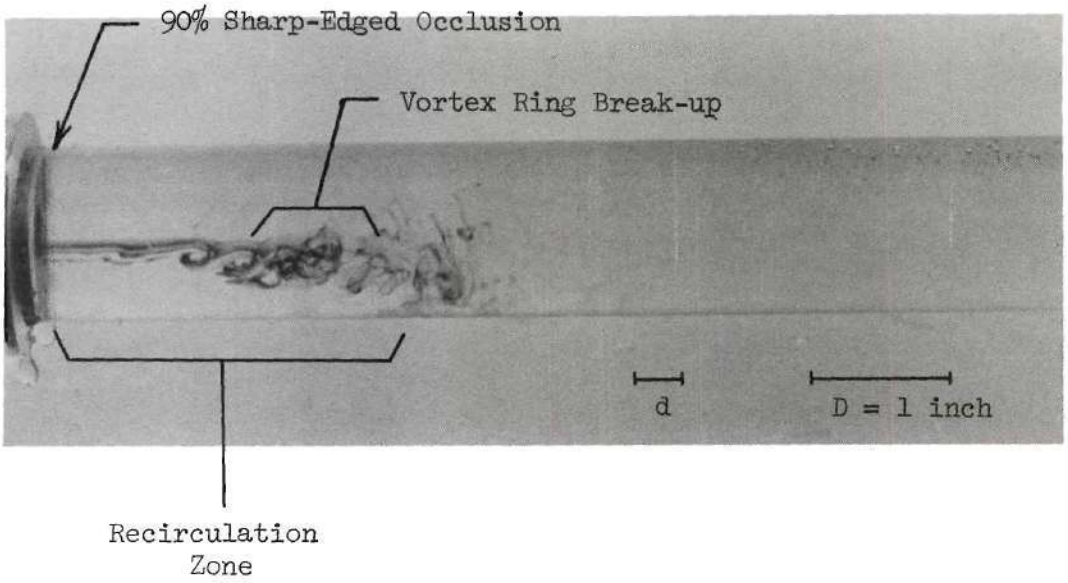

Figure 26. 90 Percent Sharp-Edged Occlusion, $R_{e_d} = 635$, $R_{e_D} = 201$

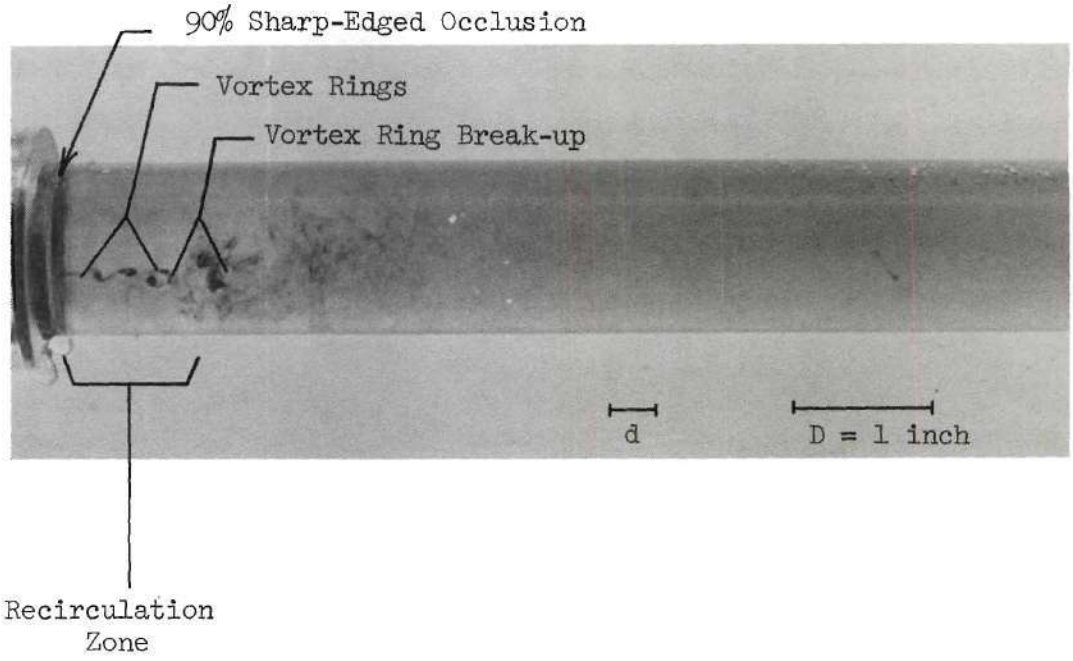

Figure 27. 90 Percent Sharp-Edged Occlusion, $R_{e_d} = 1270$, $R_{e_D} = 402$

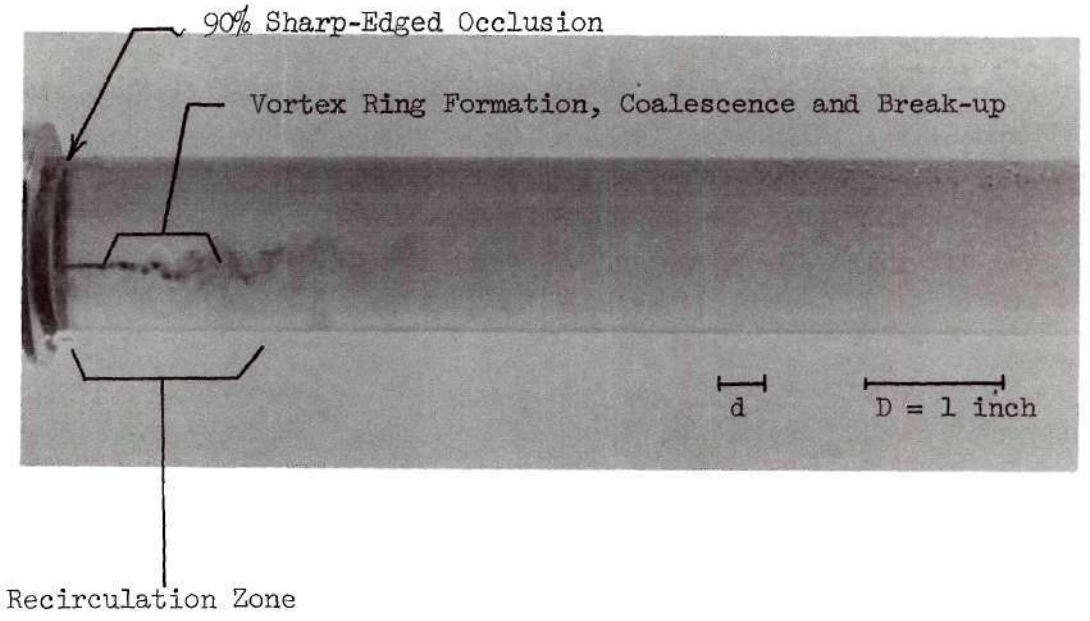

Figure 28. 90 Percent Sharp-Edged Occlusion, $R_{e_d} = 2540$, $R_{e_D} = 802$

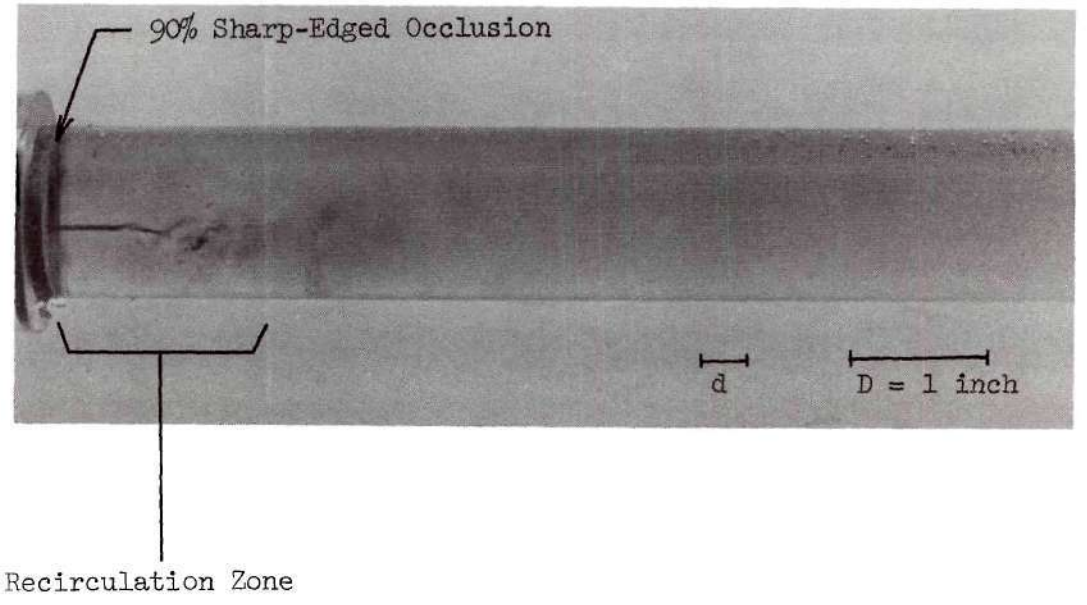

Figure 29. 90 Percent Sharp-Edged Occlusion, $R_{e_d} = 5080$, $R_{e_D} = 1604$

region, or entrainment zone, caused by the presence of the wall.

The free jet is not radially confined and the entrainment flow is unhindered along its inward path from the surroundings, as shown in Figure 30(a).

The confined jet, however, is fed entrained flow from its own self-formed recirculation region. This has the effect of the jet "seeing" reverse flow near its boundary for a portion of the expansion as in Figure 30(b). This effect causes the jet-like flow structure to be dissipated much quicker than in the free jet case.

Beavers and Wilson[17] presented photographs of free jets issuing from sharp-edged orifices at Reynolds numbers of 160 to 1990. At R_{ed} = 760, the vortex rings break-up at approximately 7 to 8 orifice diameters downstream from the orifice lip. The break-up occurs at approximately 6 diameters fro R_{ed} = 970 and at approximately 4 to 5 diameters for R_{ed} = 1640. The presently reported flow visualization of the comfined jets indicate the vortex rings break-up sooner than the free jets. This can be seen for R_{ed} = 635 in Figure 18 with the 75 percent sharp-edged occlusion and in Figure 26 with the 90 percent sharp-edged occlusion where the vortex ring pattern breaks up at approximately 5 to 6 diameters downstream from the orifice. At a higher Reynolds number of 1270, shown in Figure 20 for the 75 percent occlusion and in Figure 27 for the 90 percent occlusion, the break-up occurs at approximately 2 to 3 diameters downstream. Therefore, it is concluded that the general trend of vortex ring break-up is the same for both the free jet and confined jet, i.e., the break-up distance decreases as Reynolds number increases, but the confined jet vortex

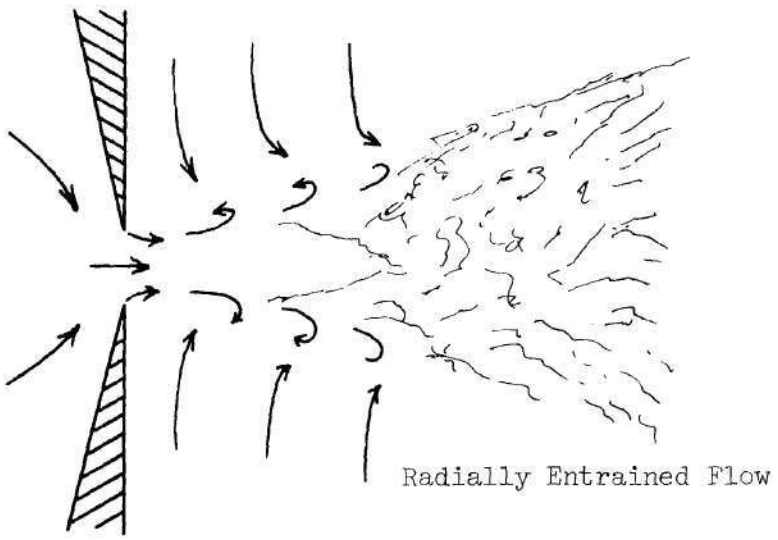

Figure 30 (a). Free Jet Flow Field

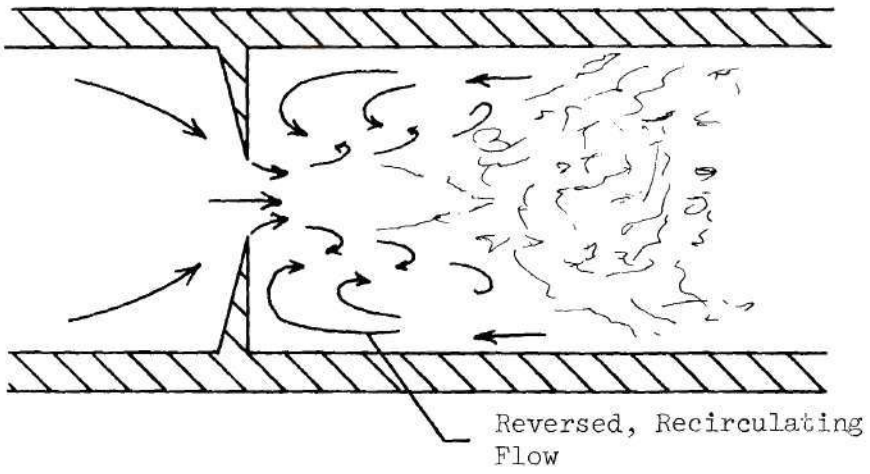

Figure 30 (b). Confined Jet Flow Field

ring break-up occurs closer to the orifice than the free jet at about the same Reynolds number. This same trend can be seen in the 50 percent sharp edged occlusion data. For example, Figure 14 for R_{ed} = 1796 indicates that the vortex rings begin to break-up at approximately 1.5 d from the orifice, whereas the Beavers and Wilson[17] photographs indicate that the vortex rings persist out to approximately 4 d from the orifice at R_{ed} = 1640 to 1990. Therefore, interaction of the vortex rings with the wall have definitely initiated a faster vortex pattern break-up. At lower R_{ed}, the 50 percent sharp-edged occlusion photographs do not indicate a break-up of the vortex ring pattern, but rather the interaction of the jet flow with the wall tends to stabilize the flow so that fully developed vortex rings do not occur. This can be seen in Figures 10 and 12 for R_{ed} = 449 and 898 respectively. The Beavers and Wilson[17] data in this Reynolds number range indicate that vortex rings develop at about 1 d to 4 d downstream from the orifice.

CHAPTER V

STEADY FLOW MEAN VELOCITY RESULTS AND DISCUSSION

The following sections present the axial and radial mean velocity profiles obtained downstream of the occlusions for three different Reynolds numbers. In addition, the radial velocity profiles obtained upstream of the occlusions are shown for comparison. These results demonstrate the overall flow development and show the axial and radial extent of the influence of the occlusion-generated jet.

5.1 Upstream Radial Velocity Profiles

The mean velocity data obtained 3 D upstream of the sharp-edged occlusions and 4 D upstream of the contoured occlusions are shown in Figure 31. The profiles are flat for about the central 80 percent of the tube diameter for all flow rates.

5.2 Axial Velocity Profiles of Sharp-Edged and Contoured Occlusions

Figure 32 shows the trends of the centerline mean velocity in the region downstream of the 50 percent occlusions. Also indicated is the velocity at the occlusion minimum area as calculated from the one-dimensional continuity equation using the known total flow rate and the minimum area of the occlusion. It was not possible to measure the velocity at the minimum area location with the hot film probes used in this investigation. There does not appear to be any significant

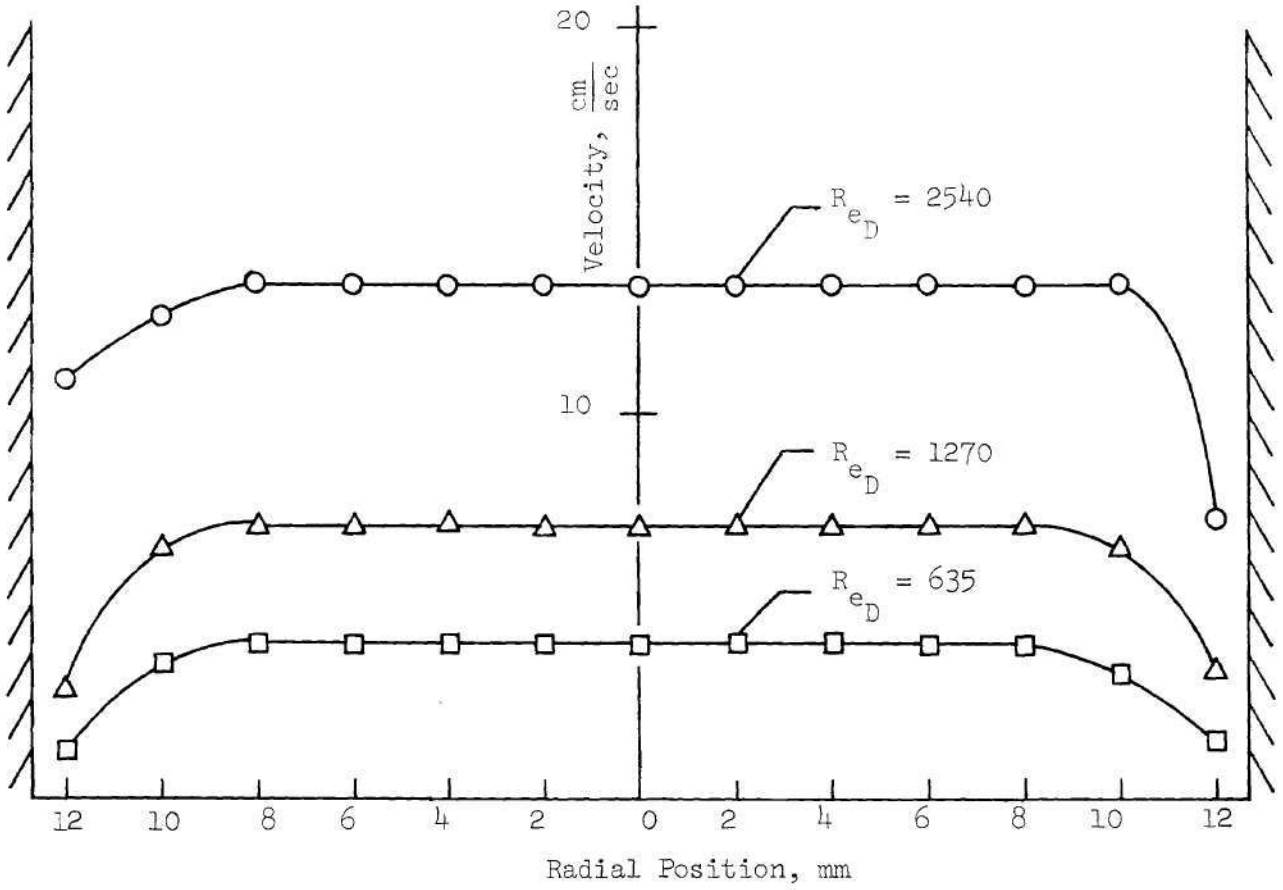

Figure 31. Mean Velocity Profile Upstream of Occlusion

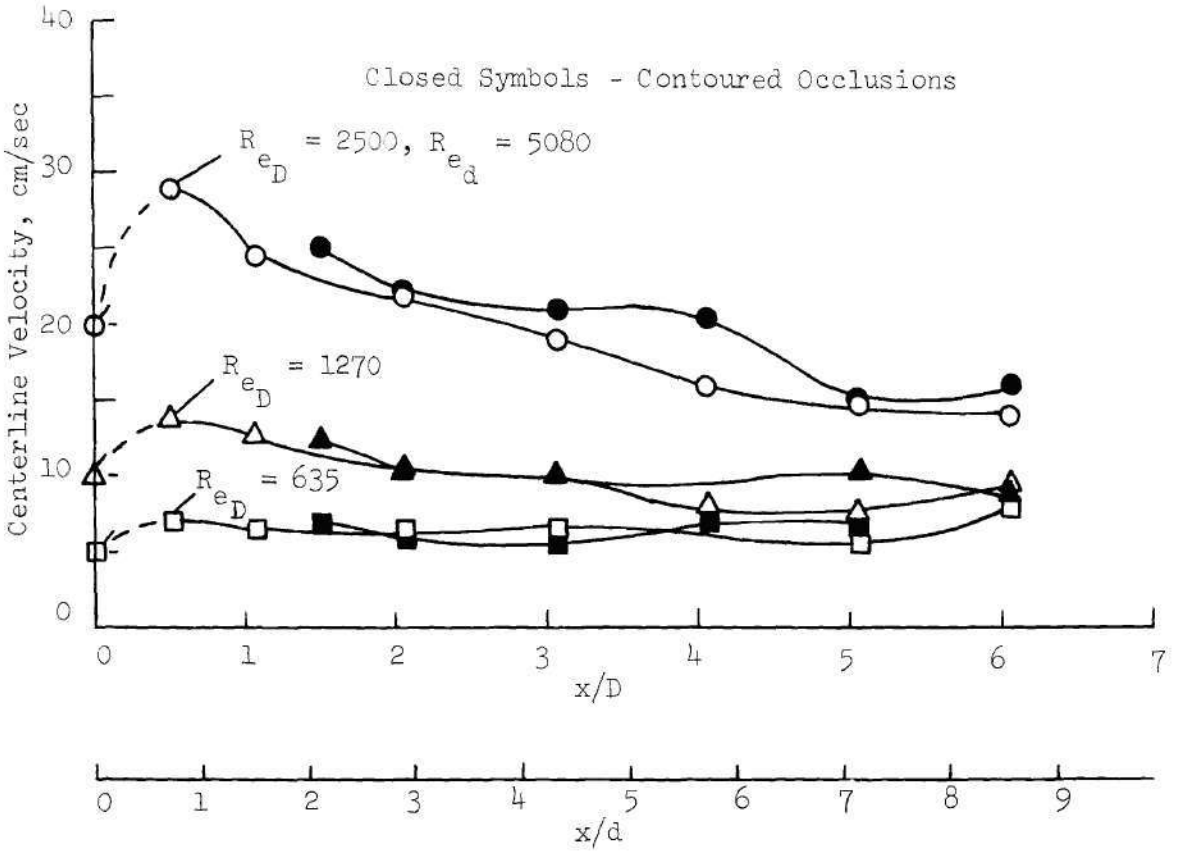

Figure 32. 50% Occlusions, Centerline Axial Velocity Profiles

difference in the velocity decrease with axial distance for the sharp-edged or contoured occlusions. However, at x/D's greater than about 4, the contoured occlusion velocities tend to be slightly greater than the corresponding sharp-edged results.

Figure 33 reveals that for the 75 percent occlusions the velocities for the contoured constriction tend to be slightly higher for d/D greater than about 4. The velocities with the contoured occlusion for x/D less than 1.5 were not measured since the hot film probe mount could not be used any closer to the occlusion minimum area.

The 90 percent occlusion centerline mean velocity data shown in Figure 34 indicates clearly that the centerline velocity peaks at an x/d of about 2 for all flow rates. Downstream of this point the velocity decreases smoothly.

5.3 Radial Variations of Mean Velocity For Sharp-Edged and Contoured Occlusions

The radial profiles of the mean velocity for the 50 percent occlusions are shown in Figures 35, 36, and 37 for three different R_{eD} and several axial positions. For $R_{eD} = 2540$, the sharp occlusion profile indicates a higher velocity near the centerline at x/d = 0.707 which decreases rapidly for radial positions outside the direct jet flow. This is indicative of a large and distinct recirculation region. Farther downstream at x/d = 4.419, the radial positions near the wall show a significant velocity which indicates the absence of a low energy recirculatory flow region at this location. At x/d = 8.66, the sharp-edged case shows a uniform velocity distribution across the

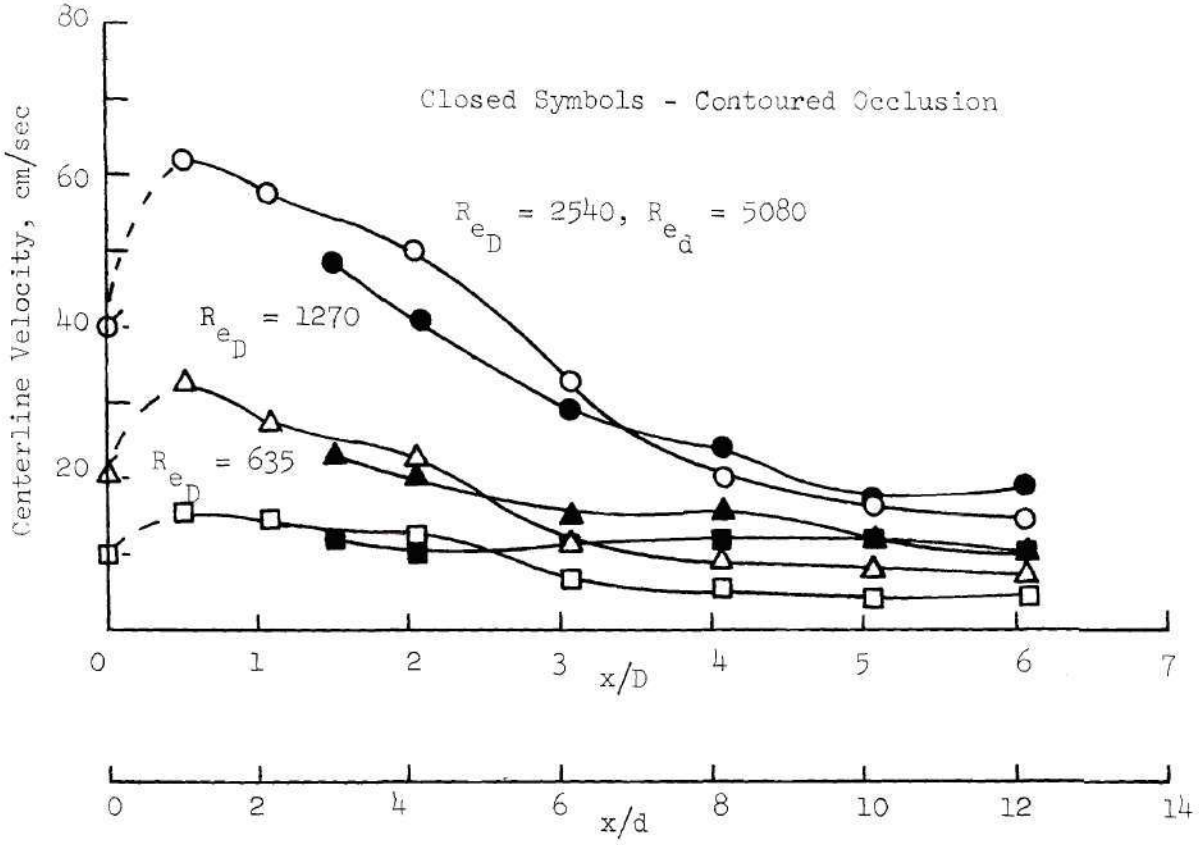

Figure 33. 75% Occlusions, Centerline Axial Velocity Profiles

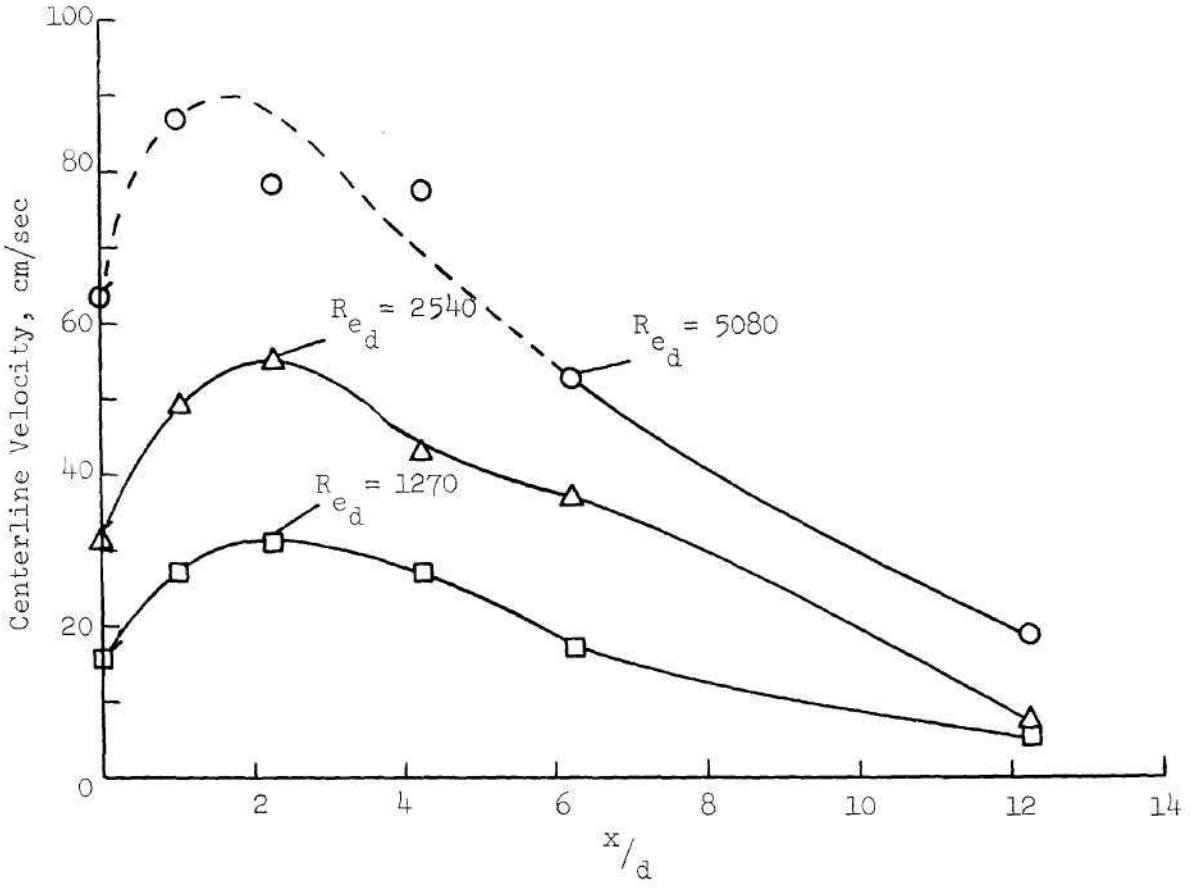

Figure 34. 90% Sharp-Edged Occlusion, Centerline Axial Velocity Profile

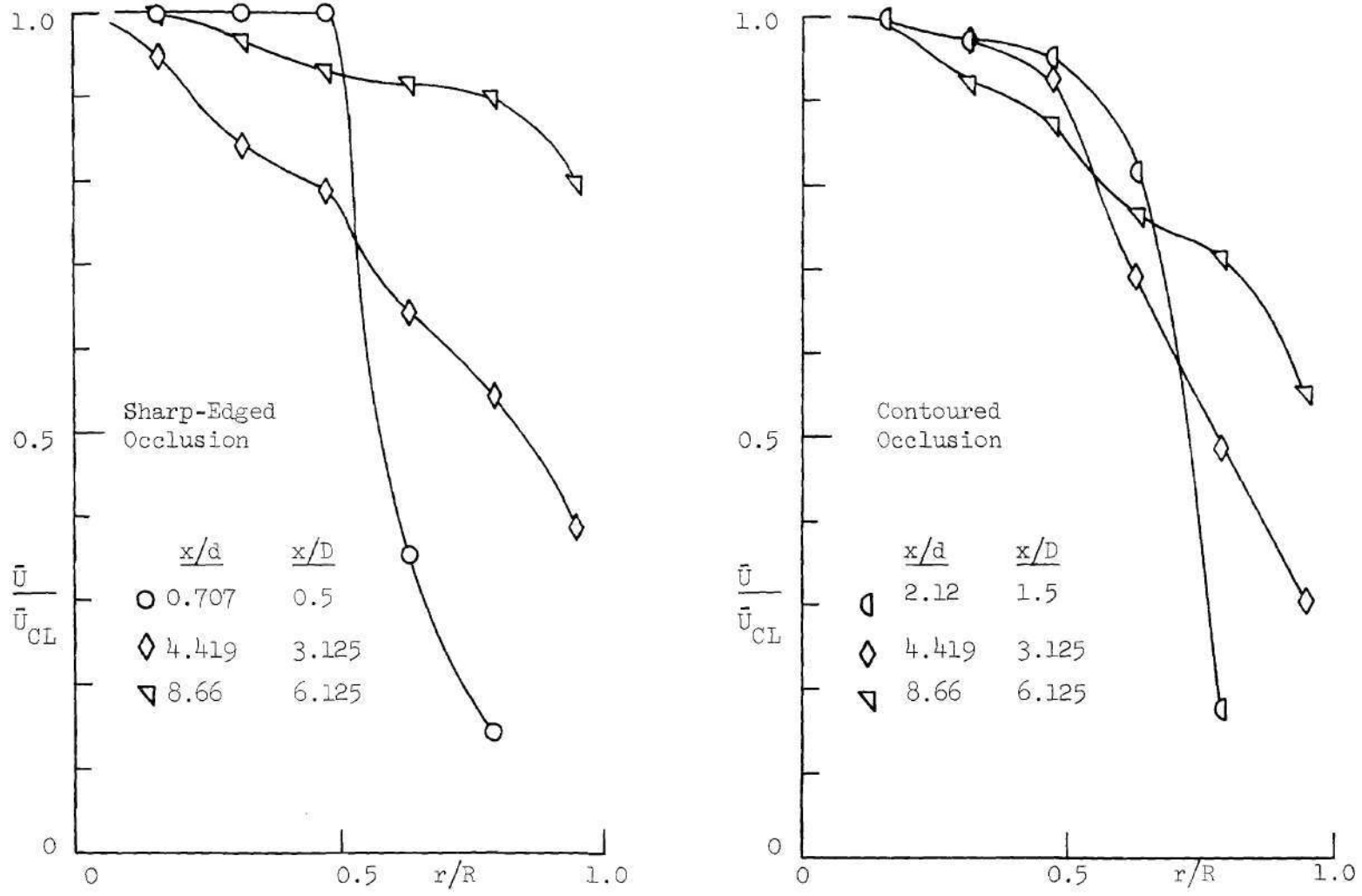

Figure 35. Mean Velocity Profile, 50% Occlusions, R_{e_D} = 3540

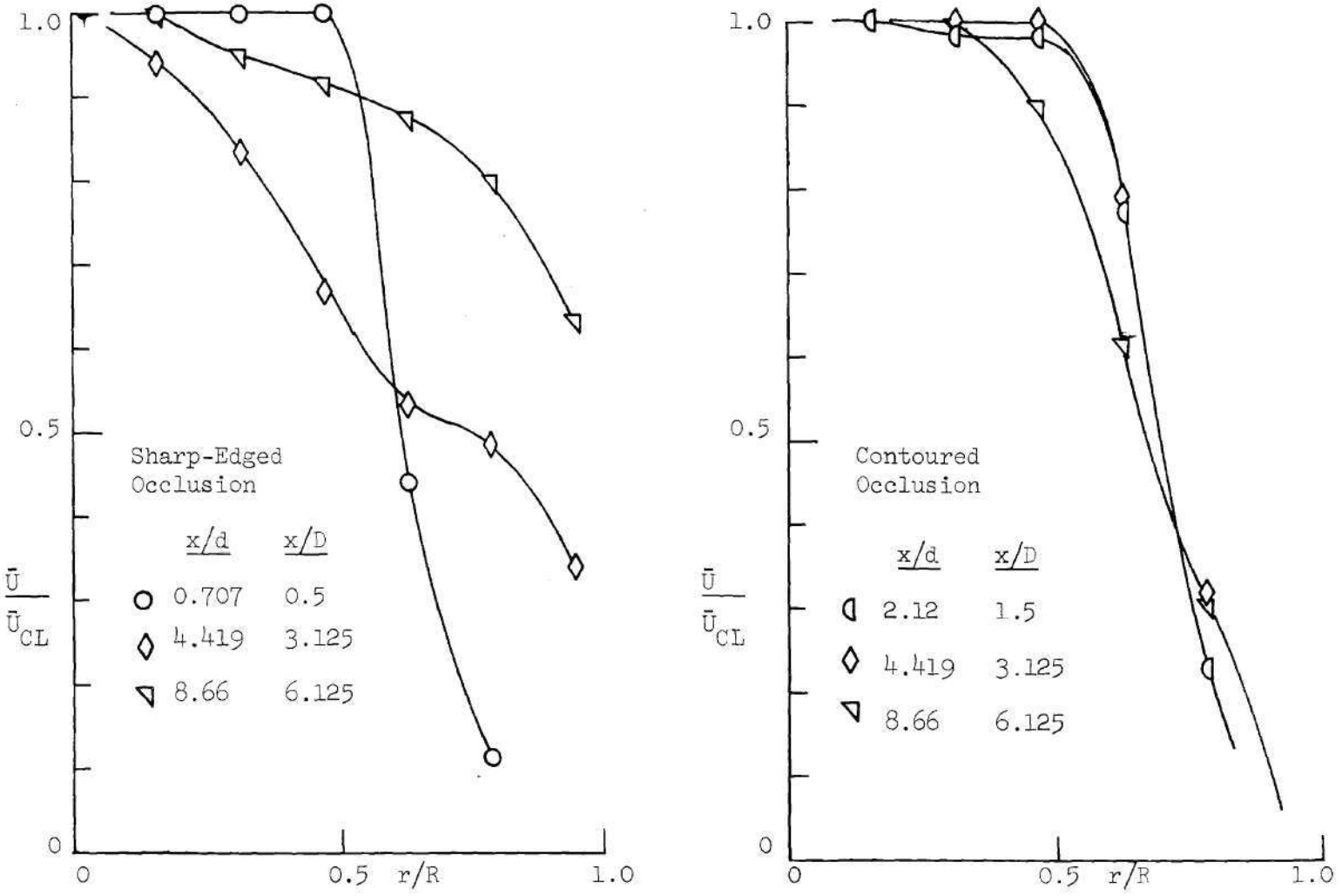

Figure 36. Mean Velocity Profile, 50% Occlusion, R_{e_D} = 1270

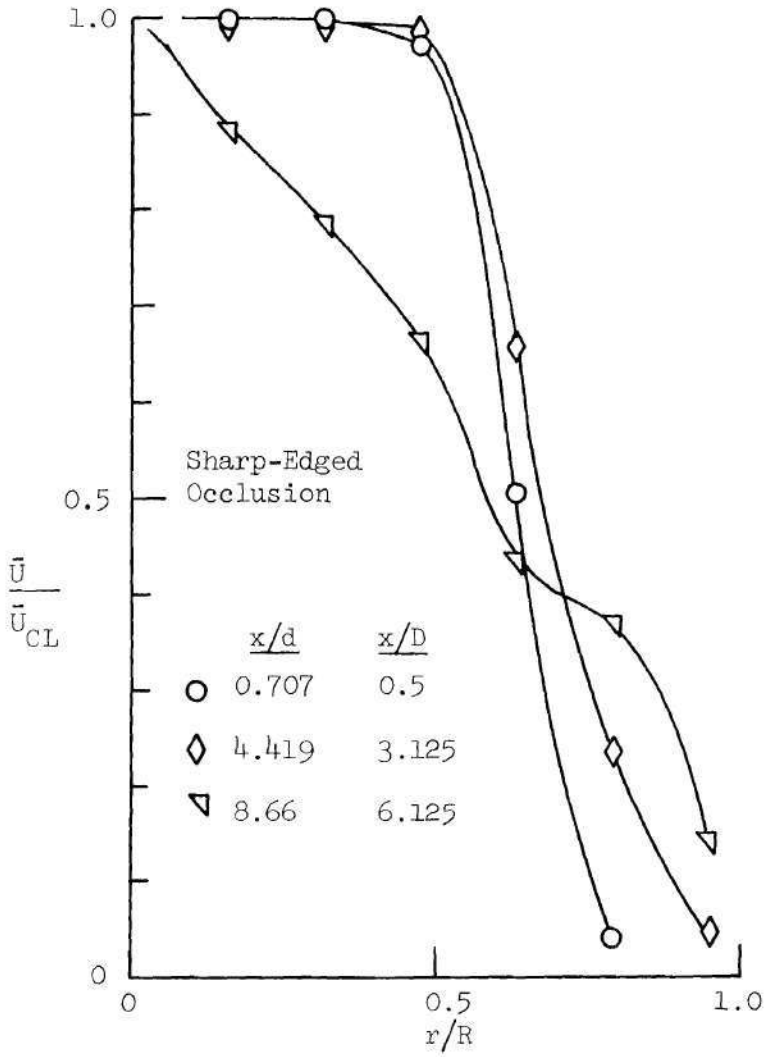

Figure 37. Mean Velocity Profile, 50% Occlusion, $R_{e_D} = 635$

tube similar to that expected for fully developed turbulent pipe flow. The contoured occlusion results for R_{eD} = 2540 show a broader profile near the occlusion than did the sharp-edged case which is indicative of a smaller recirculation zone. At more downstream locations the profiles still exhibit a shape which is distinctly peaked at the center-line indicating a reduced effect of turbulence in distributing energy uniformly across the tube diameter. The results for R_{eD} = 1270 for both occlusions show similar trends as were discussed in the R_{eD} = 2540 cases. However, the contoured occlusion profiles show an even more pronounced tendency toward a laminar type of profile.

Figures 38, 39, and 40 present the radial velocity profiles for the 75 percent occlusions. At the highest R_{eD} of 2540, the profiles are almost identical for the two different geometries for the same x/d positions. Both cases demonstrate the effects of turbulence at the most downstream position, x/d = 12.25, in generating a flat profile The R_{eD} = 1270 profiles shown in Figure 39 indicate that the sharp-edged occlusion generated a more intense turbulent field which results in a flatter profile than the contoured occlusion case at the more downstream positions (x/D = 3.125 and 6.125). A similar but more pronounced trend can be seen in Figure 40 for the R_{eD} = 635 results. The turbulence in the sharp-edged case has dissipated the main jet at the x/d = 6.25 position; whereas for the contoured results, the jet is still very much intact at the x/d = 6.25 position.

The 90 percent sharp-edged occlusion results are presented in Figures 41, 42, and 43 which are for the same R_{ed} as were used in the 75 percent occlusion cases. The dissipation of the jet emerging from

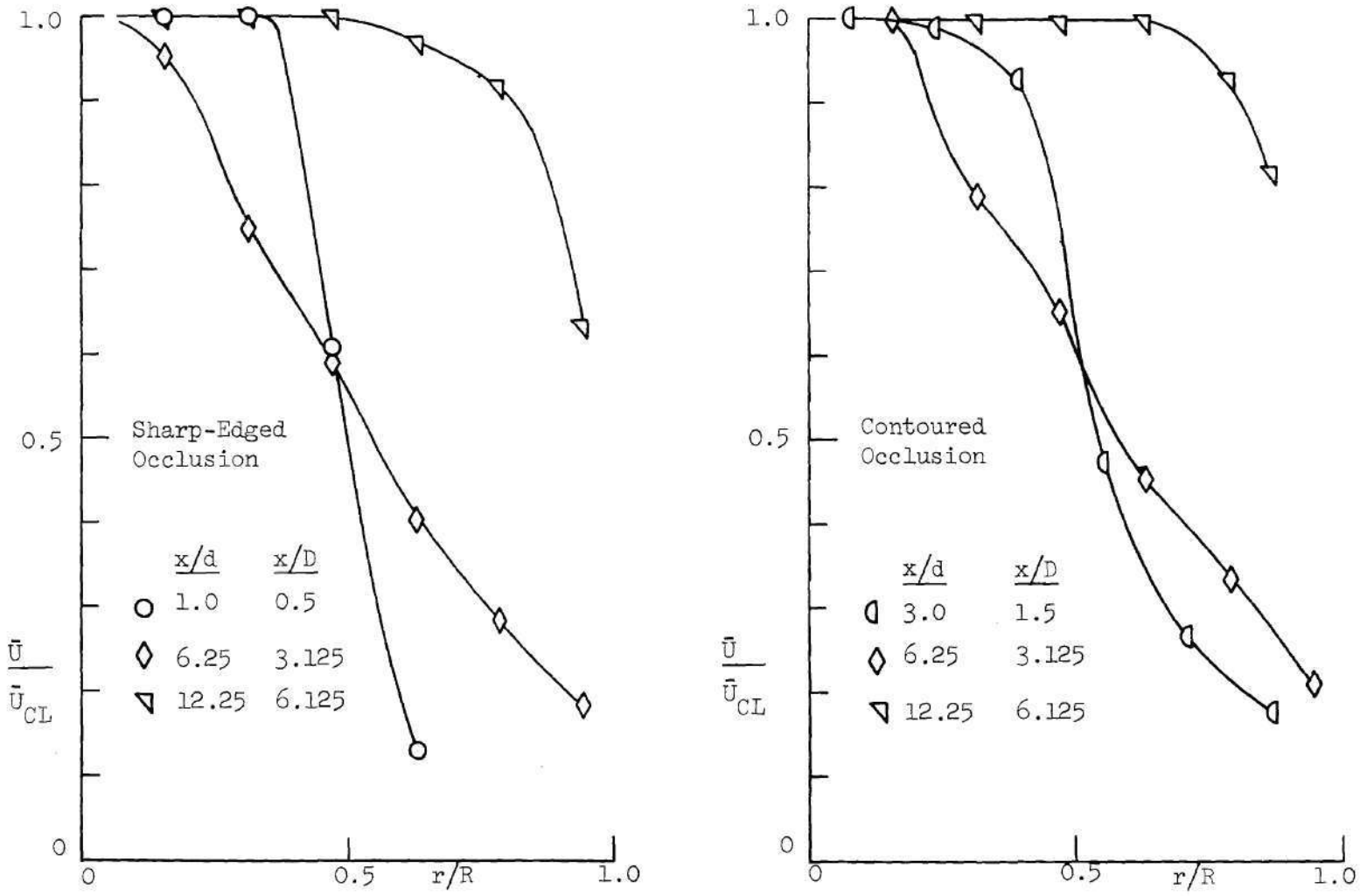

Figure 38. Mean Velocity Profile, 75% Occlusion, R_{e_D} = 2540, R_{e_d} = 5080

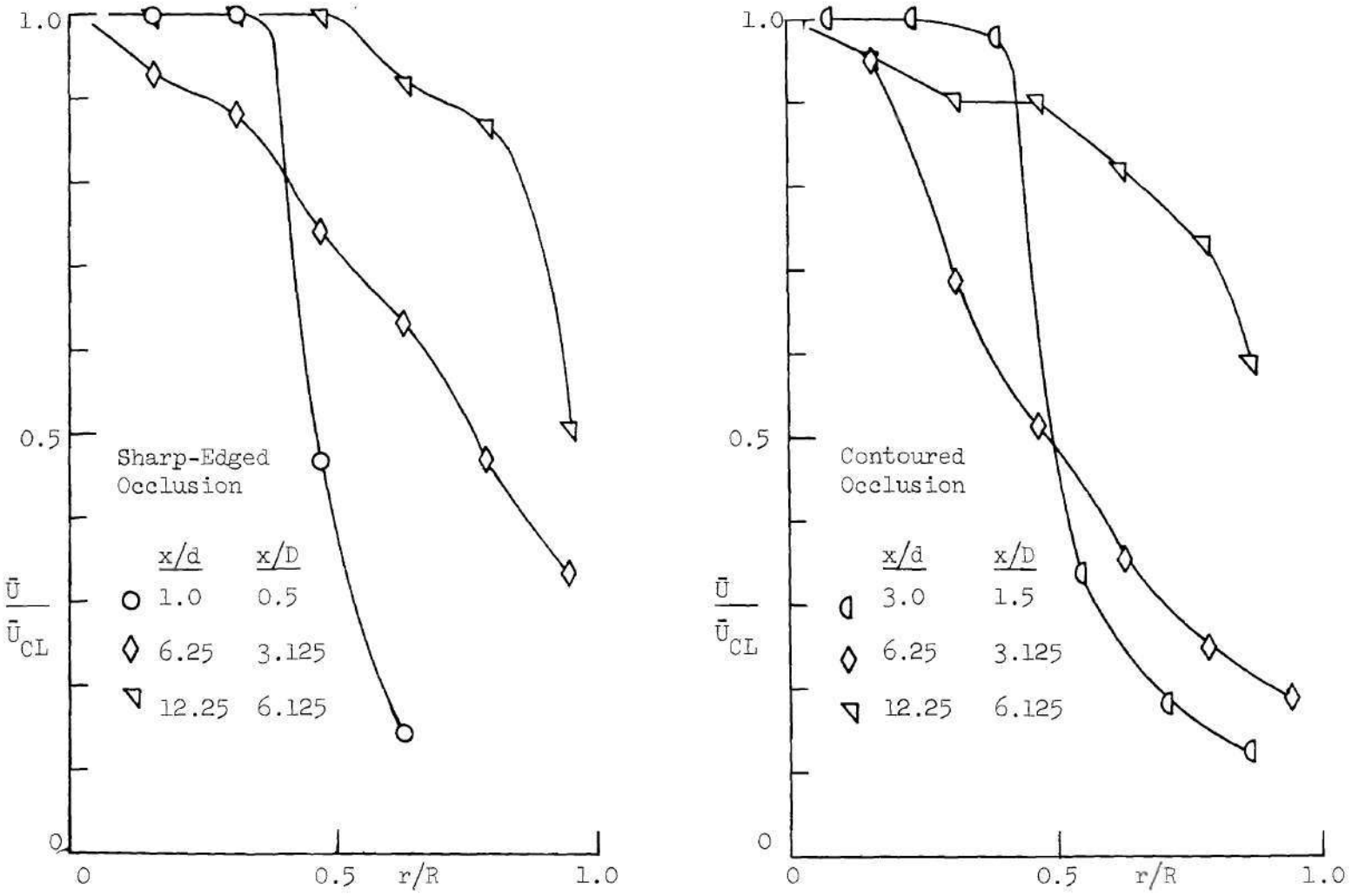

Figure 39. Mean Velocity Profile, 75% Occlusion R_{e_D} = 1270, R_{e_d} = 2540

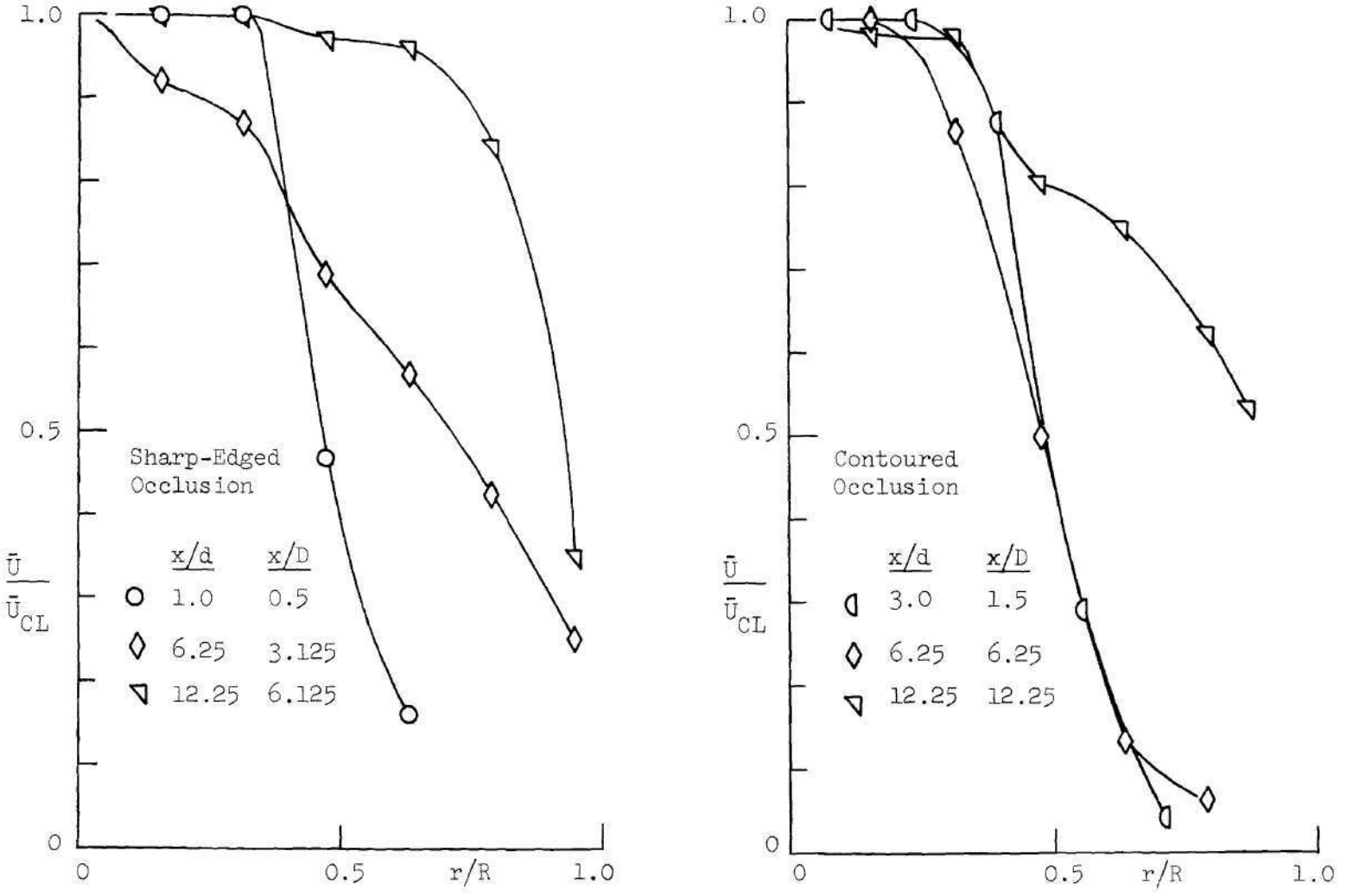

Figure 40. Mean Velocity Profile, 75% Occlusion, $R_{e_D} = 625$, $R_{e_d} = 1270$

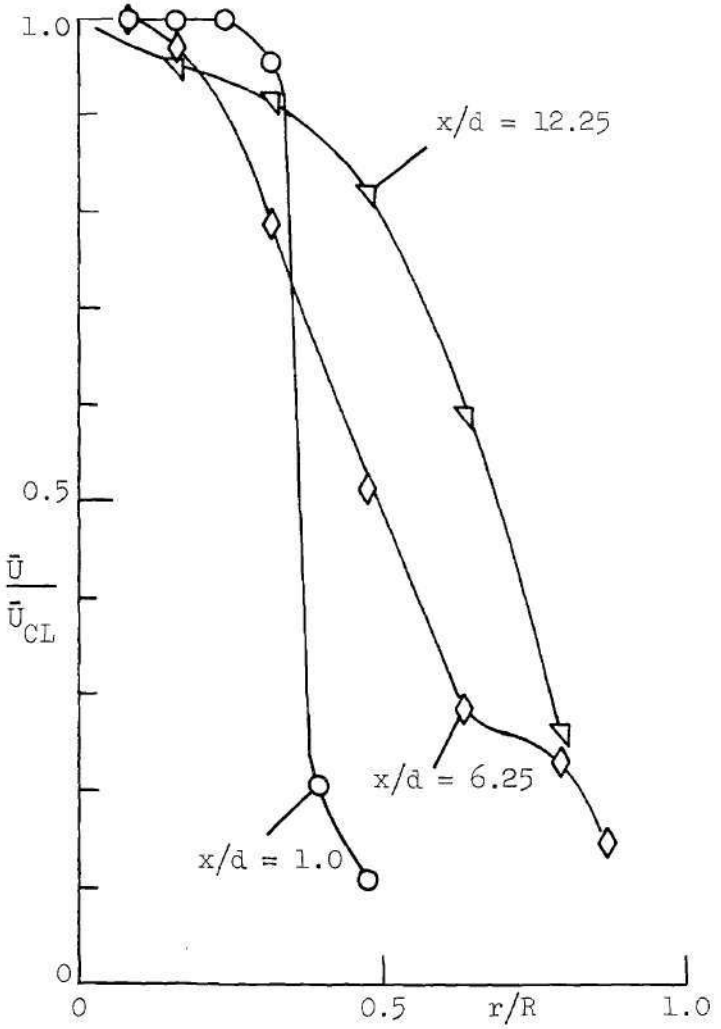

Figure 41. Mean Velocity Profile, 90% Sharp-Edged Occlusion, R_{e_d} = 5080

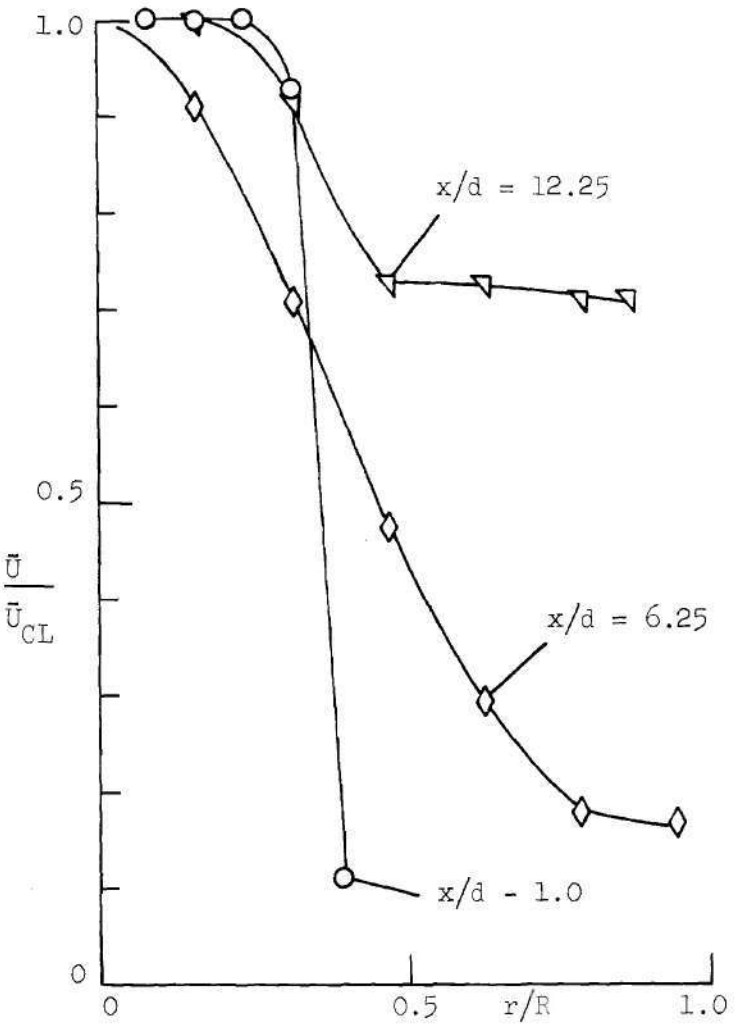

Figure 42. Mean Velocity Profile, 90% Sharp-Edged Occlusion, R_{e_d} = 2540

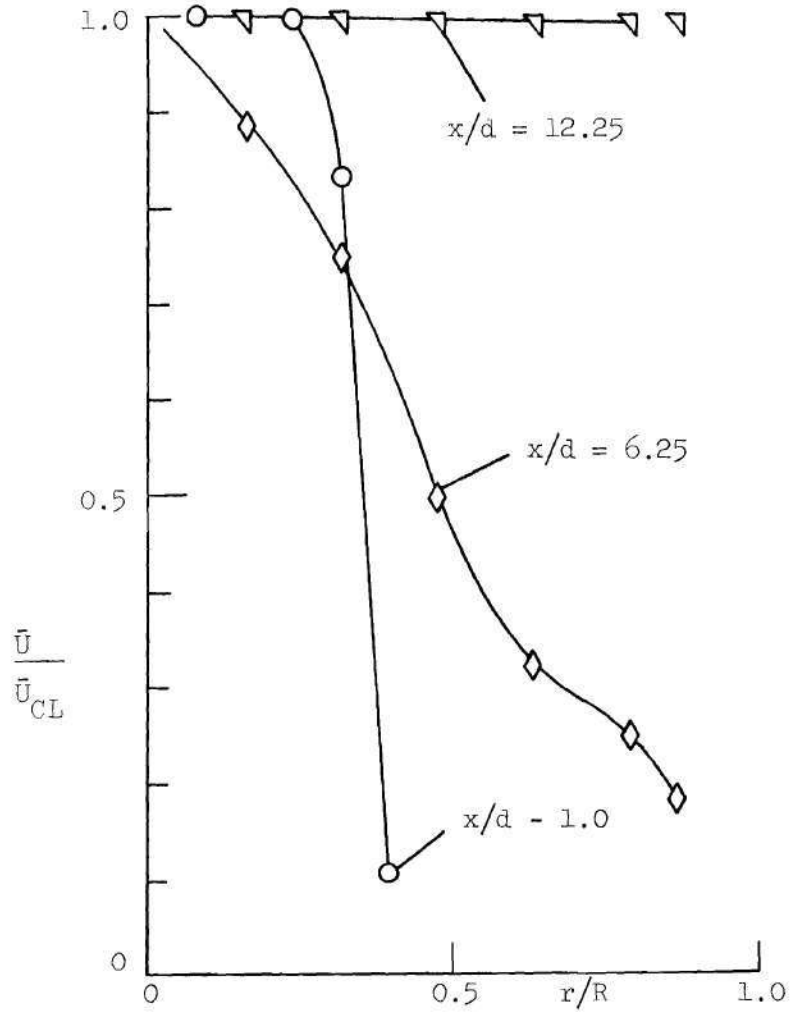

Figure 43. Mean Velocity Profile, 90% Sharp-Edged Occlusion, R_{e_d} = 1270

the orifice can be seen in the plots as a broadening of the profile at the more downstream positions. However, for the R_{ed} = 5080 and 2540 results, the most downstream axial position (x/d = 12.25) still indicates some influence of the jet in generating a velocity maximum at the centerline location. Whereas, for R_{ed} = 1270 the x/d = 12.25 profiles is flat across the entire tube diameter.

CHAPTER VI

STEADY FLOW ENERGY SPECTRA

RESULTS AND DISCUSSION

This chapter summarizes the information obtained by subjecting the linearized hot film anemometer signal to Fourier Analysis which produces the energy spectral distributions of the velocity fluctuations. The spatial extent of the turbulent velocity field was determined for each occlusion and Reynolds number by obtaining data at several off-centerline locations for each axial position. The plots show the energy of the velocity flucuations, u'^2, as a function of the frequency. Non-dimensional correlations of the energy distributions and the frequency in terms of physical variables are also presented.

6.1 Energy Spectral Distributions for the 50 Percent Occlusions

The spatial extent of the velocity fluctuations downstream of the 50 percent sharp-edged occlusion can be seen in Figures 44 through 48 for $R_{e_D} = 2540$, $R_{e_d} = 3592$. At $x/D = 0.5$, the frequency corresponding to the vortex shedding can be observed at all radial positions. However, the peak frequency at the centerline position ($r = 0$) contains considerably less energy than the peak frequencies at the off centerline positions. The energy data obtained at $r = 7$ mm indicate increased energy content at frequencies lower and higher than the shedding frequency which can be attributed to formation of a more random type of turbulence in the

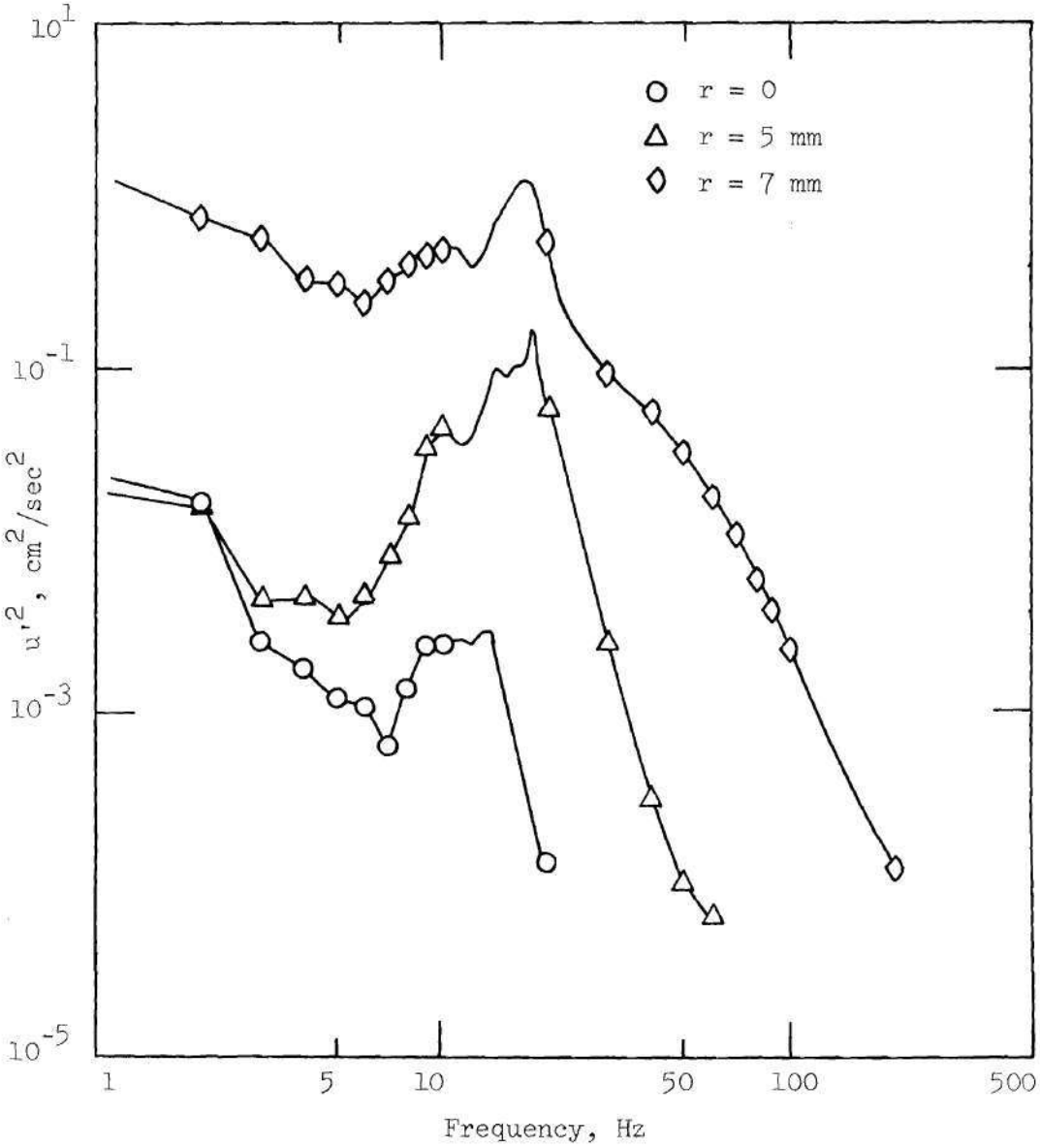

Figure 44. Energy Spectra for 50% Sharp-Edged Occlusion, x/D = 0.5, R_{e_D} = 2540, R_{e_d} = 3592

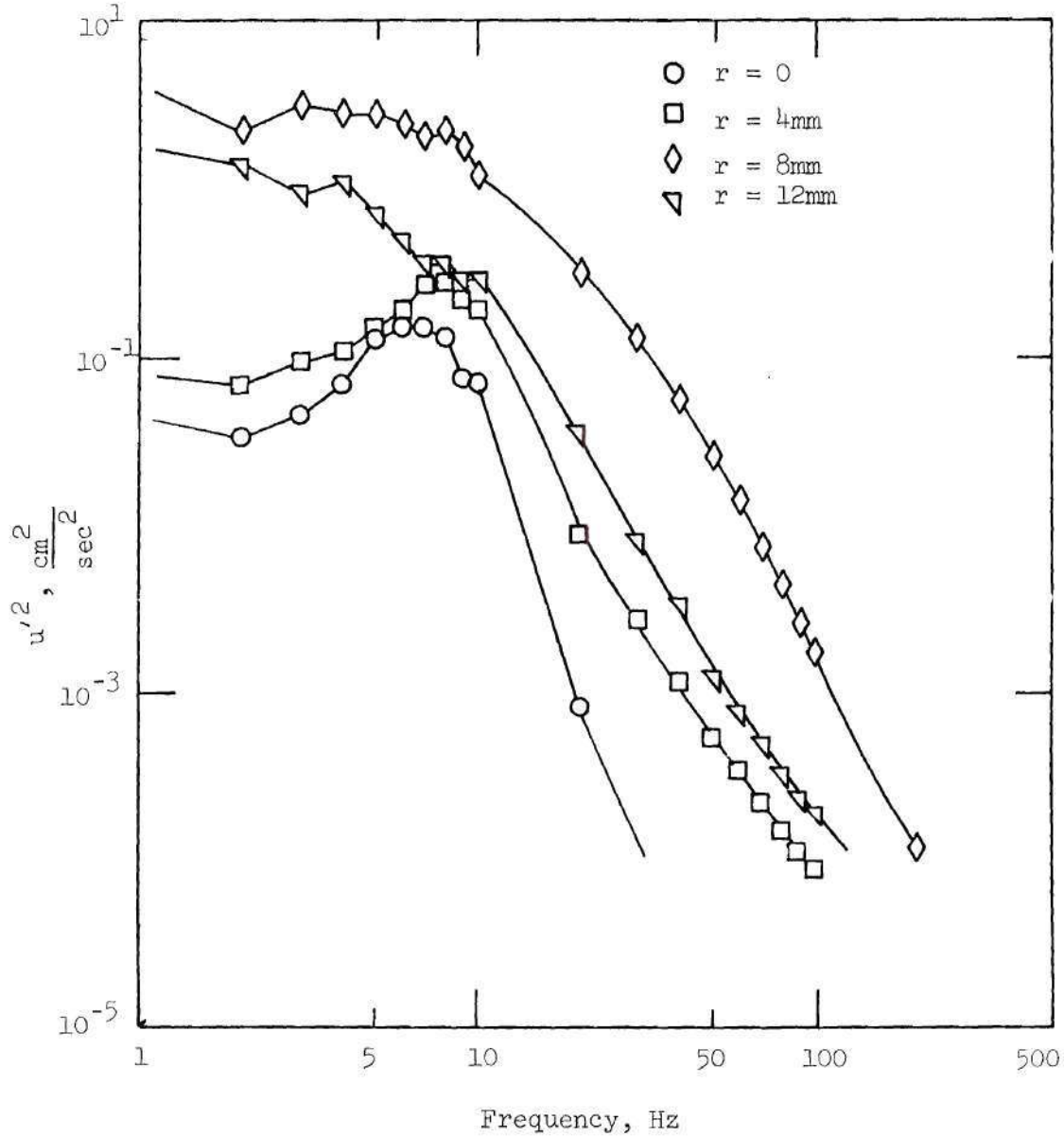

Figure 45. Energy Spectra for 50% Sharp-Edged Occlusion. x/D = 1.125, R_{e_D} = 2540, R_{e_d} = 3592.

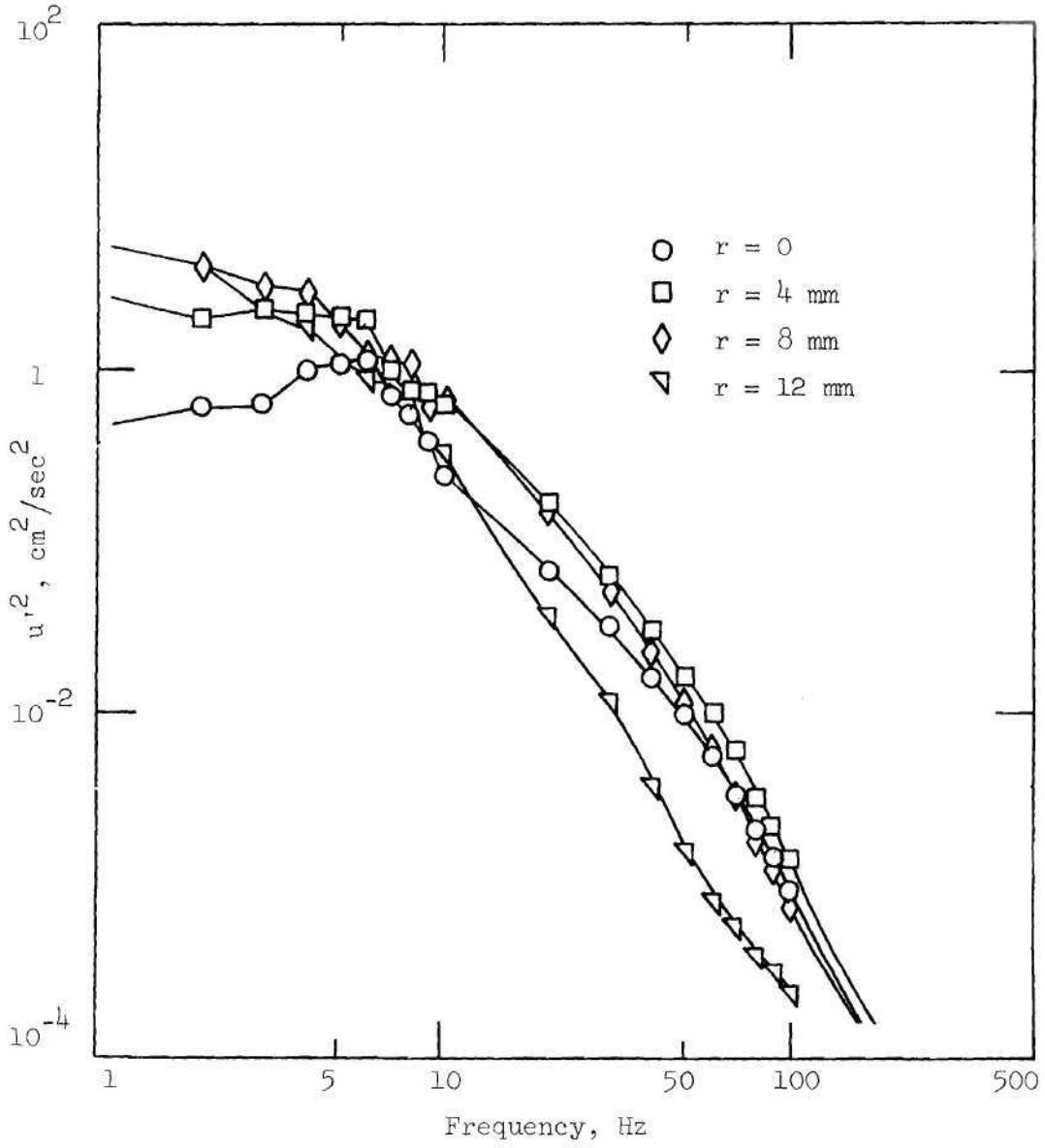

Figure 46. Energy Spectra for 50% Sharp-Edged Occlusion, x/D = 2.125, R_{e_D} = 2540, R_{e_d} = 3592

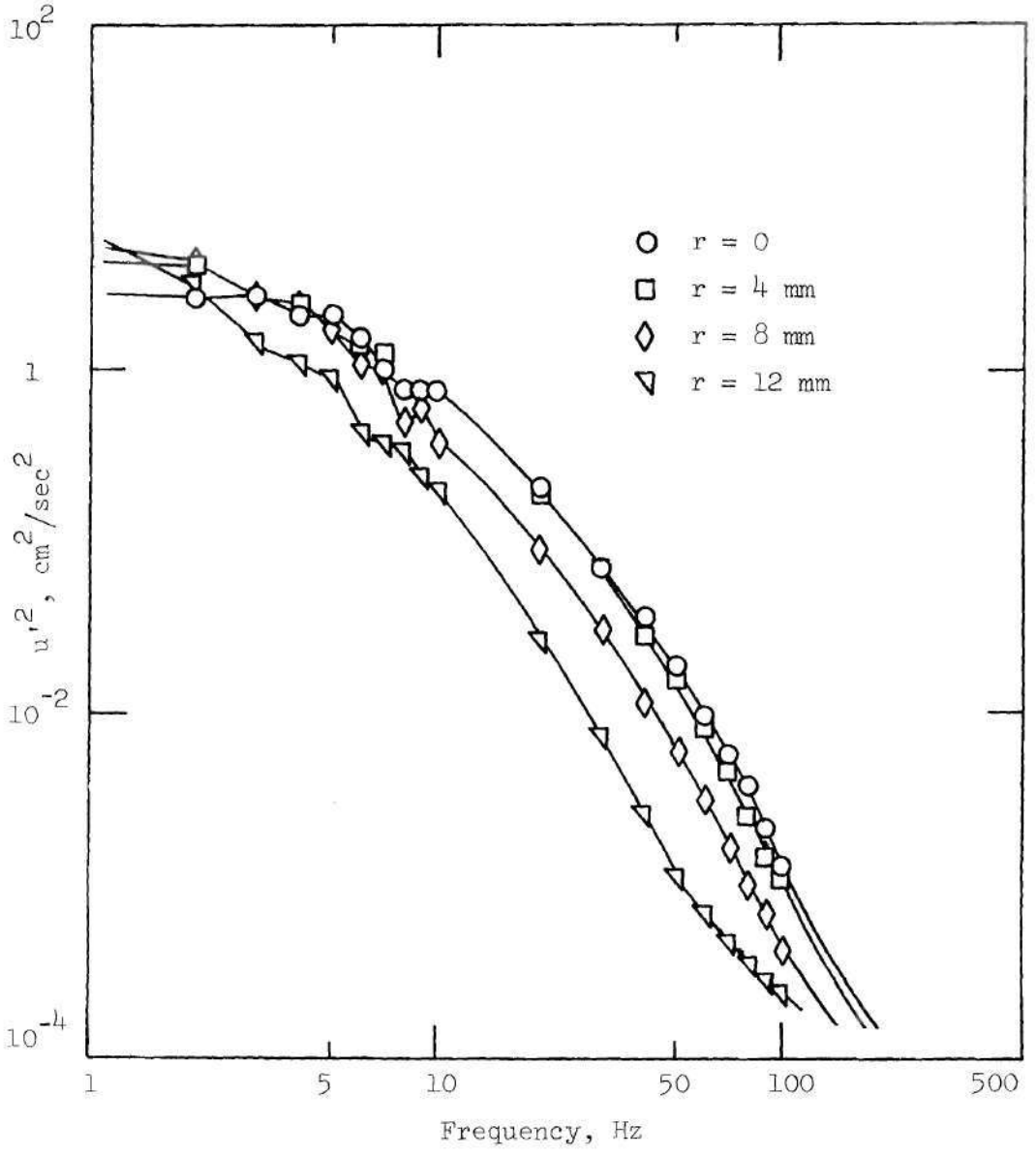

Figure 47. Energy Spectra for 50% Sharp-Edged Occlusion, x/D = 3.125, R_{e_D} = 2540, R_{e_d} = 3592

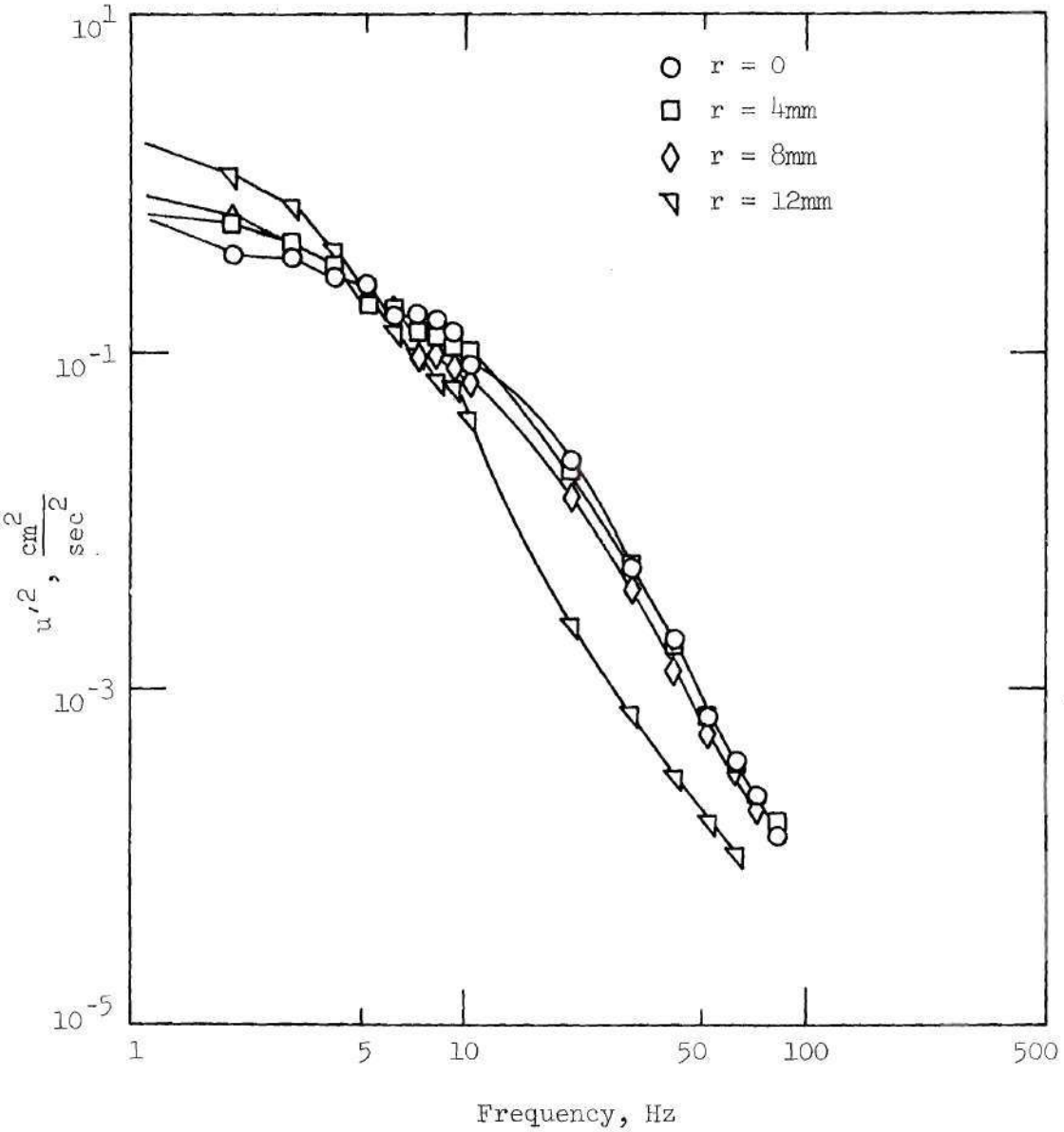

Figure 48. Energy Spectra for 50% Sharp-Edged Occlusion. x/D = 6.125, R_{e_D} = 2540, R_{e_d} = 3592.

high shear region between the jet and the recirculation zone. Farther downstream at x/D = 1.125 (Figure 45), the vortex shedding frequency dominates the centerline energy distribution and has increased in intensity over the x/D = 0.5 position but is peaked at a lower frequency than the x/D = 0.5 data. The off-centerline positions at x/D - 1.125 show a break-up of the vortex pattern due to interaction with the wall. The data at the axial positions x/D = 2.125, 3.125 and 6.125 (Figures 46, 47 and 48) indicate the complete break-up of the more ordered vortex ring structure into a random turbulent energy distribution as the flow progresses downstream. The near-wall position (r = 12 mm) at x/D = 3.125 and 6.125 show a slight decrease in overall intensity as compared with the radial positions away from the wall (r = 0, 4, 8 mm).

The energy distributions for the 50 percent contoured occlusion at R_{e_D} = 2540 are presented in Figures 49 through 52. The spectra at an axial position of x/D = 1.5, which is the location nearest to the occlusion, shows a peaked type of distribution out to r = 8 mm in contrast to the sharp-edged spectral data obtained in this general axial region (Figures 45 and 46) which shows a more dispersed distribution at r = 8 mm. The contoured occlusion flow field shows effects of the vortex shedding as far downstream as x/D = 3.125 which is indicated by the spectral peaks at r = 0 and 4 mm. However, the spectral peaks at all axial positions are at a lower intensity than the corresponding sharp occlusion data. The spectral data at x/D = 6.125 is dispersed in a manner similar to the corresponding sharp occlusion data.

At a lower Reynolds number of R_{e_D} = 1270, the flow fields of both occlusion geometries demonstrate the tendency of the vortex ring

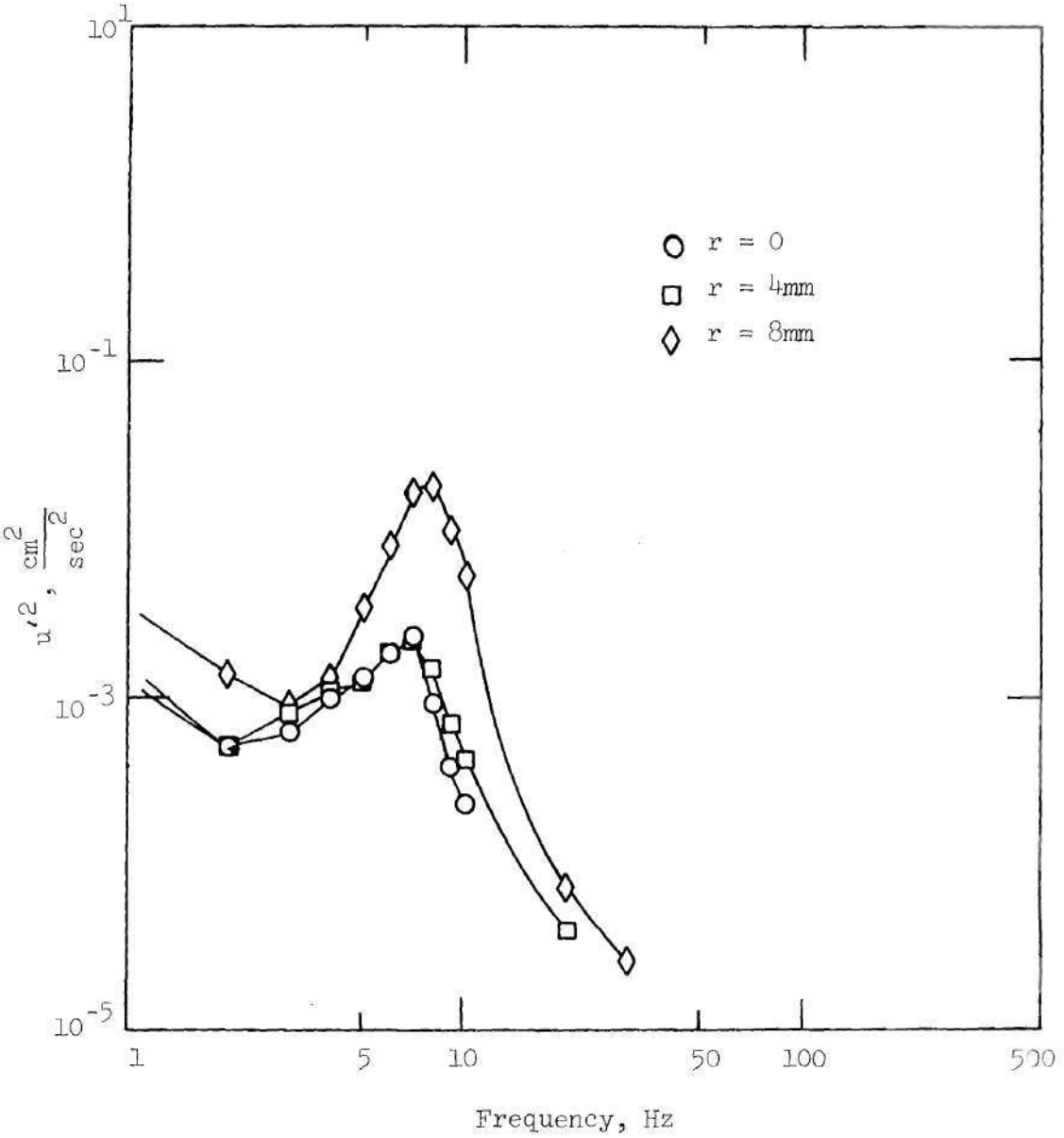

Figure 49. Energy Spectra for 50% Contoured Occlusion, $x/D = 1.5$, $R_{e_D} = 2540$, $R_{e_d} = 3592$.

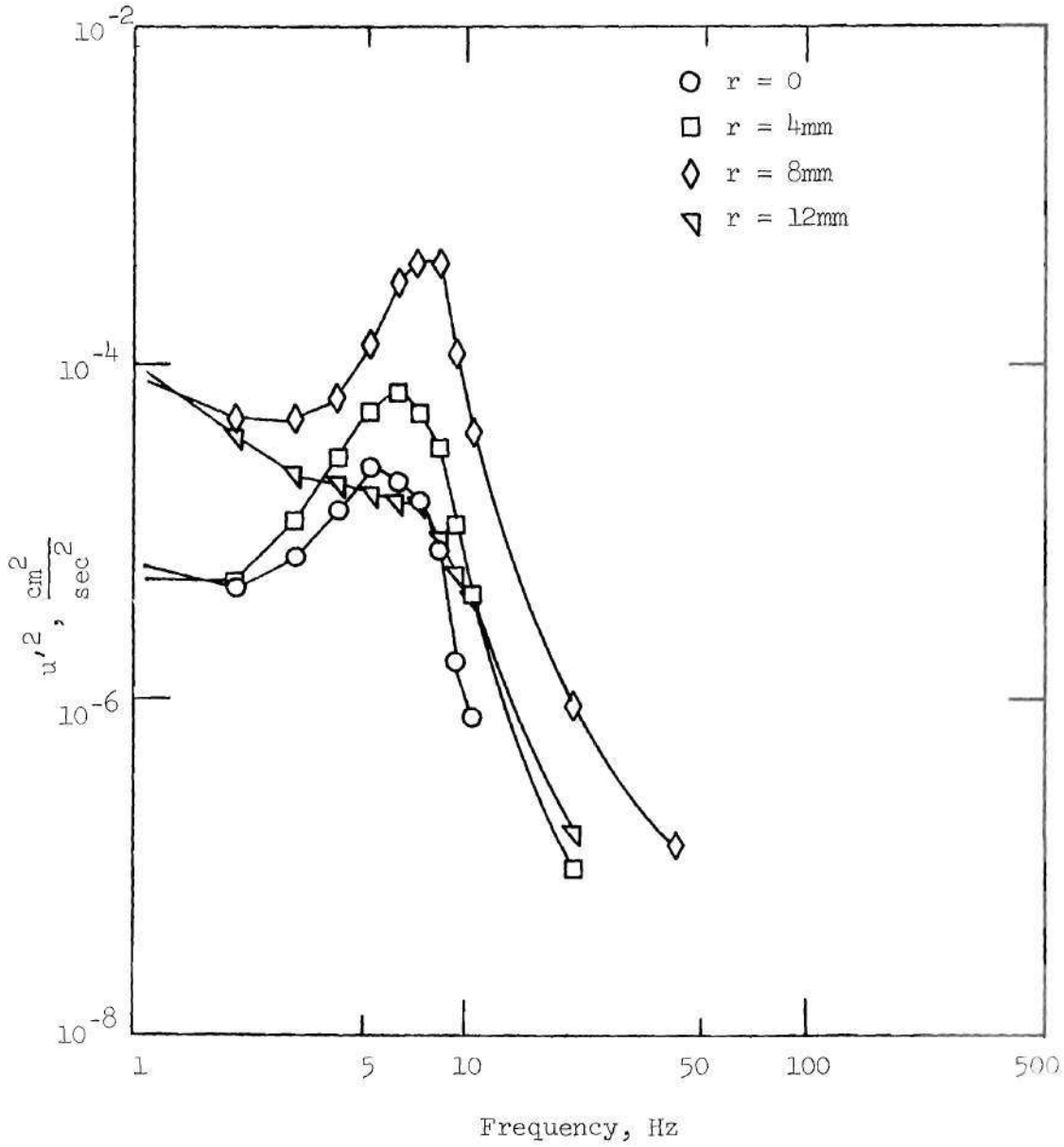

Figure 50. Energy Spectra for 50% Contoured Occlusion. x/D = 2.125, R_{e_D} = 2540, R_{e_d} = 3592.

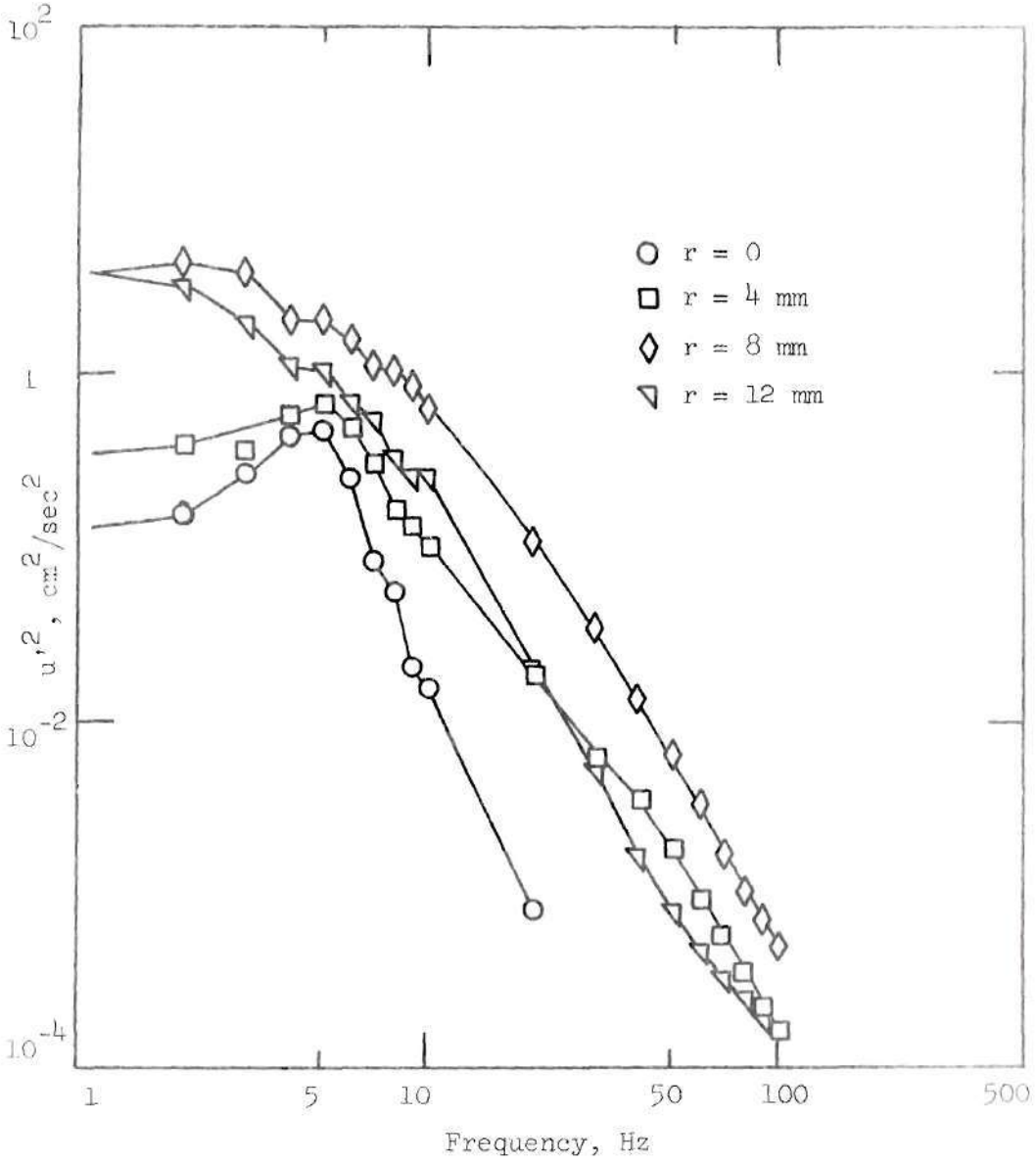

Figure 51. Energy Spectra for 50% Contoured Occlusion, x/D = 3.125, R_{e_D} = 2540, R_{e_d} = 3592

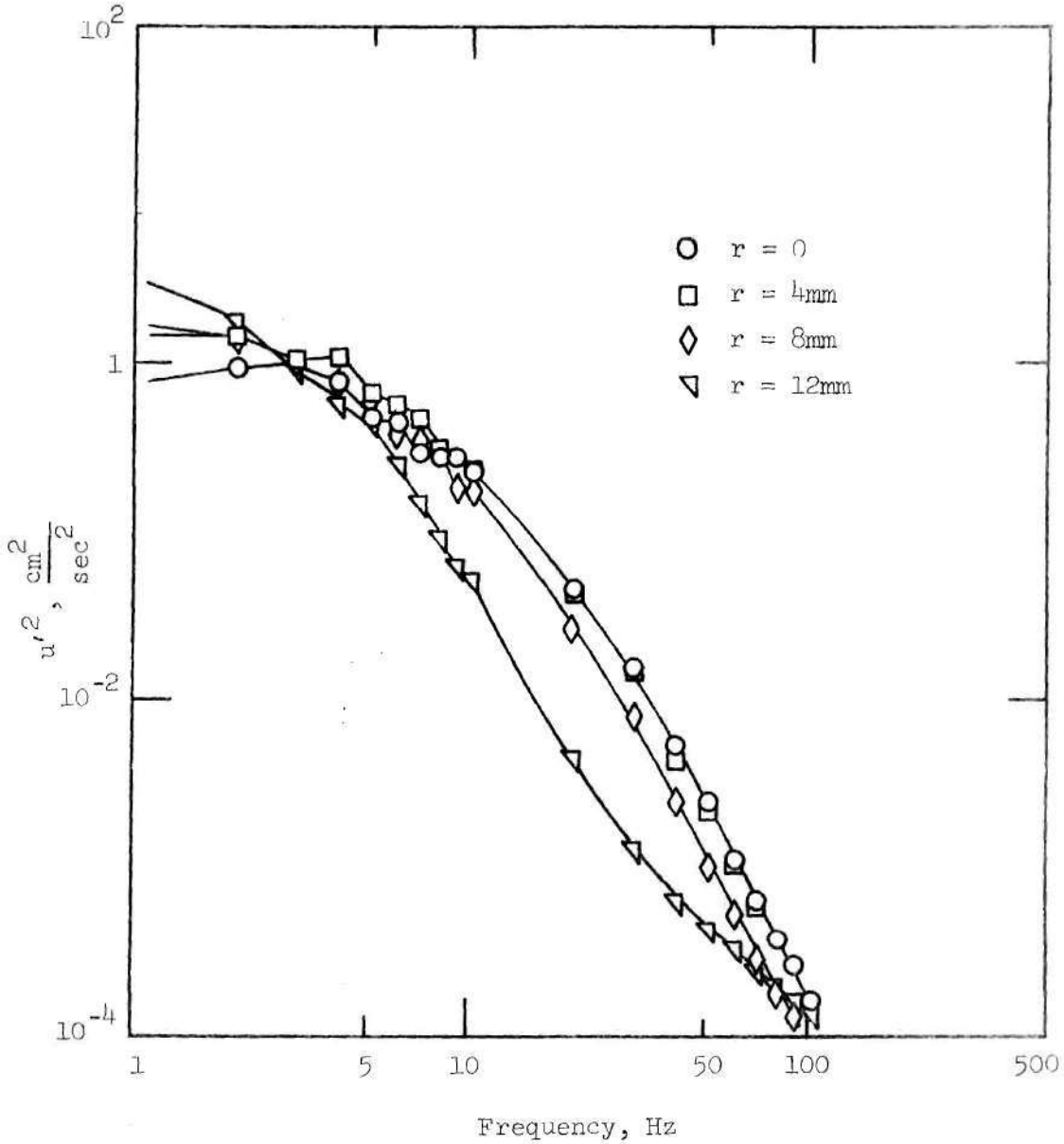

Figure 52. Energy Spectra for 50% Contoured Occlusion, x/D = 6.125, R_{e_D} = 2540, R_{e_d} = 3592.

structure to persist farther downstream before dissipating into a more random spectra. This can be seen in Figures 53 through 57 for the sharp-edged occlusions and in Figures 58 through 61 for the contoured occlusions. The trends in the off-centerline spectra also show the peaked distributions to persist closer to the wall than did the higher R_{e_D} data. The contoured occlusion spectral energy intensities are lower than the corresponding sharp-edged occlusion data.

At an even lower Reynolds number of $R_{e_D} = 635$ (Figures 62 through 66) the sharp-edged occlusion data indicates that the vortex ring structure forms in the region immediately downstream of the occlusion but then dissipates without forming any significant higher frequency turbulence (Figures 64, 65 and 66, note change in energy scale). The corresponding data for the contoured occlusion did not indicate any measureable energy except at DC and is not reported.

6.2 Energy Spectral Distributions for the 75 percent Occlusions

The energy spectra distributions obtained at $R_{e_D} = 2540$ for a range of radial and axial positions using the 75 percent occlusions are shown in Figures 67 through 75. The trends in the distributions are similar for both occlusions; i.e., a peaked distribution near the centerline immediately downstream of the occlusion and a broader turbulent-like distribution at the off-centerline and more downstream positions. The energy levels for the contoured occlusions are slightly lower than the corresponding sharp occlusion results.

At a lower Reynolds number of $R_{e_D} = 1270$, the sharp-edged occlusion spectra show a more distinct spectral peak at r = 0 and 4 mm (Figure 76) than did the data at the higher Reynolds number. The flow

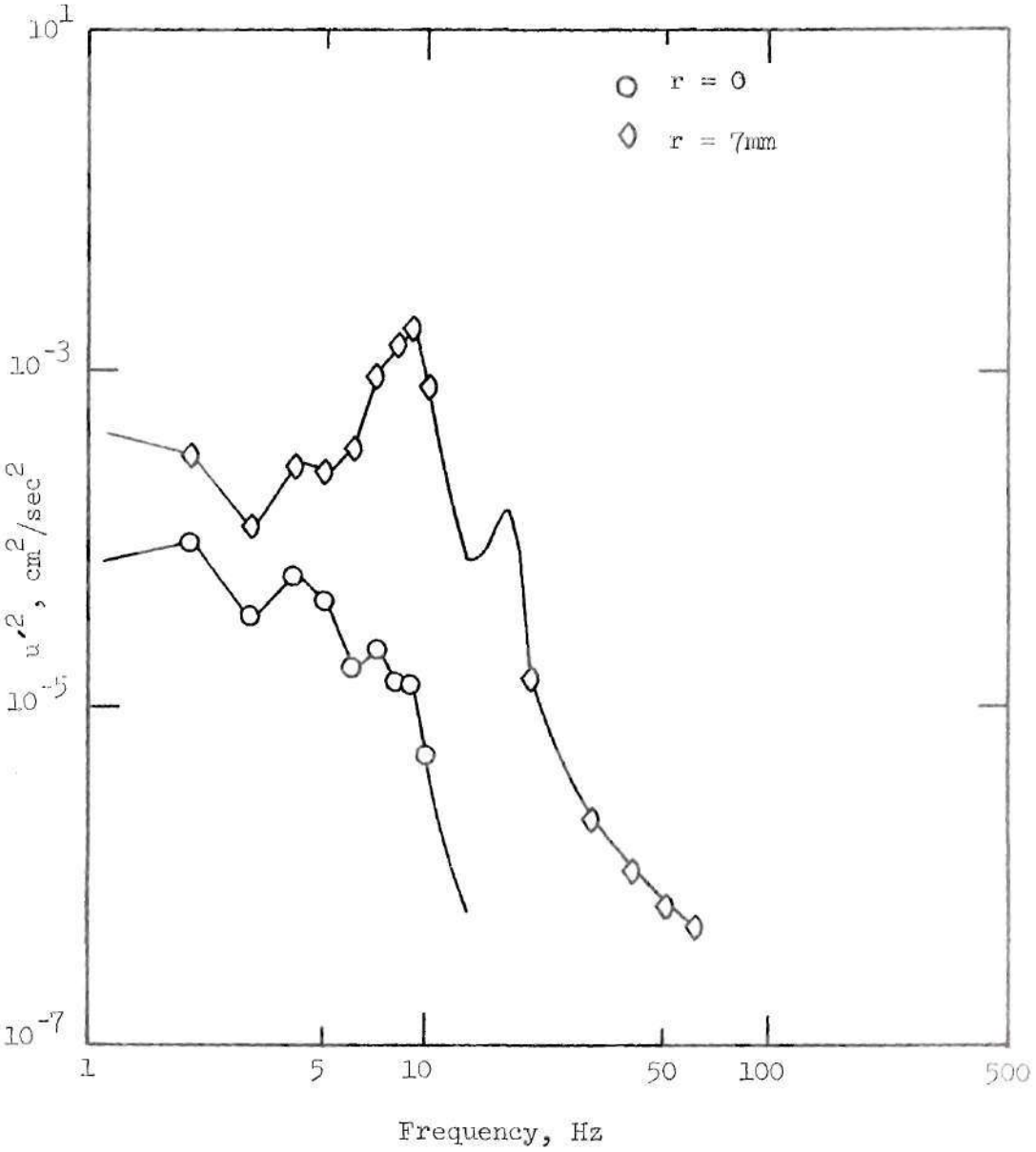

Figure 53. Energy Spectra for 50% Sharp-Edged Occulusion, $x/D = 0.5$, $R_{e_D} = 1270$, $R_{e_d} = 1796$

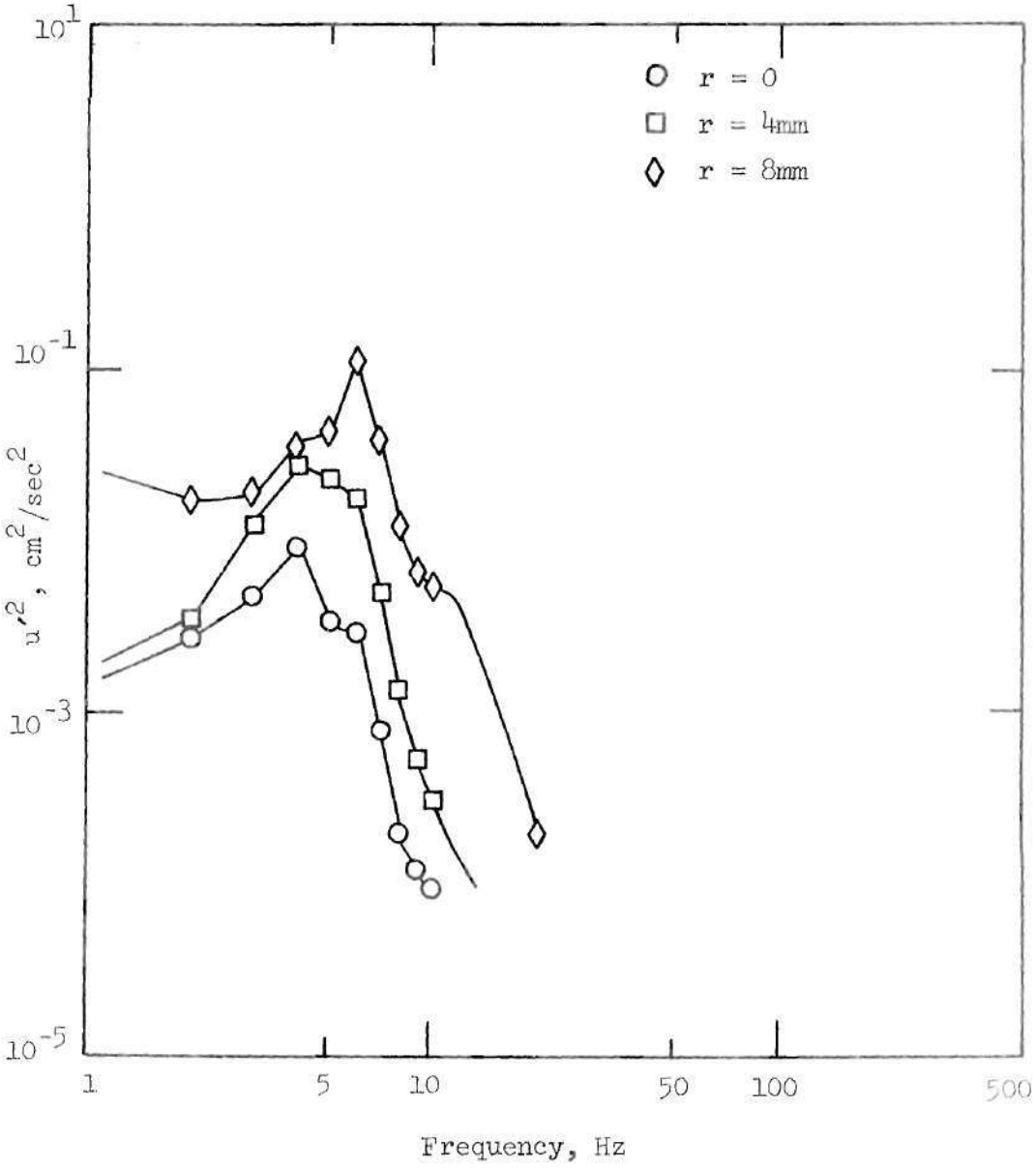

Figure 54. Energy Spectra for 50% Sharp-Edged Occulusion, $x/D = 1.125$, $R_{e_D} = 1270$, $R_{e_d} = 1796$

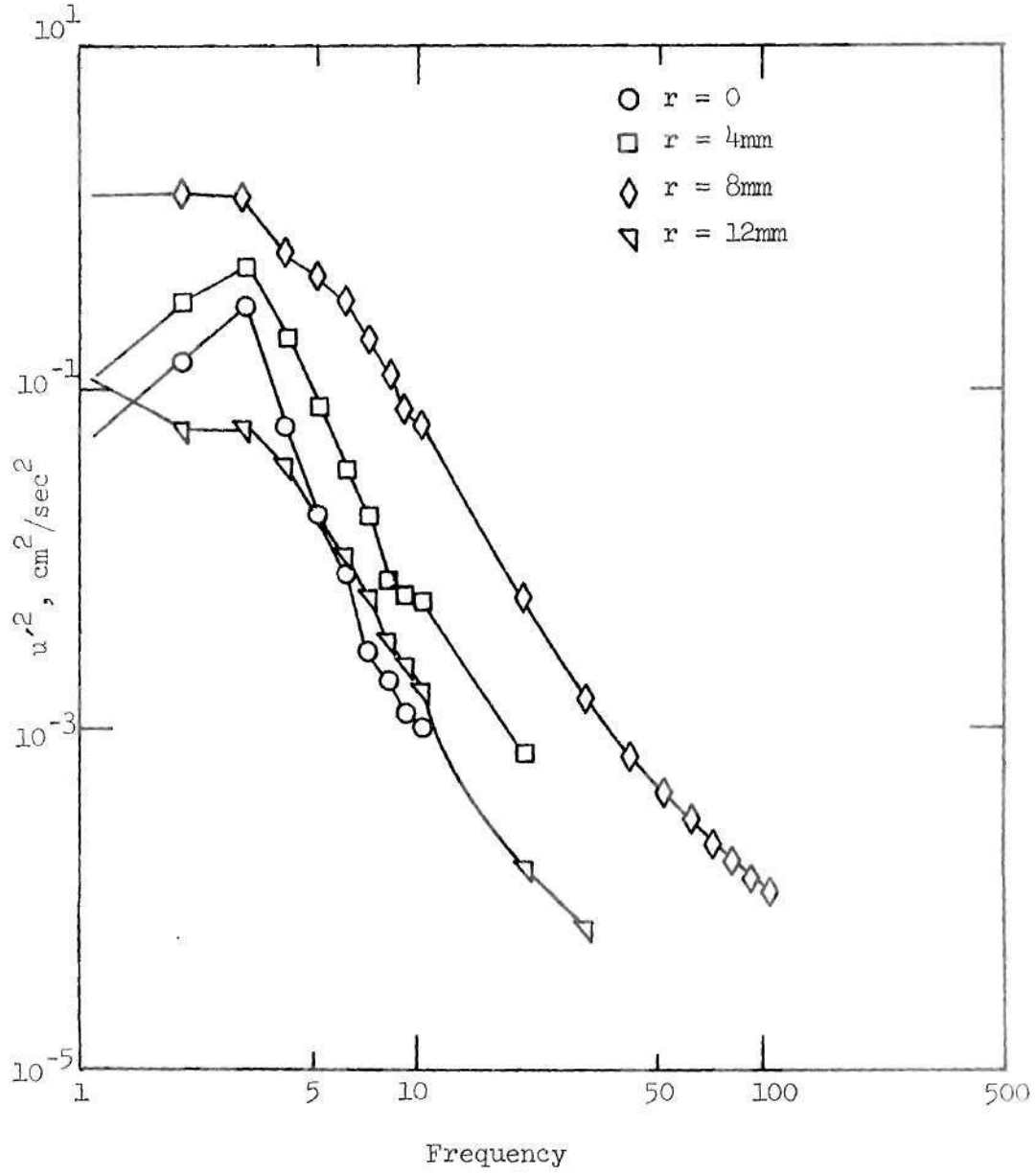

Figure 55, Energy Spectra for 50% Sharp-Edged Occlusion, $x/D = 2.125$, $R_{e_D} = 2.125$, $R_{e_d} = 1796$.

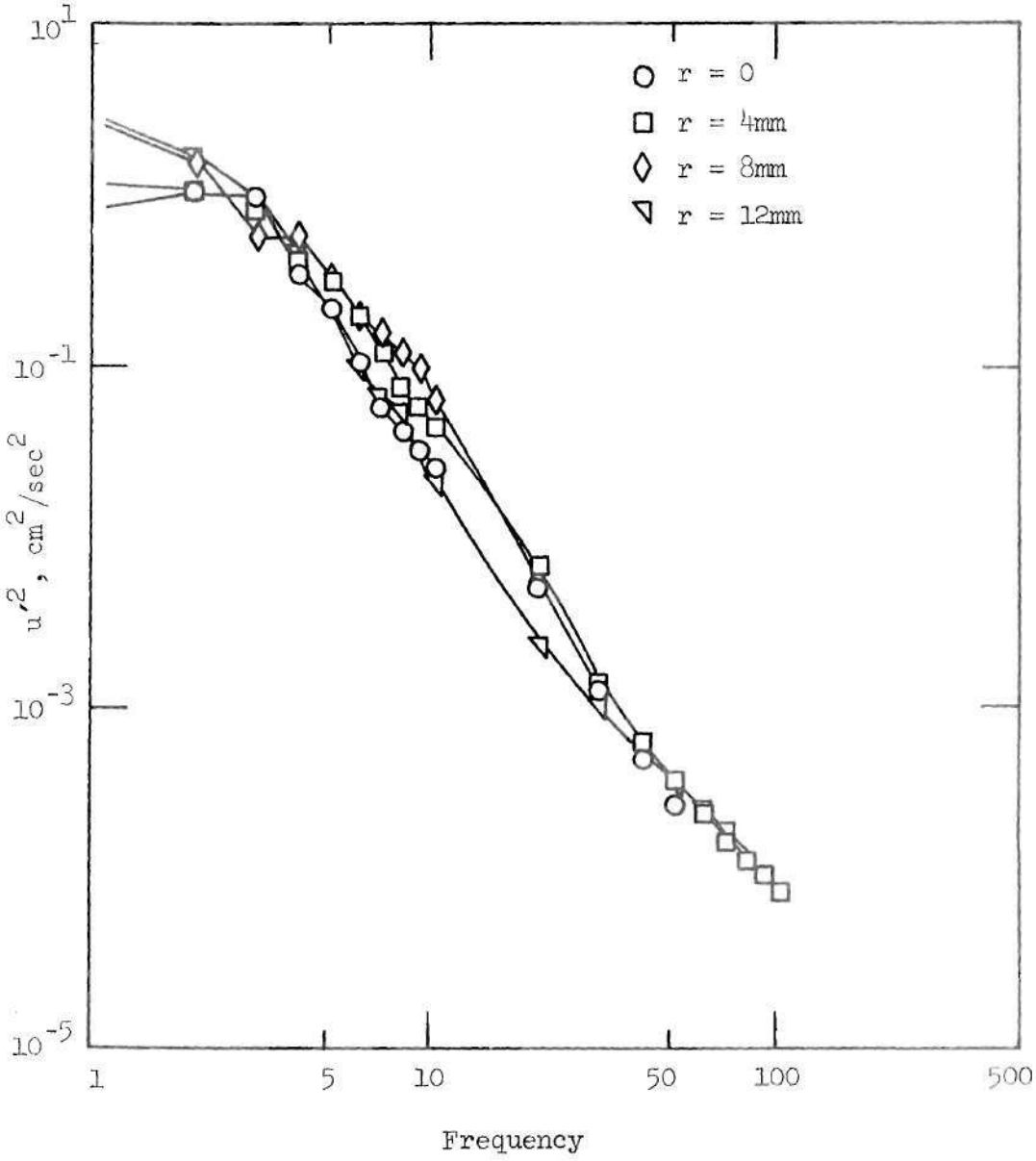

Figure 56. Energy Spectra for 50% Sharp-Edged Occlusion, x/D = 3.125, R_{e_D} = 1270, R_{e_d} = 1796.

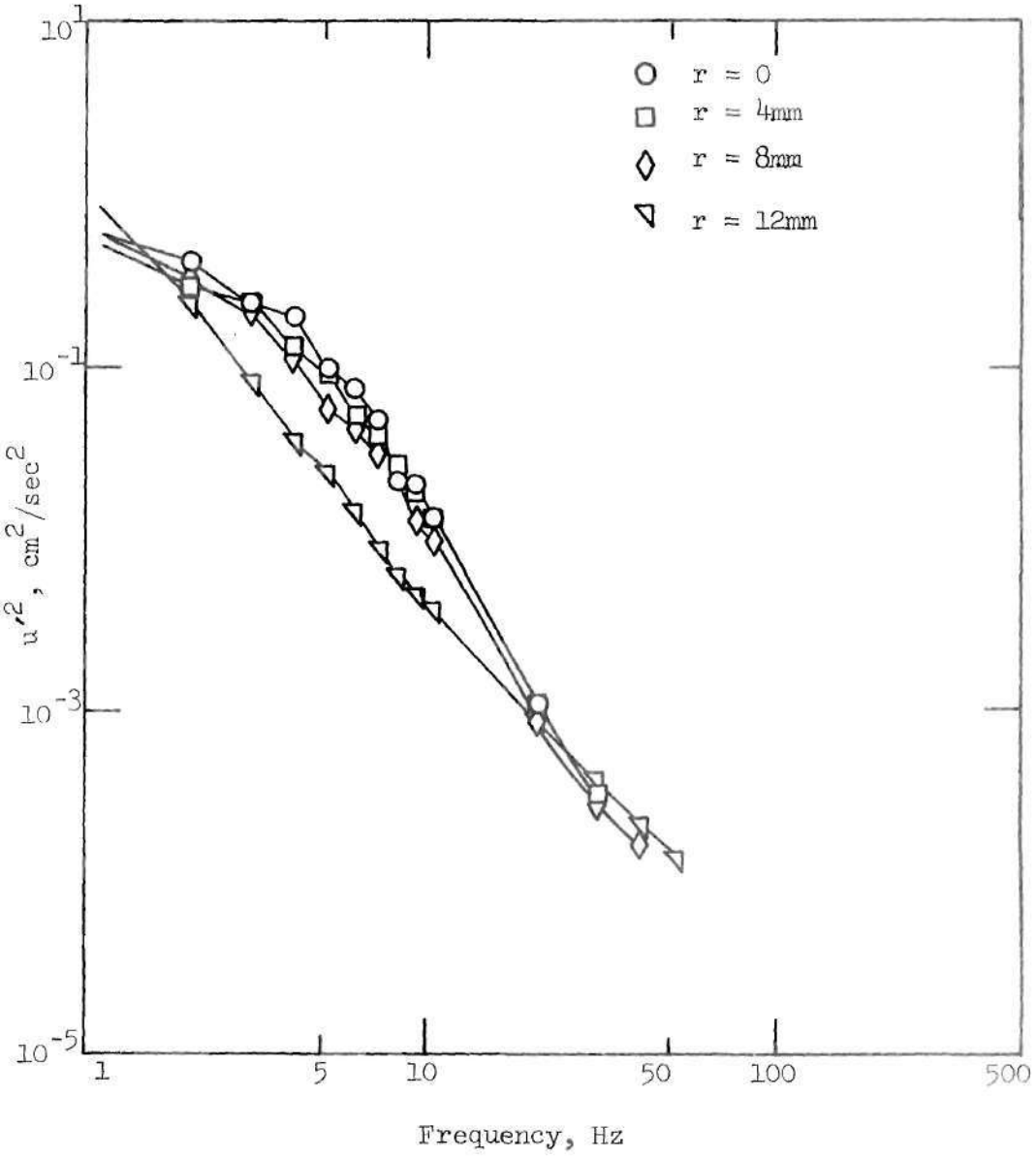

Figure 57. Energy Spectra for 50% Sharp-Edged Occlusion, $x/D = 6.125$, $R_{e_D} = 1270$, $R_{e_d} = 1796$.

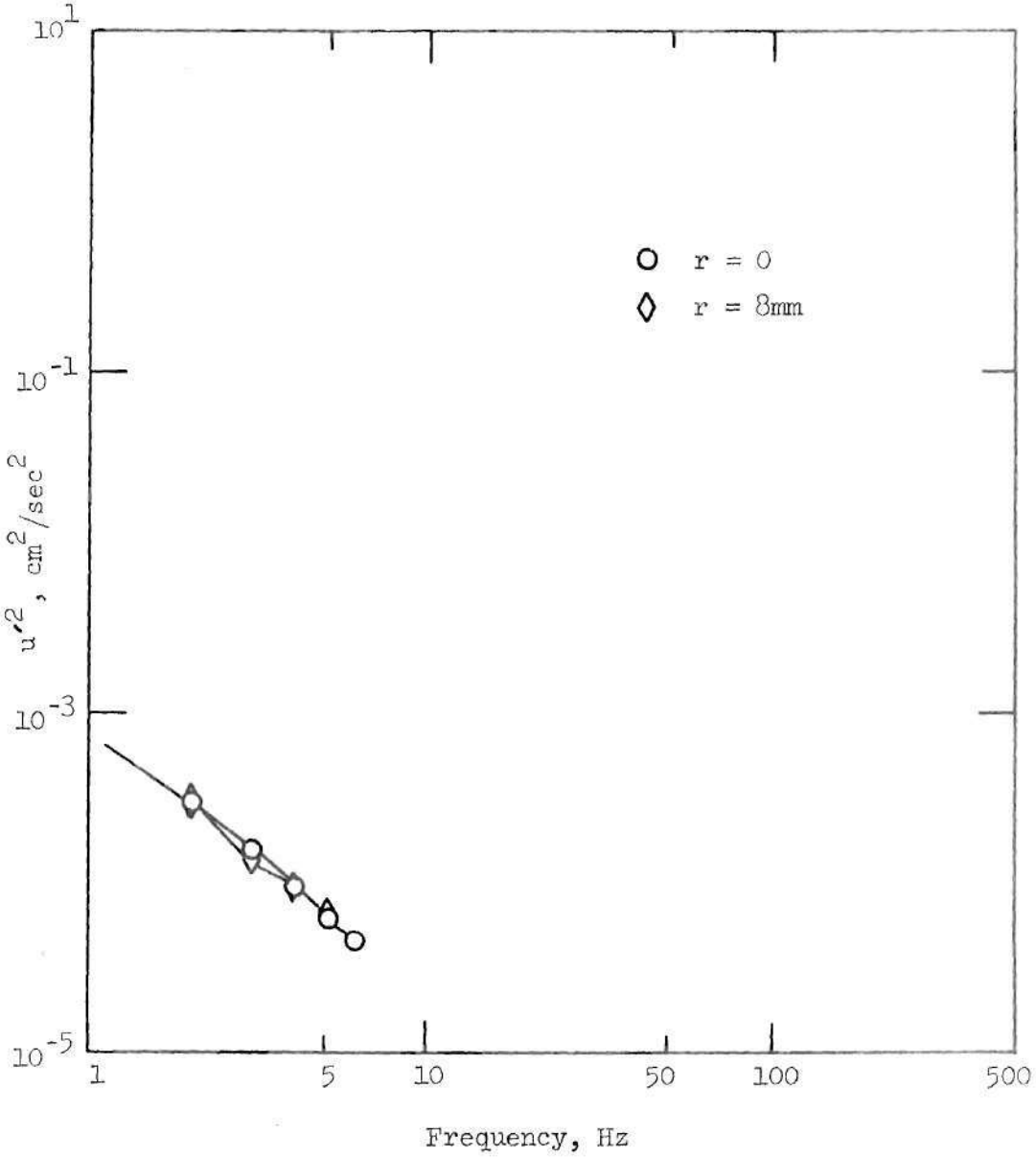

Figure 58. Energy Spectra for 50% Contoured Occlusion, x/D = 1.5, R_{e_D} = 1270, R_{e_d} = 1796.

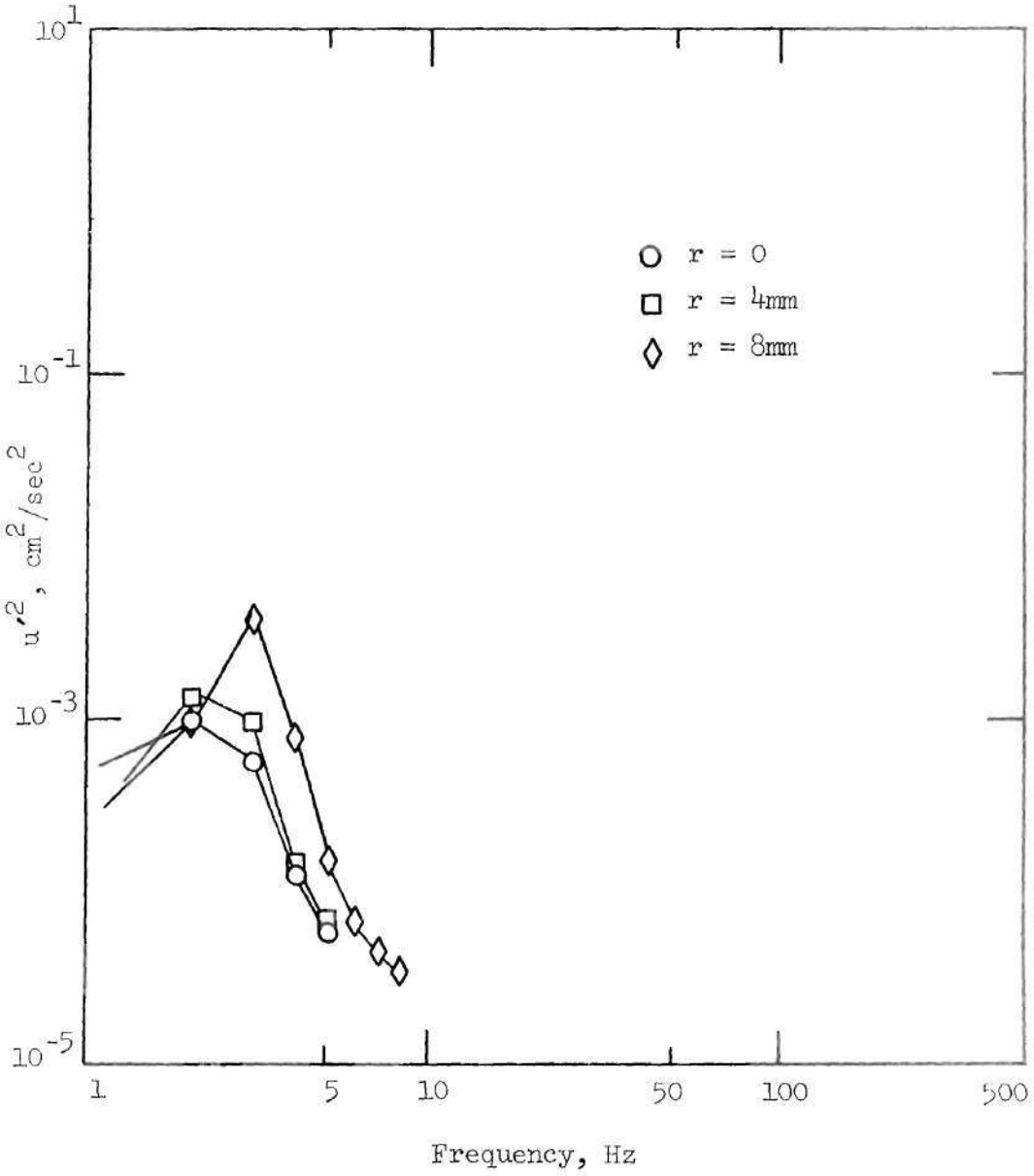

Figure 59. Energy Spectra for 50% Contoured Occlusion, x/D = 2.125, R_{e_D} = 1270, R_{e_d} = 1796.

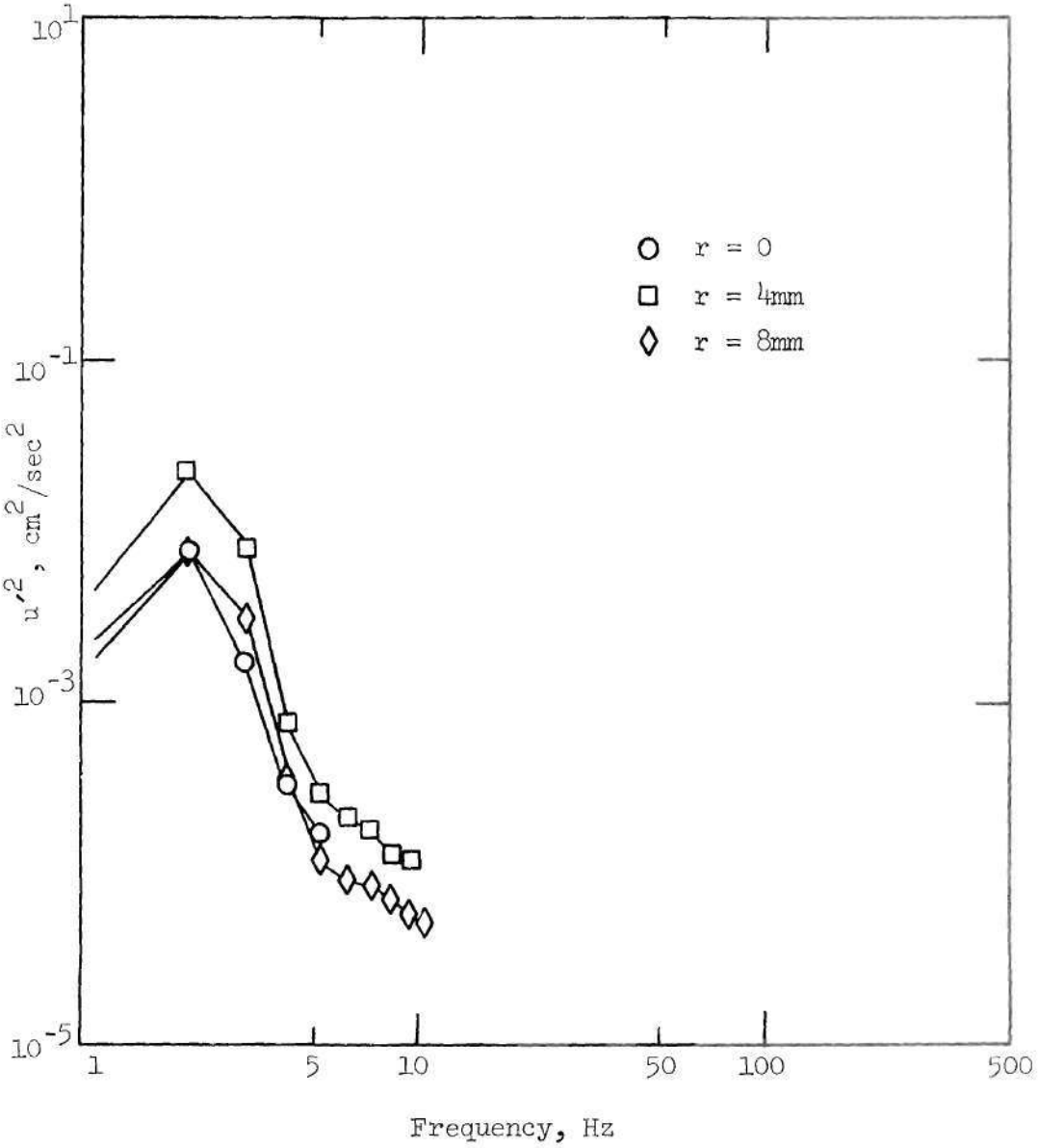

Figure 60. Energy Spectra for 50% Contoured Occlusion, x/D = 3.125, R_{e_D} = 1270, R_{e_d} = 1796.

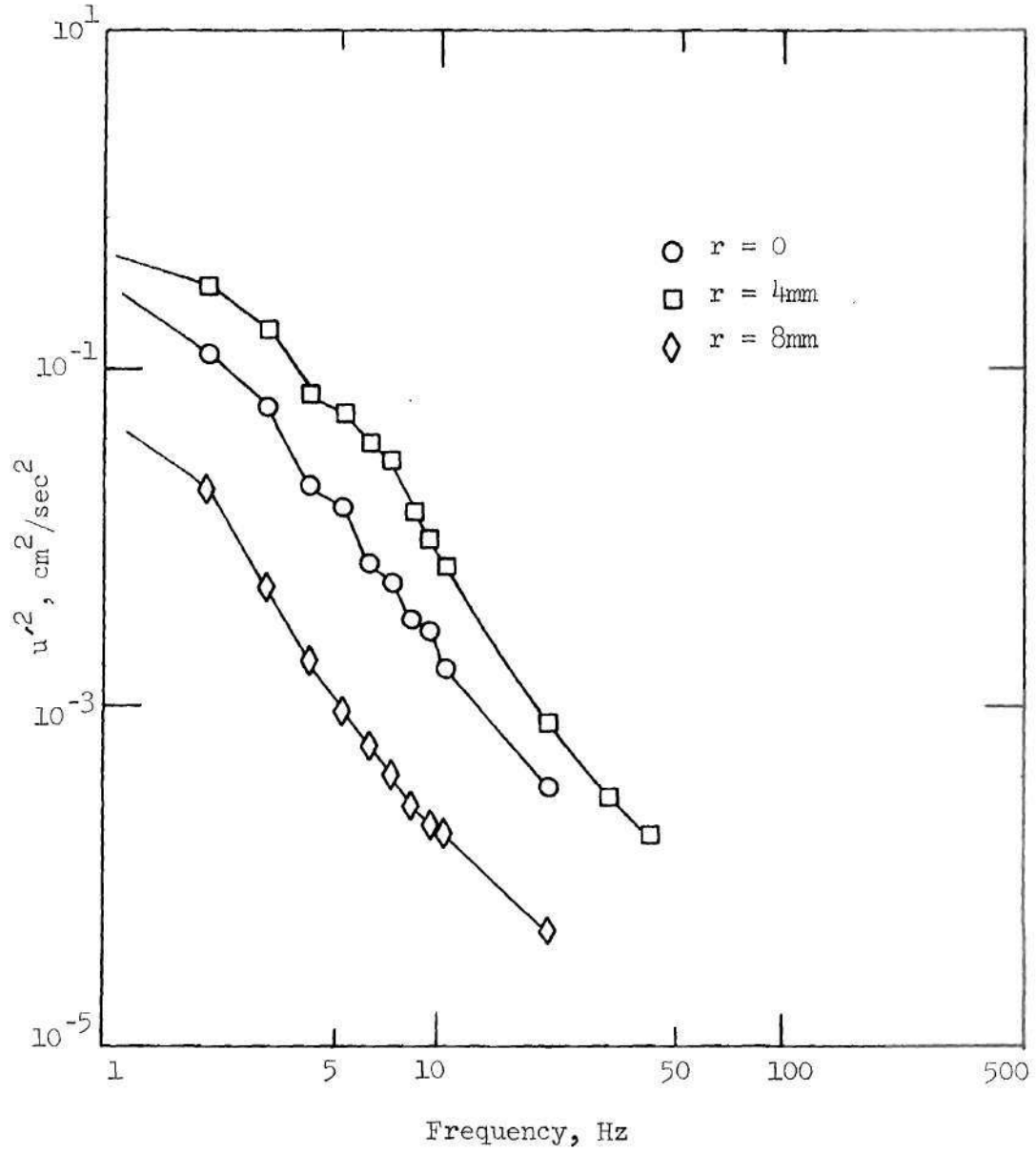

Figure 61. Energy Spectra for 50% Contoured Occlusion, x/D = 6.125, R_{e_D} = 1270, R_{e_d} = 1796.

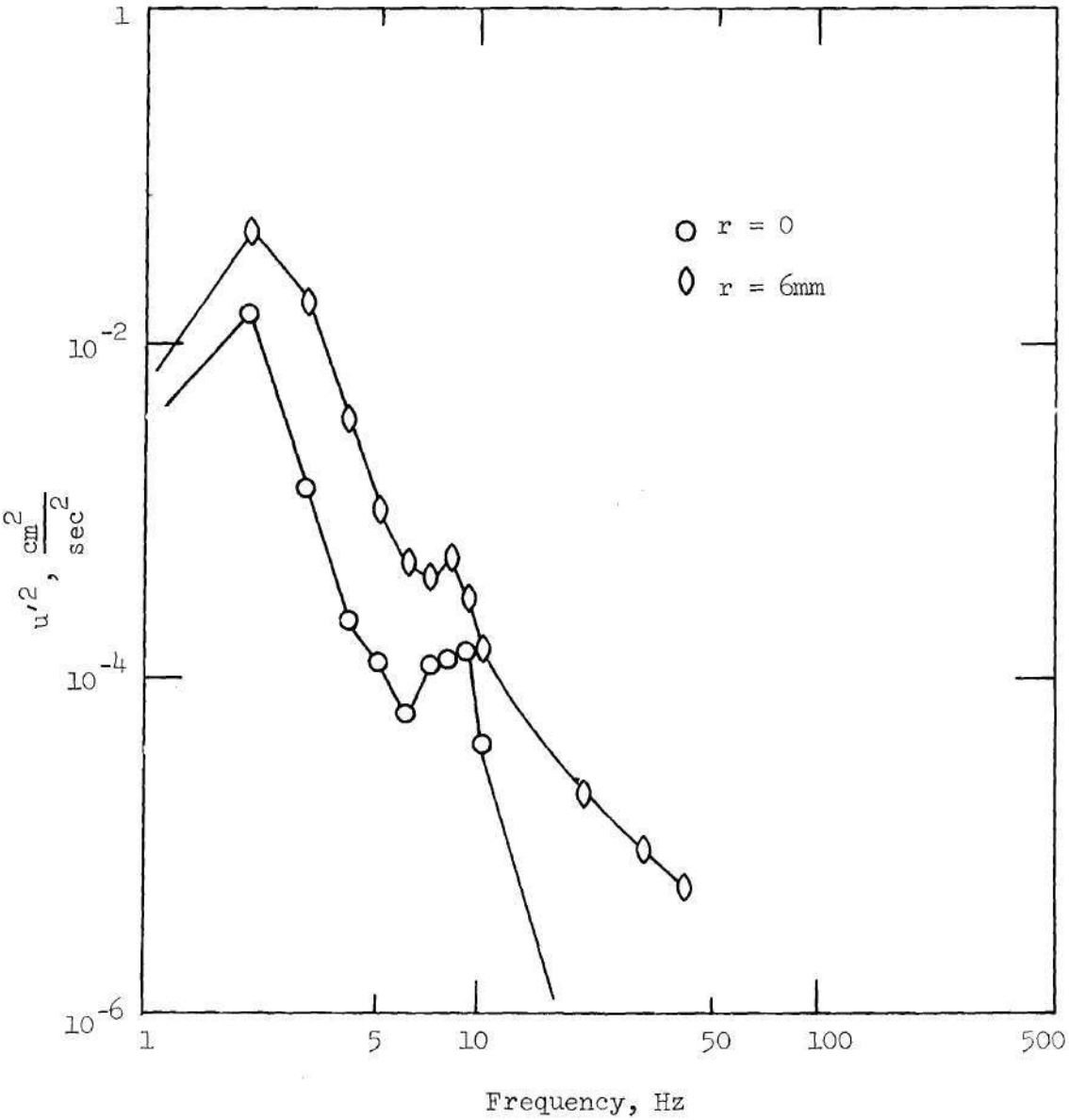

Figure 62. Energy Spectra for 50% Sharp-Edged Occlusion, $x/D = 0.5$, $R_{e_D} = 635$, $R_{e_d} = 898$.

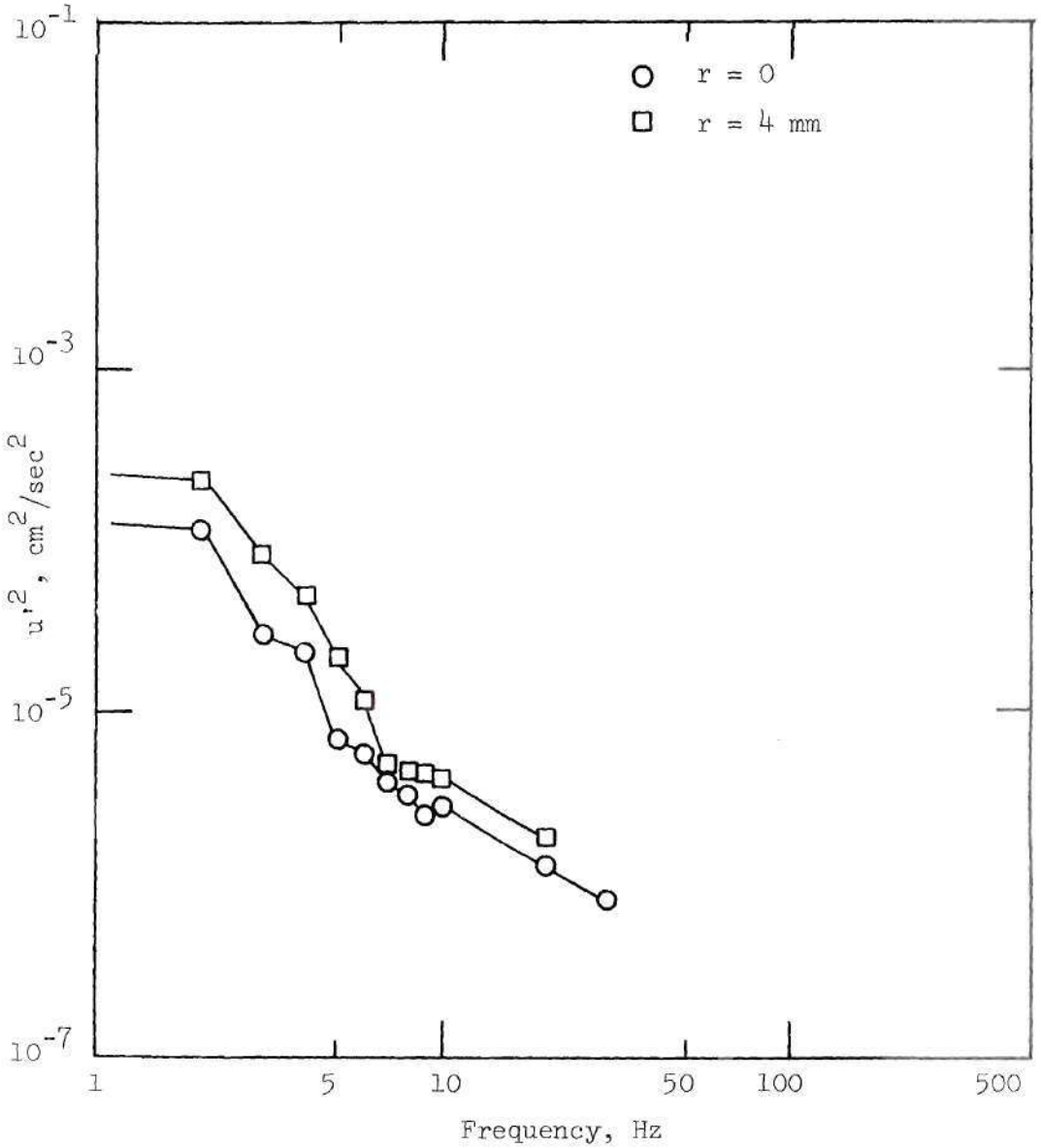

Figure 63. Energy Spectra for 50% Sharp-Edged Occlusion, x/D = 1.125, R_{e_D} = 635, R_{e_d} = 898

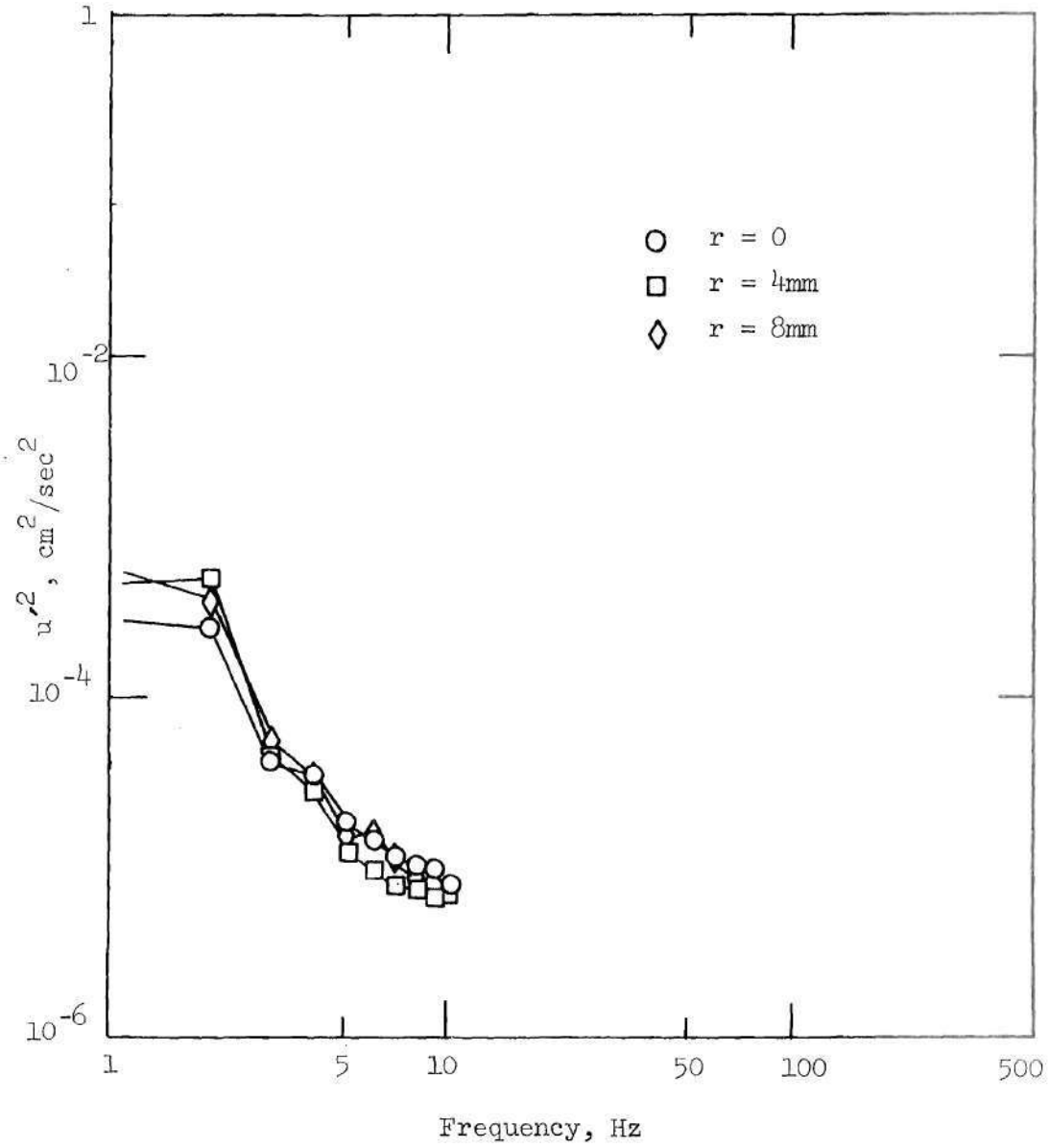

Figure 64. Energy Spectra for 50% Sharp-Edged Occlusion, x/D = 2.125, R_{e_D} = 635, R_{e_d} = 898.

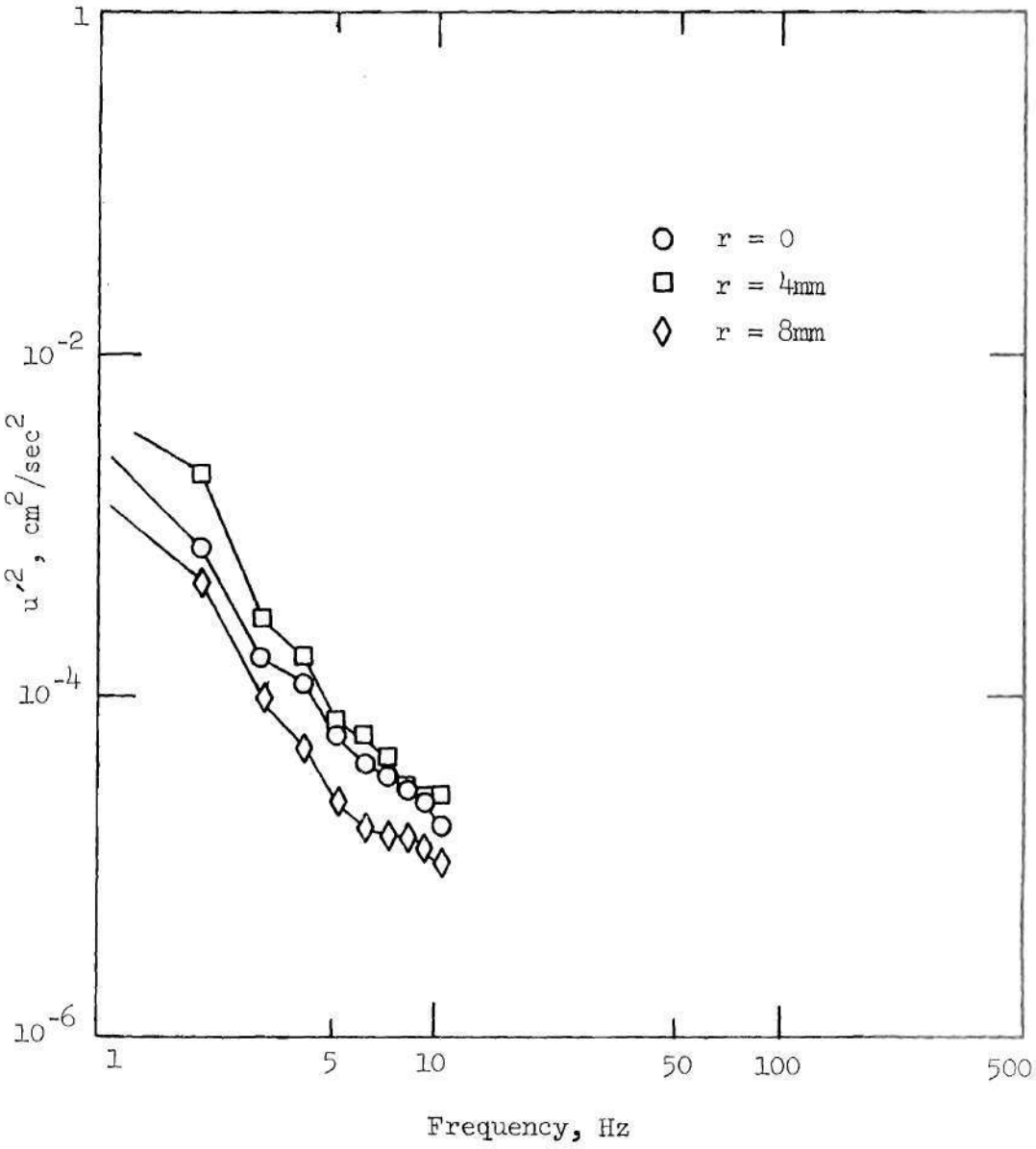

Figure 65. Energy Spectra for 50% Sharp-Edged Occlusion, x/D = 3.125, R_{e_D} = 635, R_{e_d} = 898.

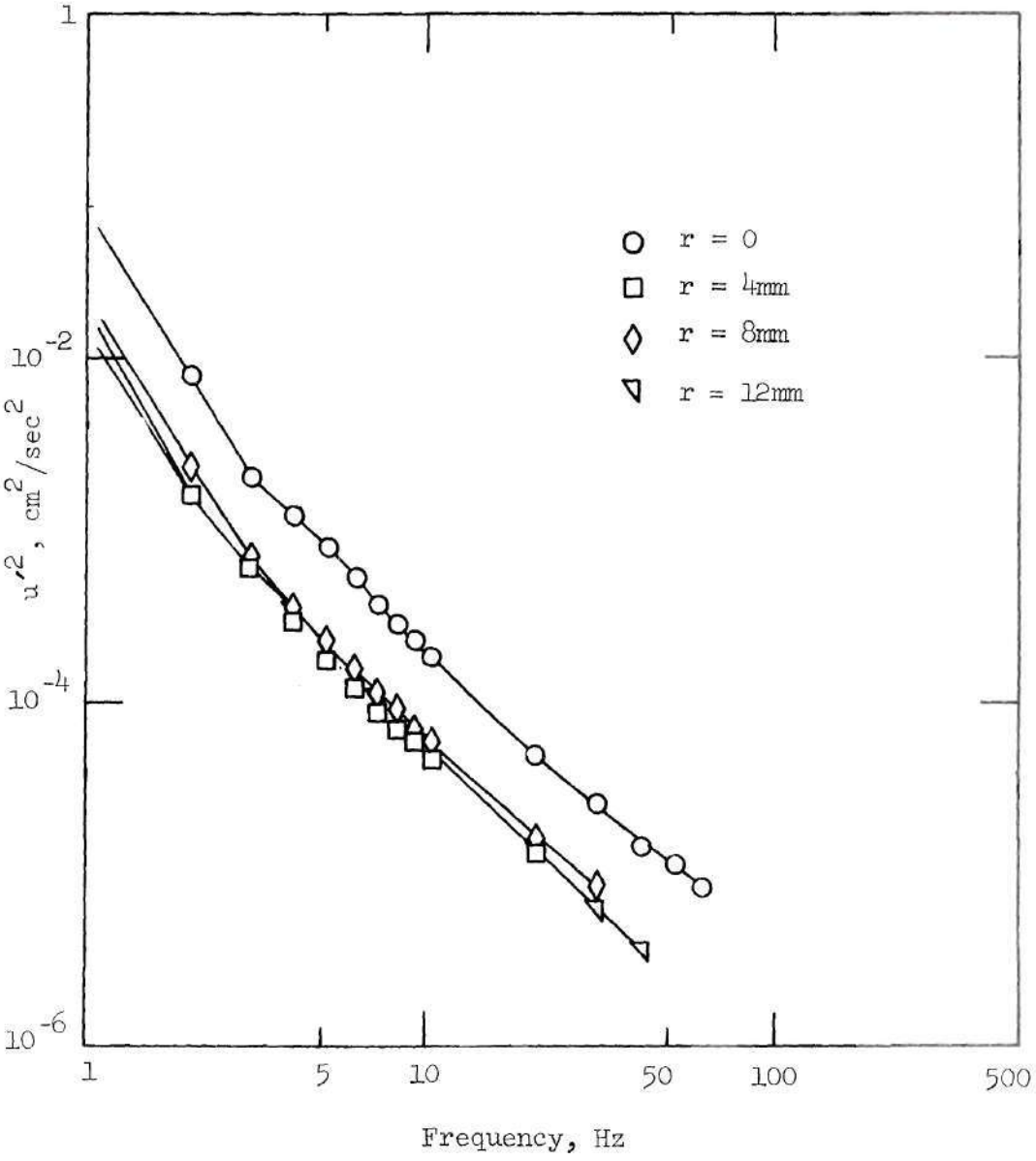

Figure 66. Energy Spectra for 50% Sharp-Edged Occlusion, x/D = 6.125, R_{e_D} = 635, R_{e_d} = 898.

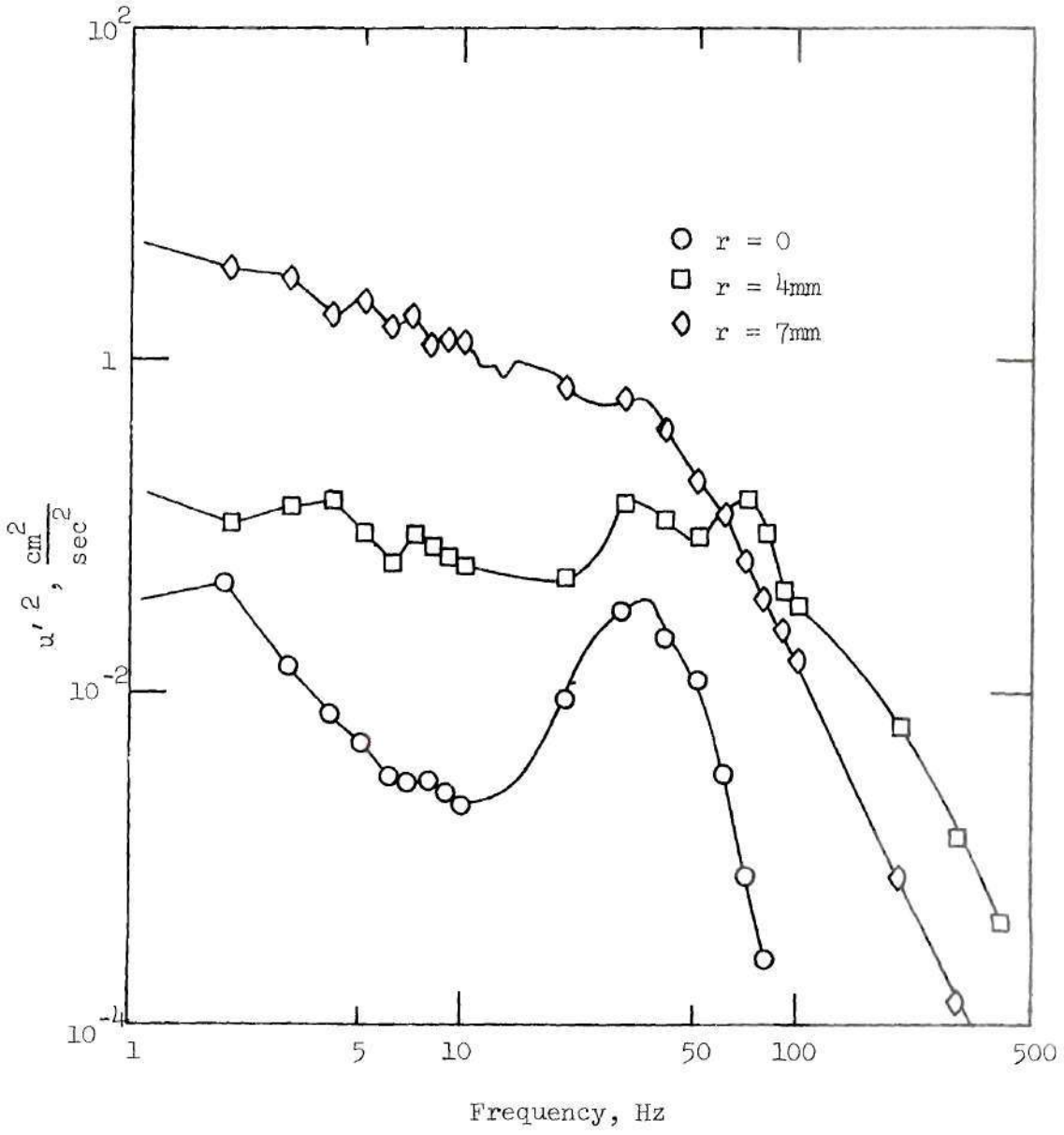

Figure 67. Energy Spectra for 75% Sharp-Edged Occlusion, x/D = 0.5, R_{e_D} = 2540, R_{e_d} = 5080.

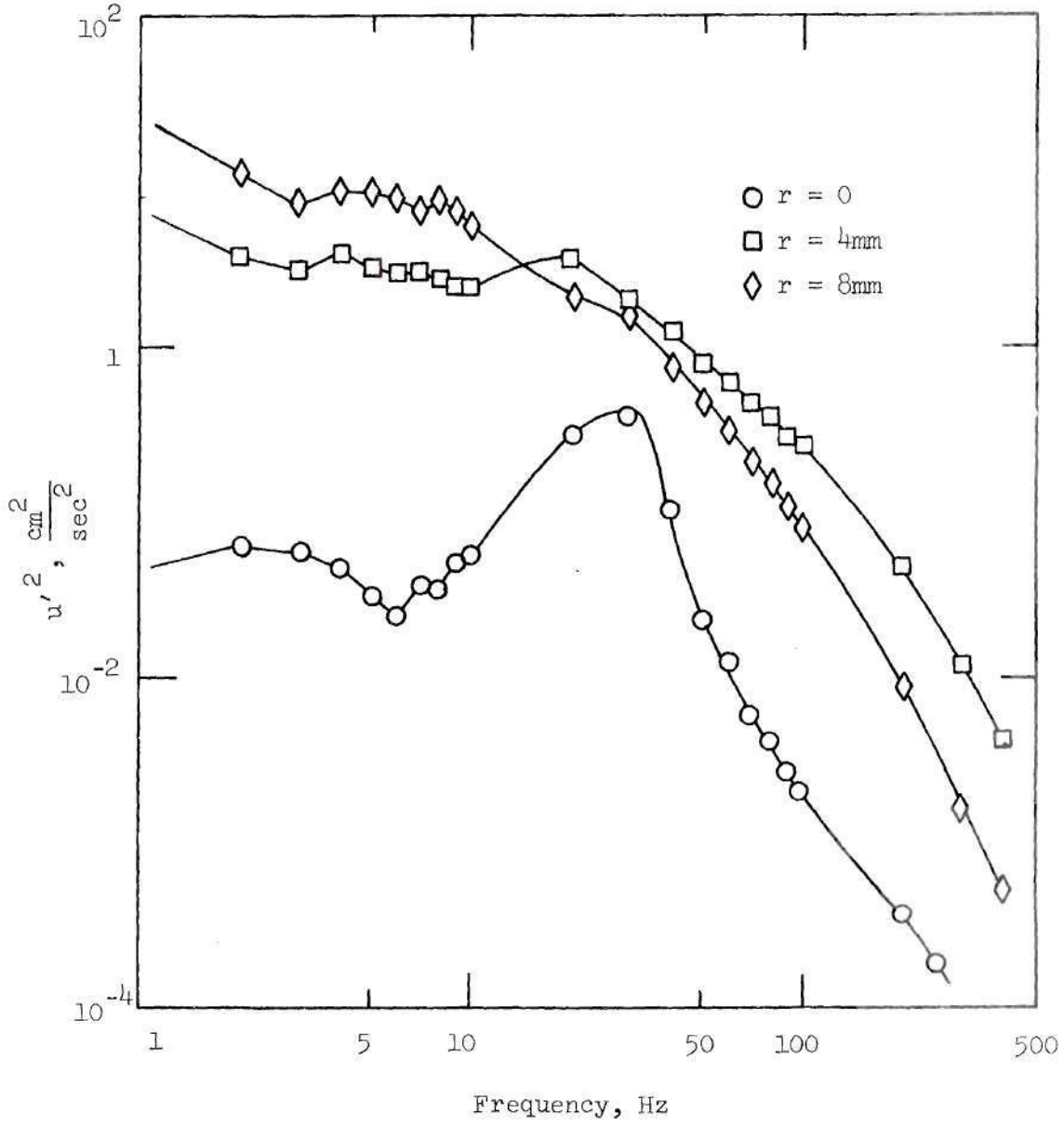

Figure 68. Energy Spectra for 75% Sharp-Edged Occlusion, $x/D = 1.125$, $R_{e_D} = 2540$, $R_{e_d} = 5080$.

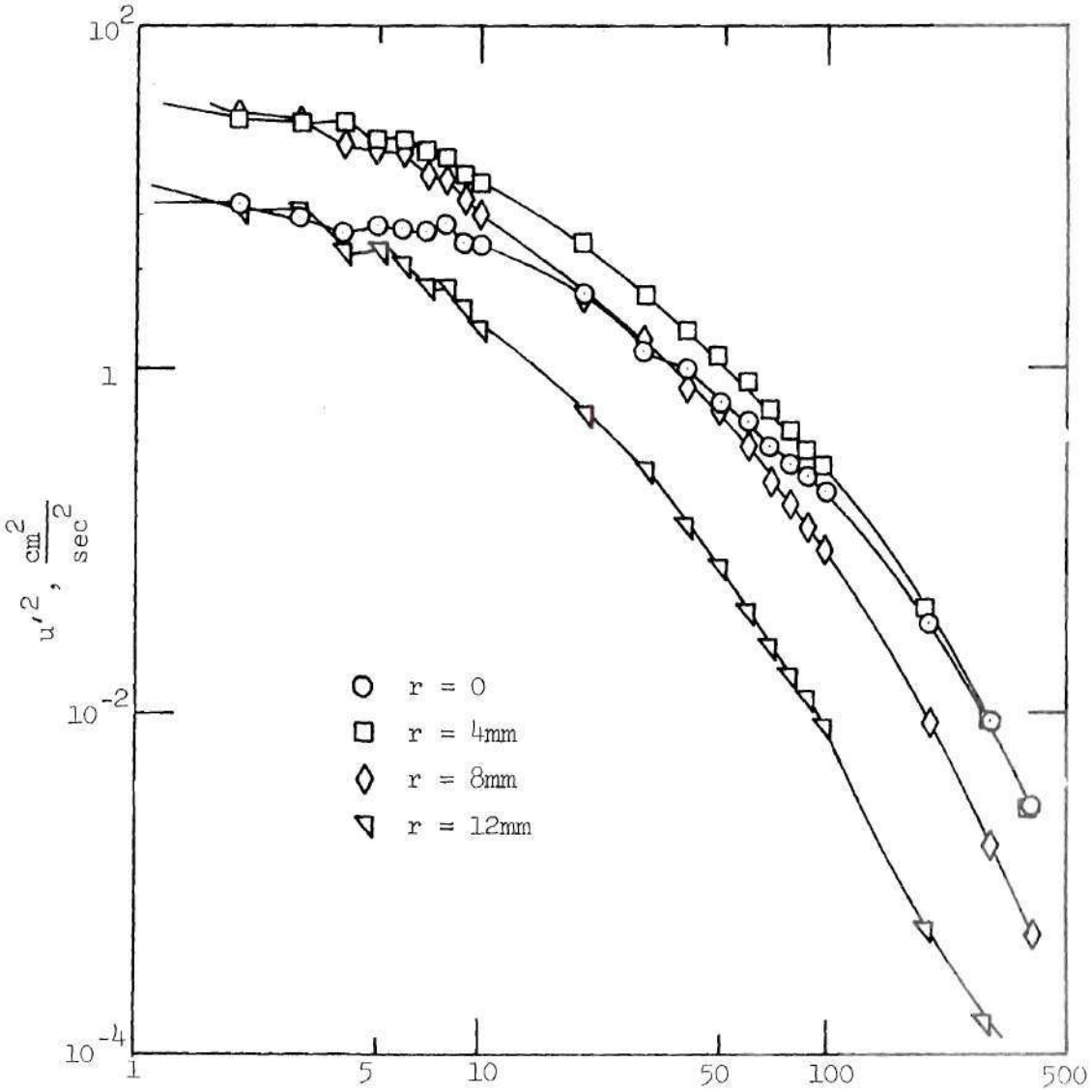

Figure 69. Energy Spectra for 75% Sharp-Edged Occlusion, x/D = 2.125, R_{e_D} = 2540, R_{e_d} = 5080.

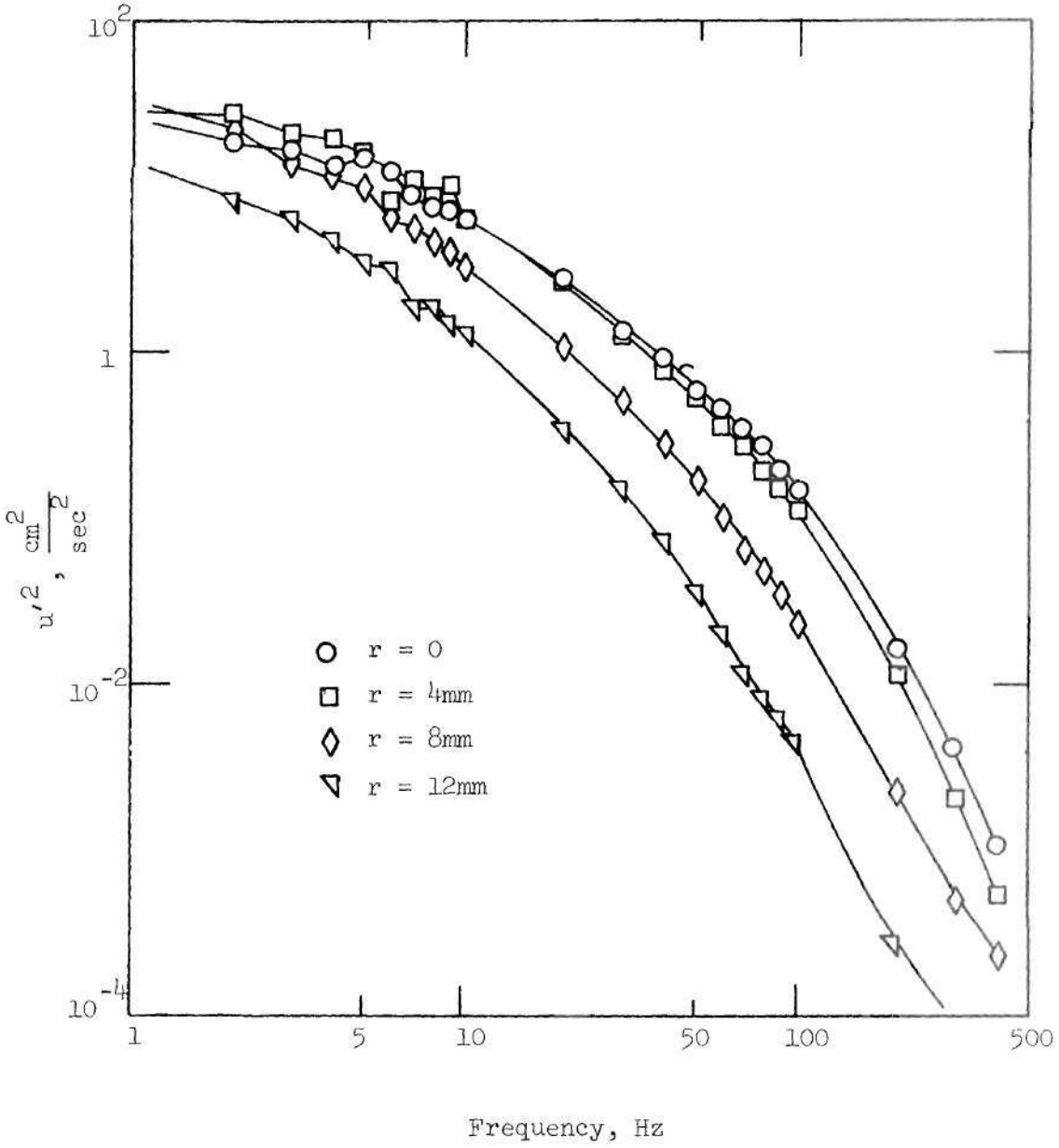

Figure 70. Energy Spectra for 75% Sharp-Edged Occlusion, $x/D = 3.125$, $R_{e_D} = 2540$, $R_{e_d} = 5080$.

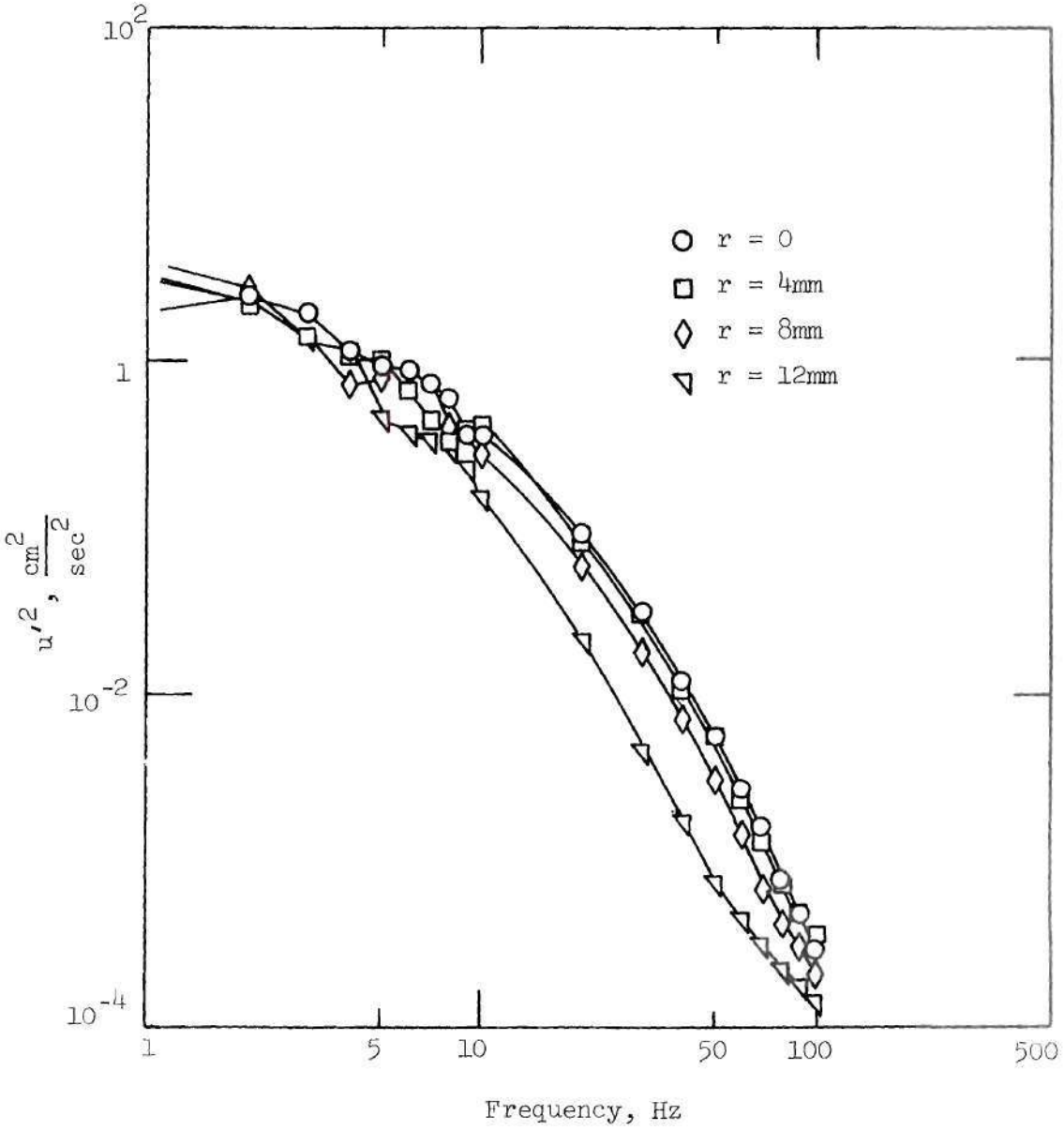

Figure 71. Energy Spectra for 75% Sharp-Edged Occlusion, $x/D = 6.125$, $R_{e_D} = 2540$, $R_{e_d} = 5080$.

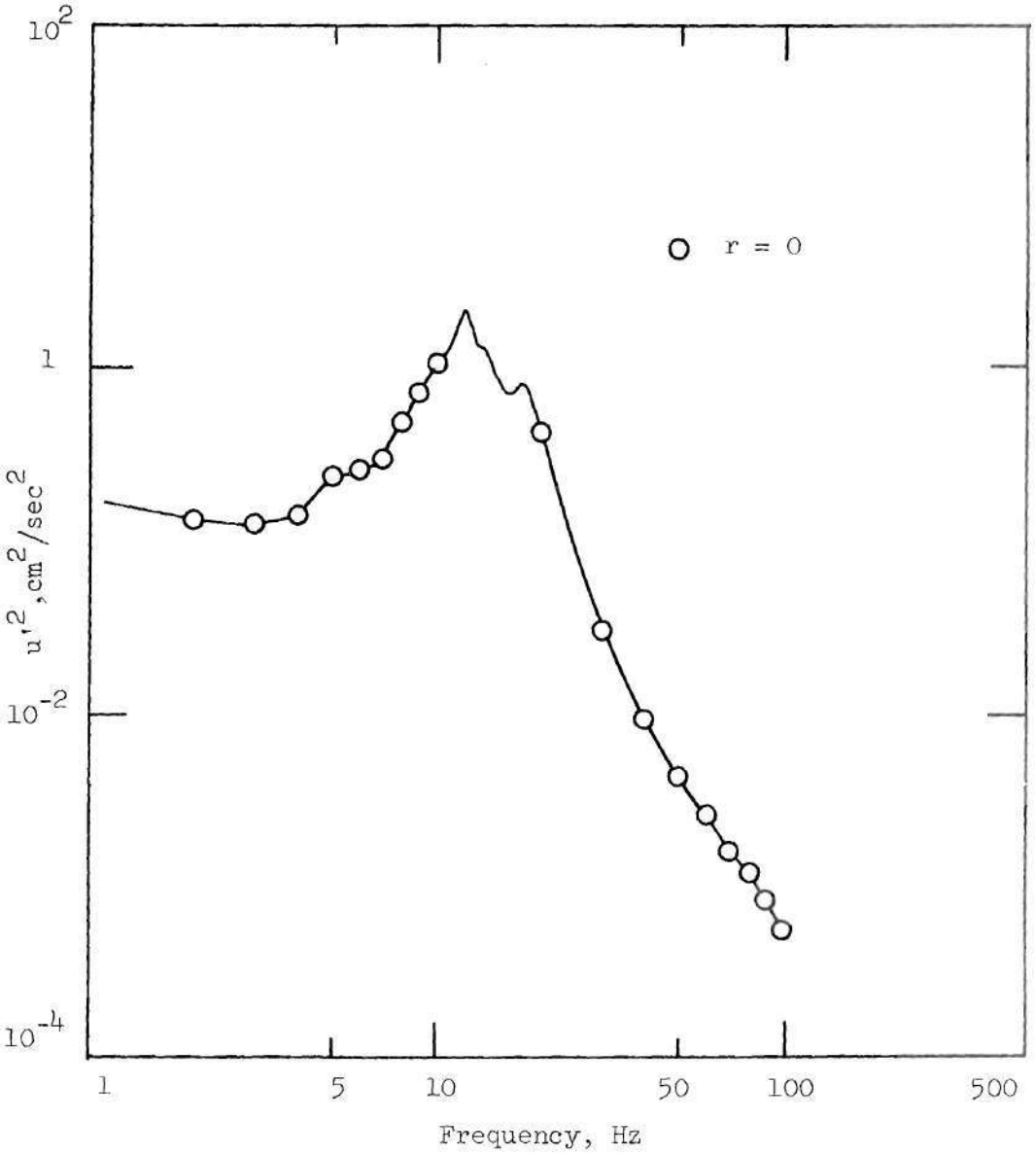

Figure 72. Energy Spectra for 75% Contoured Occlusion, x/D = 1.5, R_{e_D} = 2540, R_{e_d} = 5080

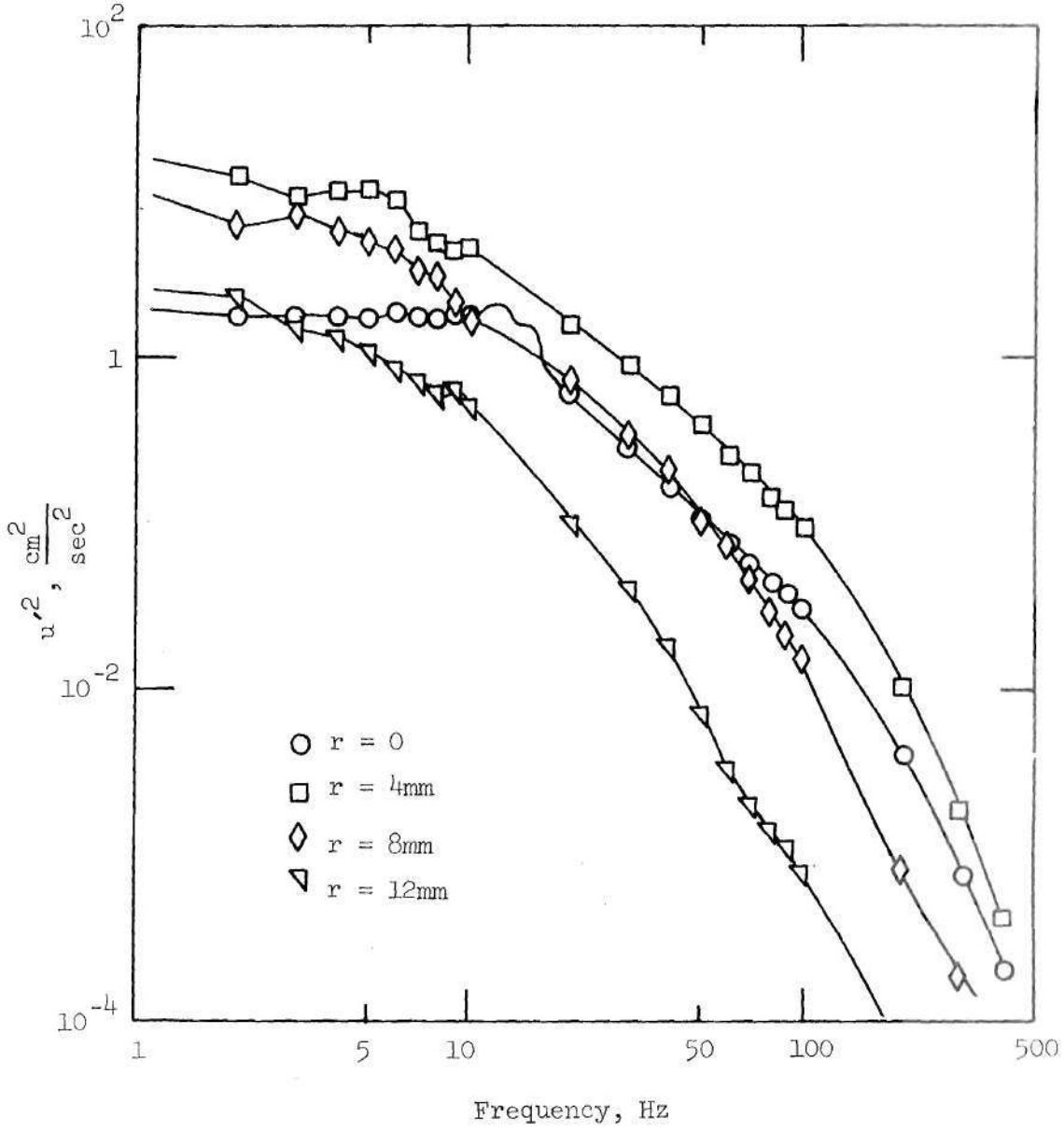

Figure 73. Energy Spectra for 75% Contoured Occlusion, $x/D = 2.125$, $R_{e_D} = 2540$, $R_{e_d} = 5080$.

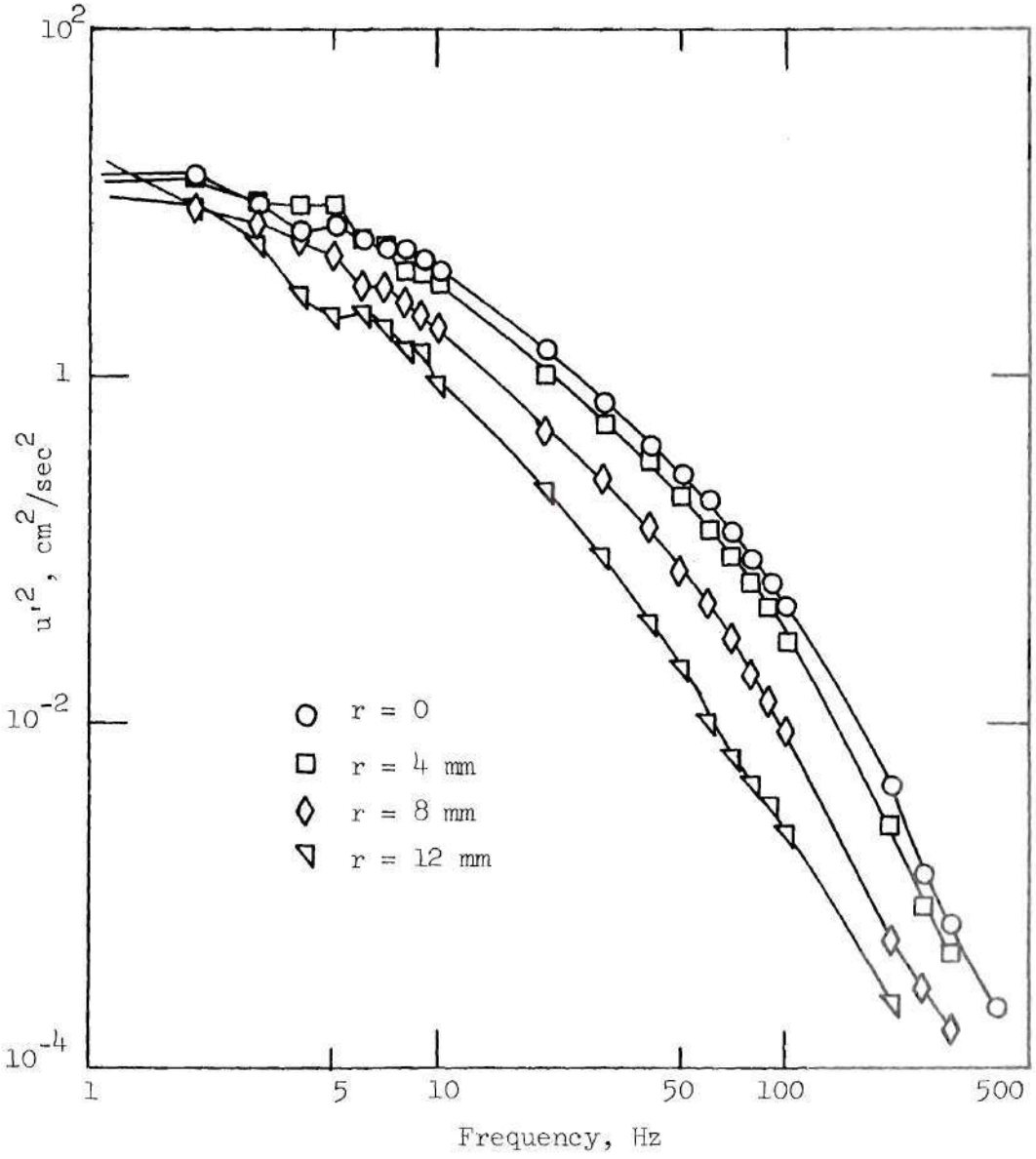

Figure 74. Energy Spectra for 75% Contoured Occlusion, x/D = 3.125, R_{e_D} = 2540, R_{e_d} = 5080

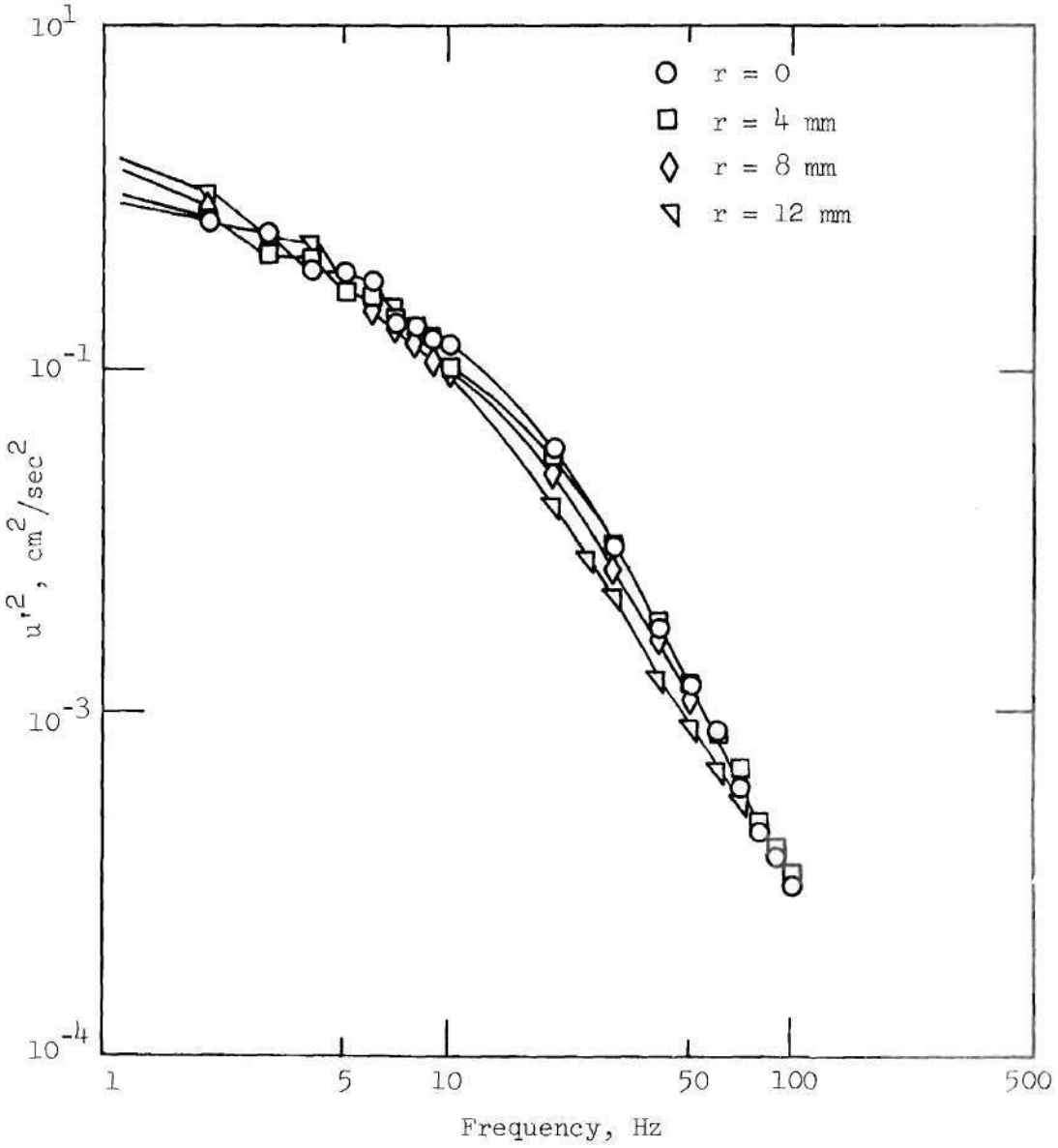

Figure 75. Energy Spectra for 75% Contoured Occlusion, $x/D = 6.125$, $R_{e_D} = 2540$, $R_{e_d} = 5080$

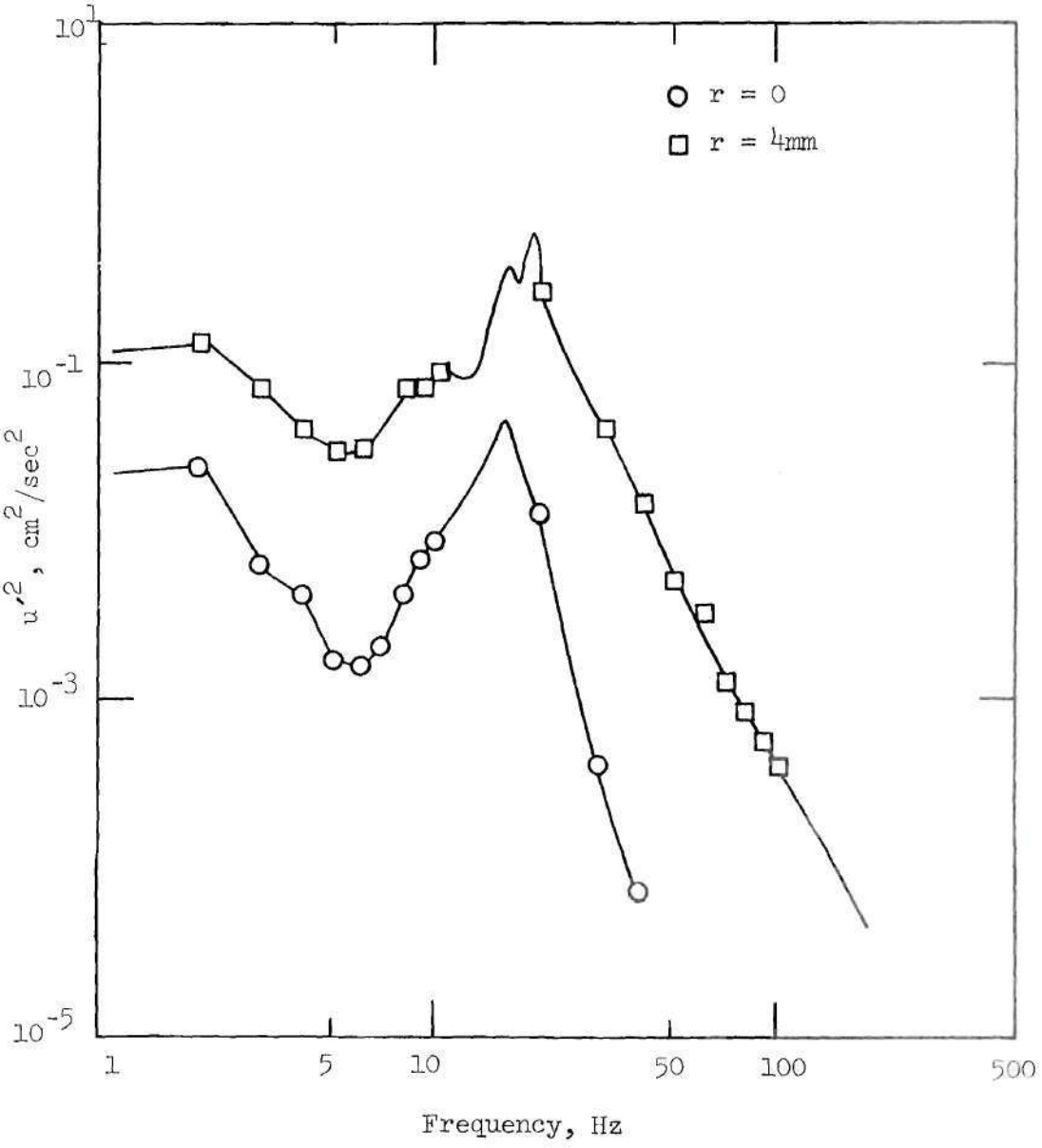

Figure 76. Energy Spectra for 75% Sharp-Edged Occlusion, $x/D = 0.5$, $R_{e_D} = 1270$, $R_{e_d} = 2540$.

again degenerates into a more dispersed distribution at the downstream positions (Figures 77, 78, 79 and 80) in a manner similar to the higher R_{e_D} data, but the overall energy levels are somewhat reduced. The contoured occlusion spectra at x/D = 1.5 (Figure 81) show a distinct peak on the centerline which is also still prevalent at the next downstream position, x/D = 2.125 (Figure 82). The corresponding position for a higher R_{e_D} (Figure 73) did not indicate the centerline spectral peak. The overall energy levels for the contoured occlusion results are also lower than the corresponding high R_{e_D} case.

At the lowest Reynolds number of R_{e_D} = 635, the resulting differences in the flow spectra for the two occlusion shapes become more outstanding. The sharp-edged occlusion results show evidence of a vortex ring structure on the centerline as far downstream as x/D = 2.125 (Figures 85, 86 and 87). The spectra at x/D = 1.125 have distinct peaks for the centerline and r = 4mm positions but the r = 8 mm position indicates some break-up of the peaked pattern and a slight reduction in overall intensity. The data at x/D = 3.125 (Figure 88) and 6.125 (Figure 89) show a random turbulent energy distribution at all radial positions with a significant decrease in overall intensity at the r = 12, near wall, location for x/D = 2.125 and 3.125 (Figures 87 and 88). The contoured occlusion spectra, however, show a peaked distribution at all radial positions as far downstream as x/D = 3.125 (Figures 90, 91, and 92). The more randomized distribution is in evidence only at the x/D = 6.125 position (Figure 93).

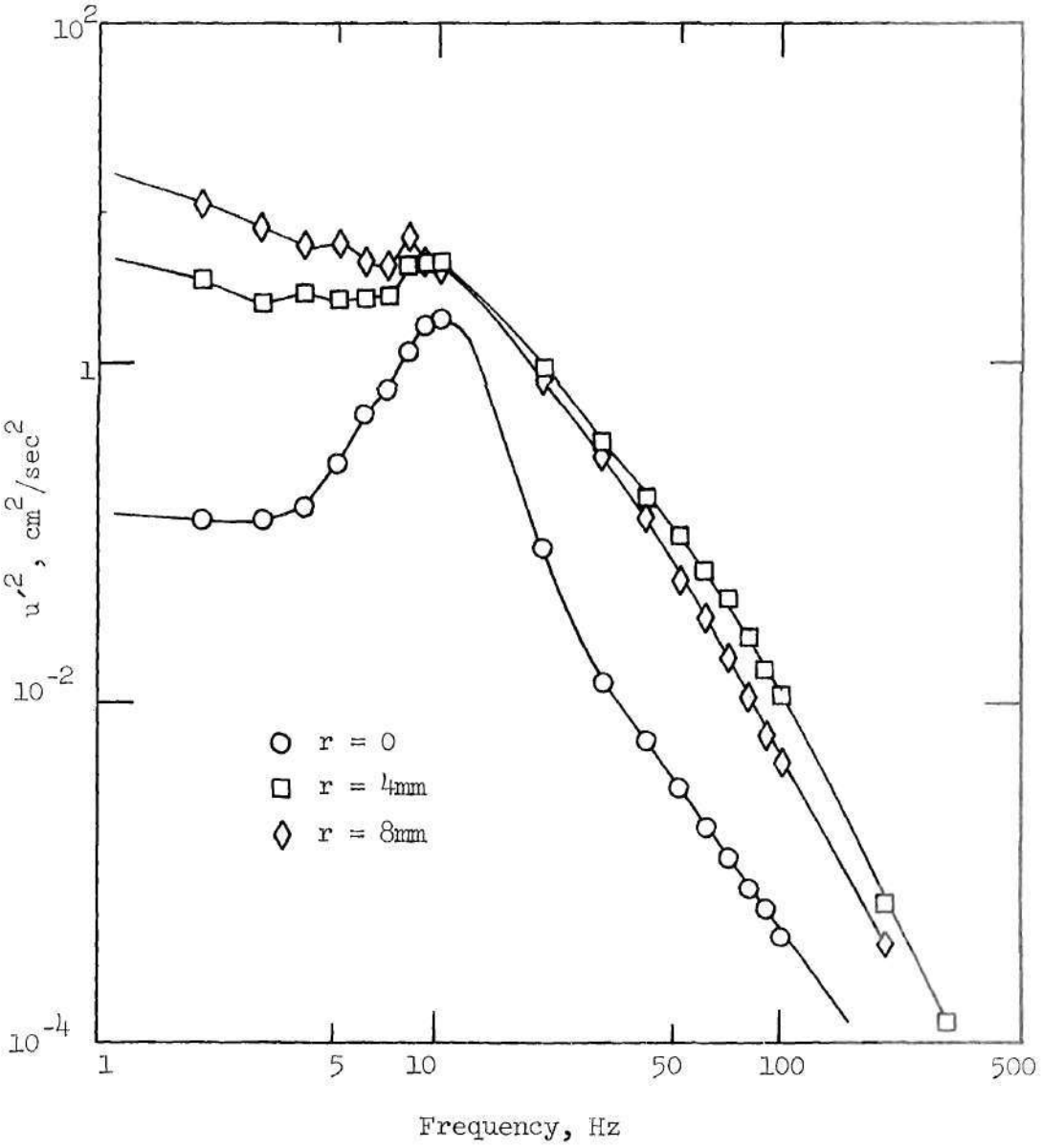

Figure 77. Energy Spectra for 75% Sharp-Edged Occlusion, x/D = 1.125, R_{e_D} = 1270, R_{e_d} = 2340.

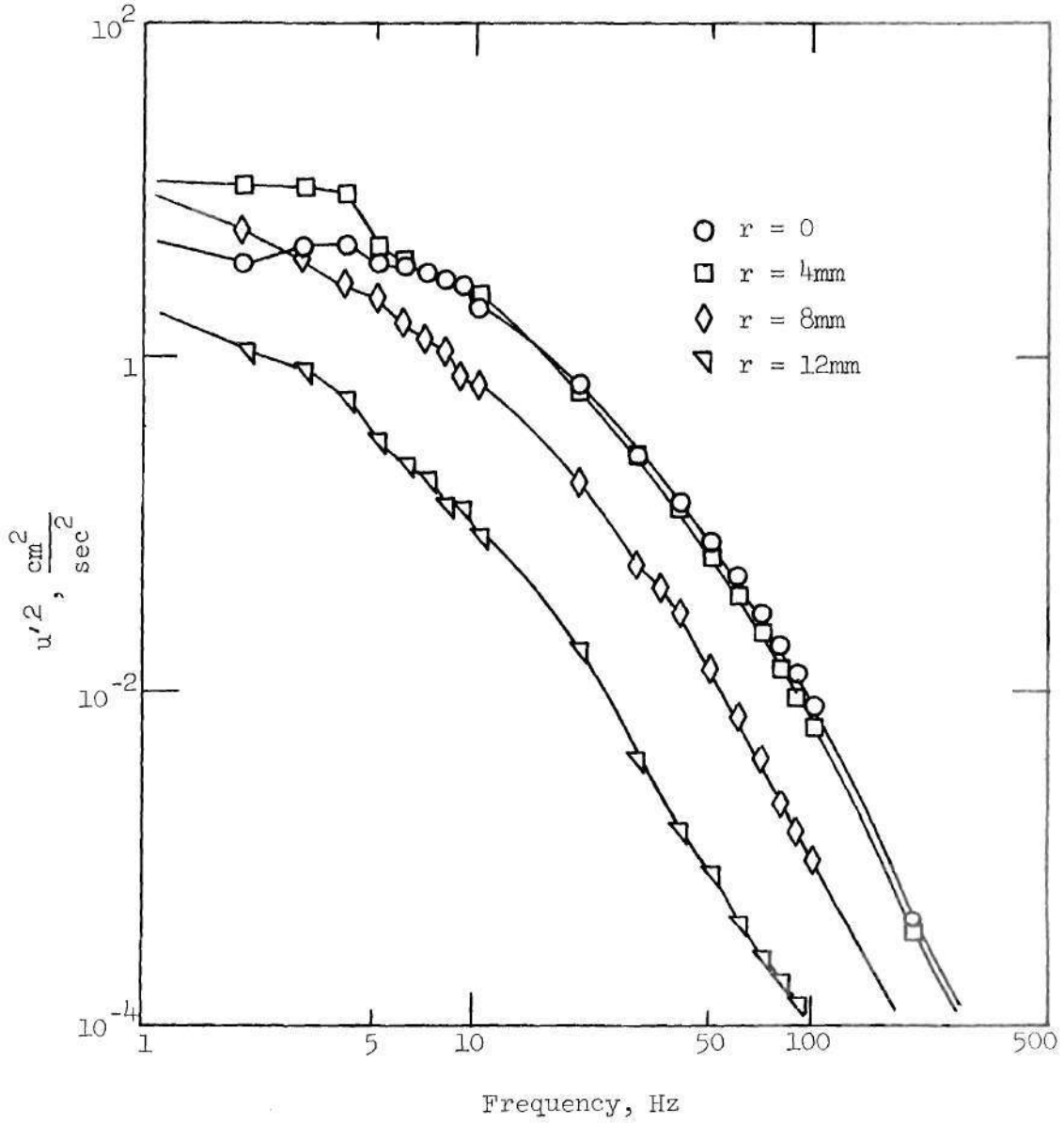

Figure 78. Energy Spectra for 75% Sharp-Edged Occlusion, $x/D = 2.125$, $R_{e_D} = 1270$, $R_{e_d} = 2540$.

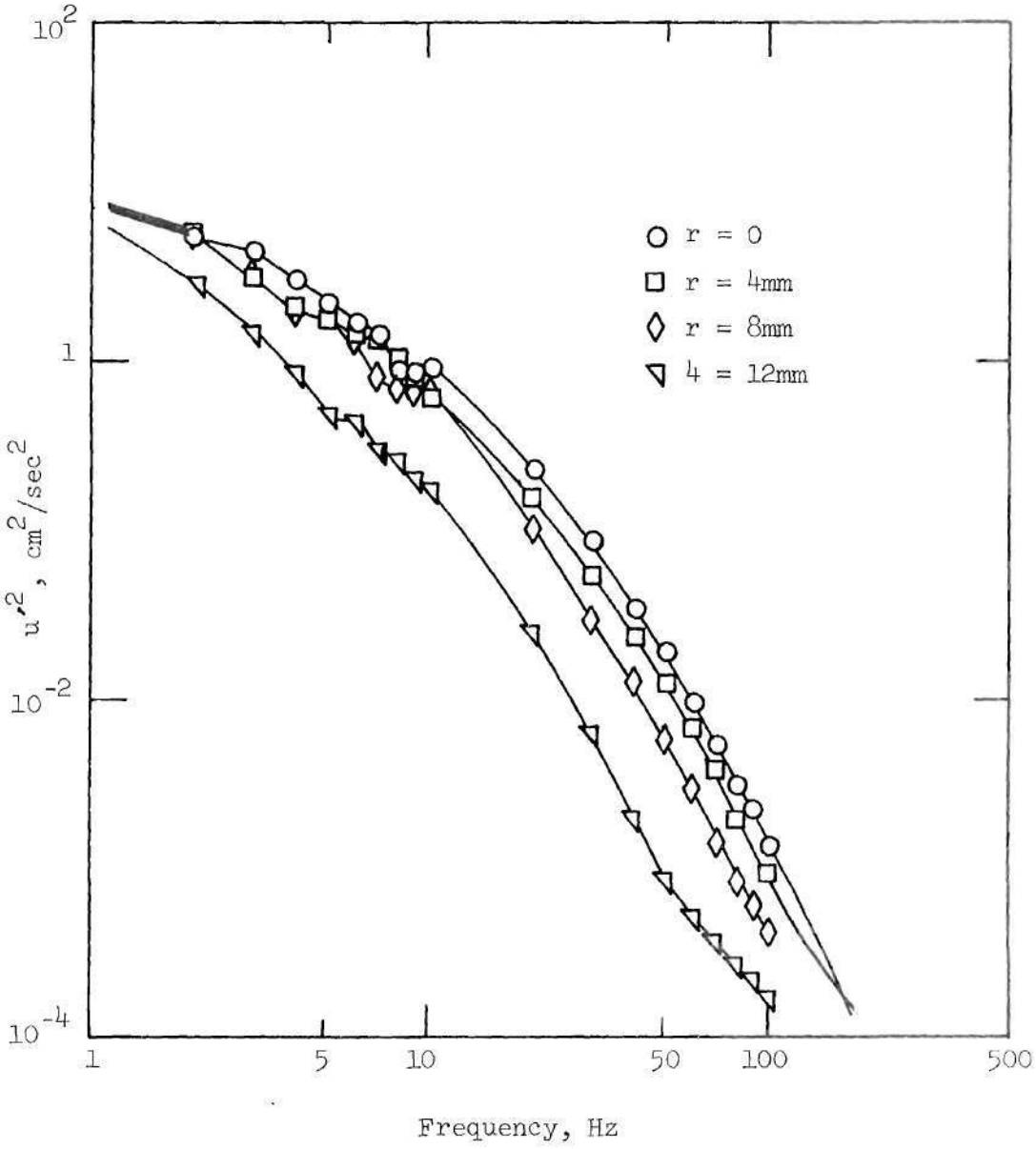

Figure 79. Energy Spectrum for 75% Sharp-Edged Occlusion, $x/D = 3.125$, $R_{e_D} = 1270$, $R_{e_d} = 2540$.

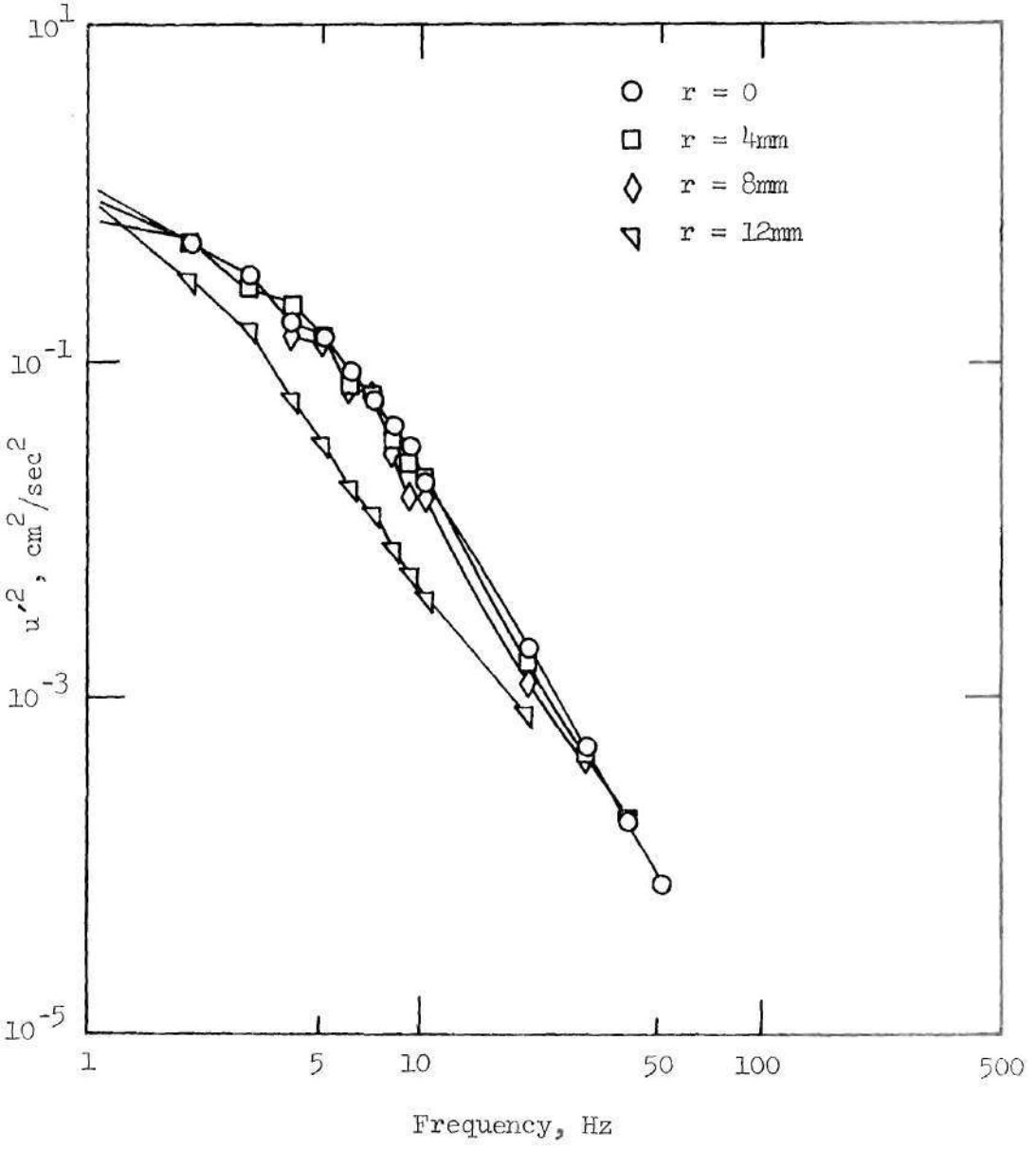

Figure 80, Energy Spectra for 75% Sharp-Edged Occlusion, $x/D = 6.125$, $R_{e_D} = 1270$, $R_{e_d} = 2540$.

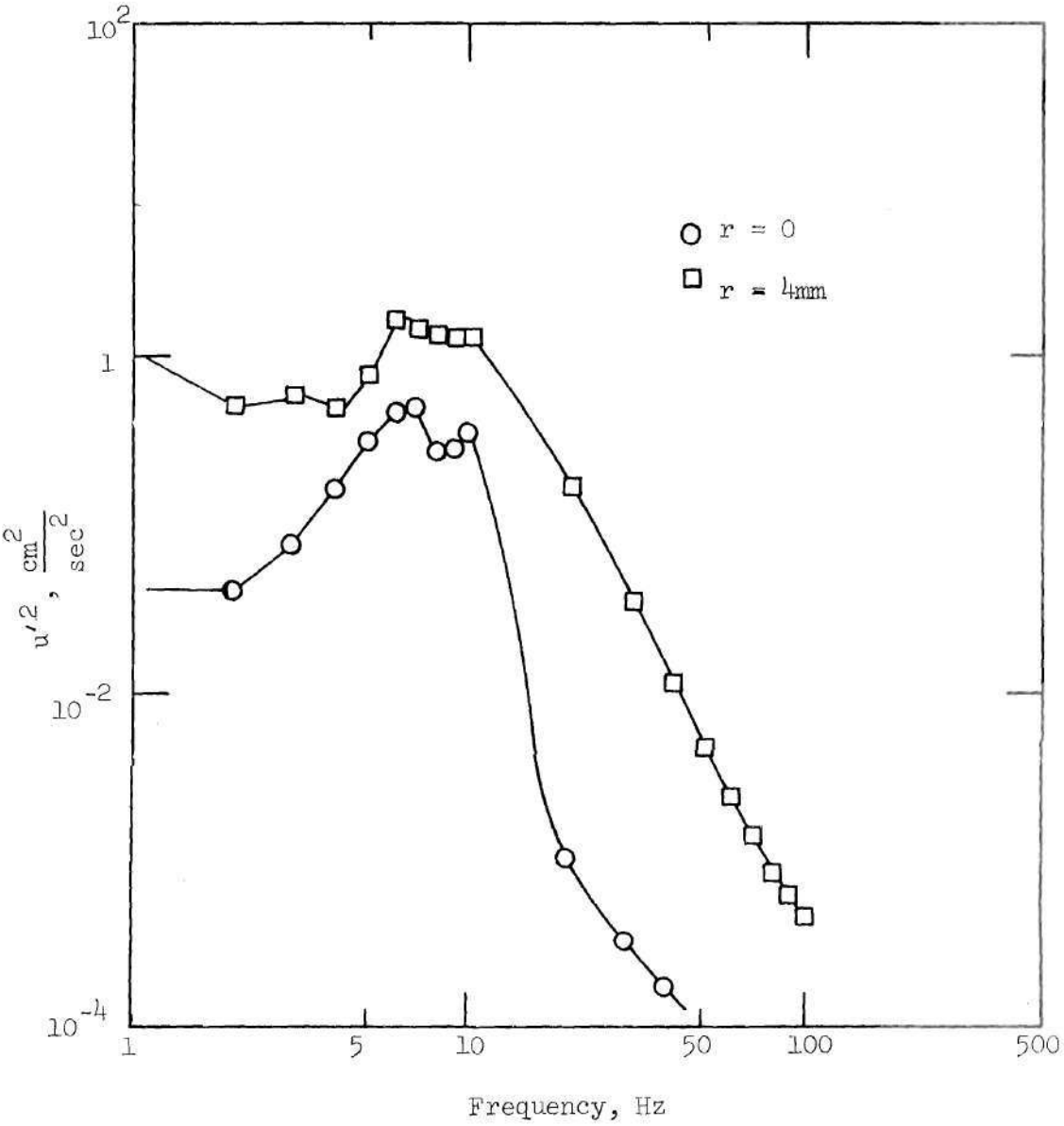

Figure 81. Energy Spectra for 75% Contoured Occlusion, x/D = 1.5, R_{e_D} = 1270, R_{e_d} = 2540.

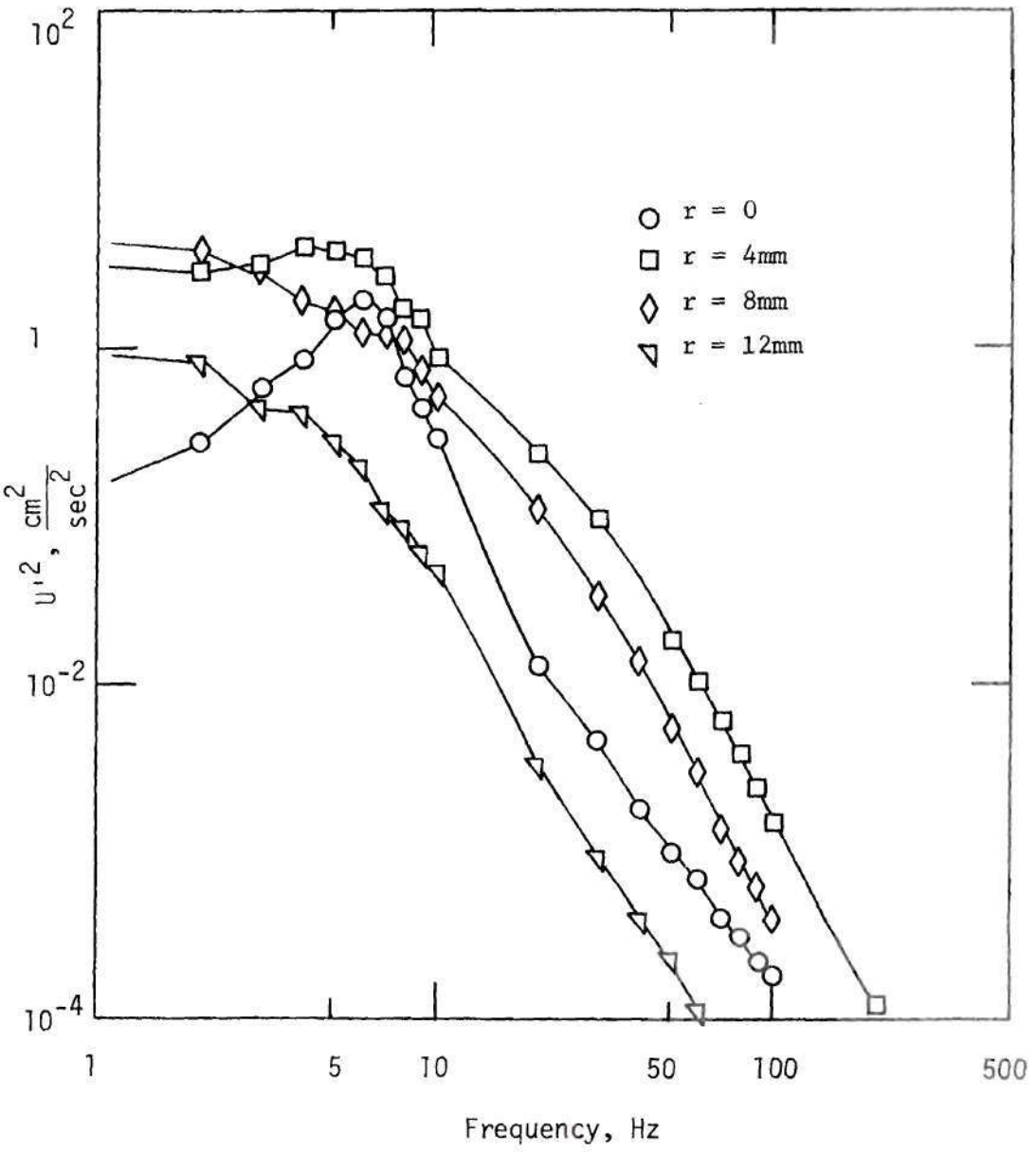

Figure 82. Energy Spectra for 75% Contoured Occlusion, x/D = 2.125, Re_D = 1270, Re_d = 2540.

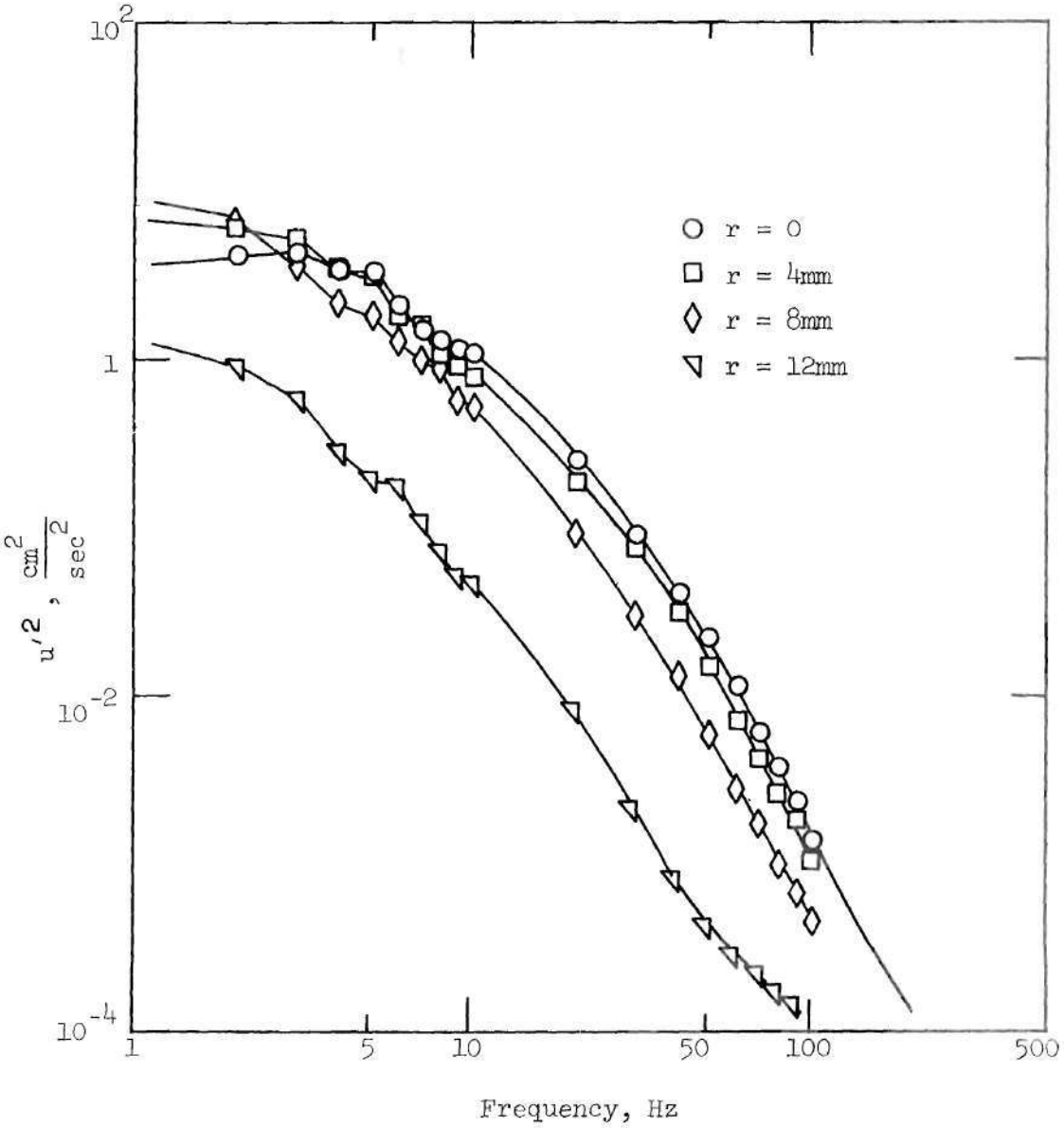

Figure 83. Energy Spectra for 75% Contoured Occlusion, $x/D = 3.125$, $R_{e_D} = 1270$, $R_{e_d} = 2540$

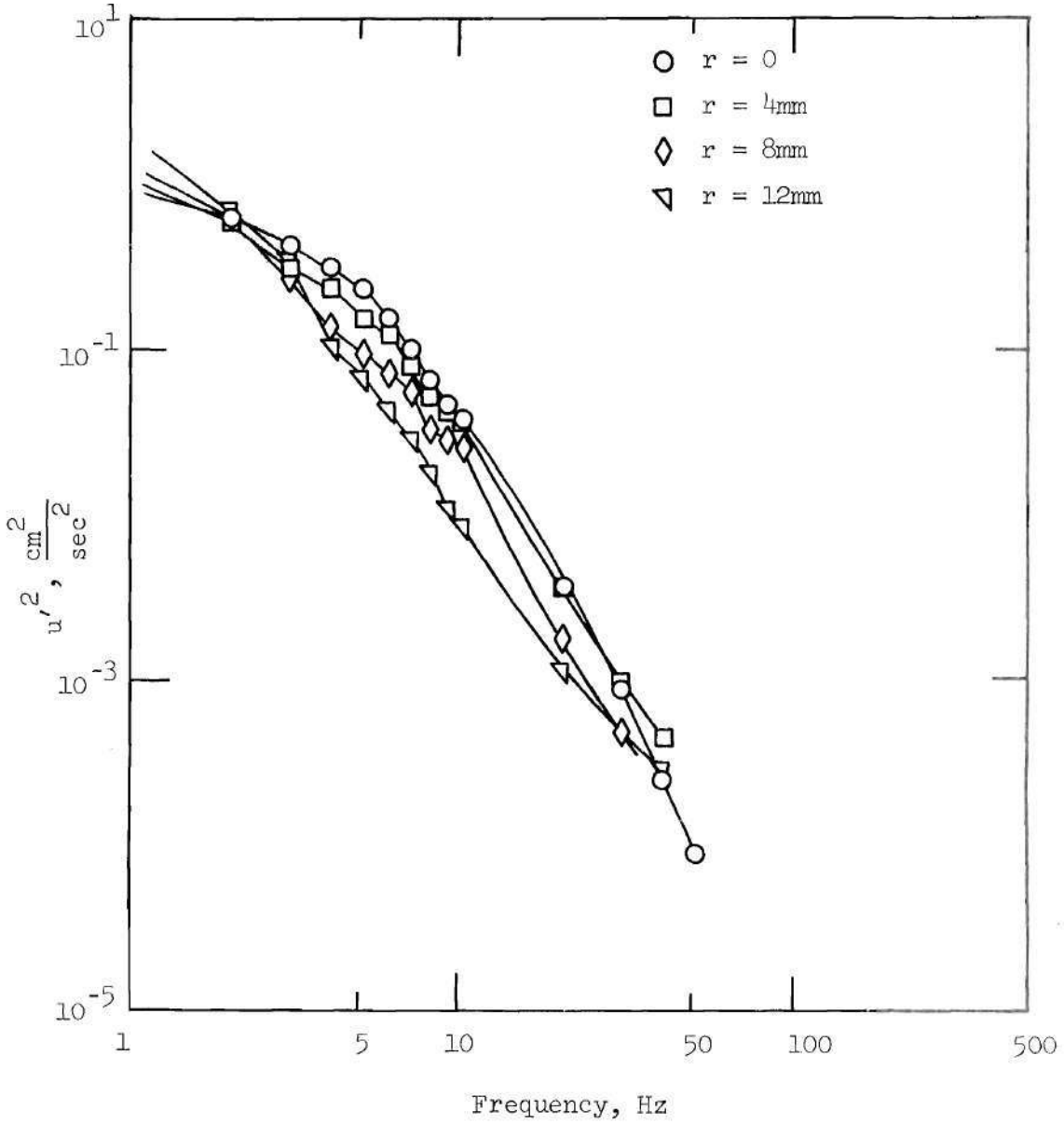

Figure 84. Energy Spectra for 75% Contoured Occlusion, $x/D = 6.125$, $R_{e_D} = 1270$, $R_{e_d} = 2540$.

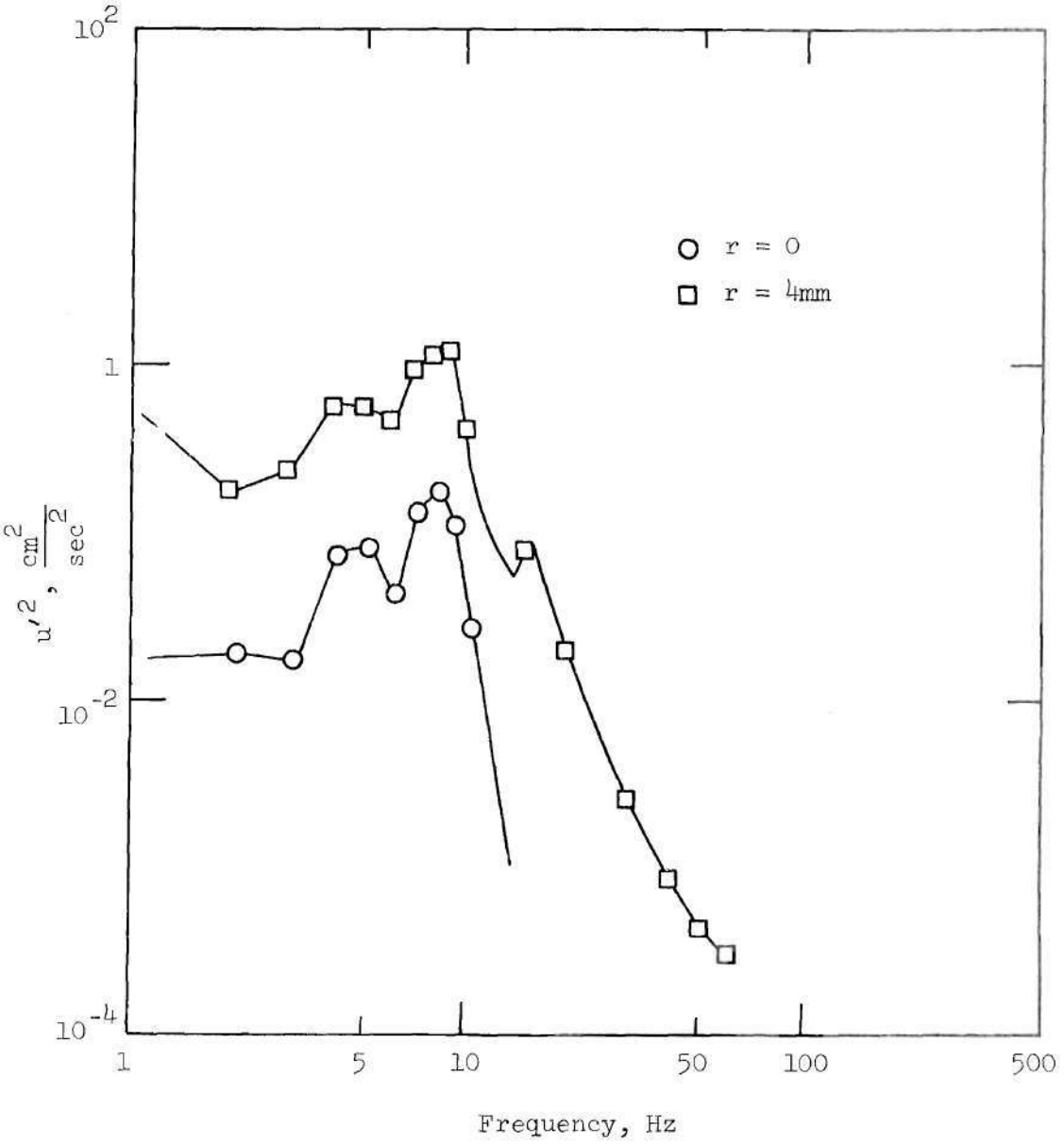

Figure 85. Energy Spectra for 75% Sharp-Edged Occlusion, $x/D = 0.5$, $R_{e_D} = 635$, $R_{e_d} = 1270$.

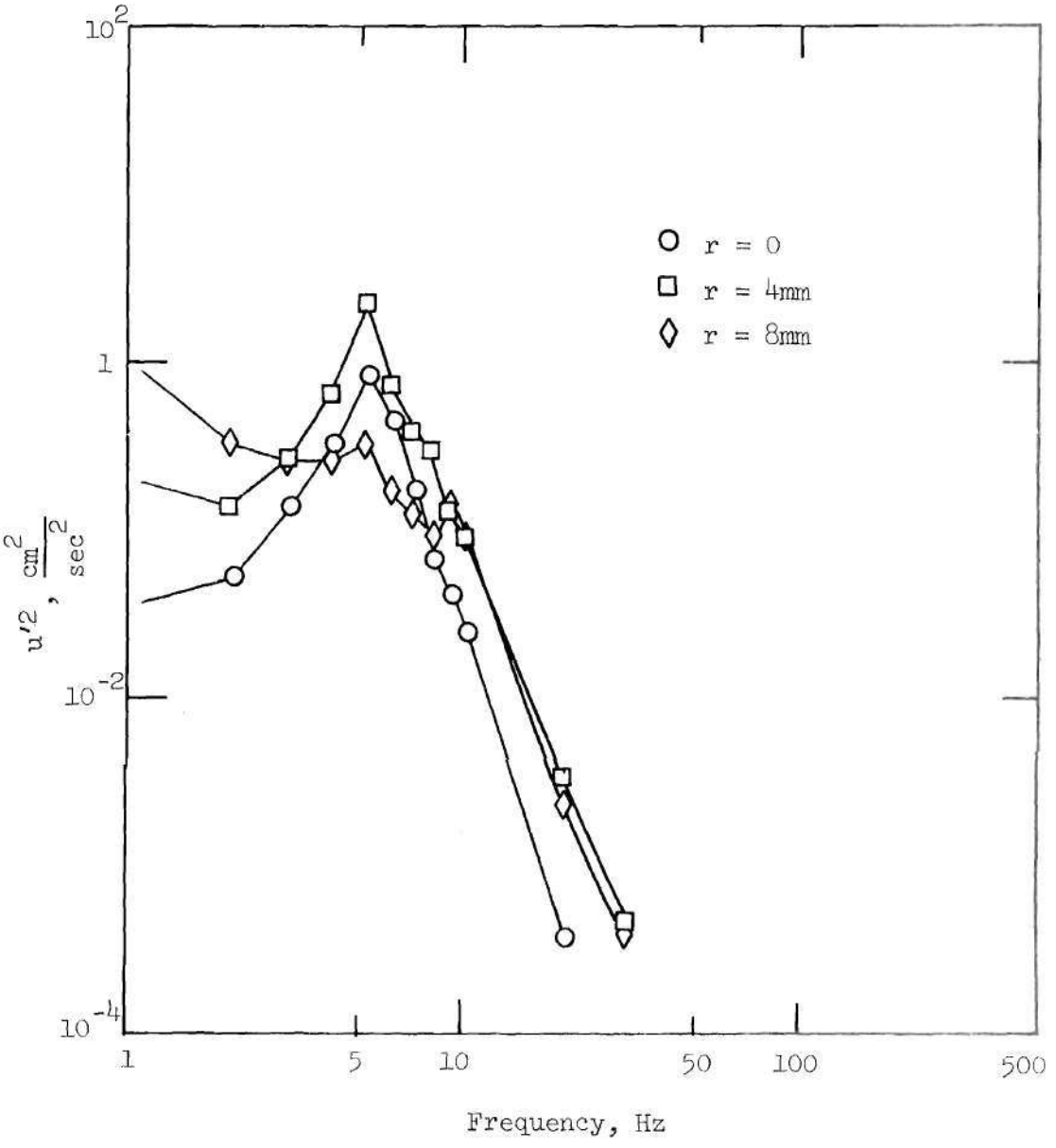

Figure 86. Energy Spectra for 75% Sharp-Edged Occlusion, x/D = 1.125, R_{e_D} = 635, R_{e_d} = 1270.

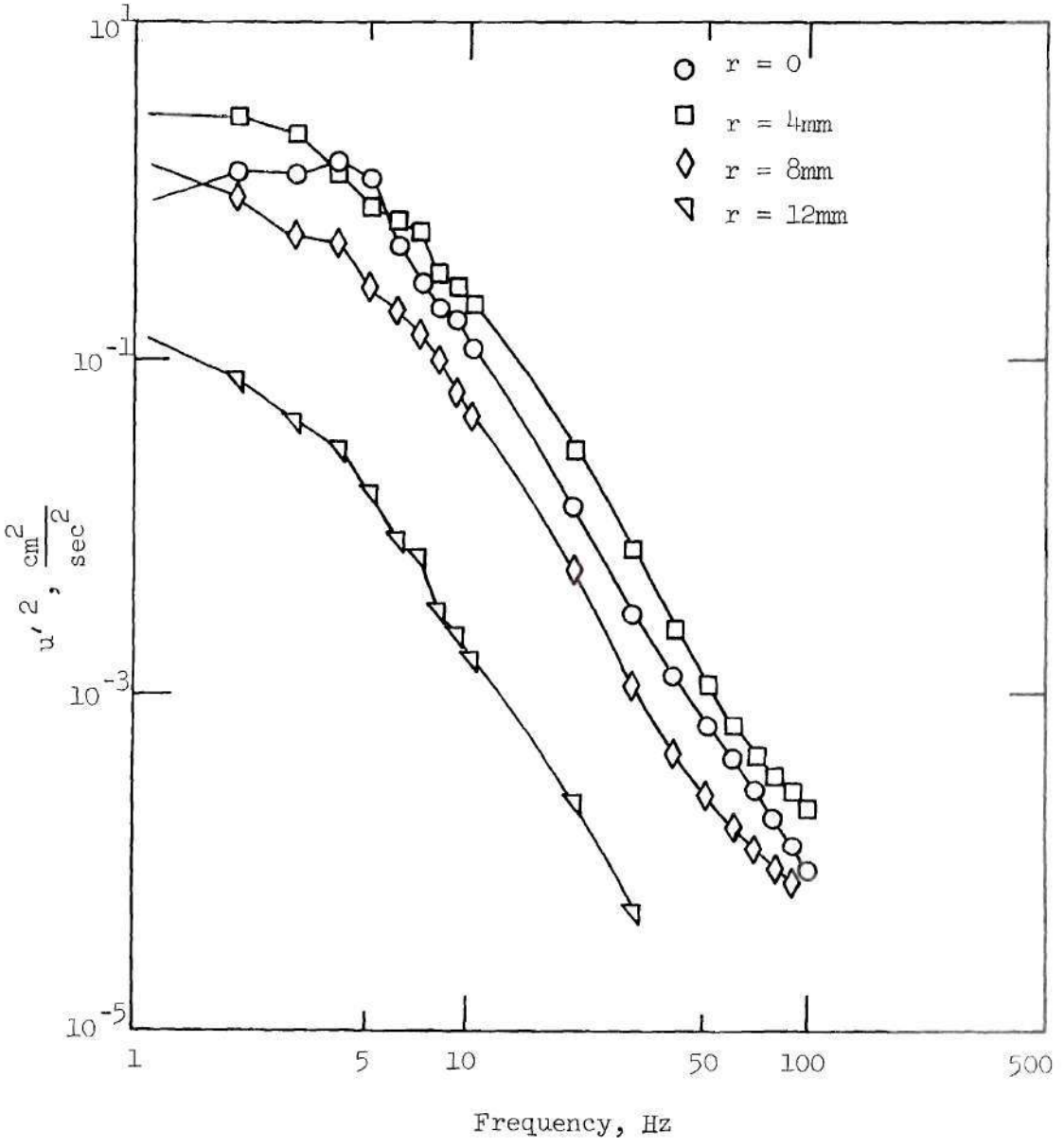

Figure 87. Energy Spectra for 75% Sharp-Edged Occlusion, x/D = 2.125, R_{e_D} = 635, R_{e_d} = 1270.

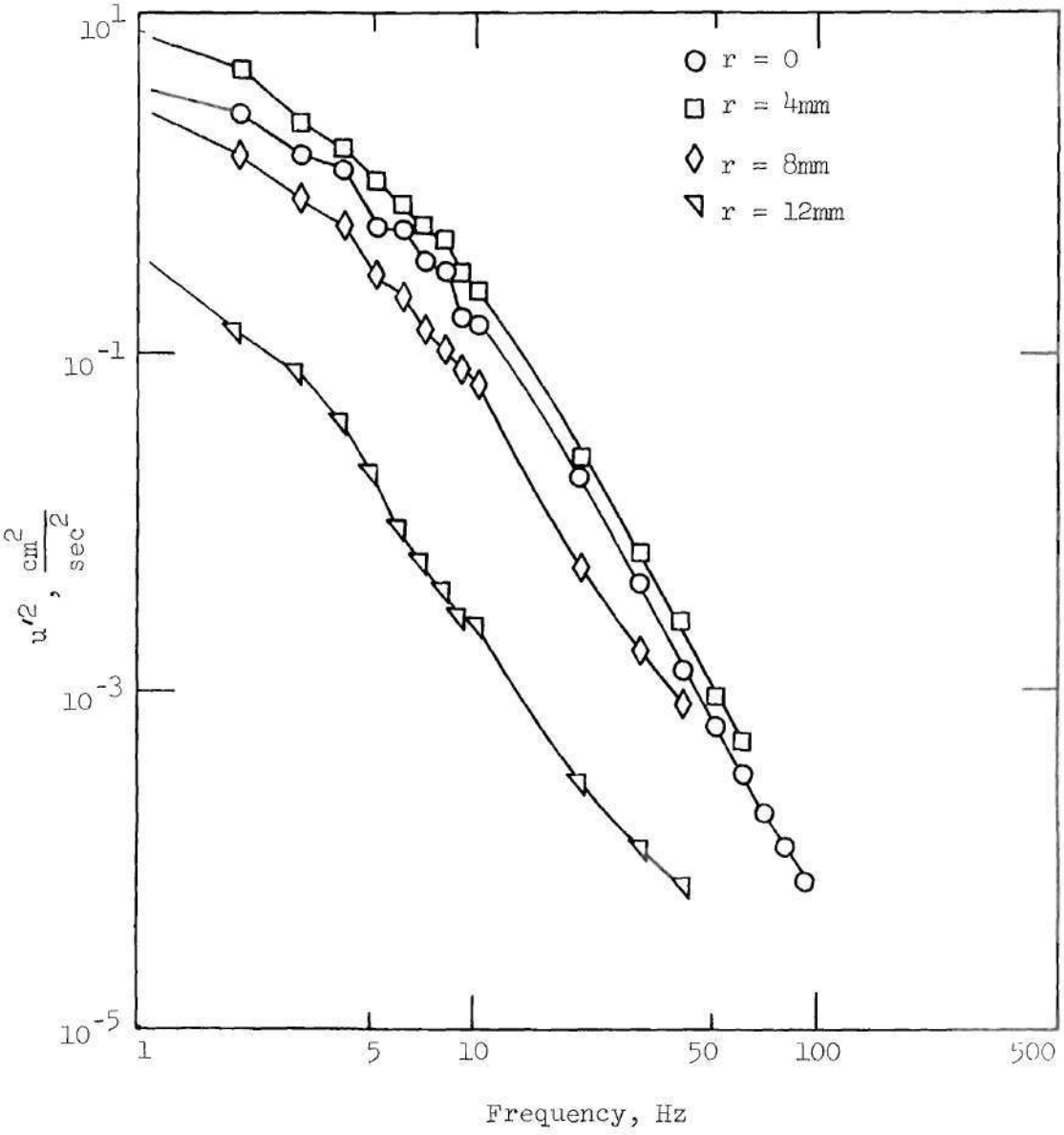

Figure 88. Energy Spectra for 75% Sharp-Edged Occlusion, x/D = 3.125, R_{e_D} = 635, R_{e_d} = 1270.

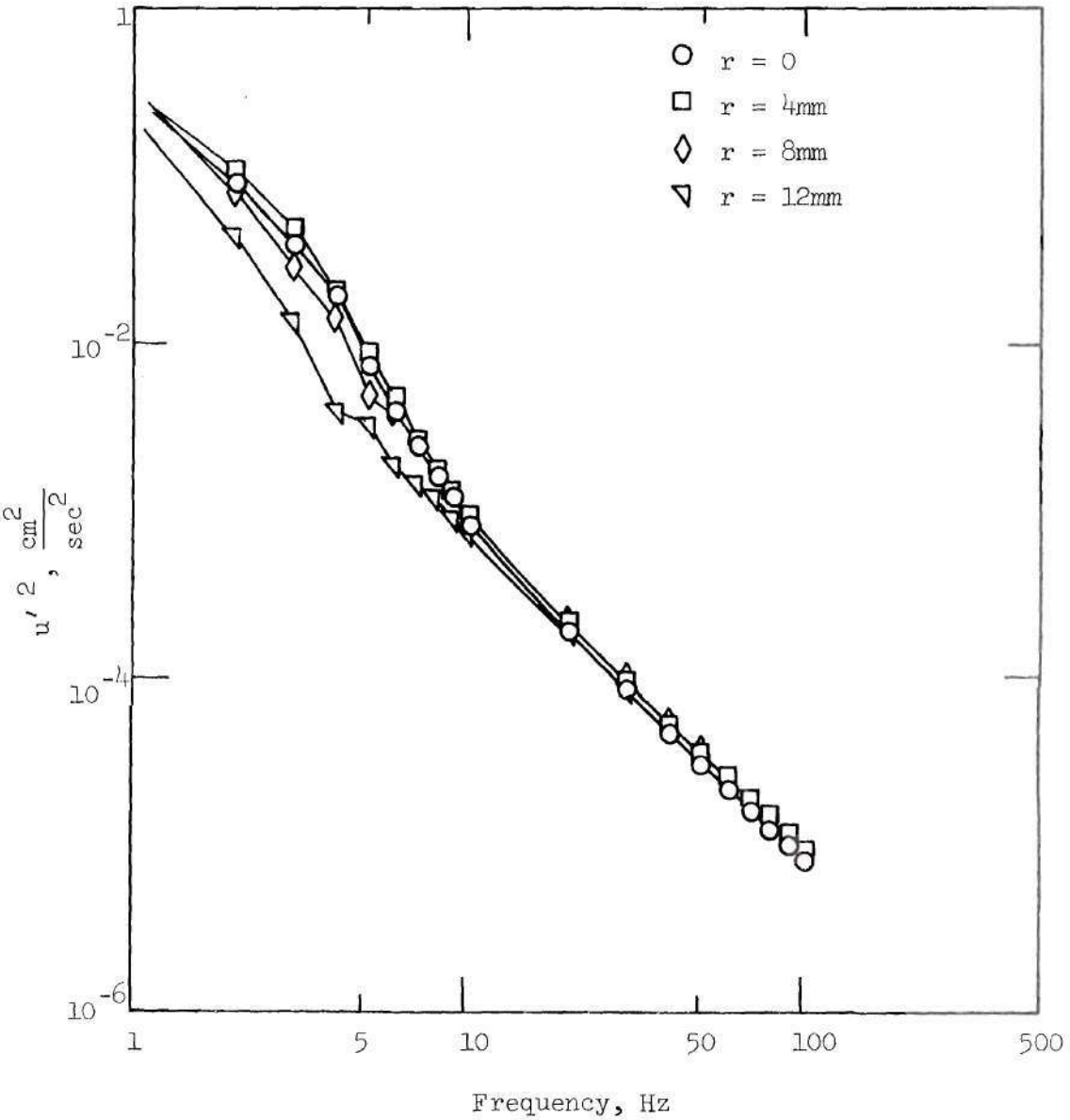

Figure 89. Energy Spectra for 75% Sharp-Edged Occlusion, $x/D = 6.125$, $R_{e_D} = 635$, $R_{e_d} = 1270$.

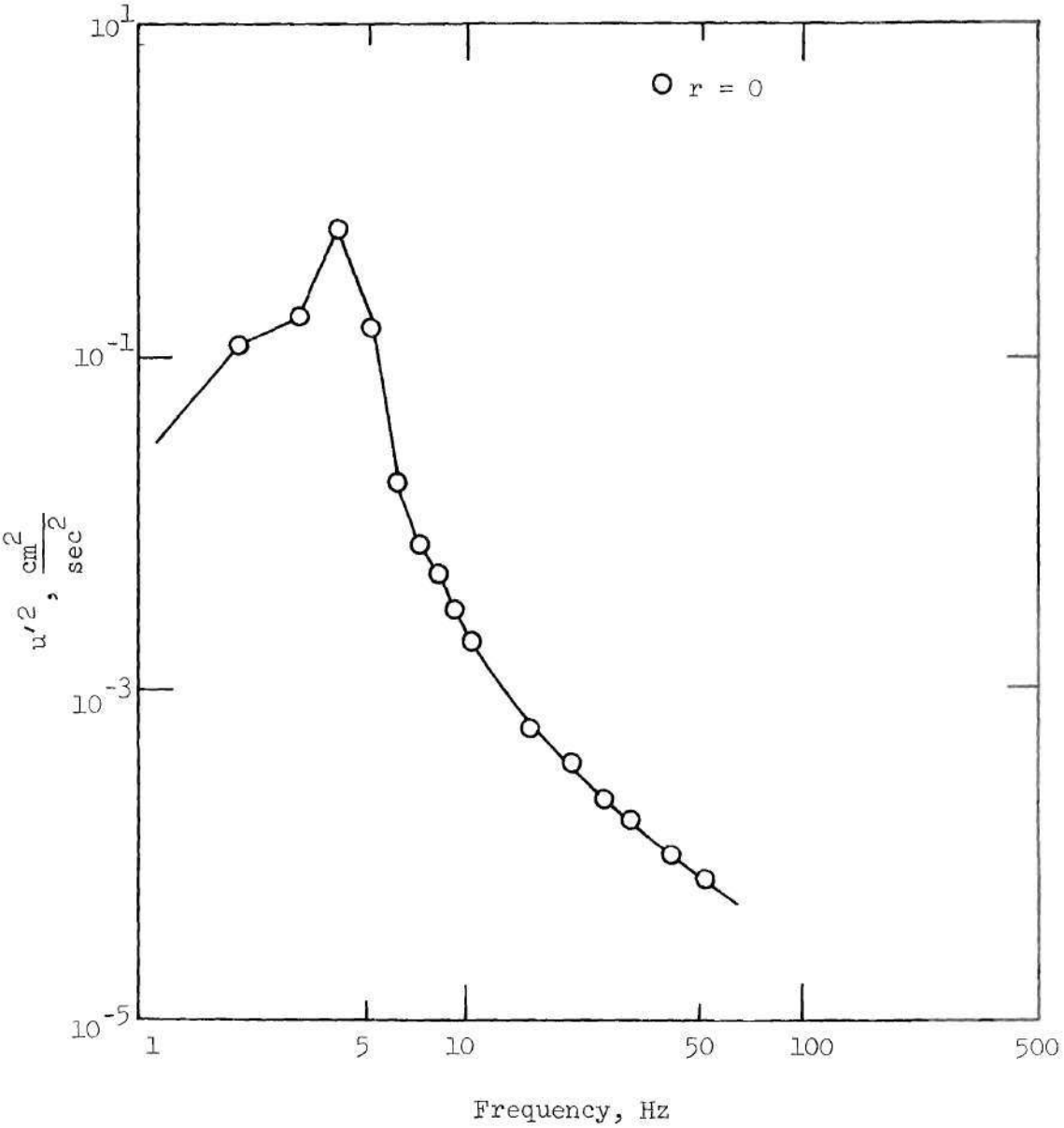

Figure 90. Energy Spectra for 75% Contoured Occlusion, x/D = 1.5, R_{e_D} = 635, R_{e_d} = 1270.

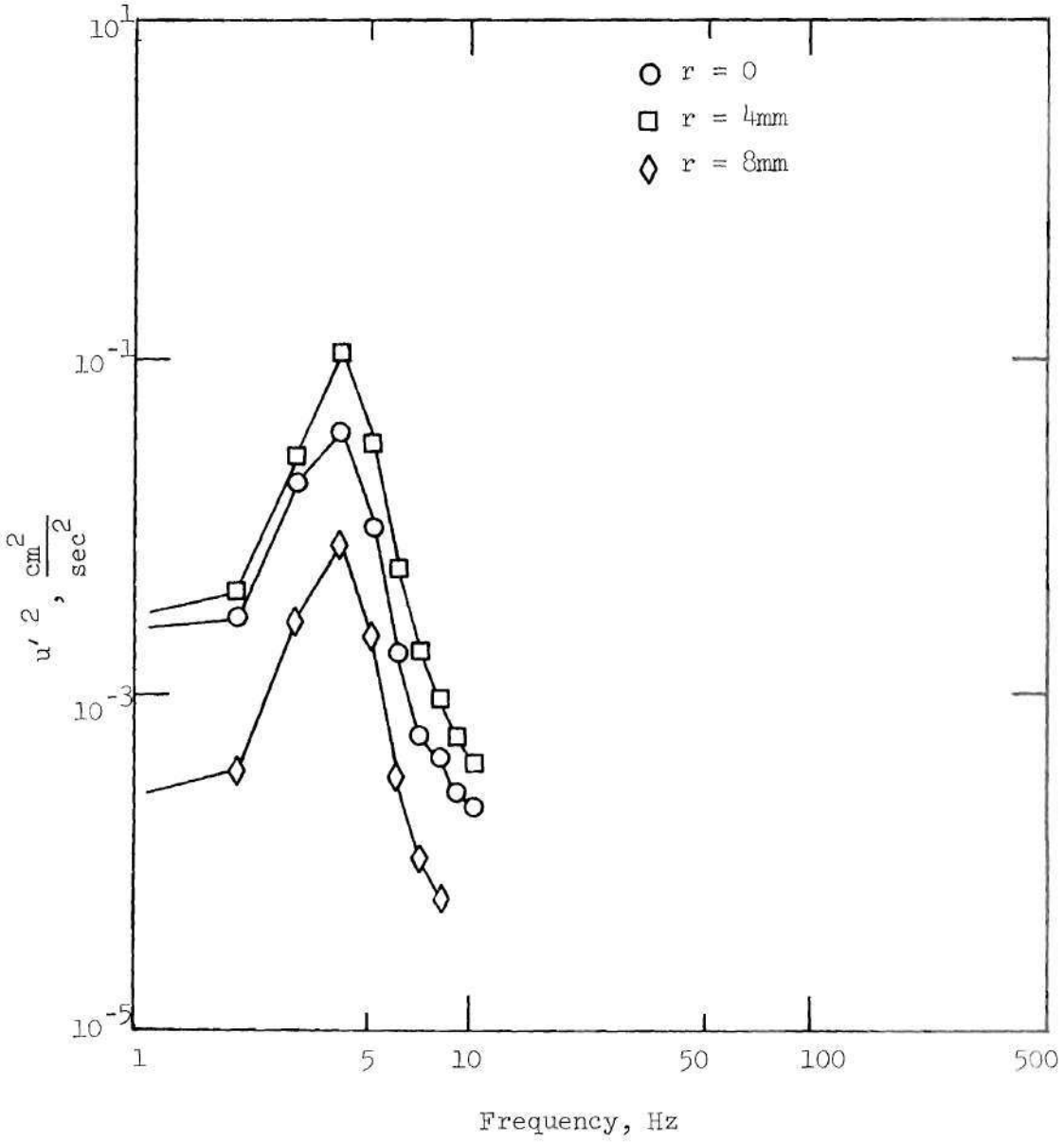

Figure 91. Energy Spectra for 75% Contoured Occlusion, x/D = 2.125, R_{e_D} = 635, R_{e_d} = 1270.

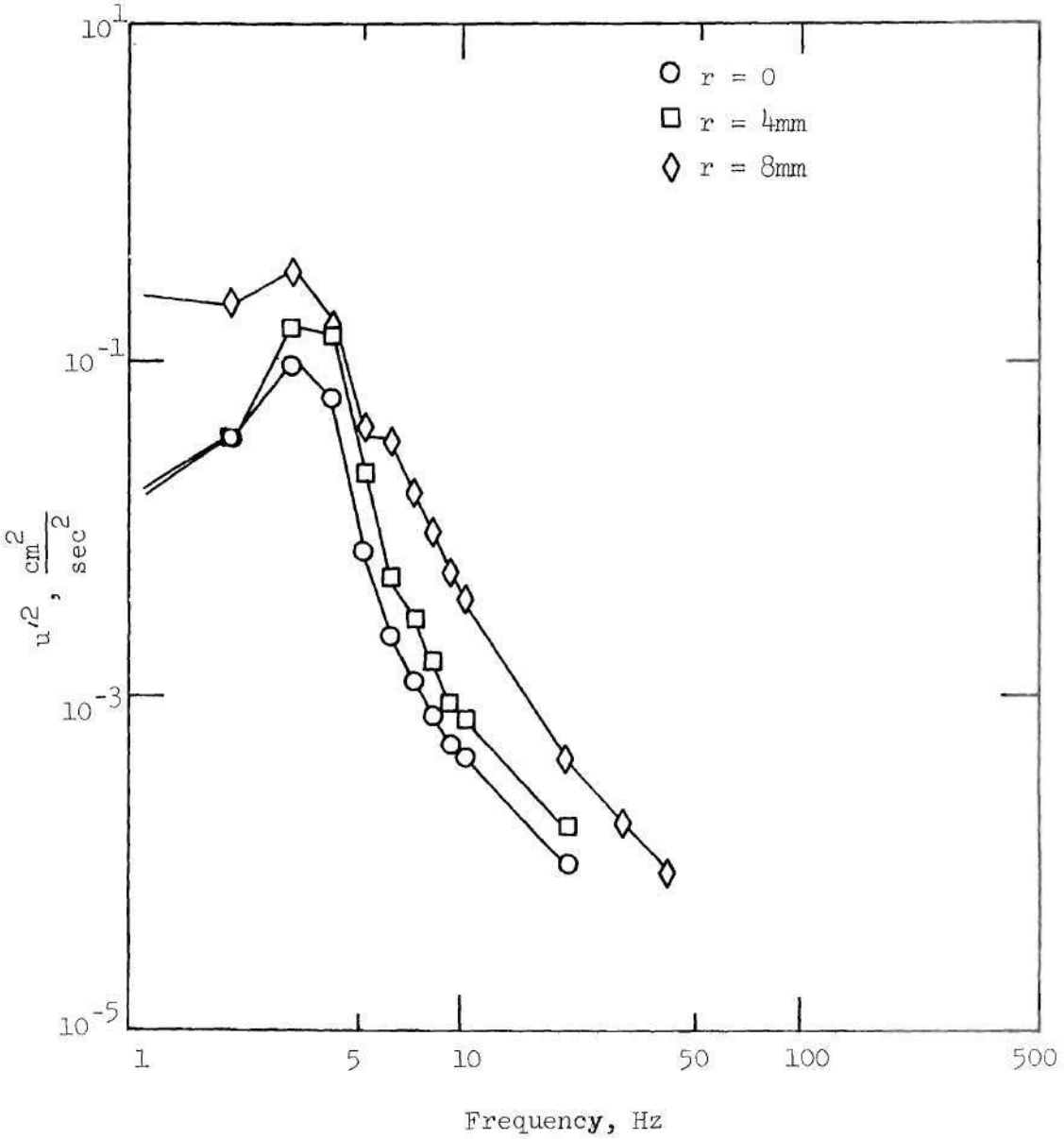

Figure 92. Energy Spectra for 75% Contoured Occlusion, $x/D = 3.125$, $R_{e_D} = 635$, $R_{e_d} = 1270$.

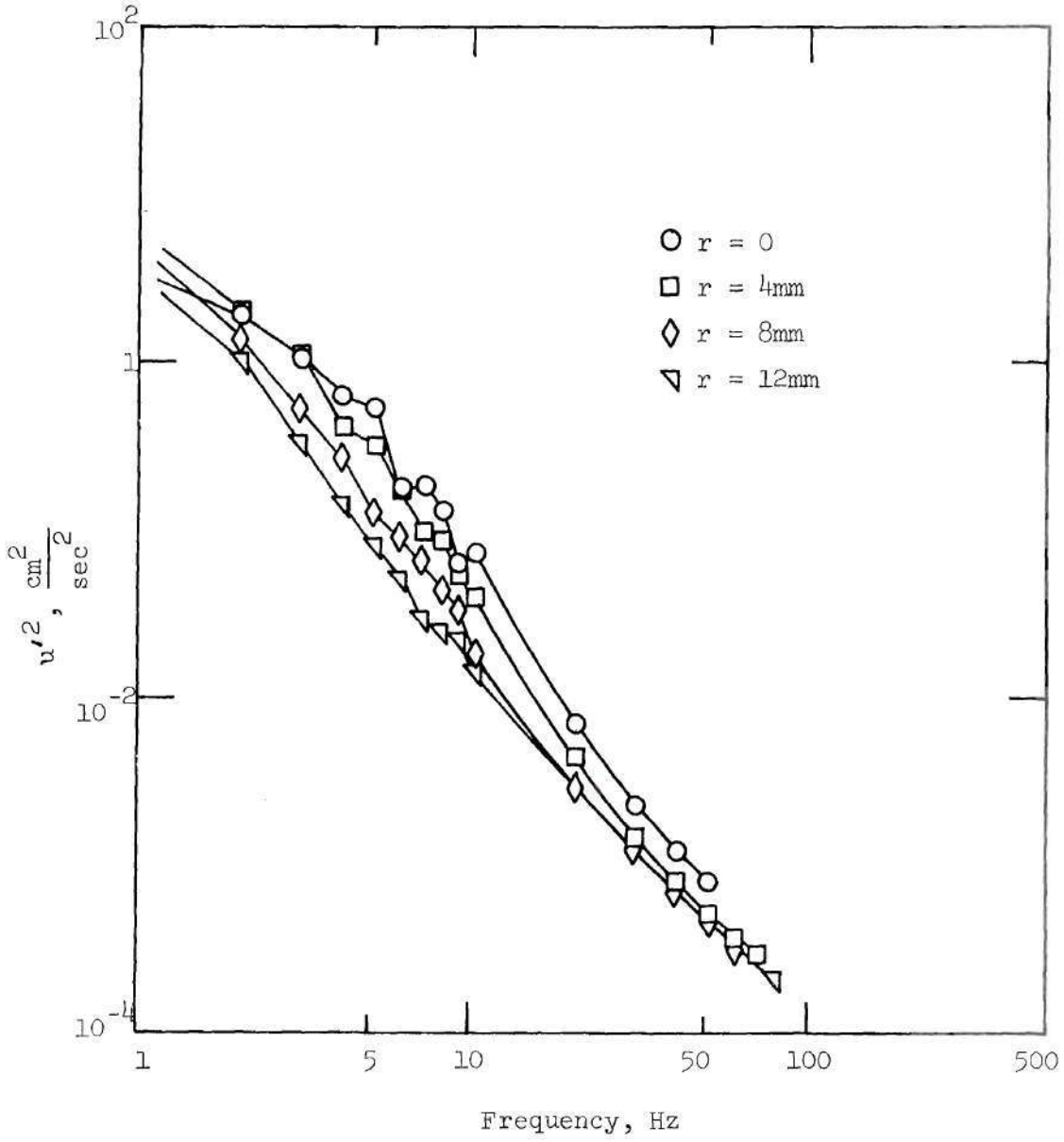

Figure 93. Energy Spectra for 75% Contoured Occlusion, x/D = 6.125, R_{e_D} = 635, R_{e_d} = 1270.

6.3 Energy Spectral Distributions for The 90 Percent Sharp Occlusions

These energy spectra were obtained for axial positions corresponding to the same x/d locations which were used with the 75 percent sharp occlusions and using the same Reynolds number based on the orifice area conditions; i.e., R_{e_d} = 1270, 2540 and 5080. This was done to determine any significant changes in the spectra due to the manner in which the jet flow interacts with the recirculation region and the tube wall.

The results of this comparison scheme are presented in Figures 94 through 98 for R_{e_d} = 5080, Figures 99 through 103 for R_{e_d} = 2540, and Figures 104 through 108 for R_{e_d} = 1270. The spectra in all of these plots, when compared with the corresponding plots for the 75 percent sharp occlusion at the same R_{e_d} and x/d, show remarkable similarity. For a given R_{e_d}, the spectral peaks due to the vortex rings dissipate into random turbulence at the same x/d for both occlusions. The trends displayed as a function of radial location are also similar; i.e., the peaked spectra broadens into a more random spectra near the recirculation region and near the wall. The near-wall spectra also show an overall decrease in intensity below the near-centerline positions. This similarity for these two occlusion sizes as a function of x/d, r/d and R_{e_d} indicates that the flow characteristics in the vortex shedding region are not measurably affected by any differences in wall interaction but are influenced principally by the interaction of the jet flow with

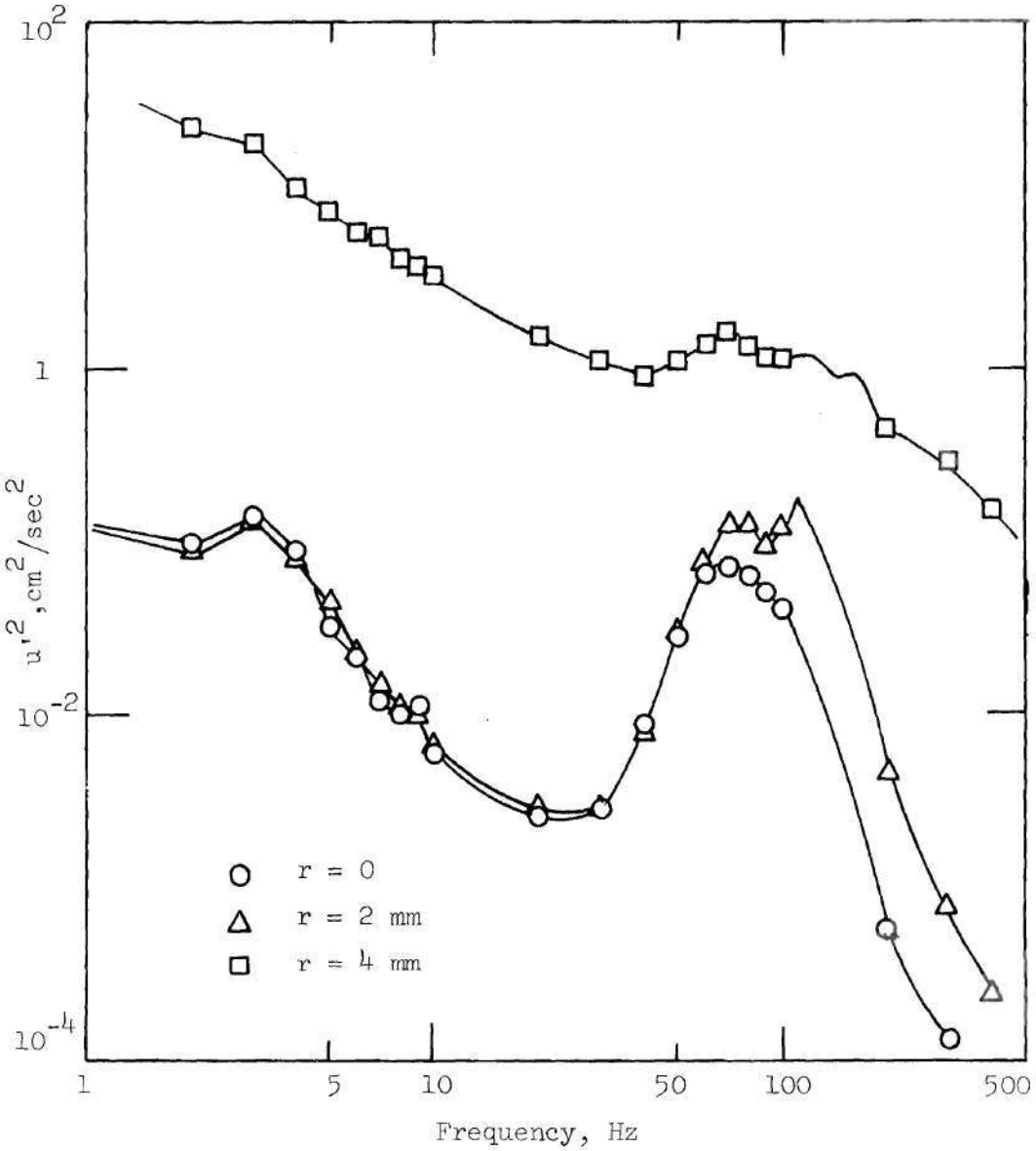

Figure 94. Energy Spectra for 90% Sharp-Edged Occlusion, x/d = 1, R_{e_D} = 1608, R_{e_d} = 5080

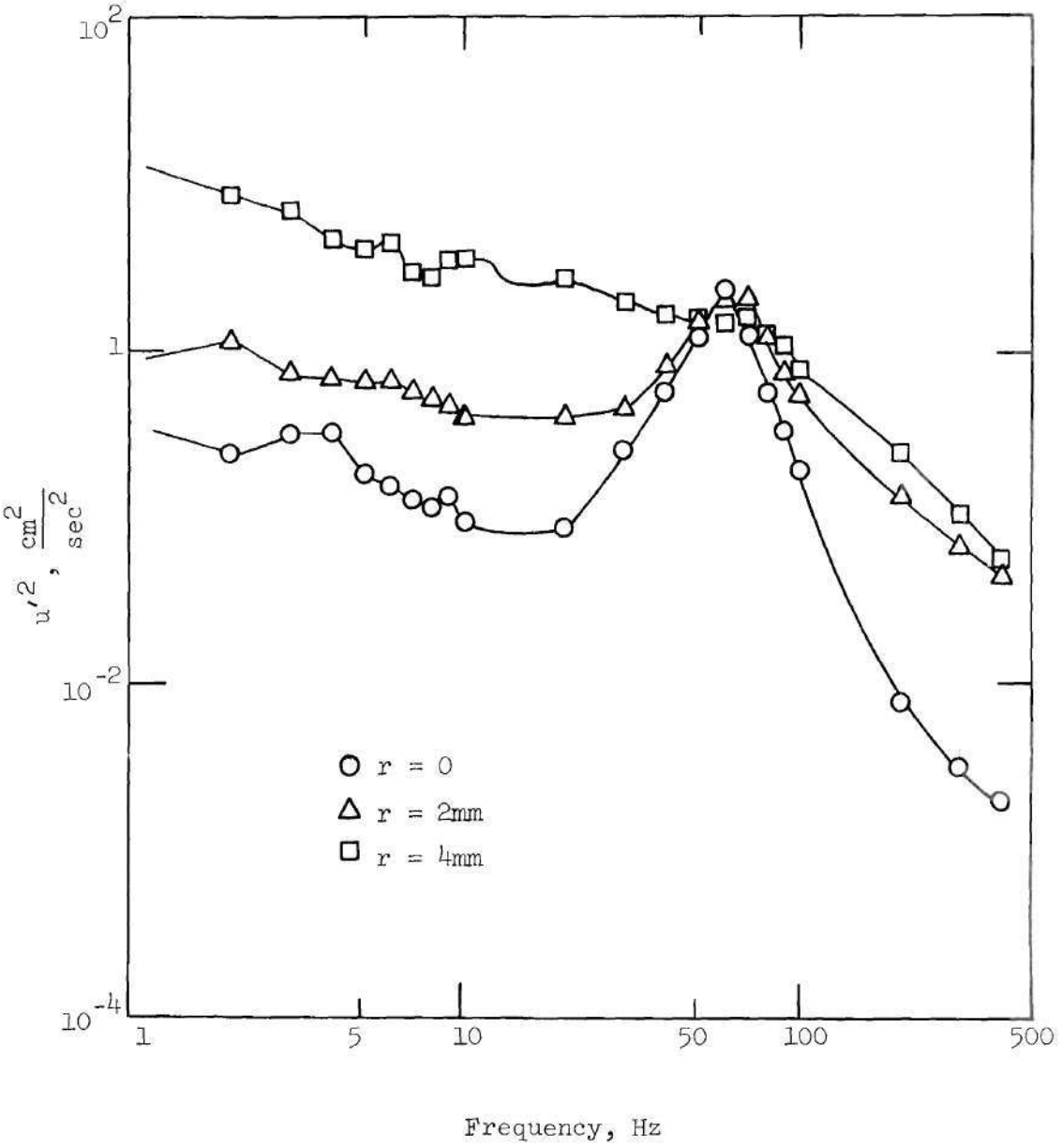

Figure 95. Energy Spectra for 90 % Sharp-Edged Occlusion, x/d = 2.25, R_{e_D} = 1608, R_{e_d} = 5080.

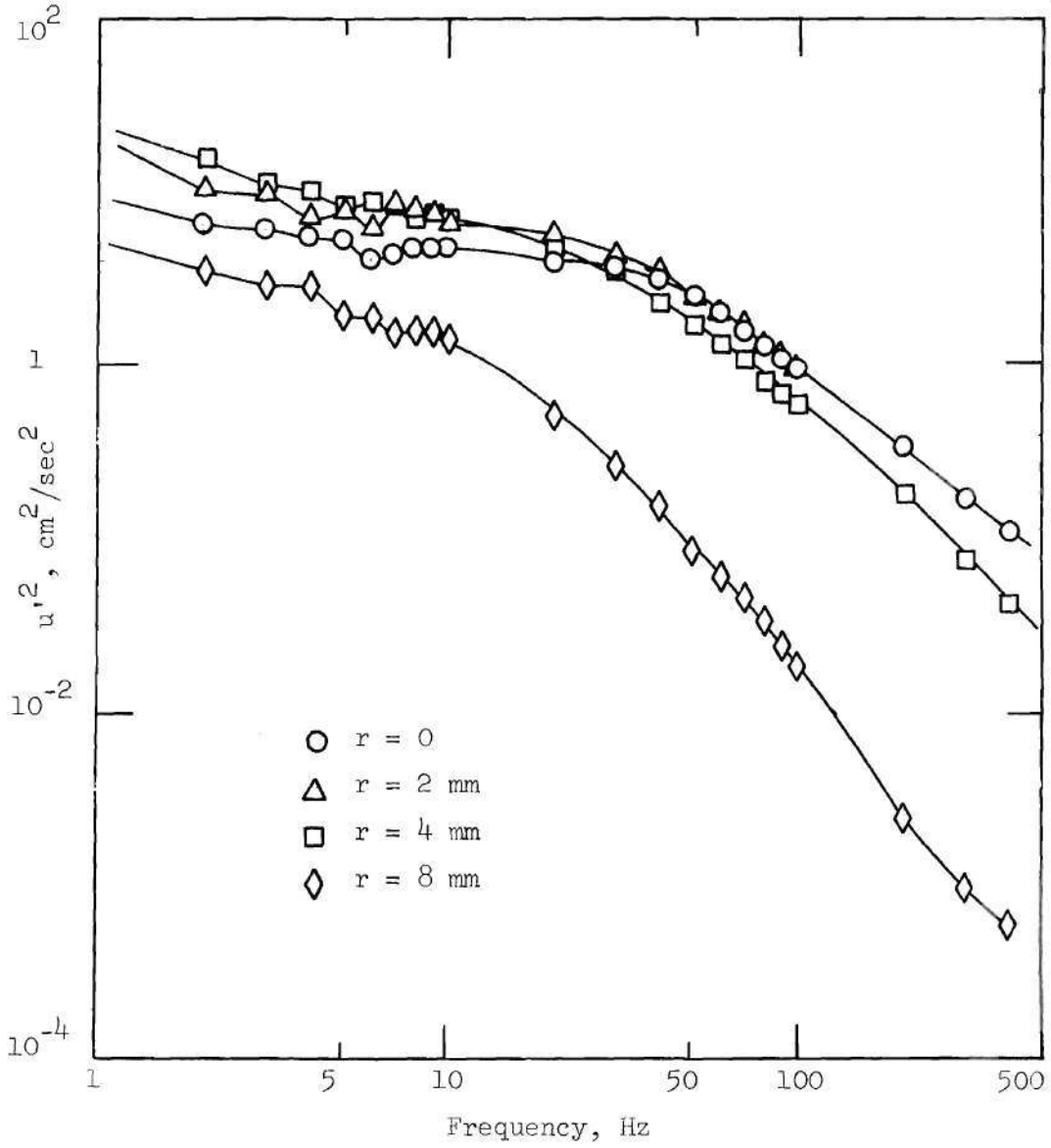

Figure 96. Energy Spectra for 90% Sharp-Edged Occlusion, $x/d = 4.25$, $R_{e_D} = 1608$, $R_{e_d} = 5080$

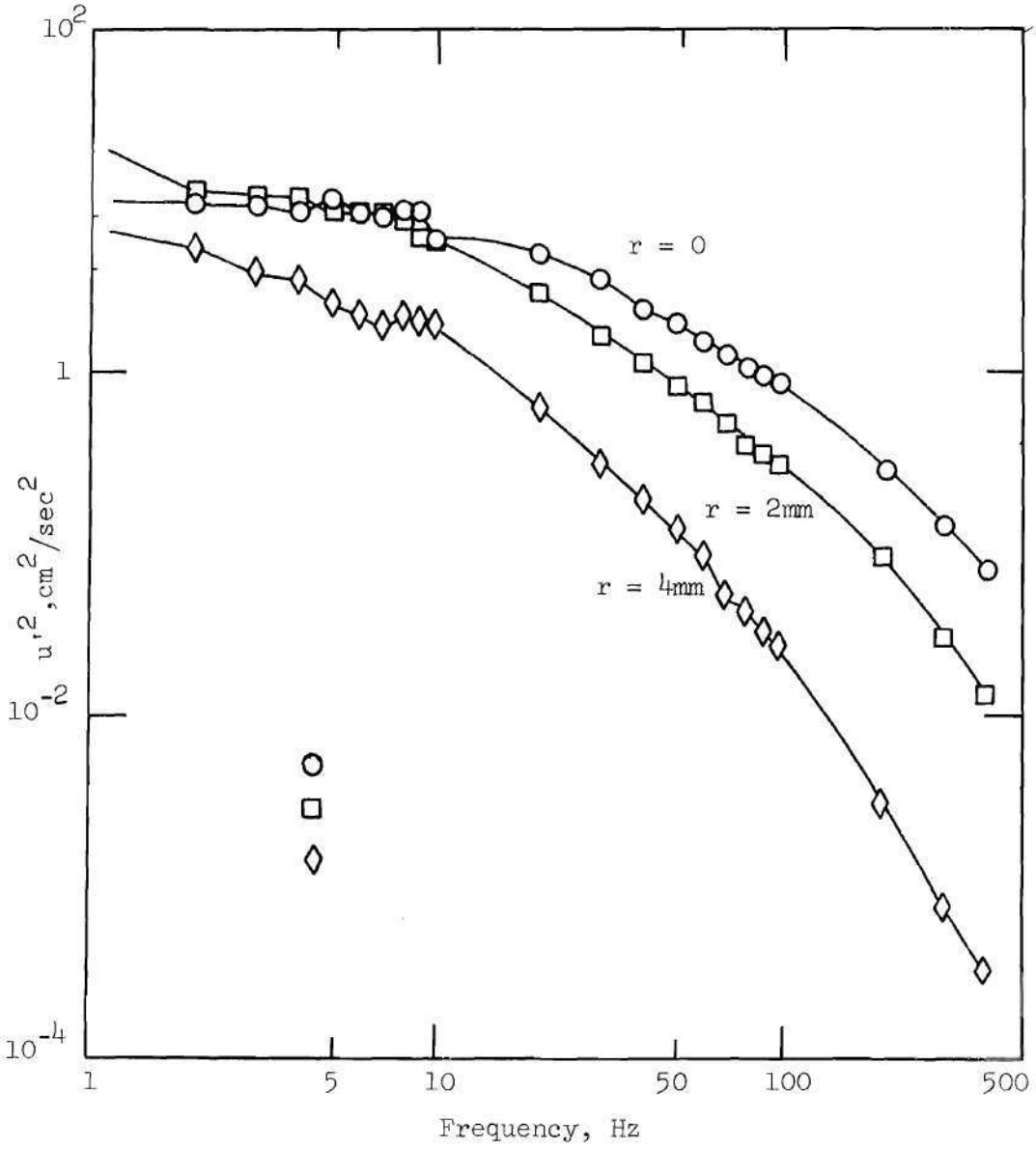

Figure 97. Energy Spectra for 90% Sharp-Edged Occlusion, x/d = 6.25, R_{e_D} = 1608, R_{e_d} = 5080

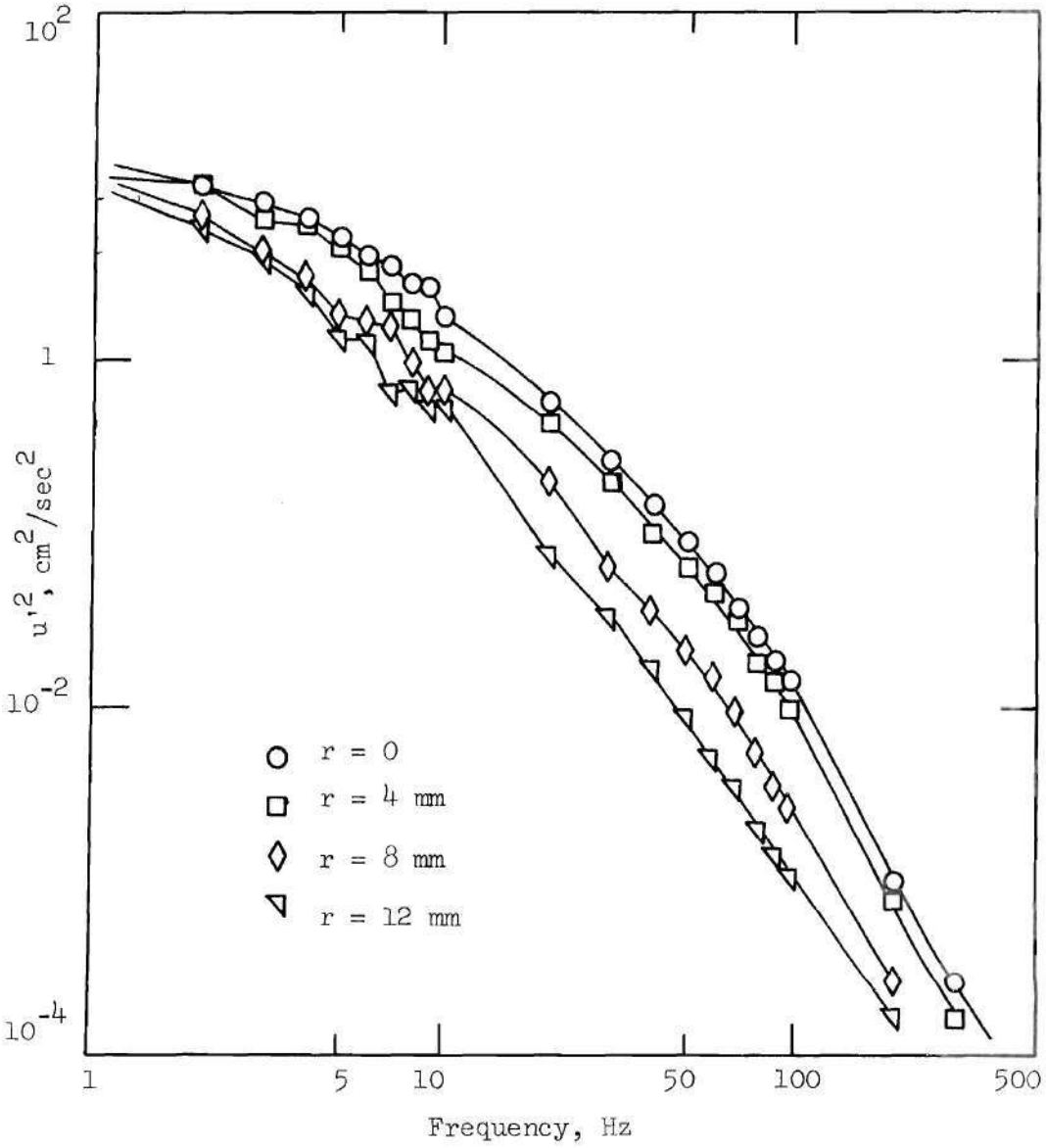

Figure 98. Energy Spectra for 90% Sharp-Edged Occlusion, x/d = 12.25, R_{e_D} = 1608, R_{e_d} = 5080

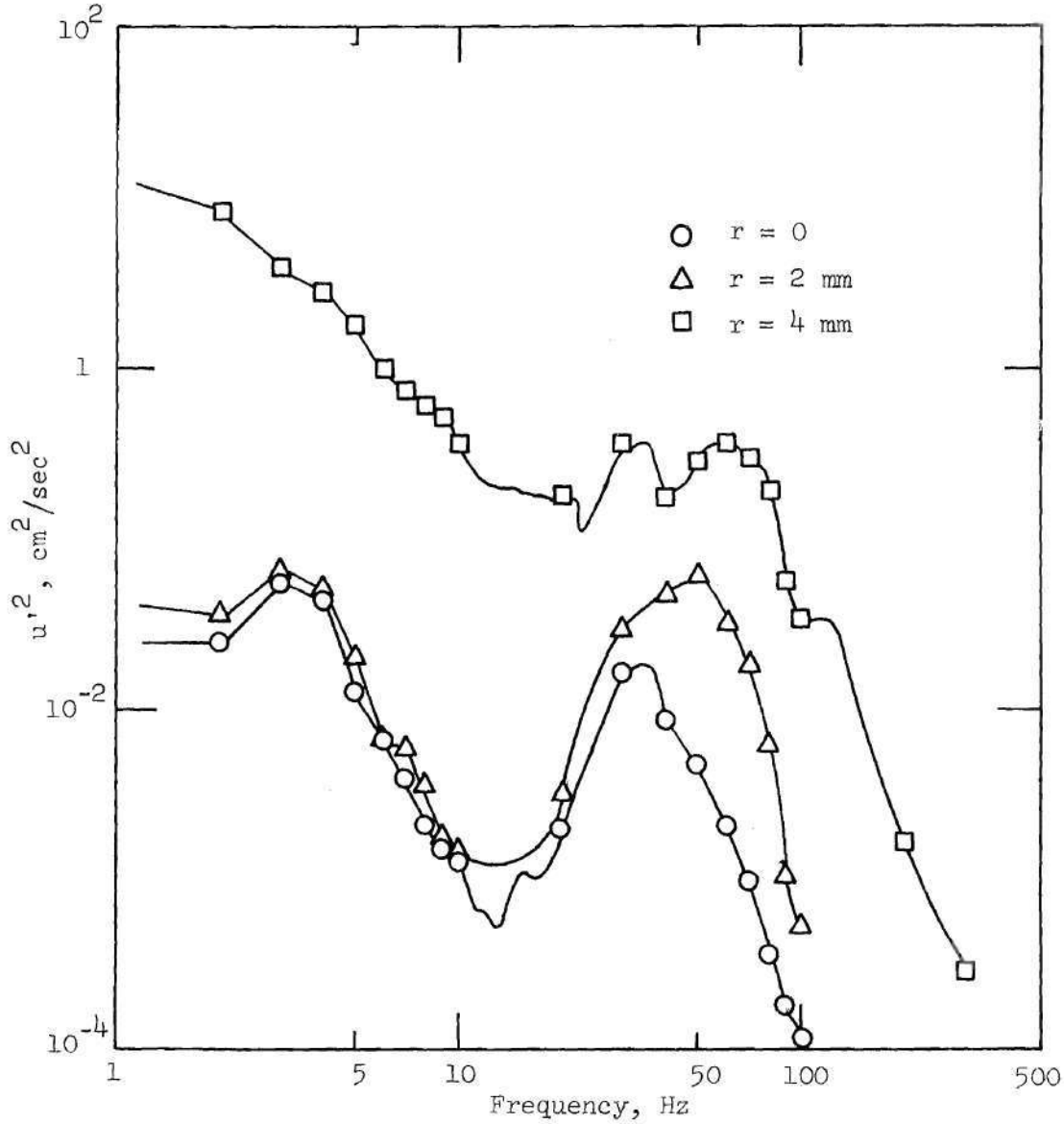

Figure 99. Energy Spectra for 90% Sharp-Edged Occlusion, x/d = 1, R_{e_D} = 804, R_{e_d} = 2540

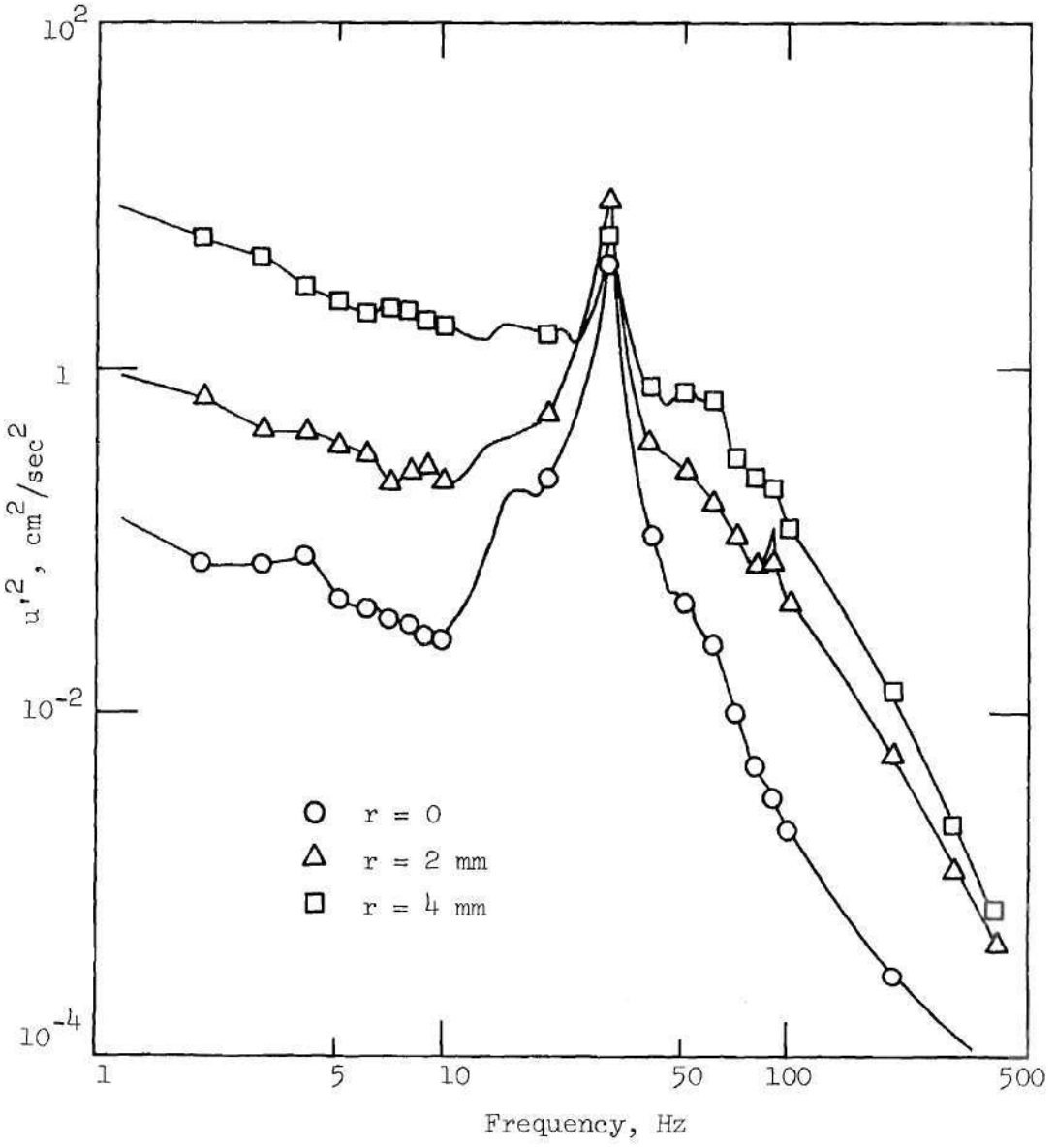

Figure 100. Energy Spectra for 90% Sharp-Edged Occlusion, x/d = 2.25, R_{e_D} = 804, R_{e_d} = 2540

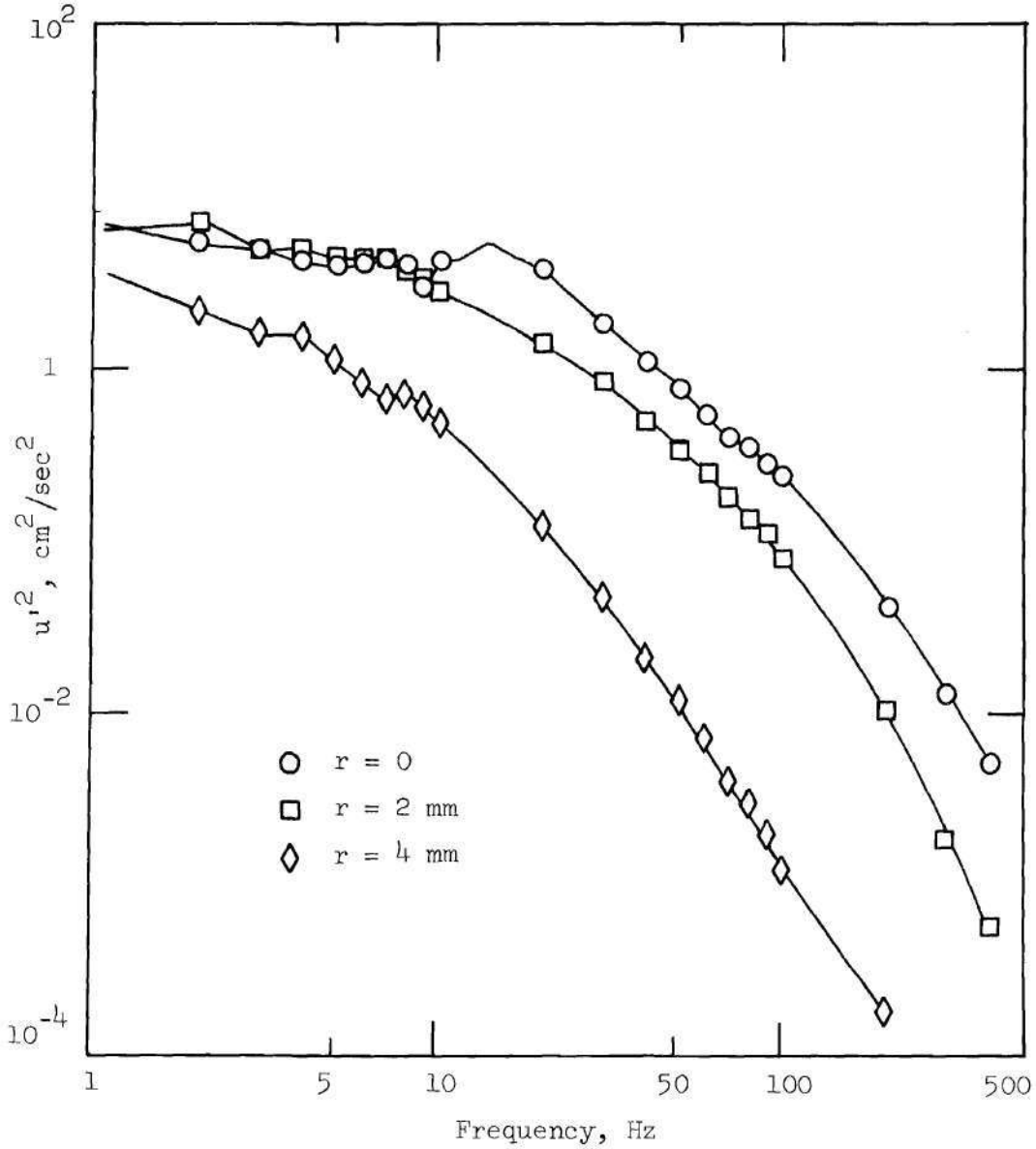

Figure 101. Energy Spectra for 90% Sharp-Edged Occlusion, x/d = 4.25, R_{e_D} = 804, R_{e_d} = 2540

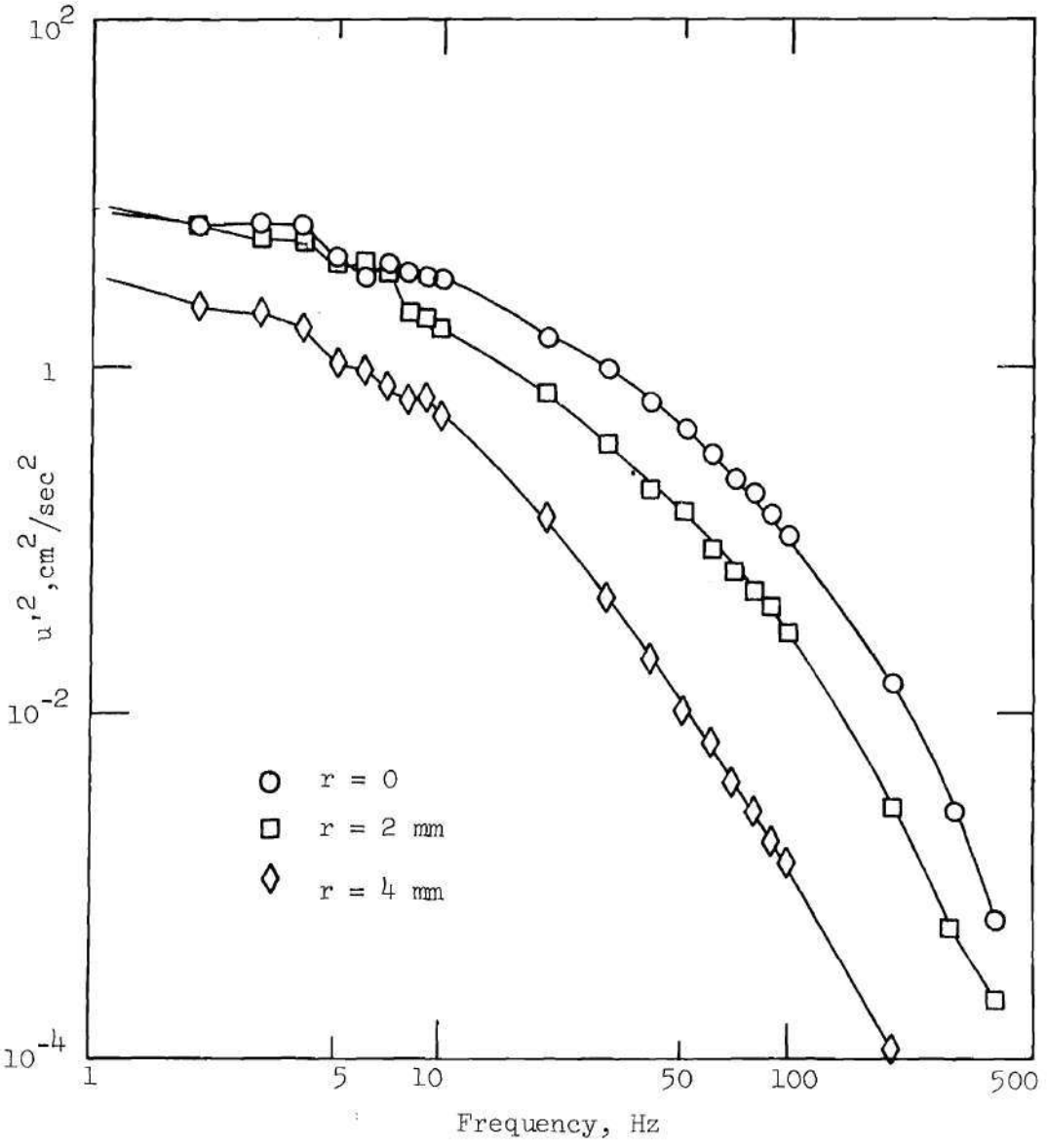

Figure 102. Energy Spectra for 90% Sharp-Edged Occlusion, x/d = 6.25, R_{e_D} = 804, R_{e_d} = 2540

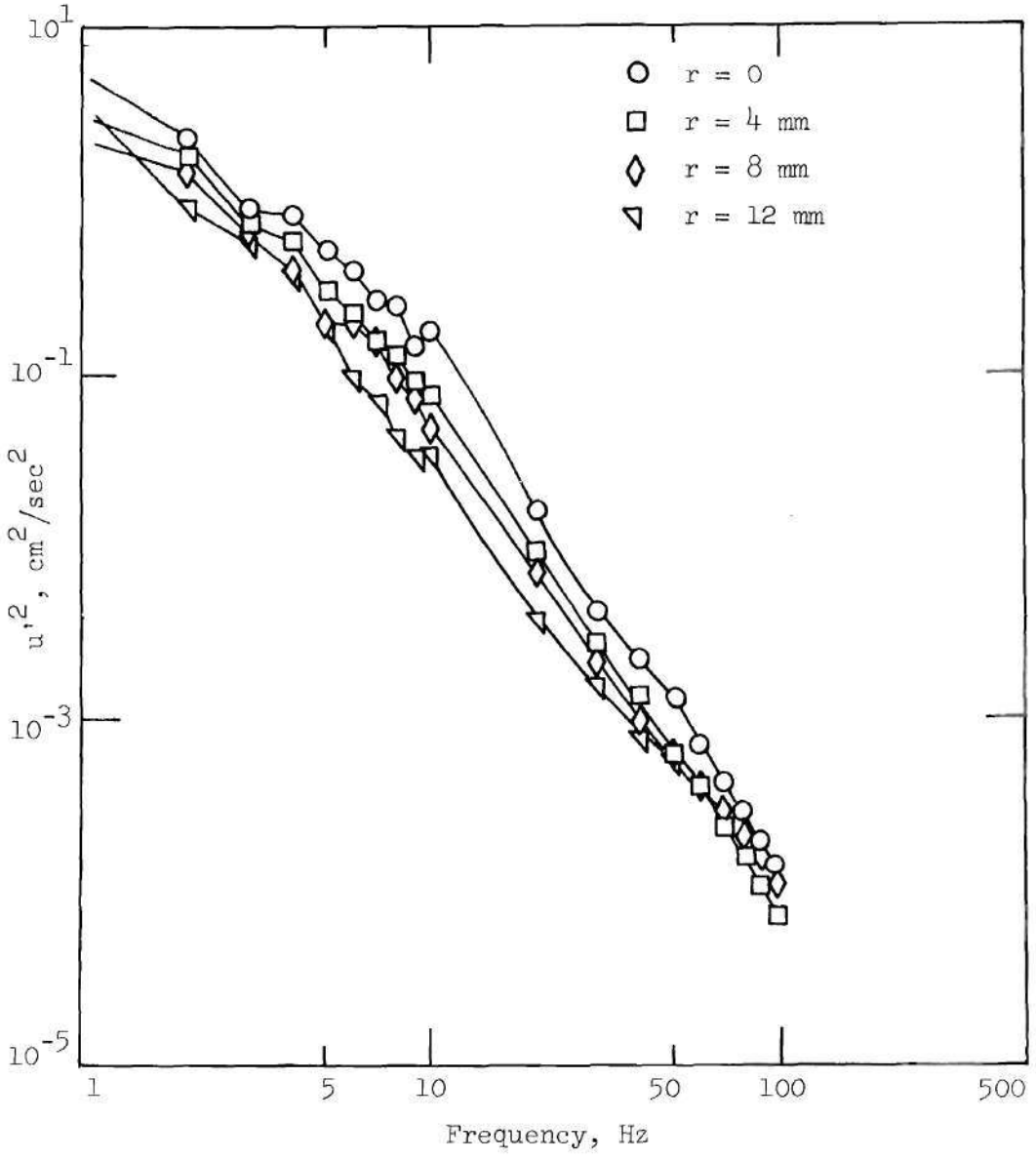

Figure 103. Energy Spectra for 90% Sharp-Edged Occlusion, x/d = 12.25, R_{e_D} = 804, R_{e_d} = 2540

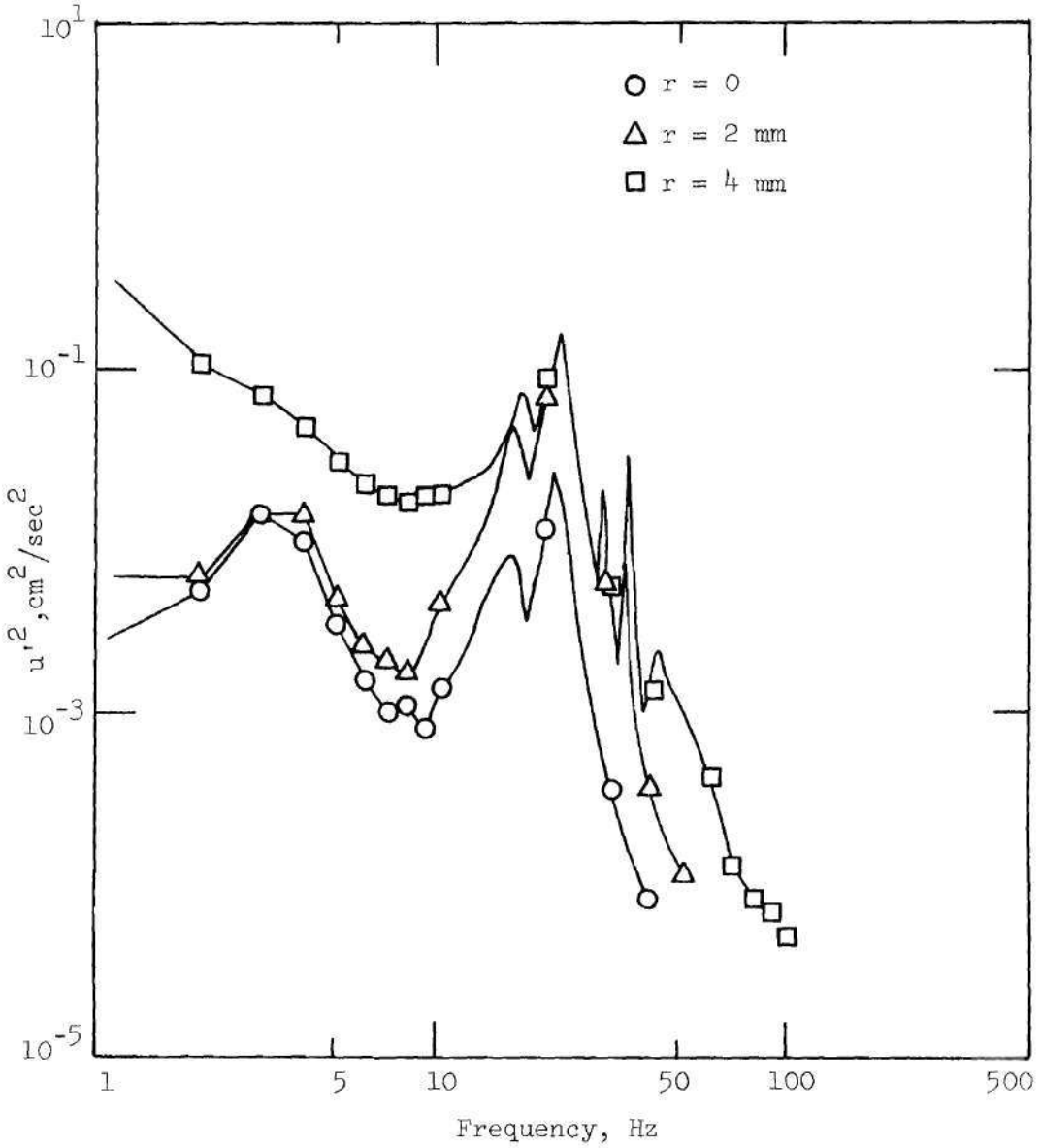

Figure 104. Energy Spectra for 90% Sharp-Edged Occlusion, x/d = 1, R_{e_D} = 402, R_{e_d} = 1270

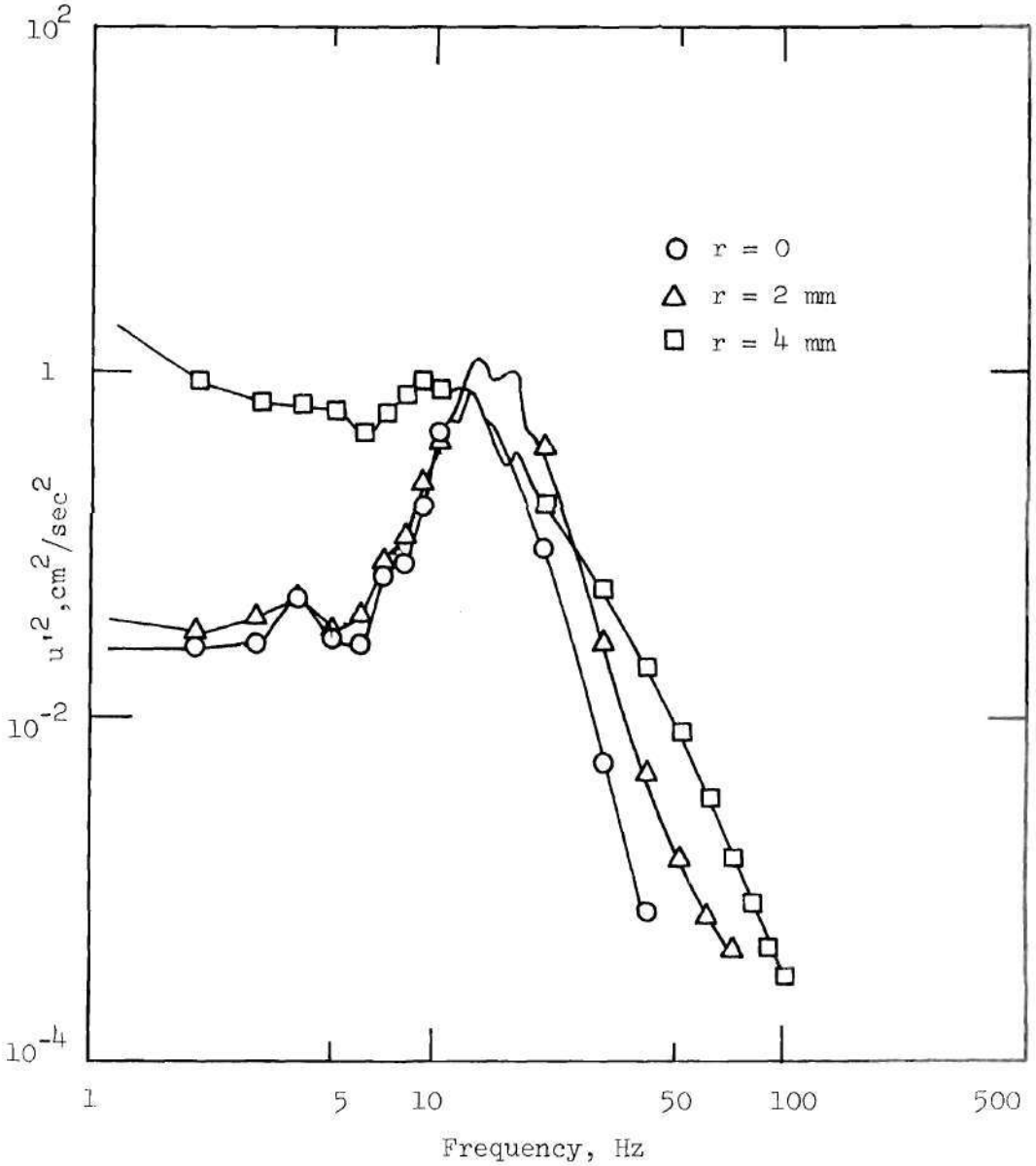

Figure 105. Energy Spectra for 90% Sharp-Edged Occlusion, x/d - 2.25, R_{e_D} = 402, R_{e_d} = 1270

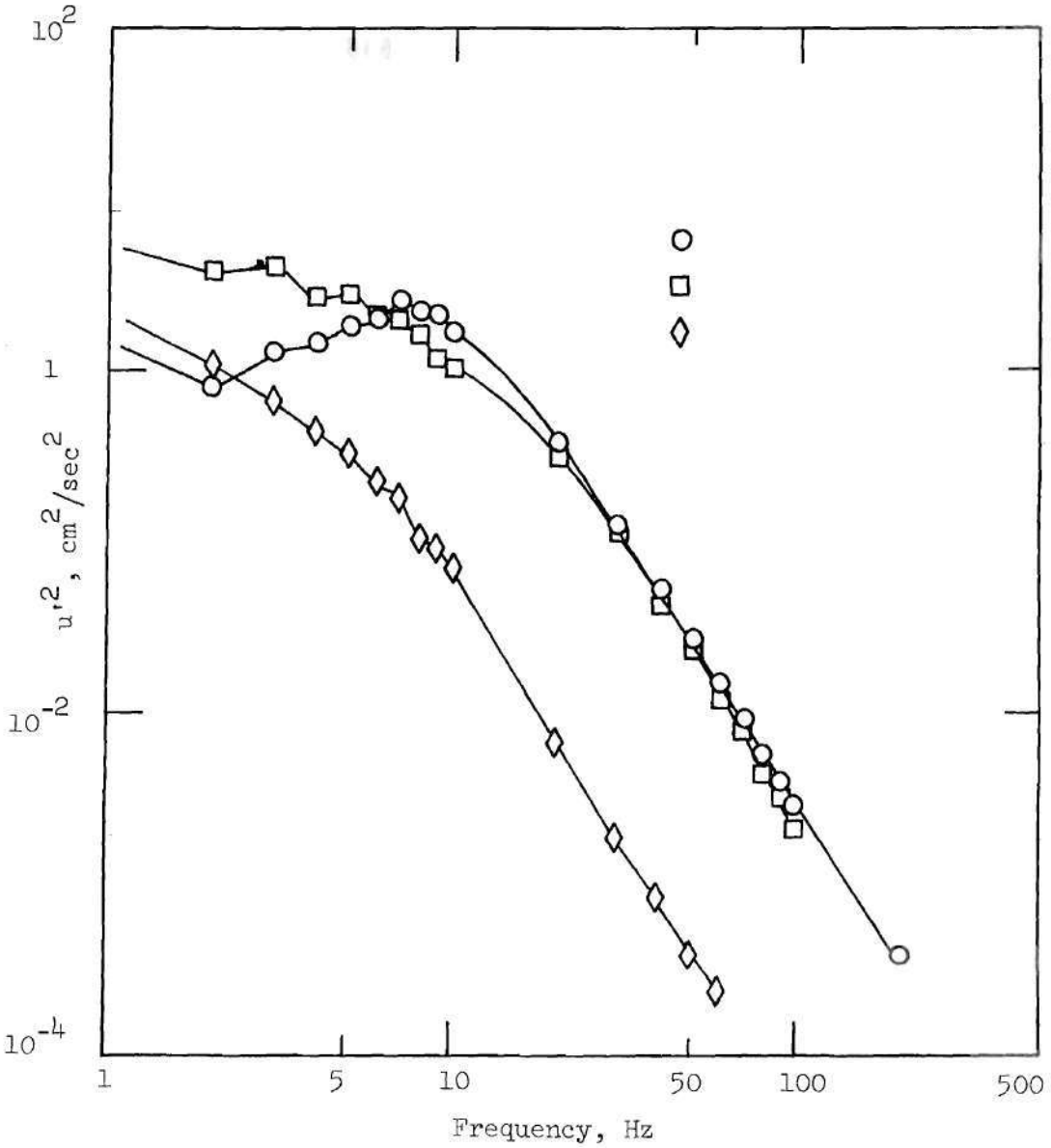

Figure 106. Energy Spectra for 90% Sharp-Edged Occlusion, x/d = 4.25, R_{e_D} = 402, R_{e_d} = 1270

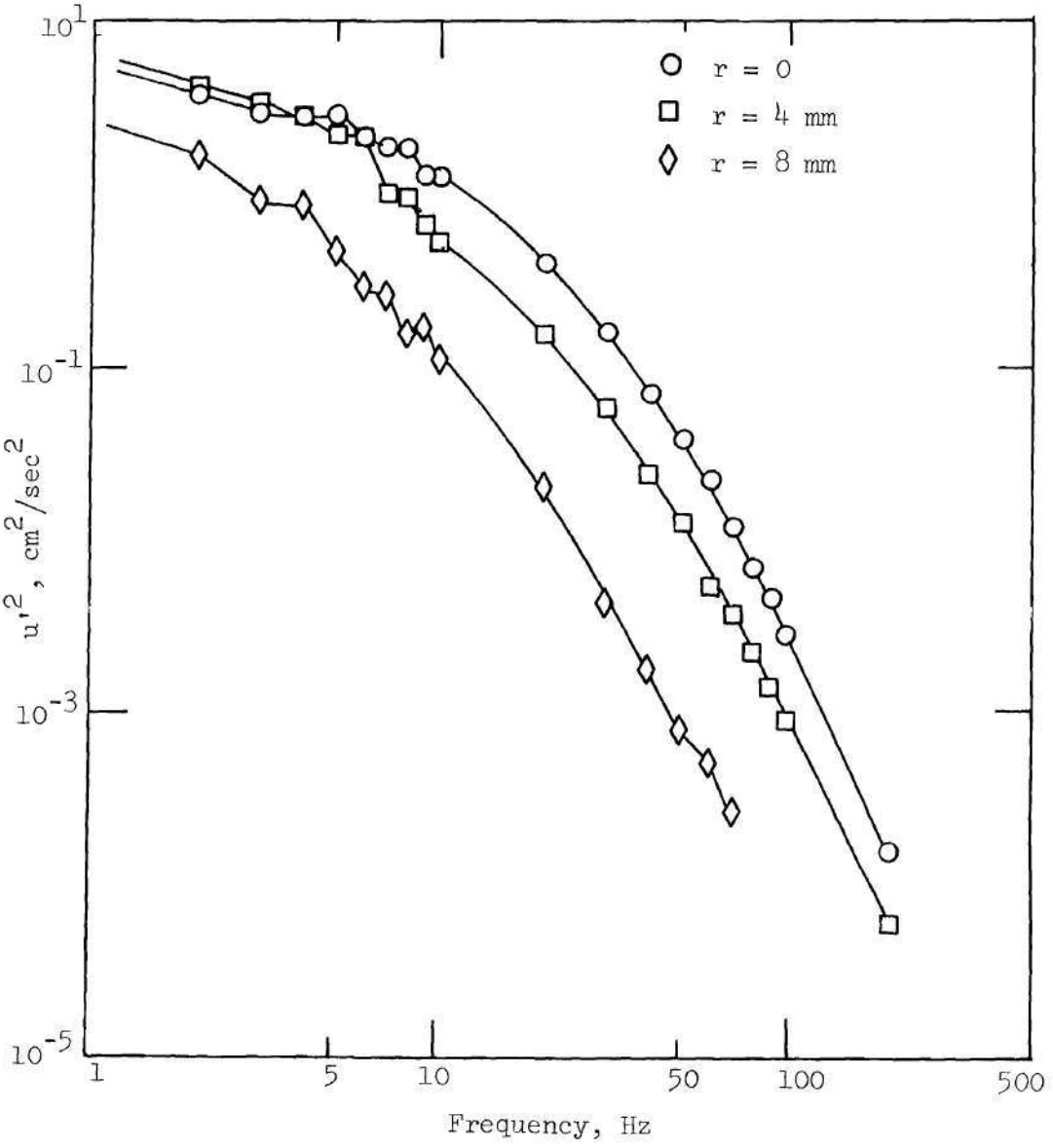

Figure 107. Energy Spectra for 90% Sharp-Edged Occlusion, $x/d = 6.25$, $R_{e_D} = 402$, $R_{e_d} = 1270$

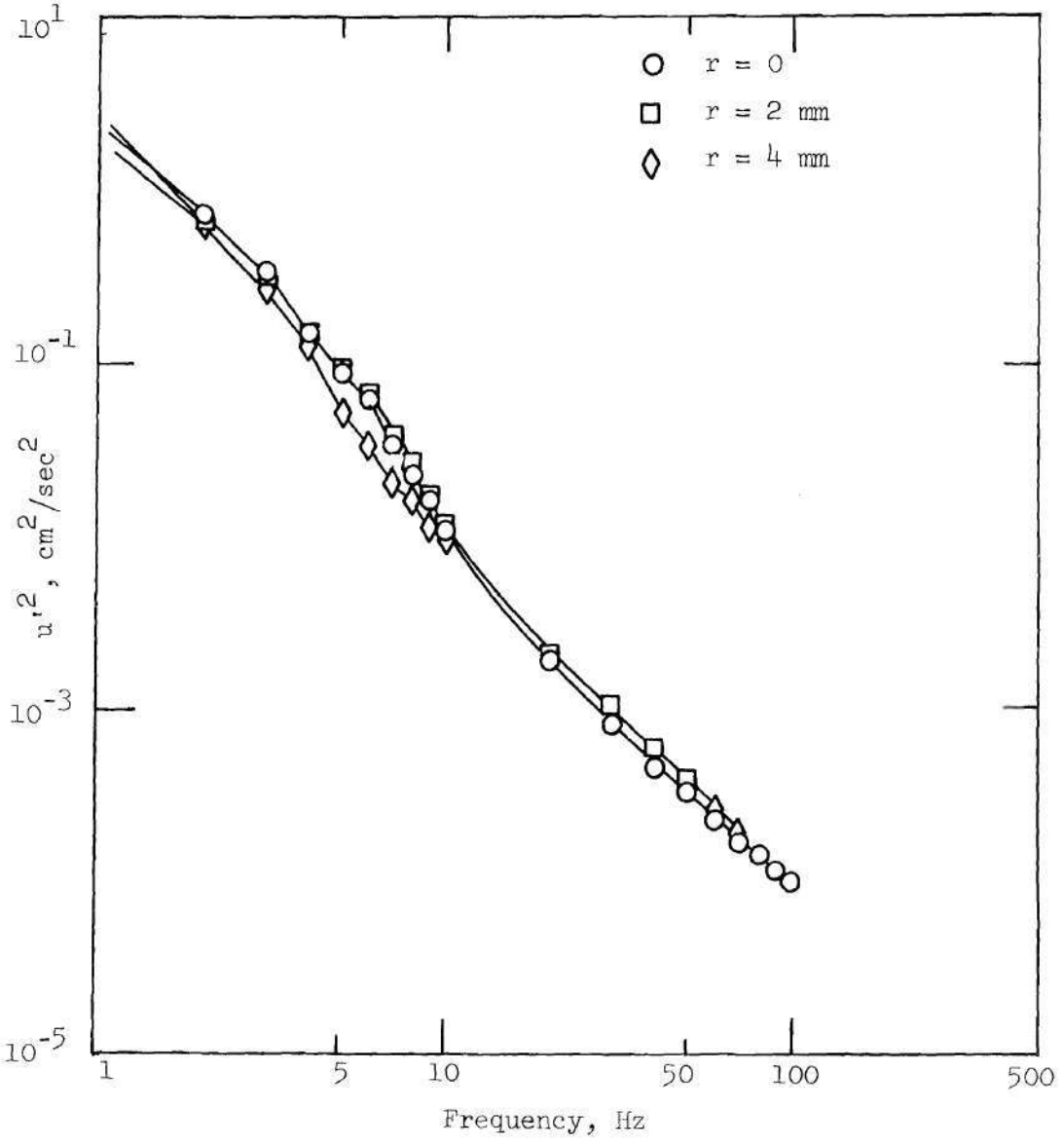

Figure 108. Energy Spectra for 90% Sharp-Edged Occlusion, $x/d = 12.25$, $R_{e_D} = 402$, $R_{e_d} = 1270$

the recirculation flow. The high shear region between the jet and recirculation flows of the two occlusions has comparable influences on vortex ring formation since this high shear region is sufficiently removed from the wall in both cases.

6.4 Steady Flow Energy Spectra Data Summary

The foregoing sections of this chapter have discussed the steady flow energy spectra data and the salient features of the data are summarized in the following statements:

1. The sharp-edged occlusion is more likely to produce initial instabilities and the turbulent-like spectra occur over a greater spatial range and have a higher intensity for a given flow Reynolds number than the corresponding contoured occlusion.

2. The fundamental vortex shedding frequency increases with R_e at a fixed x/d and r, decreases with x/d at a fixed R_e, r and degree of occlusion, increases with r at a fixed x/D, R_e and degree of occlusion, and increases with degree of occlusion at a fixed R_{e_D}, x/D and r.

3. The vortex ring maintains its integrity better at lower R_e and for the contoured occlusions.

4. Complete relaminarization does not occur within the distance spanned by the experiments for any occlusion and flow condition which produced an initial flow disturbance.

5. The intensity of the velocity flucuations of the vortex or turbulent fields reaches a maximum and then decreases with x/D.

6. For a given R_{e_D} and occlusion shape the vortex rings breaks up faster for greater degree of occlusion.

7. For a given R_{e_D}, occlusion shape and x/D the intensity of the velocity flucuations increases for a greater degree of occlusion.

8. Discrete vortex shedding was observed for almost all cases which is in contrast to the results reported by Kim and Cocoran[8].

9. Even for low R_{e_D}, the larger degrees of blockage can "trip" the flow distal to the occlusion and create substantial turbulence downstream.

6.5 Nondimensional Correlations

The purposes of presenting energy spectra correlations for the various constriction geometries and flow conditions are: (1) to determine the applicability of nondimensional parameters to the scaling of the distal flow field, (2) to compare the relative intensities of the velocity flucuations produced by two occlusion geometries for a given flow condition, (3) to relate the Strouhal number of the vortex shedding frequency to the data cited in the literature and (4) to compare the Strouhal numbers of the two occlusion geometries.

Since the data presented in the references is often correlated with Strouhal number based on the conditions at the jet orifice or pipe exit, it is appropriate to replot the present data in a similar manner. In these plots, the energy is nondimensionalized by the velocity at the constriction calculated by dividing the flow rate by the constriction area, $Q/A_o = U_o$. The frequency is nondimensionalized by the constriction diameter, d, and the constriction velocity, U_o. The centerline spectral data are shown in each figure for both the sharp-edged and contoured occlusions. By plotting the data in this manner,

the development of the most intense spectral peaks can be demonstrated along with a direct comparison of the results obtained with the two different occlusion geometries.

Figure 109 shows the Strouhal number data for the 50 percent occlusions at R_{eD} = 2540. In the near distal field (x/D = 0.5) of the sharp occlusion, the Strouhal number of the spectral peak is about 1.0 and decreases to a value of about 0.5 to 0.6 at the more distal positions (x/D = 1.125 and 2.125) before the onset of the turbulent-like dispersed spectra at x/D = 3.125. The intensity of the spectral peak also reaches a maximum at fd/U_o = 0.6 before dissipating in random turbulence at more downstream positions. The contoured occlusion data show the spectral peak to occur at a Strouhal number of about 0.5 to 0.6 at all positions shown. Hence, both occlusion geometries yield Strouhal numbers of the maximum spectral peak of about 0.6. However, the sharp-edged occlusion yields more intense spectral peaks, as compared to the total kinetic energy available at the occlusion, U_o^2, than did the contoured occlusion. At a lower R_{eD} = 1270 (Figure 110), a similar Strouhal number and velocity fluctuation energy trend can be seen although the peaks are not quite as distinct.

The Strouhal number correlations for the 75 percent occlusions are shown in Figures 111, 112, and 113. In general, the sharp-edged occlusion results for all R_{eD} show the Strouhal number, fd/U_o, of the spectral peak to be about 1.0 near the orifice with the peak energy increasing as the flow progresses downstream to a final peak Strouhal number of about 0.6 immediately before breaking-up into more random turbulence. The contoured occlusion results at R_{eD} = 2540 (Figure 111)

demonstrated a behavior which is similar to the sharp-edged results, although the overall energy levels are somewhat lower at corresponding axial locations. At a lower R_{eD} of 1270 (Figure 112) and 635 (Figure 113), the contoured occlusion flow field produced spectral peaks at $x/D = 2.125$ at a Strouhal number of about 0.5 whereas the sharp-edged occlusion produced a more dispersed spectra. However, the contoured occlusion spectral intensities are still lower than the sharp-edged occlusion intensities. In fact, at $R_{eD} = 635$, the spectral peaks actually decrease in amplitude relative to U_o^2 as the flow moves downstream. These plots have demonstrated that both occlusion geometries produce vortex shedding frequencies whose Strouhal numbers, fd/U_o, is about 0.6 at its highest energy intensity, but, in general, the sharp-edged occlusion is more "efficient" in producing a dominant vortex ring system for a given orifice velocity, U_o, than is the contoured occlusion.

Several other interesting features of this correlation can be observed by plotting the spectral data for the different degrees of occlusion on the same plot. These plots are shown for the sharp-edged occlusions for the two highest R_{eD} which were used in the experiments. These higher R_{eD} resulted in flow field which contained regions of laminar flow, laminar vortices and fully developed turbulent flow; whereas, the lowest R_{eD} of 635 resulted in flow instabilities which decayed rather than developed into random turbulence.

The sharp-edged occlusion data shown in Figures 114 through 118 for highest Reynolds number indicates that the 75 percent and 90 percent

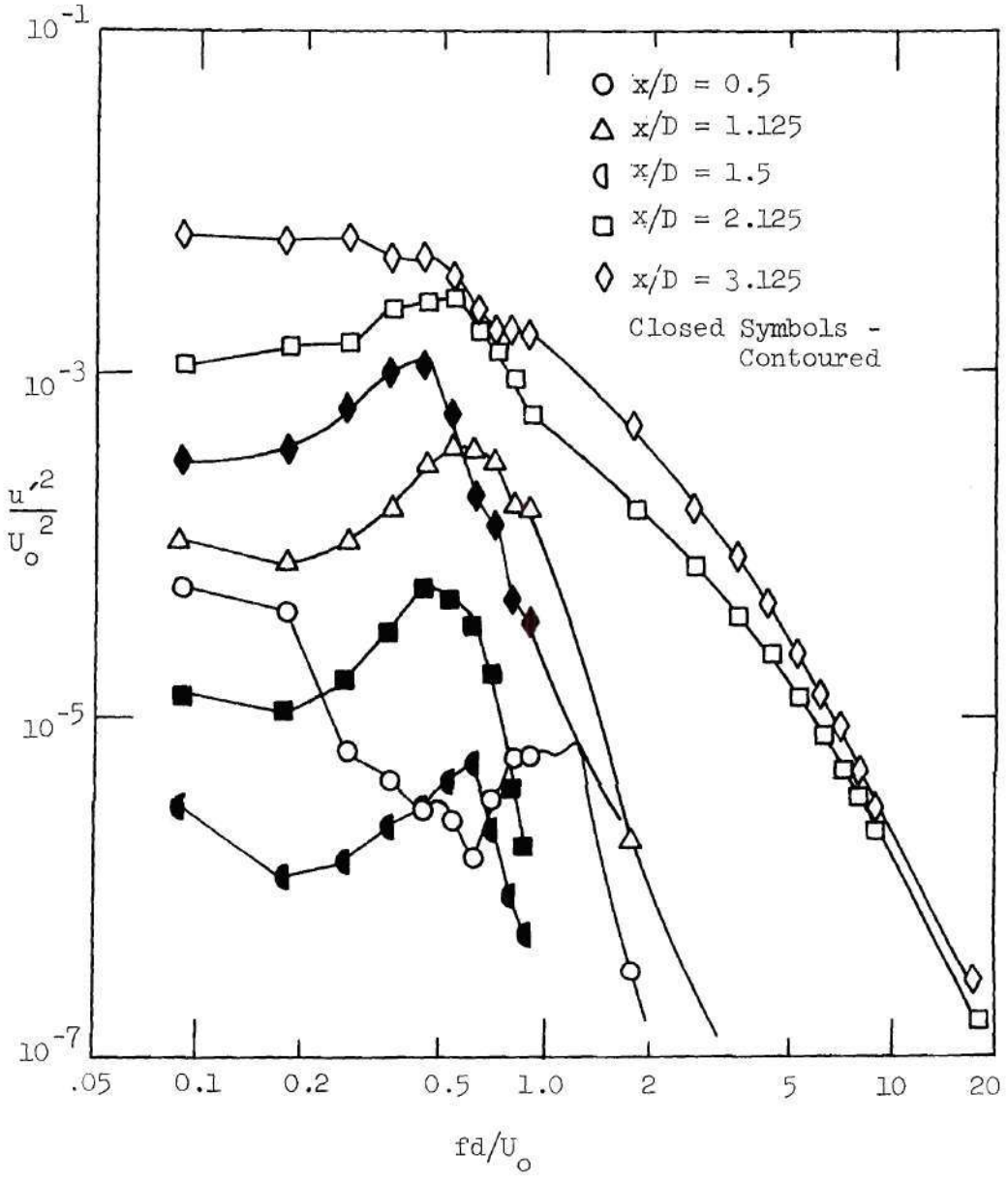

Figure 109. Strouhal Number Correlation for 50% Occlusions, $R_{e_D} = 2540$, $R_{e_d} = 3592$.

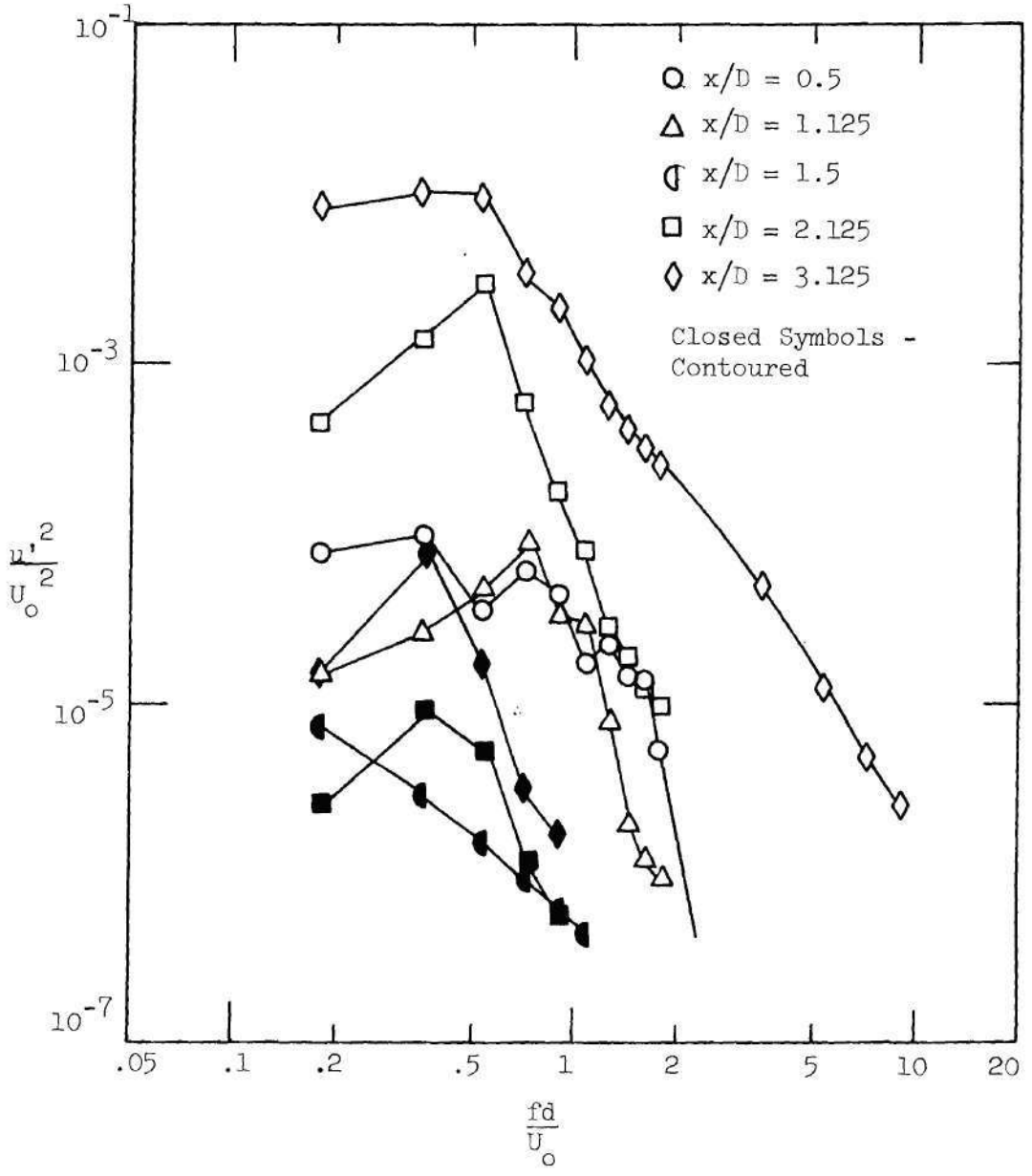

Figure 110. Strouhal Number Correlation for 50% Occlusions, R_{e_D} = 1270, R_{e_d} = 1796

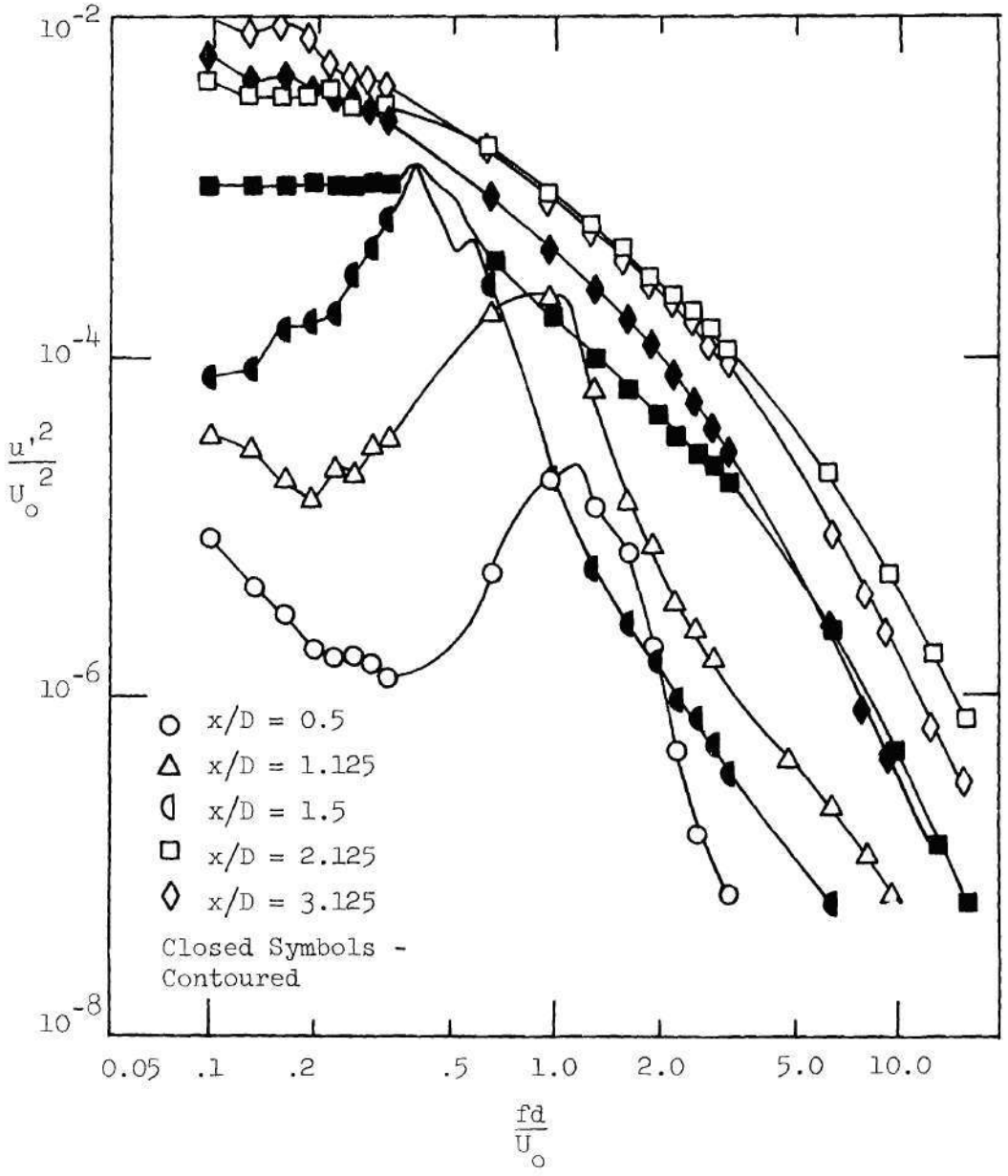

Figure 111. Strouhal Number Correlation for 75% Occlusions, R_{e_D} = 2540, R_{e_d} = 5080

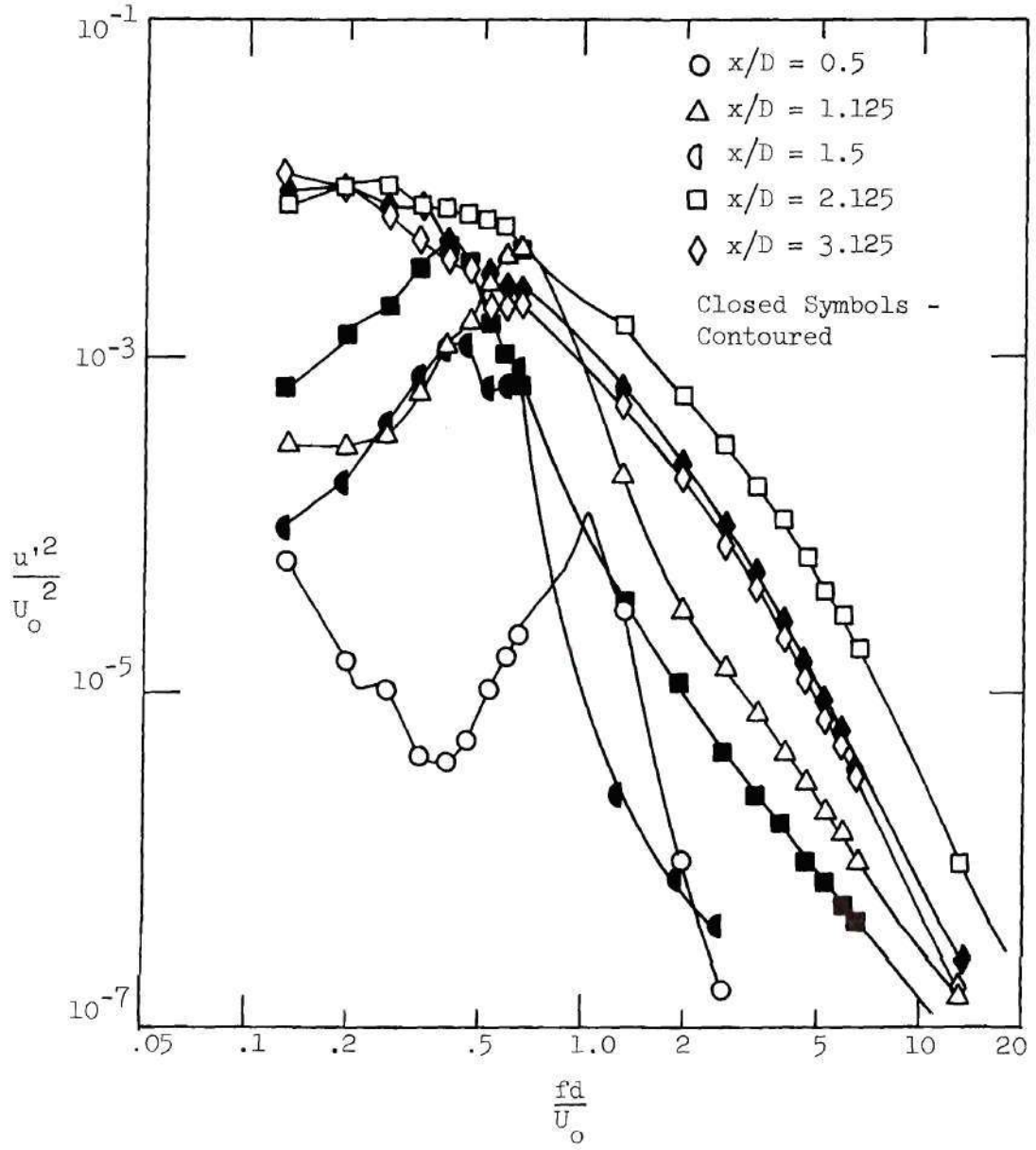

Figure 112. Strouhal Number Correlation for 75% Occlusions, R_{e_D} = 1270, R_{e_d} = 2540

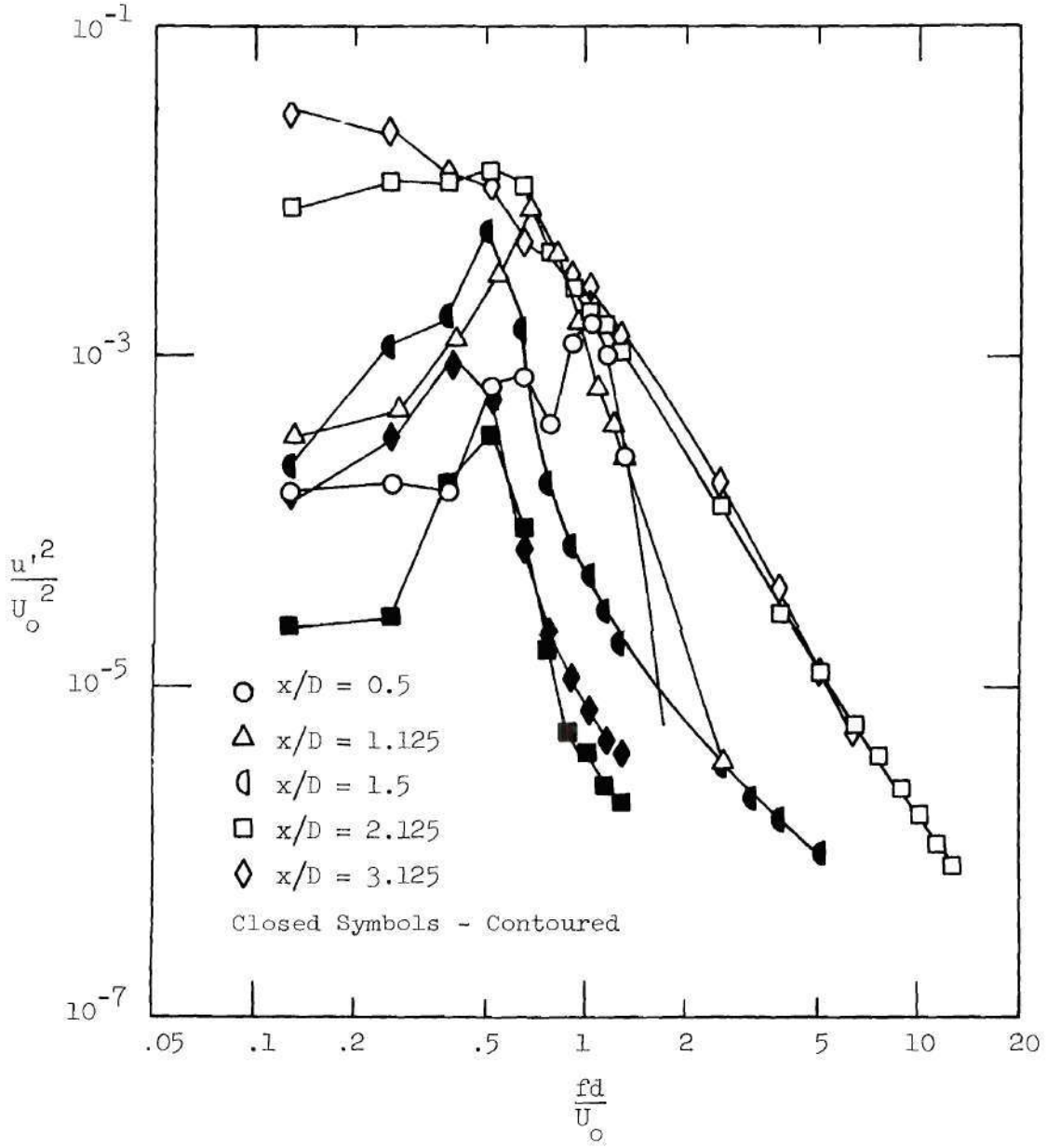

Figure 113. Strouhal Number Correlation for 75% Occlusions, R_{e_D} = 635, R_{e_d} = 1270

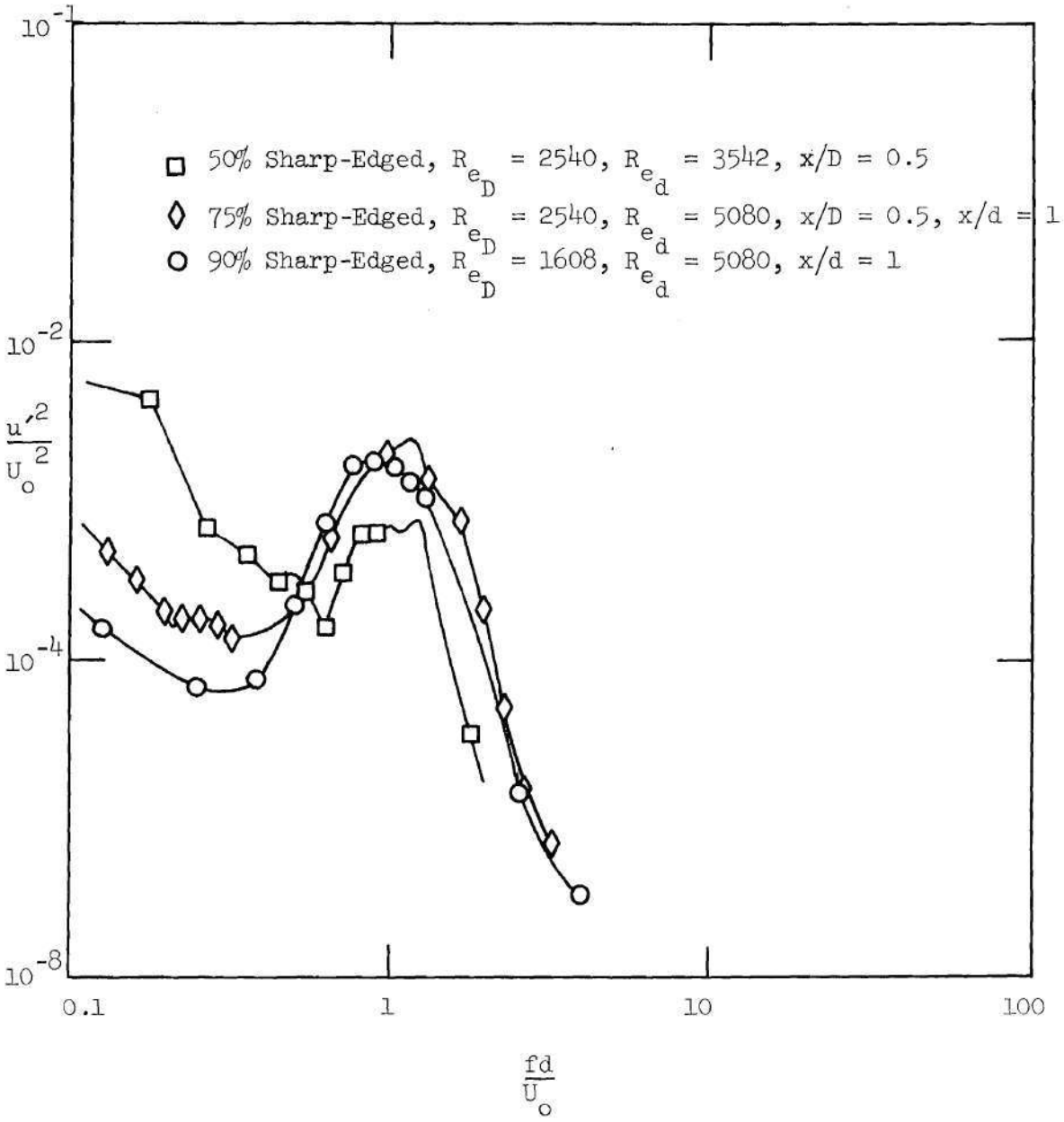

Figure 114. Strouhal Number Correlation at x/D = 0.5, x/d = 1.0, R_{e_D} = 2540 and R_{e_d} = 5080 for Sharp-Edged Occlusions.

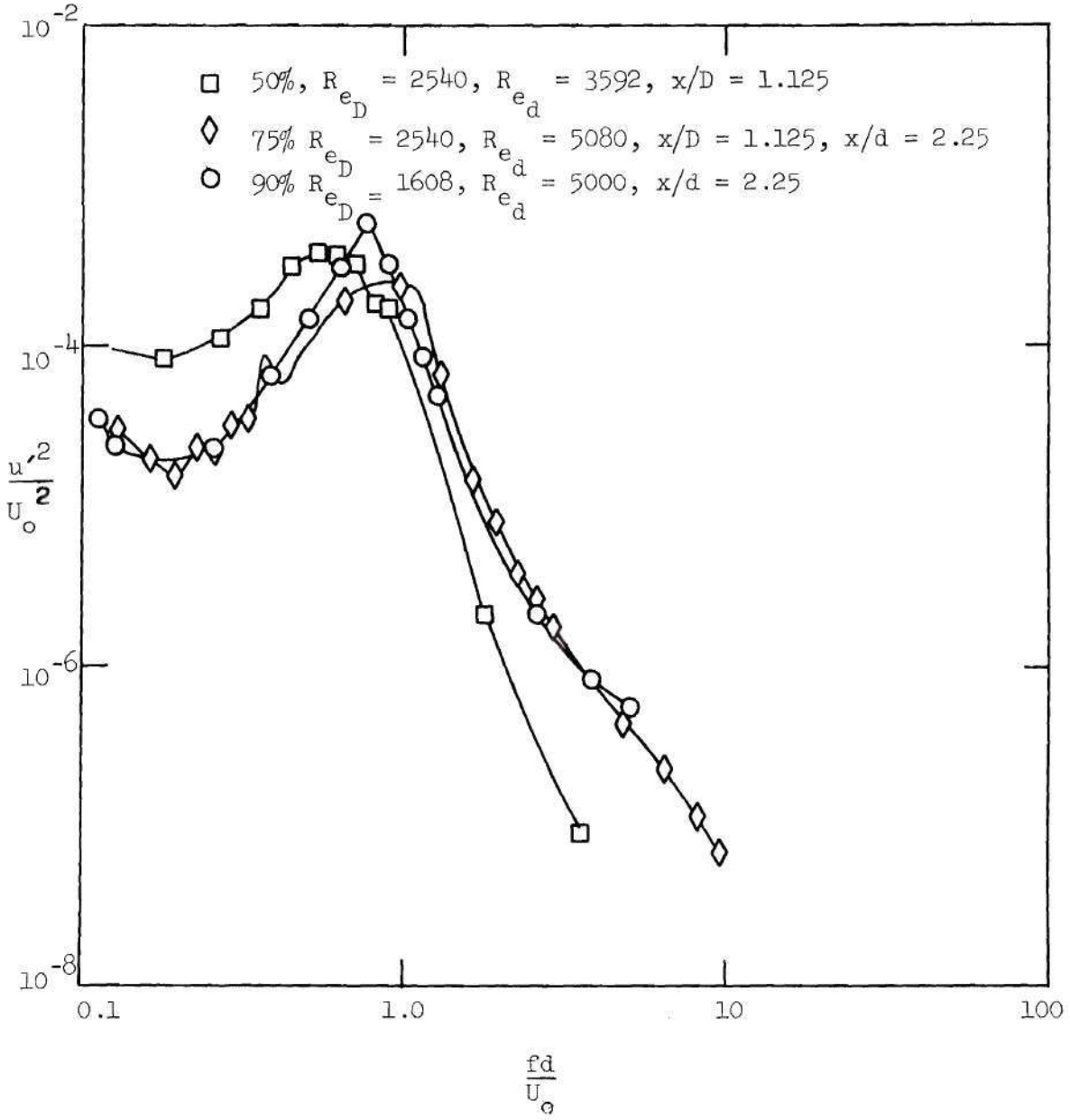

Figure 115. Strouhal Number Correlation at x/D = 1.125, x/d = 2.25, R_{e_D} = 2540, and R_{e_d} = 5080 for Sharp-Edged Occlusions.

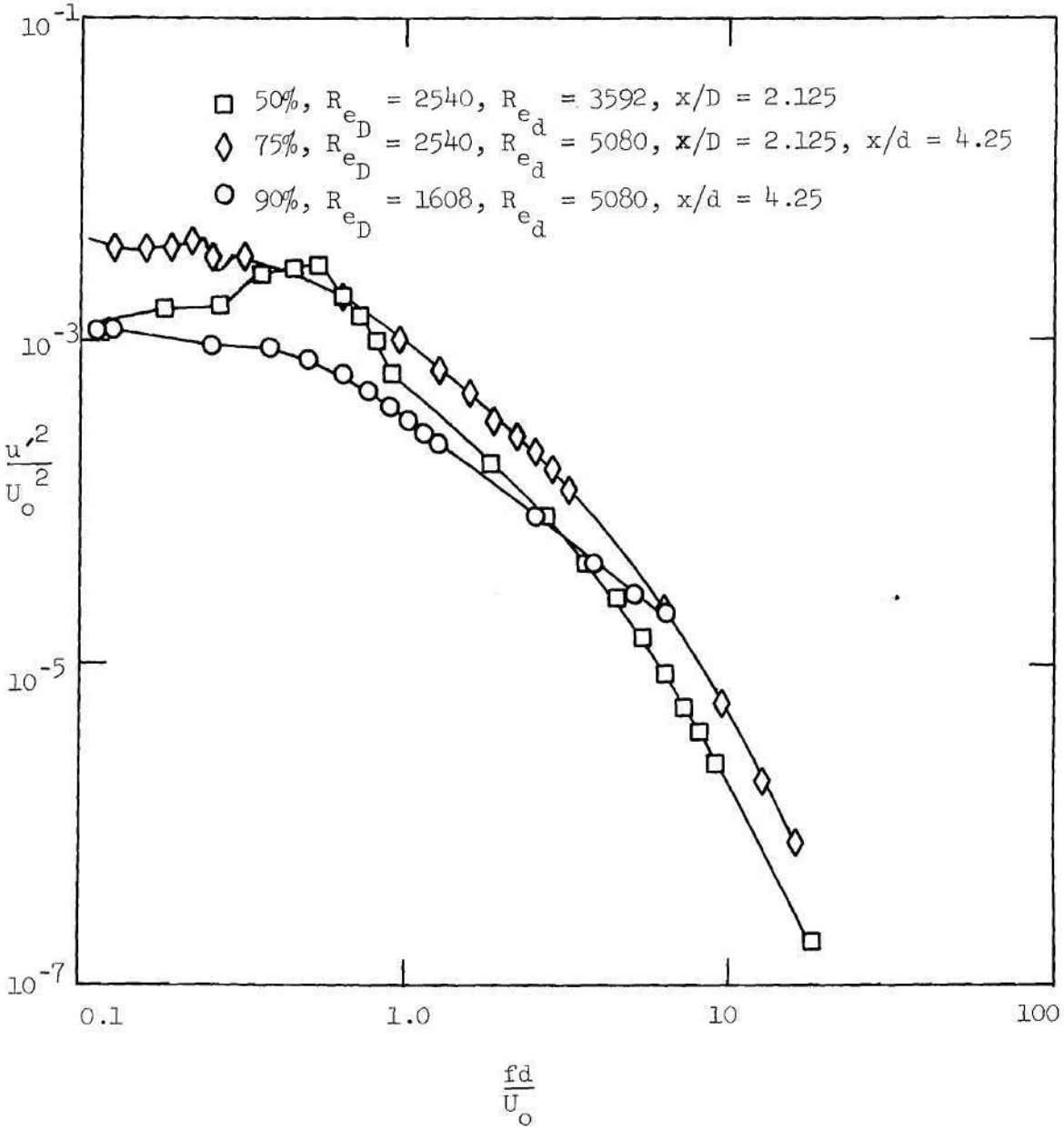

Figure 116. Strouhal Number Correlation at x/D = 2.125, x/d = 4.25, R_{e_D} = 2540, and R_{e_d} = 5080 for Sharp-Edged Occlusions.

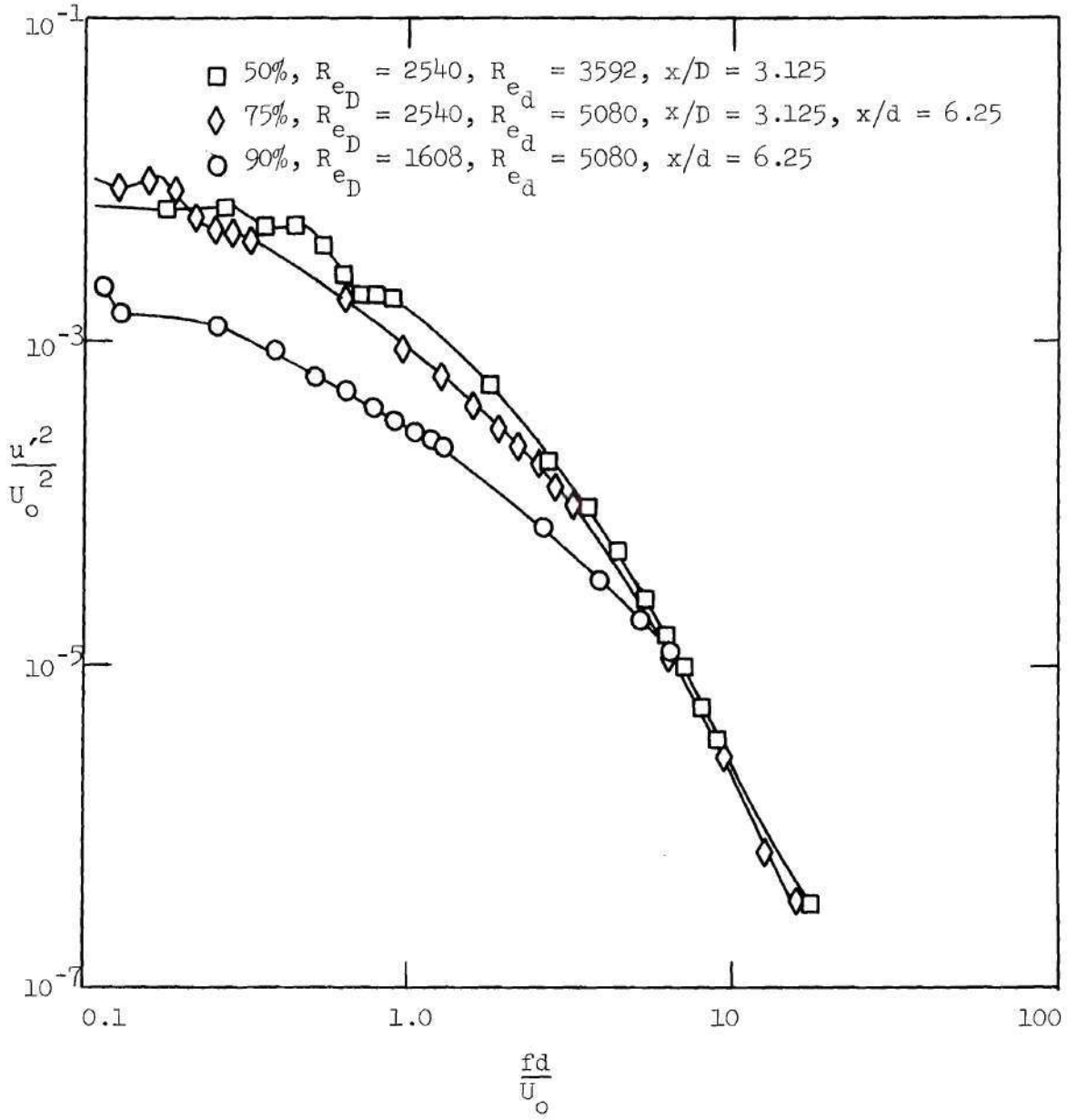

Figure 117. Strouhal Number Correlation at x/D = 3.125, x/d = 6.25, R_{e_D} = 2540, and R_{e_d} = 5080 for Sharp-Edged Occlusions.

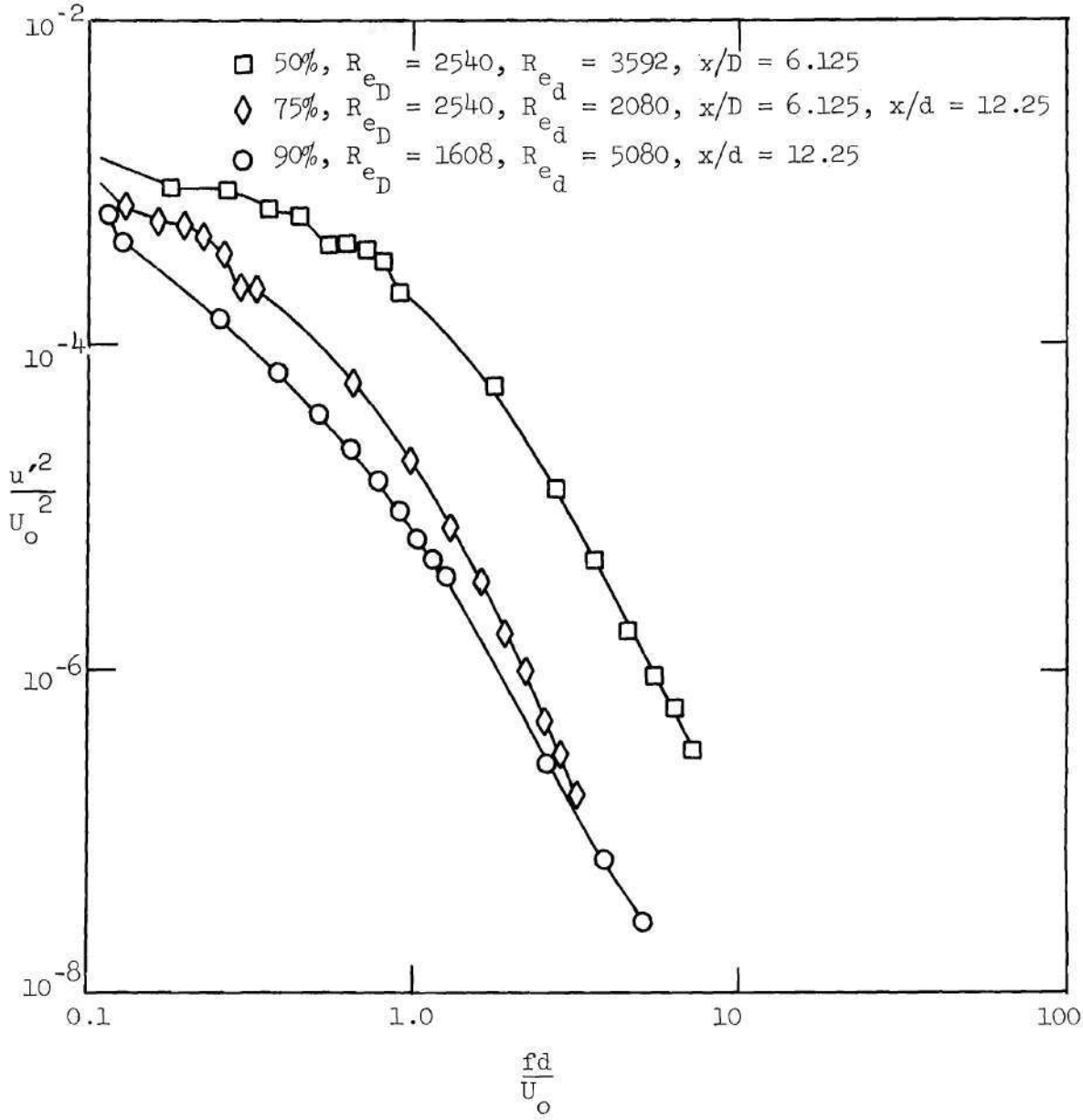

Figure 118. Strouhal Number Correlation at x/D = 6.125, x/d = 12.25, R_{e_D} = 2540, R_{e_d} = 5080 for Sharp-Edged Occlusions.

occlusion data, at the same R_{ed} = 5080 and same x/d positions, correlates well with this particular nondimensionalization for the near-distal field where the direct wall interaction is minimized. This correlation is not as good farther downstream where the direct influence of the jet flow has been somewhat nullified by wall interaction effects. The 50 percent occlusion data, which has the same R_{eD} and x/D as the 75 percent data appears to correlate reasonably well with the 75 percent spectra at x/D = 2.125 and 3.125 but this correlation is considered fortuitous. Similar trends at lower Reynolds numbers can be seen in Figures 119 through 123.

The foregoing discussion in this section has illustrated the fact that the orifice Strouhal number, fd/U_o, of the vortex shedding frequency decreases as the distance from the constriction increases. This is more clearly shown in Figure 124 for all of the steady flows which exhibited vortex shedding. Notice that the sharp-edged occlusions exhibited distinct vortex shedding near the constriction at low x/D locations, while the contoured occlusions produced this behavior farther downstream.

The same data is shown in Figure 125 with the shedding frequency nondimensionalized by a Strouhal number based on the local mean centerline velocity, $\bar{U}_L$, and an effective jet streamtube diameter, $\mathcal{D}$. The effective streamtube diameter is calculated by assuming that the effective local jet flow area is inversely proportional to the square root of the local mean centerline velocity and using the unoccluded diameter and centerline velocity, U_∞, as a reference; or,

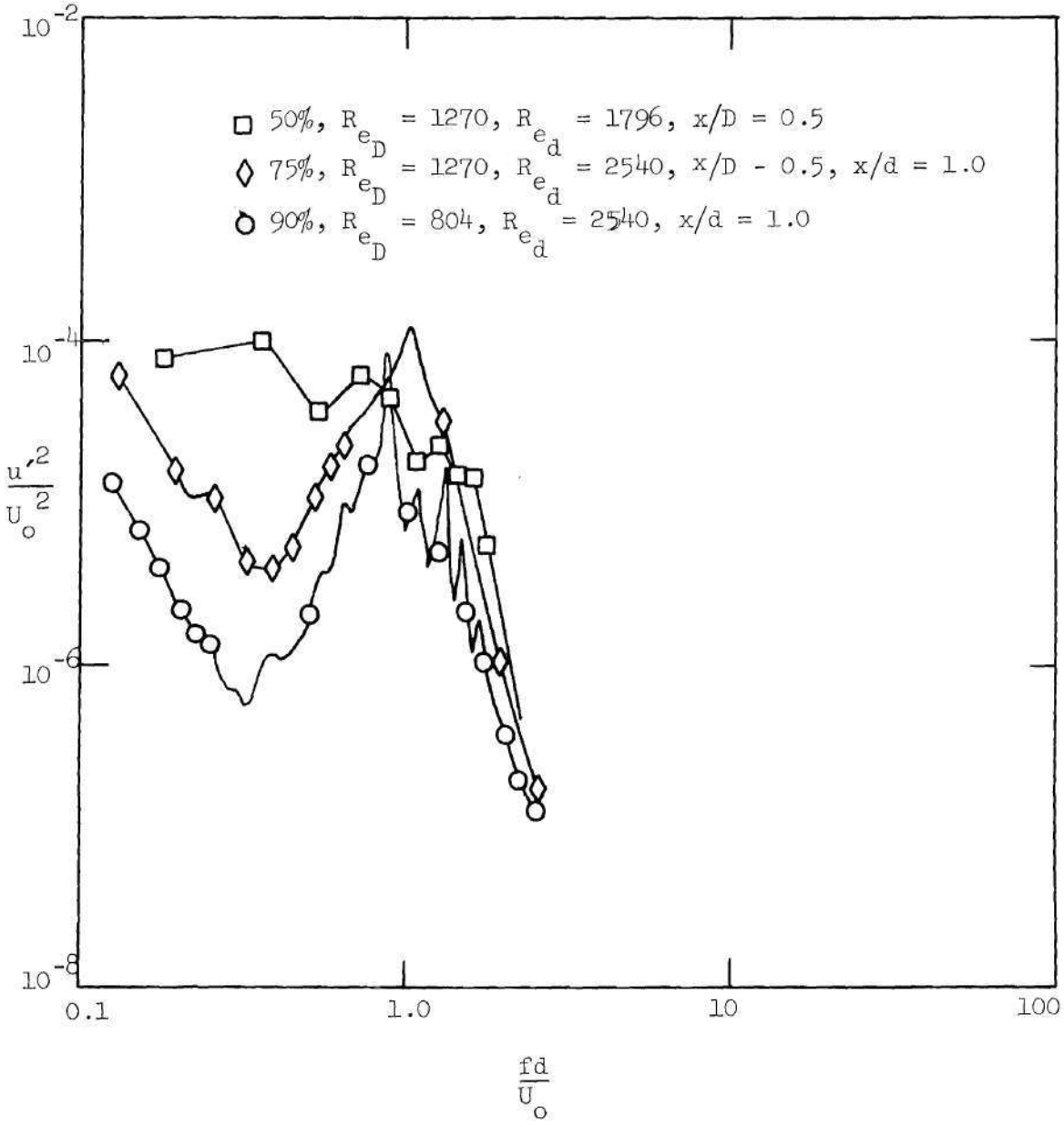

Figure 119. Strouhal Number Correlation at x/D = 0.5, x/d = 1.0, R_{e_D} = 1270, R_{e_d} = 1796 for Sharp-Edged Occlusion.

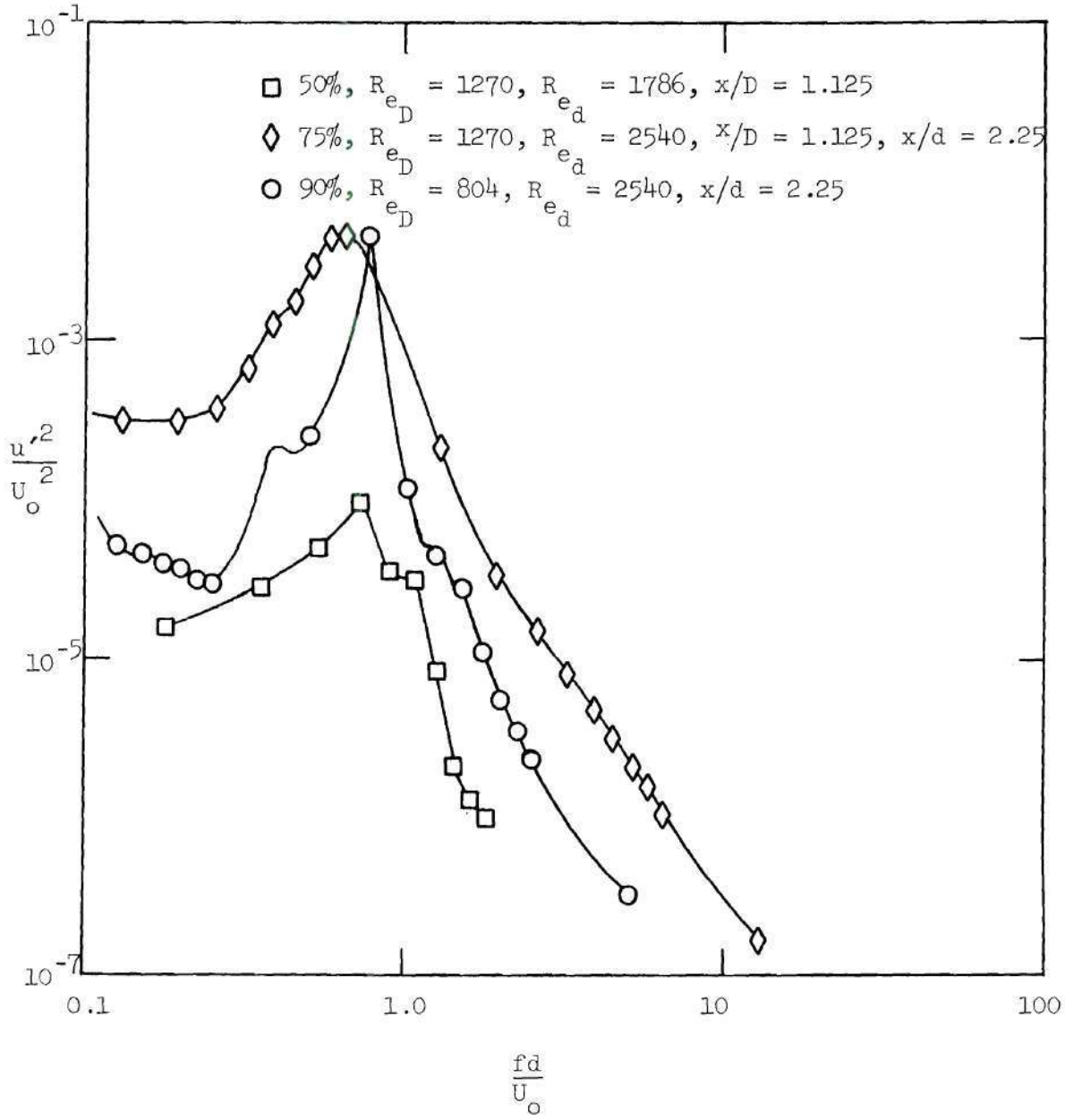

Figure 120. Strouhal Number Correlation at x/D = 1.125, x/d = 2/25 R_{e_D} = 1270, R_{e_d} = 2540 for Sharp-Edged Occlusions.

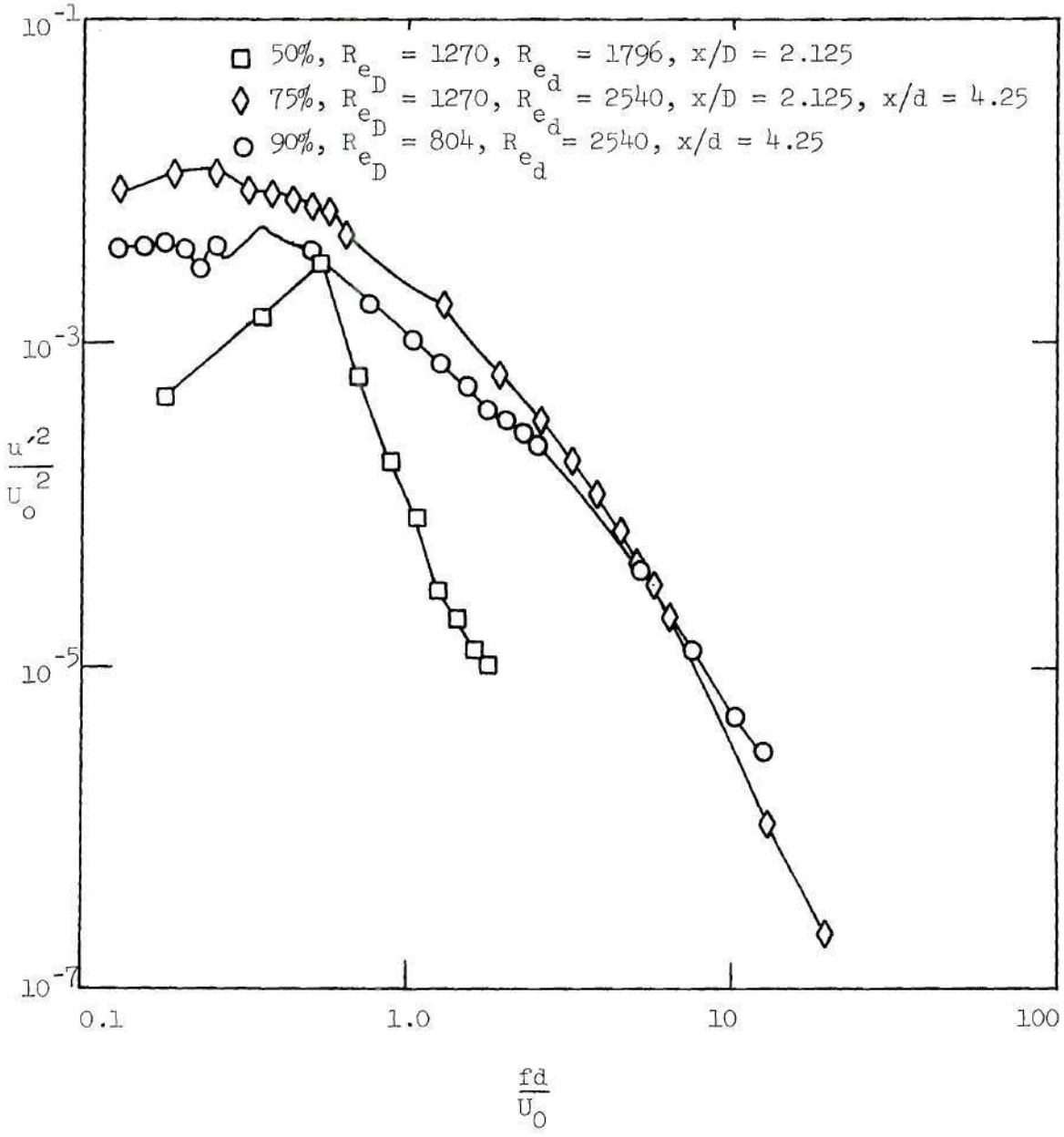

Figure 121. Strouhal Number Correlation at x/D = 2.125, x/d = 4.25, R_{e_D} = 1270, R_{e_d} = 2540 for Sharp-Edged Occlusions.

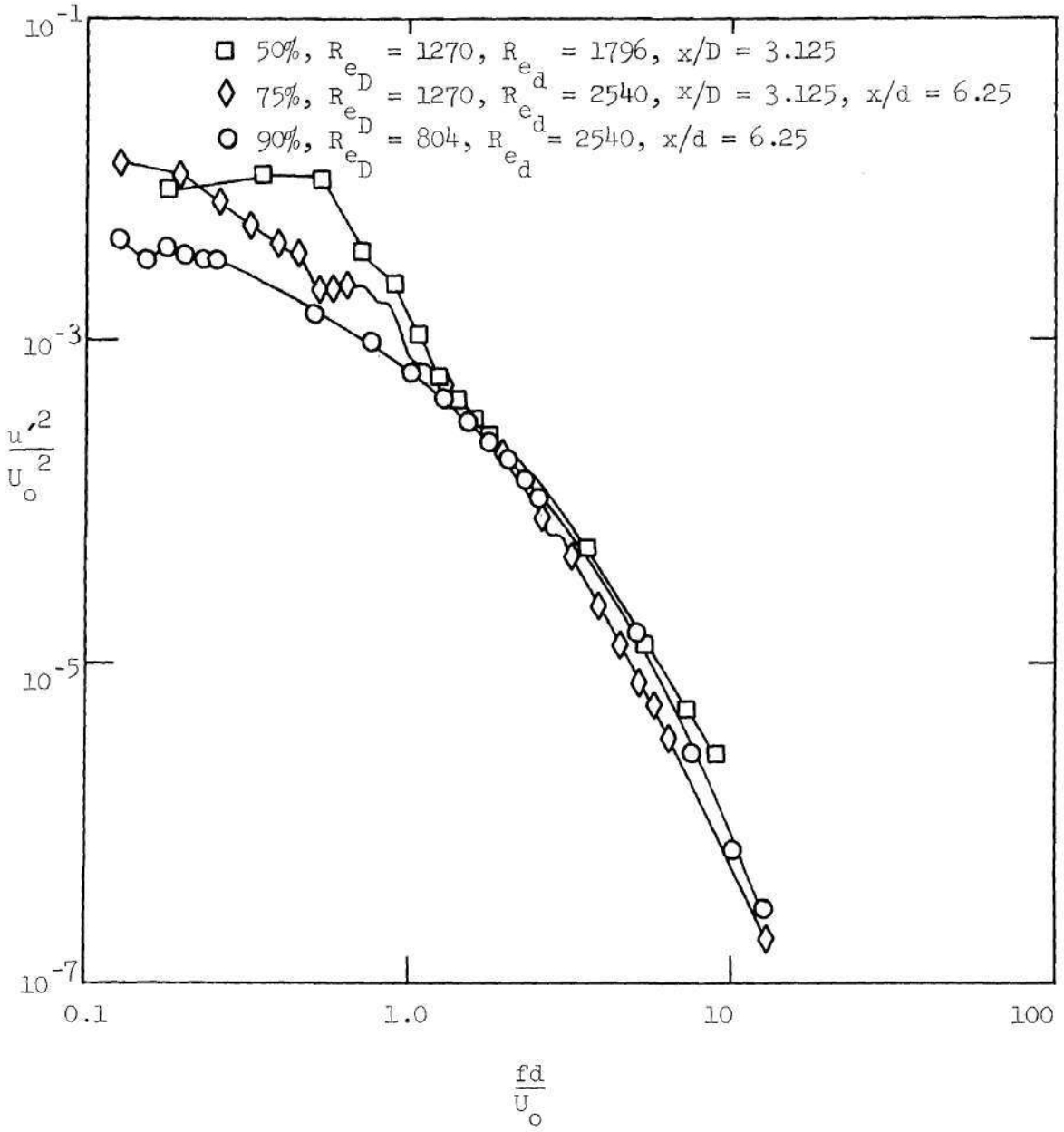

Figure 122. Strouhal Number Correlation at x/D = 3.125, x/d = 6.25 R_{e_D} = 1270, R_{e_d} = 2540 for Sharp-Edged Occlusion.

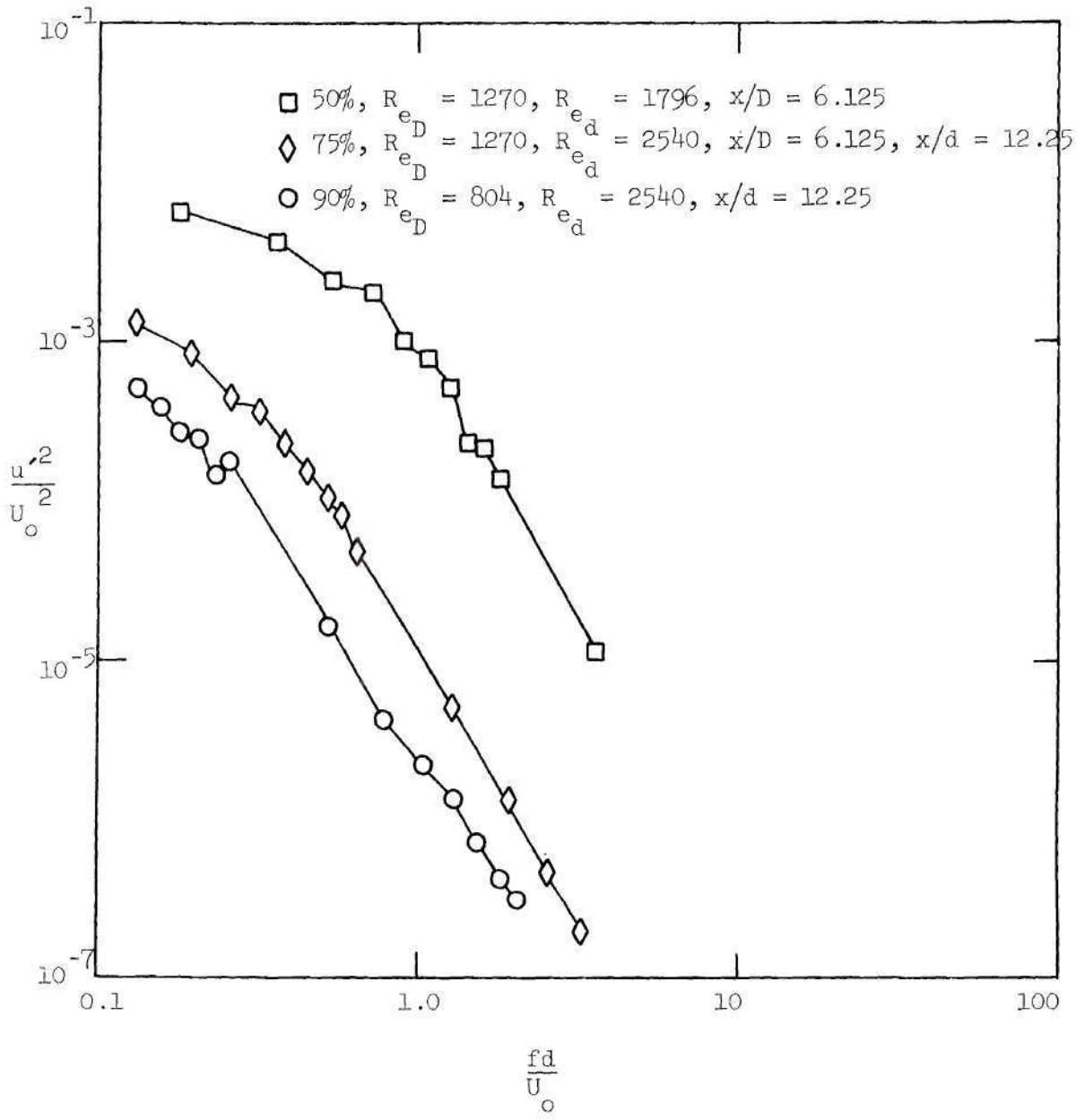

Figure 123. Strouhal Number Correlation at x/D = 6.125, x/d = 6.25, R_{e_D} = 1270, R_{e_d} = 2540 for Sharp-Edged Occlusions.

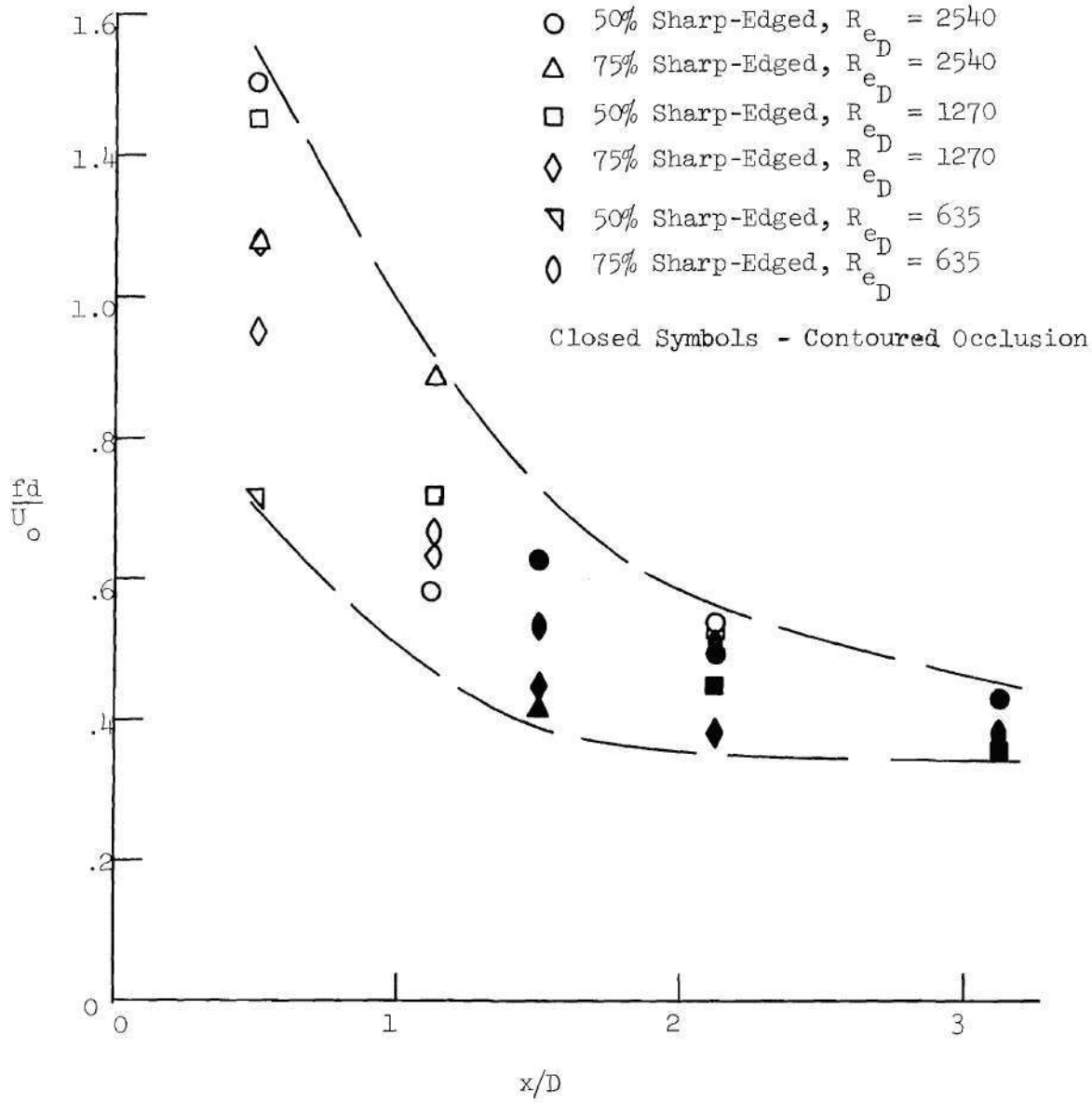

Figure 124. "Orifice" Strouhal Number of the Vortex Shedding Frequency as a Function of Axial Distance.

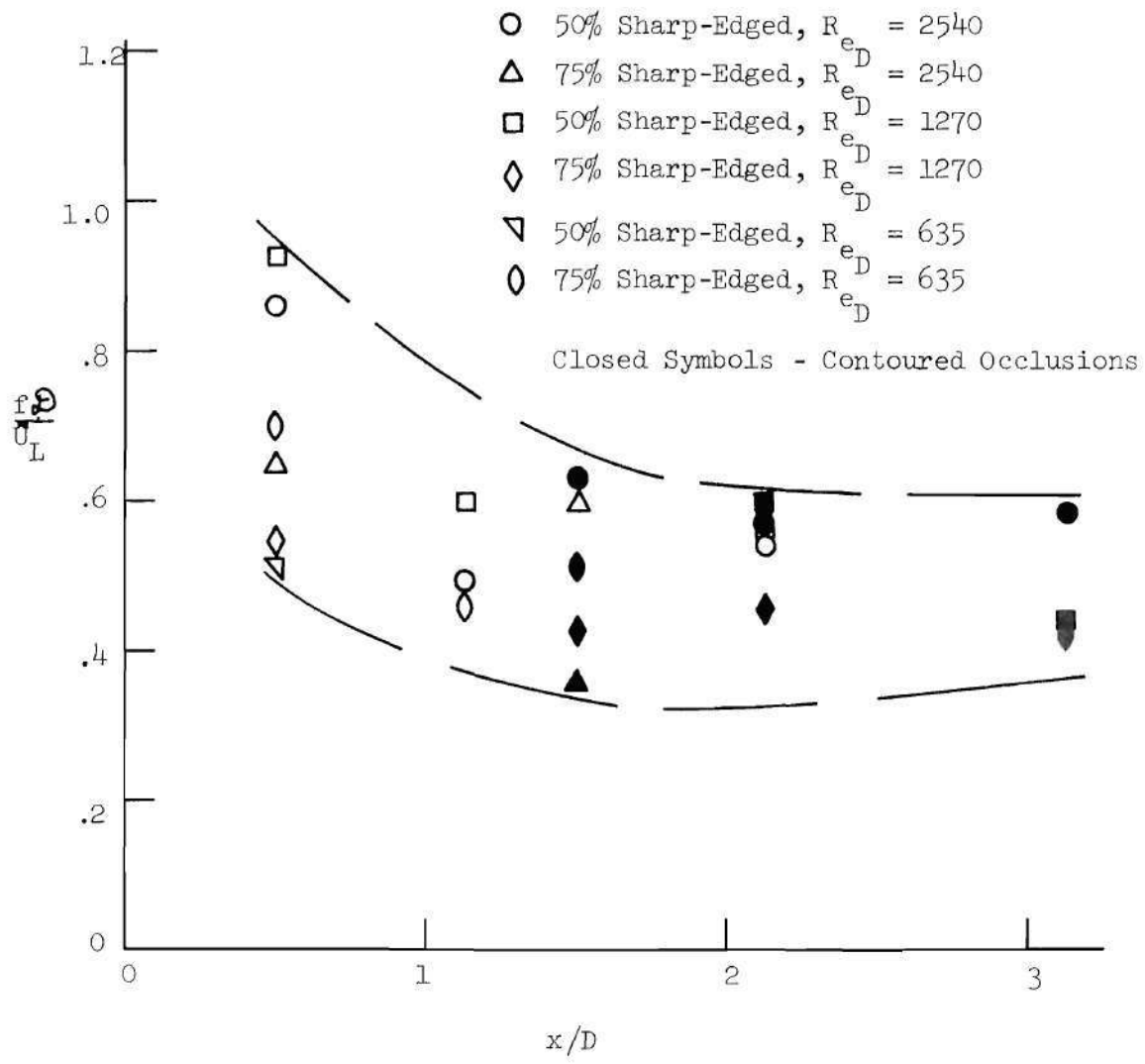

Figure 125. "Local" Strouhal Number of the Vortex Shedding Frequency as a Function of Axial Distance.

$$\mathcal{D} = D\left(\frac{U_\infty}{\bar{U}_L}\right)^{\frac{1}{2}}$$

By using these "local" parameters, the dependence of the "local" Strouhal number on x/D is reduced.

CHAPTER VII

PULSATILE FLOW VELOCITY WAVEFORM RESULTS AND DISCUSSION, $\alpha = 15$, $R_{e_{pD}} = 2540$

The characteristics of the velocity waveform distal to the occlusions can be an indication of the flow phenomena present and, in conjunction with the descriptions in Chapter II , can be used to confirm the visual observations. This chapter presents the velocity waveform results and illustrates the development of the turbulent velocity fields caused by the presence of axisymmetric stenoses. The results with the larger degree of occlusion, 75 percent reduction in area, are presented first since the phenomena to be illustrated are more outstanding for this case than for the lesser degrees of occlusion.

7.1 Velocity Waveforms for 75 percent Occlusions

Figure 126 for the sharp occlusion and Figure 127 for the contoured occlusion illustrate the velocity waveform variation with radial position in the near distal flow field. The centerline positions ($r = 0$) indicate the development of the turbulent-like velocity fluctuations as the velocity increases during the pulse. The sudden increase in velocity during the initial portion is indicative of the passing of the large swirling vortex which has been described in Chapter II. The $r = 4$ positions are considerably more turbulent than the $r = 0$ position during the high velocity region of the pulse. The $r = 8$ position also indicates

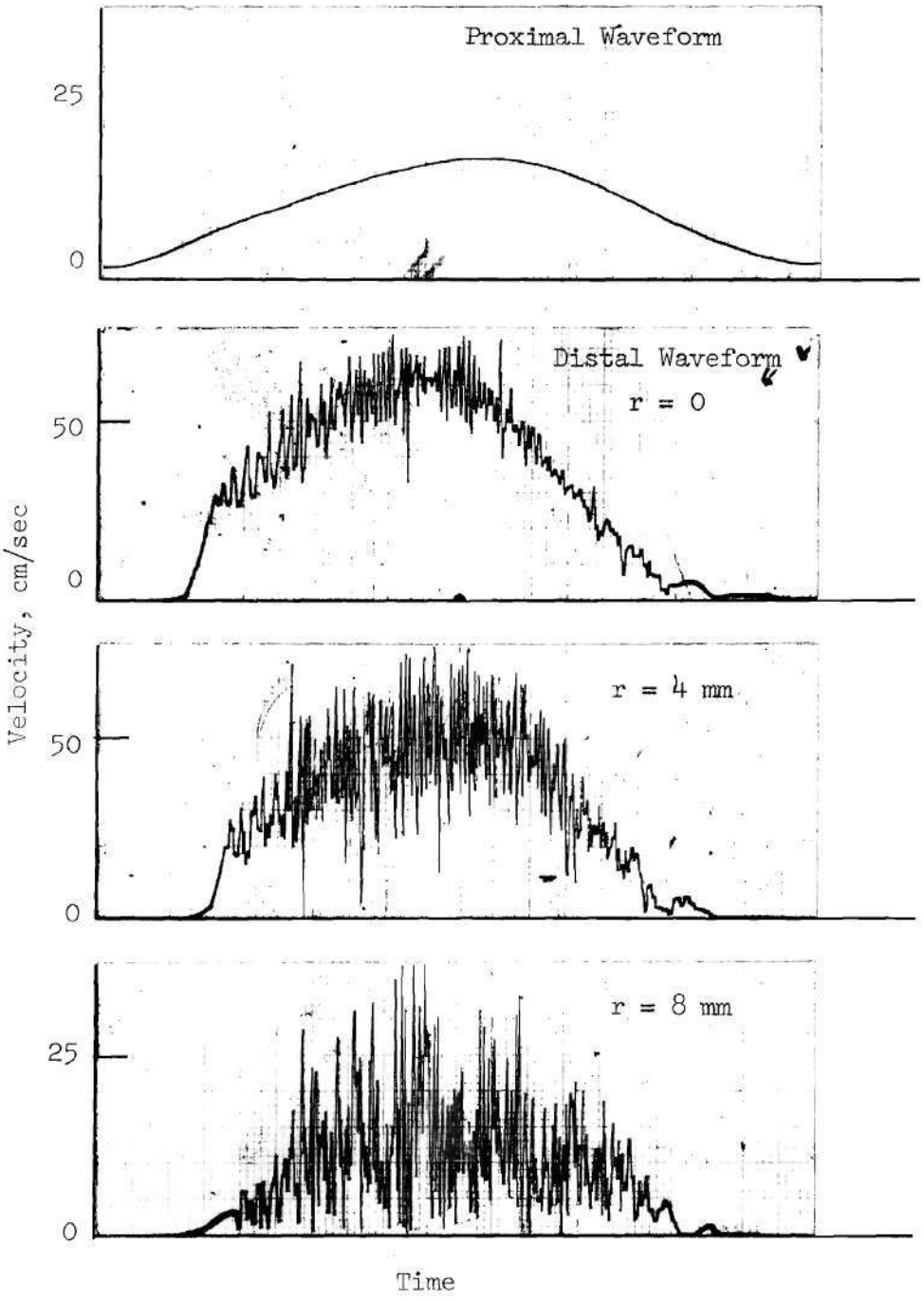

Figure 126. Radial Position Variation of Velocity Waveform for 75% Sharp Occlusion, x/D - 1.125

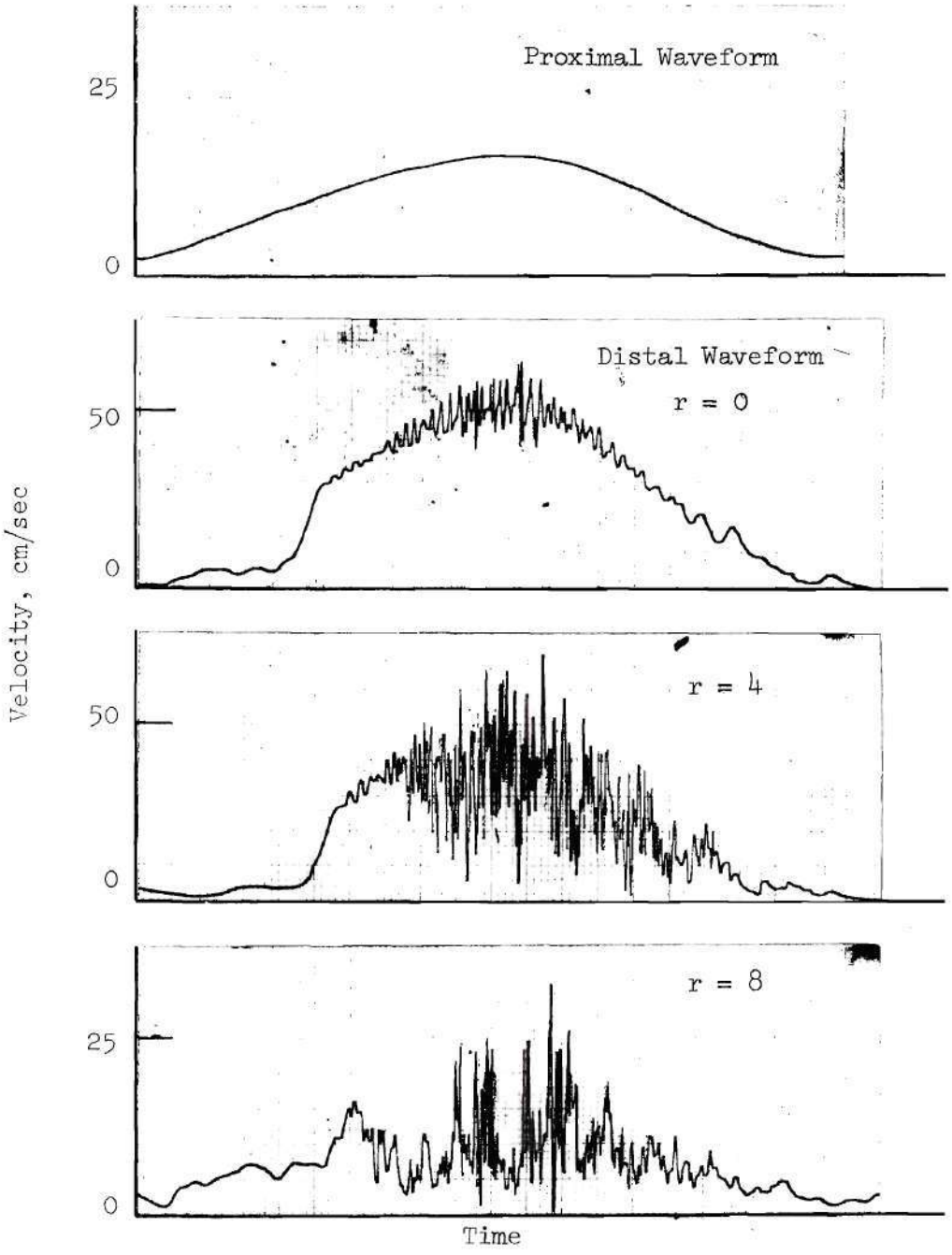

Figure 127. Radial Position Variation of Velocity Waveform for 75% Contoured Occlusion, x/D = 1.5

a high degree of turbulence but the mean velocities are noticeably lower. The low frequency turbulence in the initial segment of the pulse can be attributed to the passing of the starting vortex. The turbulence decays to an insignificant level during the low velocity portion of each pulse at all radial positions.

Figures 128 and 129 indicate the centerline axial variations of the velocity waveform. The waveforms for both occlusions show that the turbulent intensity during the high velocity portion of the pulse increases up to the x/D = 3.125 location, but the x/D = 6.125 position shows a considerable decrease in turbulence level and the turbulent fluctuations are most prevalent during the deceleration phase of the pulse. The turbulence essentially dissipates completely at all axial positions during the low velocity part of the pulse.

7.2 Velocity Waveforms for 50 Percent Occlusions

The radial variations of the velocity waveforms are shown in Figure 130 for the sharp occlusion and in Figure 131 for the contoured occlusion. The sharp occlusion waveforms at this axial location show essentially the same qualitative trends as did the 75 percent sharp waveforms. However, the passage of the intense low frequency vortex is more pronounced near the wall (r = 8 and 12 mm) than the 75 percent occlusion waveforms indicated. The contoured occlusion waveforms at the various radial positions indicate significant turbulence only during the deceleration phase of the pulse. At r = 12 mm, the passage of the low frequency vortex can be easily seen in the waveform. However, only a small degree of higher frequency turbulence is seen after the vortex

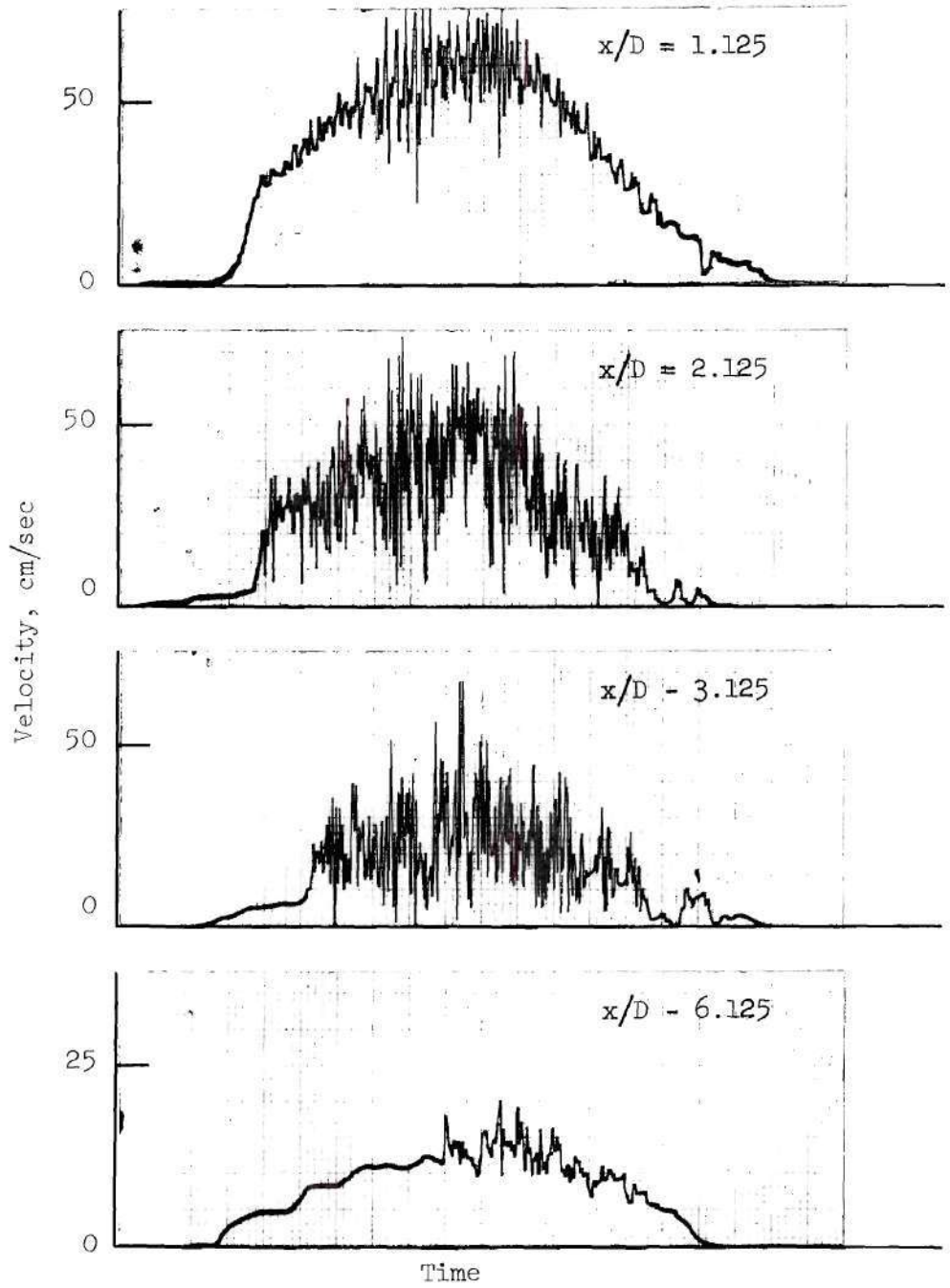

Figure 128. Axial Position Variation of Velocity Waveform for 75% Sharp Occlusion, r = 0

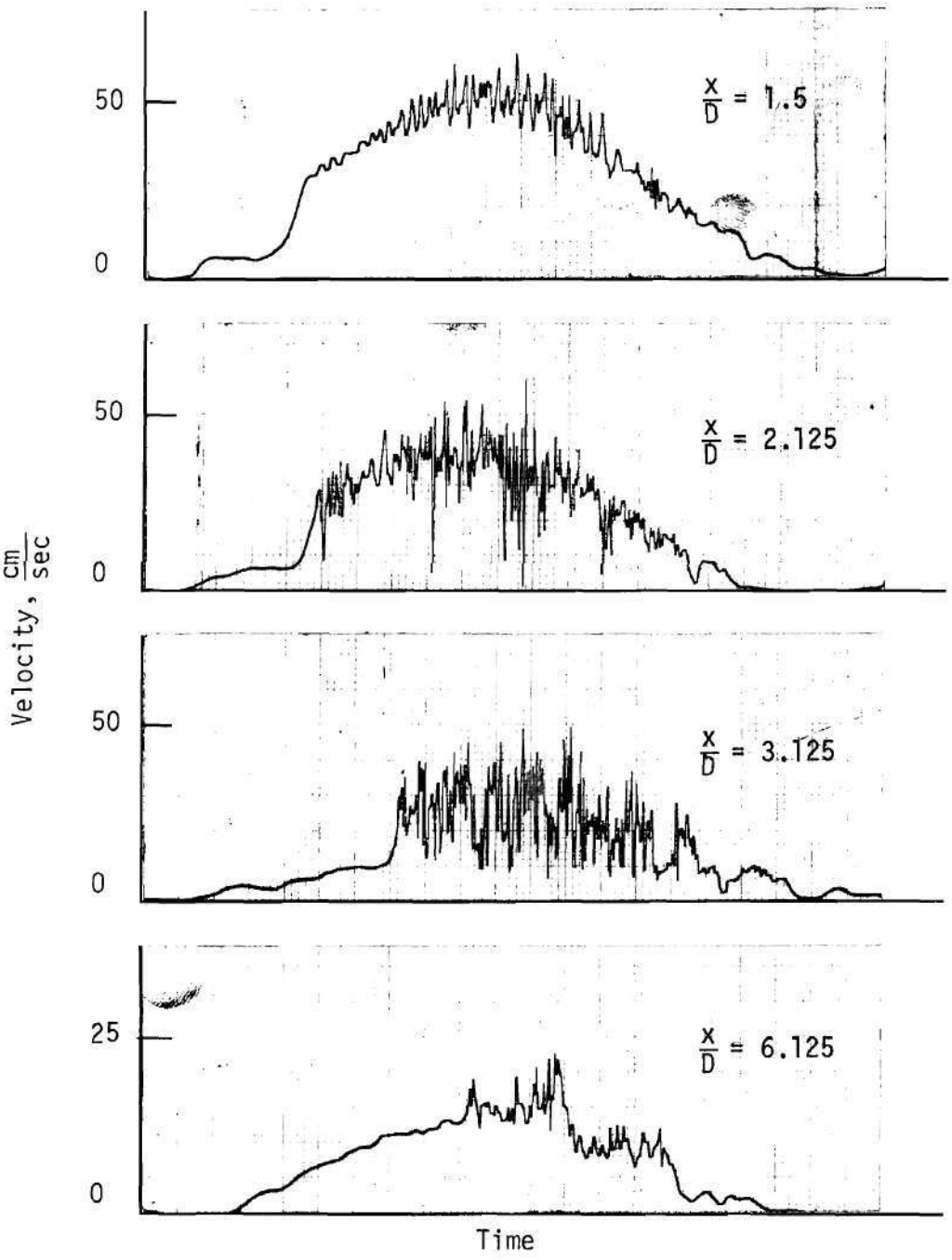

Figure 129. Axial Position Variation of Velocity Waveform for 75% Contoured Occlusion, r = 0.

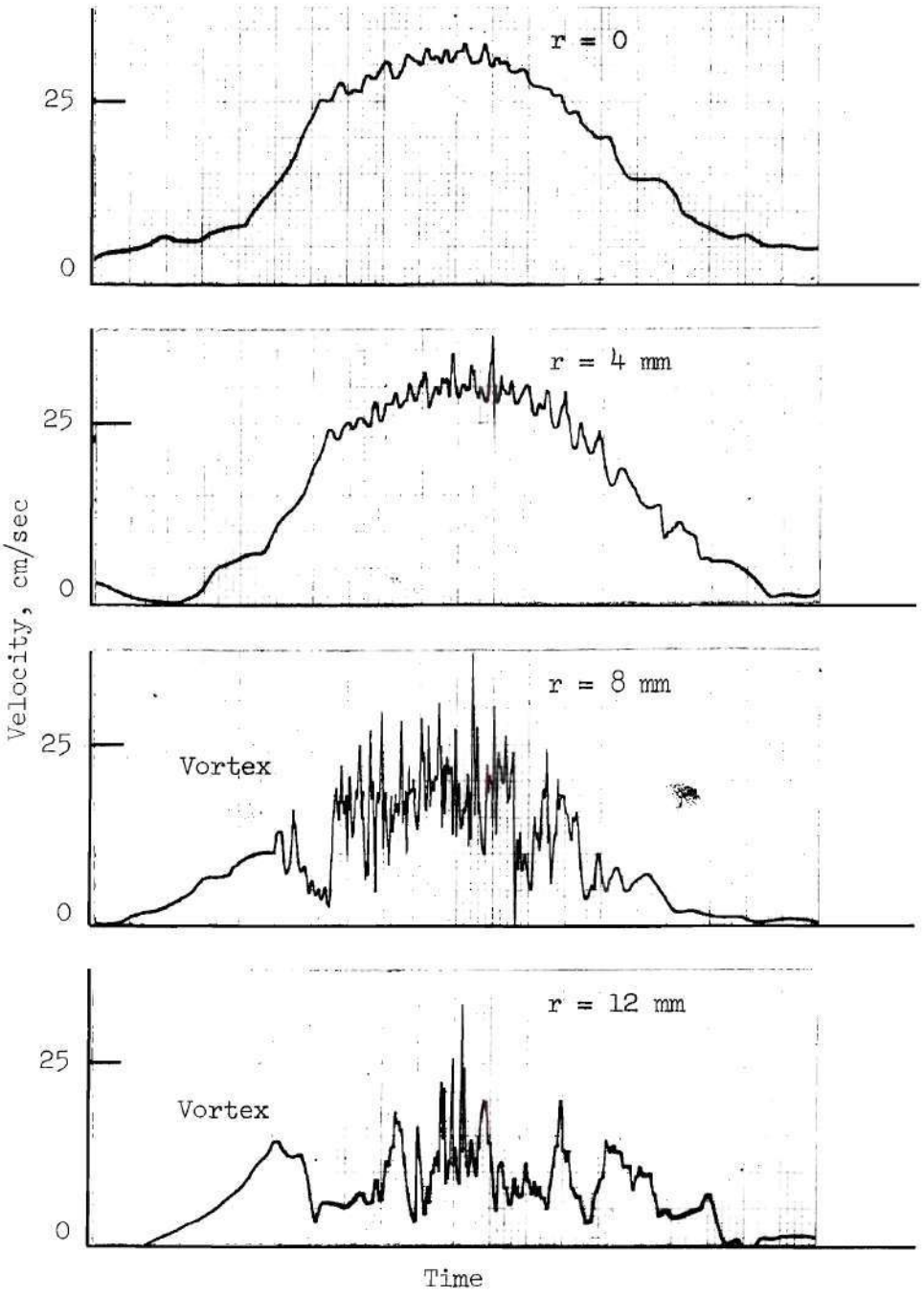

Figure 130. Radial Position Variation of Velocity Waveform for 50% Sharp Occlusion, x/D - 1.125

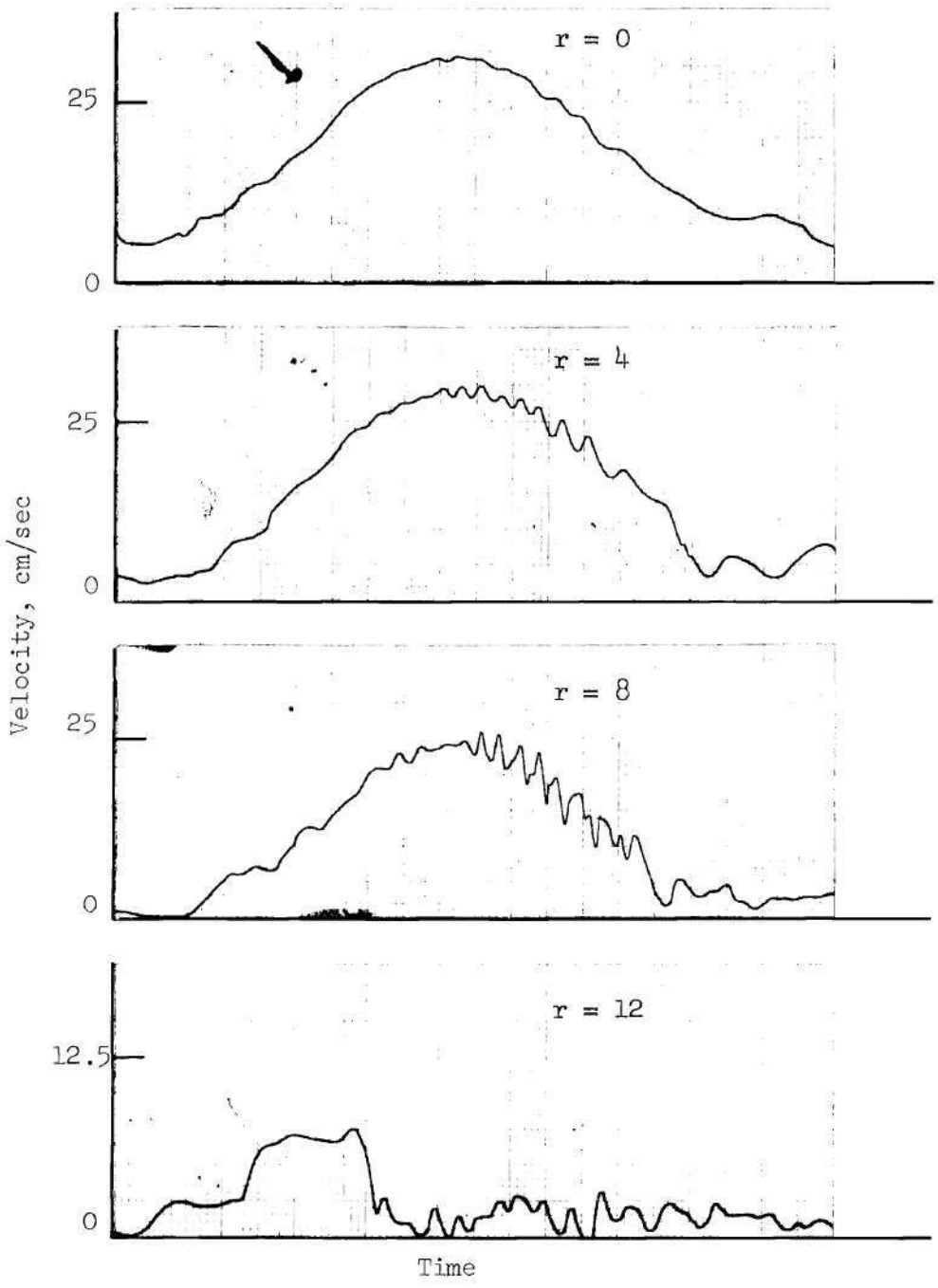

Figure 131. Radial Position Variation of Velocity Waveform for 50% Contoured Occlusion, x/D = 1.5

passes which is in contrast to the sharp occlusion results near the wall.

The centerline axial variations of the velocity waverforms are shown in Figures 132 and 133. The waveforms indicate that the turbulence dissipates between successive pulses at all axial locations for both occlusion shapes. The most outstanding difference for the different occlusions is that the contoured occlusion waveform shows significant velocity flucuations during the deceleration phase of the pulse.

7.3 Velocity Waveforms for the 25 Percent Occlusions

The waveforms for the 25 percent occlusions are especially interesting since the steady flow through the occlusions did not produce any significant turbulence. In pulsatile flow, however, low frequency instabilities are indicated on the waveforms at all axial positions. The radial variations of the waveforms are seen in Figures 134 and 135 for the two occlusion geometries. At first glance, it appears that the instabilities are occurring during the lowest velocity portion of the pulse. However, this is only partially true. The movies of the pulsatile flow cases have shown that flow instabilities are triggered during the deceleration phase. These instabilities then propagate toward the centerline during the lower velocity portion of the acceleration phase and can be seen at some axial and radial positions as velocity fluctuations during the acceleration phase. These can be observed for the various axial positions shown in Figures 136 and 137. The velocity fluctuations are somewhat more intense for the sharp-edged occlusion than for the contoured occlusion.

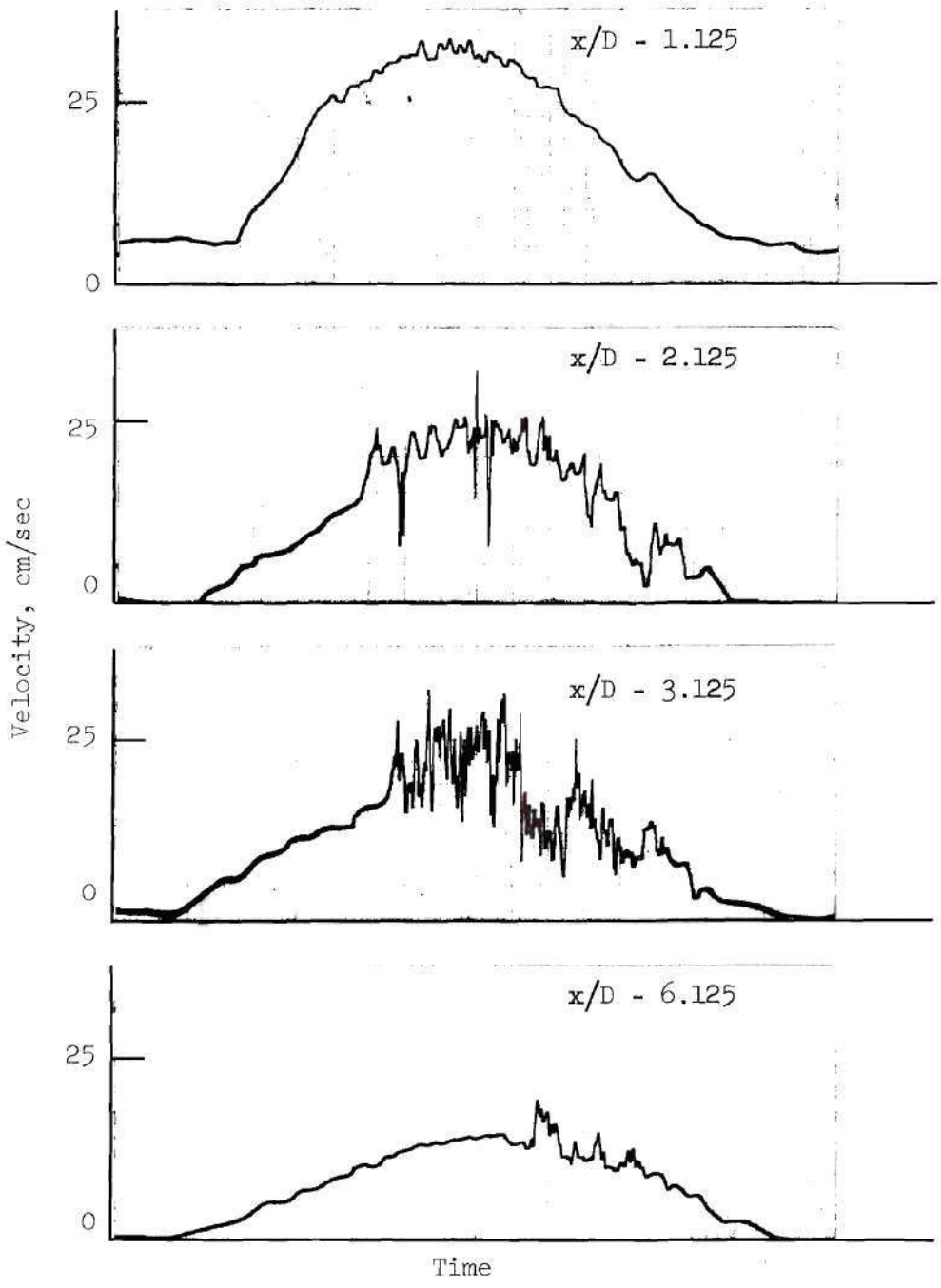

Figure 132. Axial Position Variation of Velocity Waveform for 50% Sharp Occlusion, r = 0

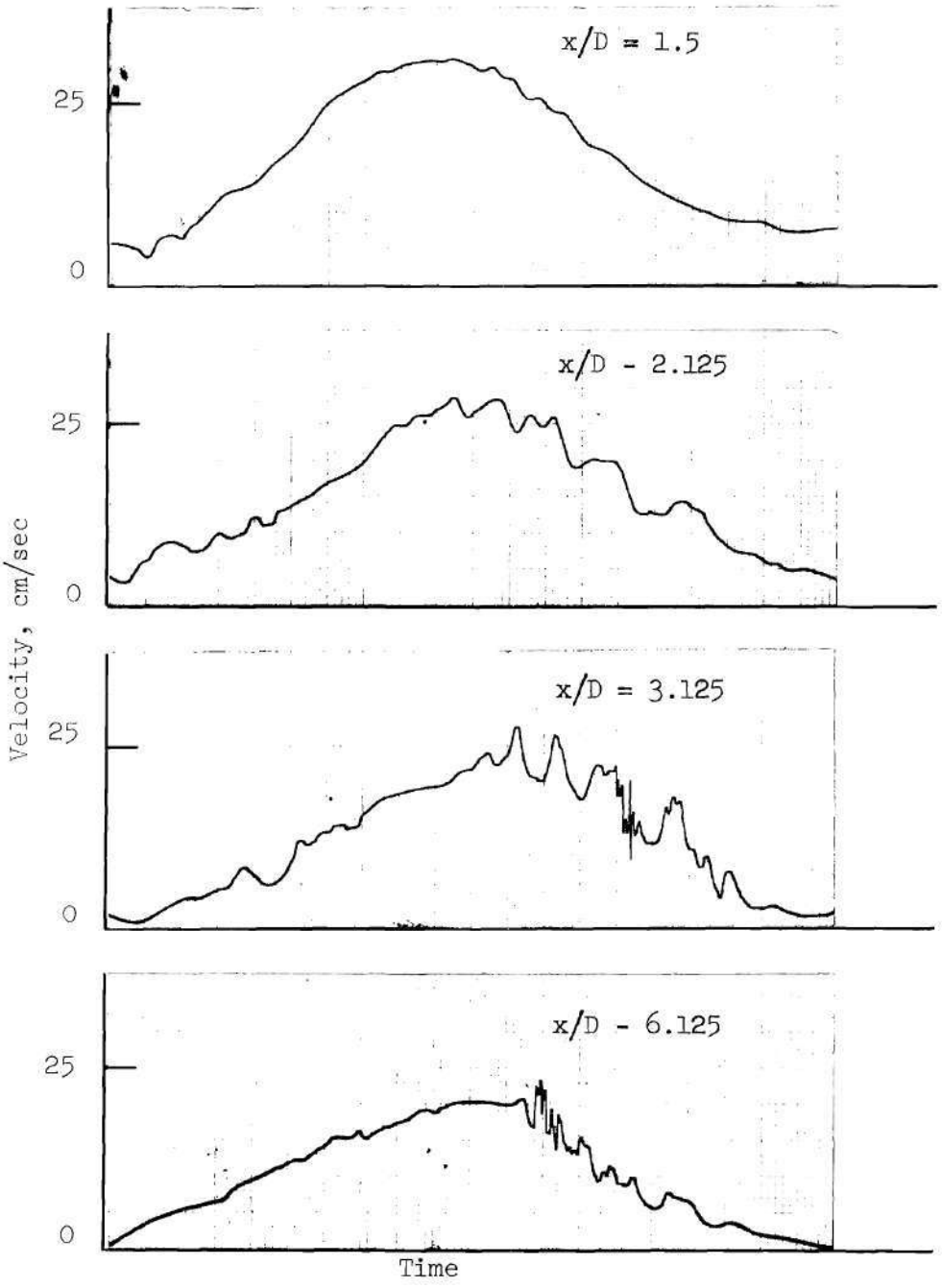

Figure 133. Axial Position Variation of Velocity Waveform for 50% Contoured Occlusion, r = 0

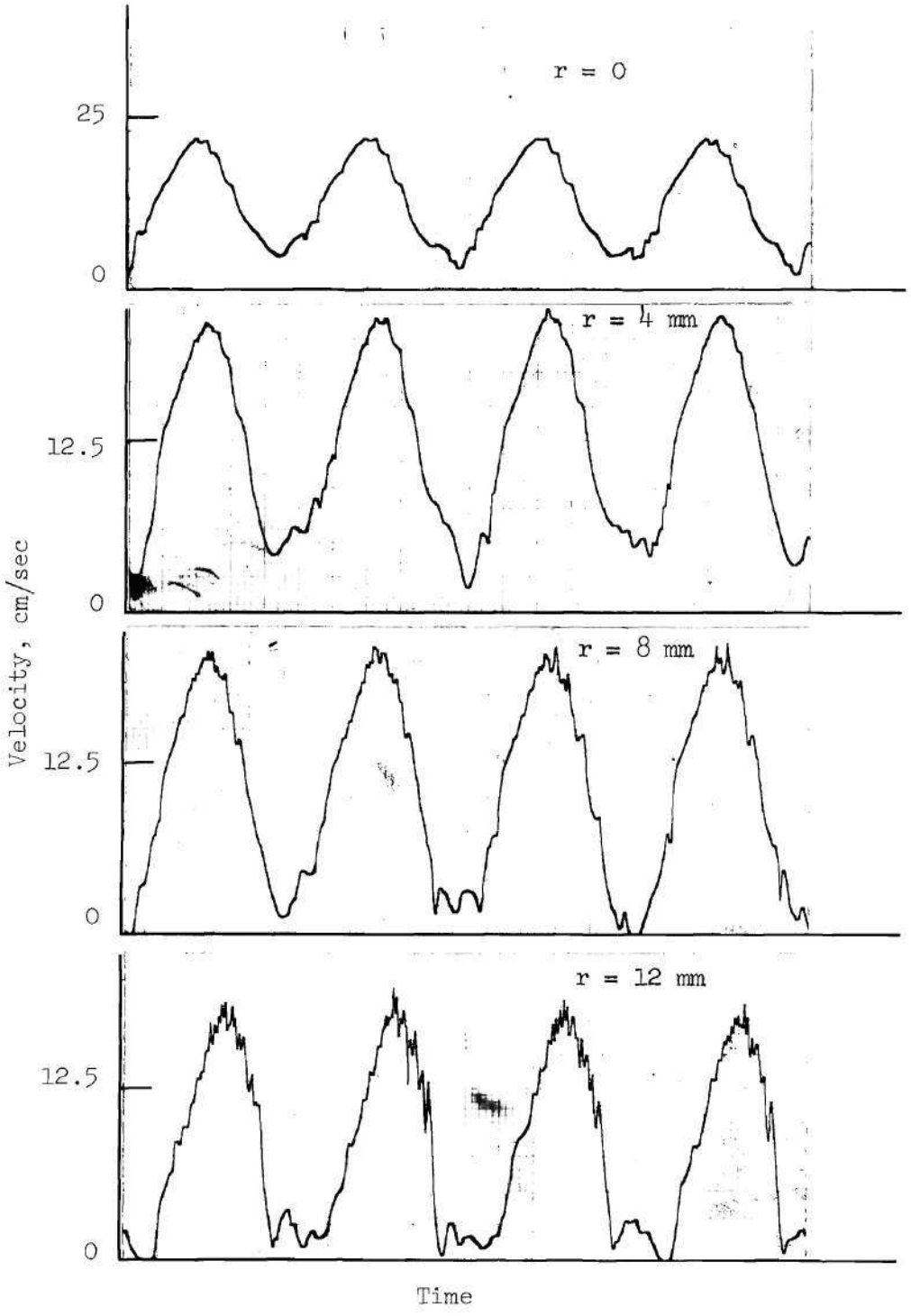

Figure 134. Radial Position Variation of Velocity Waveform for 25 % Sharp Occlusion, x/D = 1.125

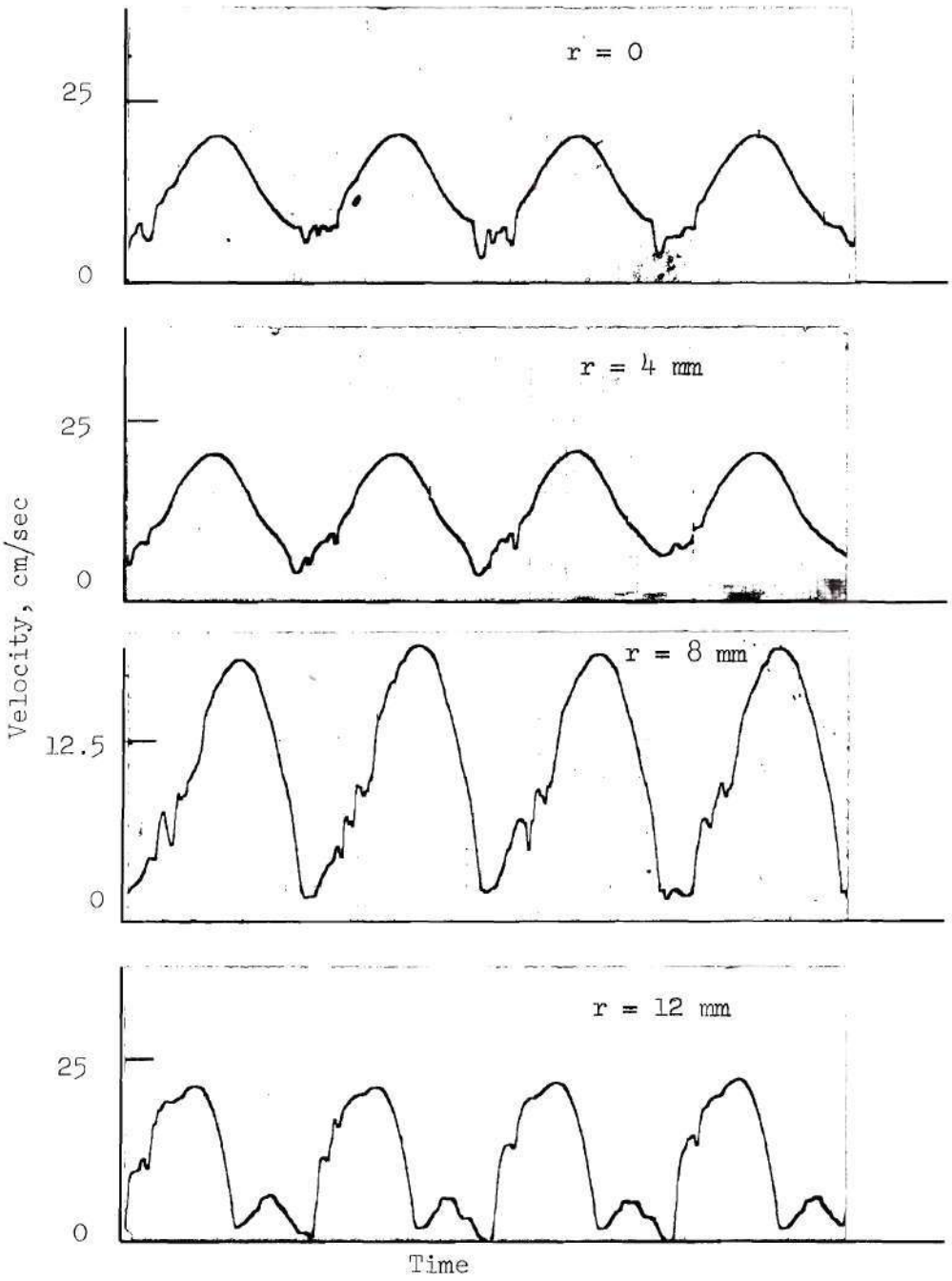

Figure 135. Radial Position Variation of Velocity Waveform for 25% Contoured Occlusion, x/D = 1.5

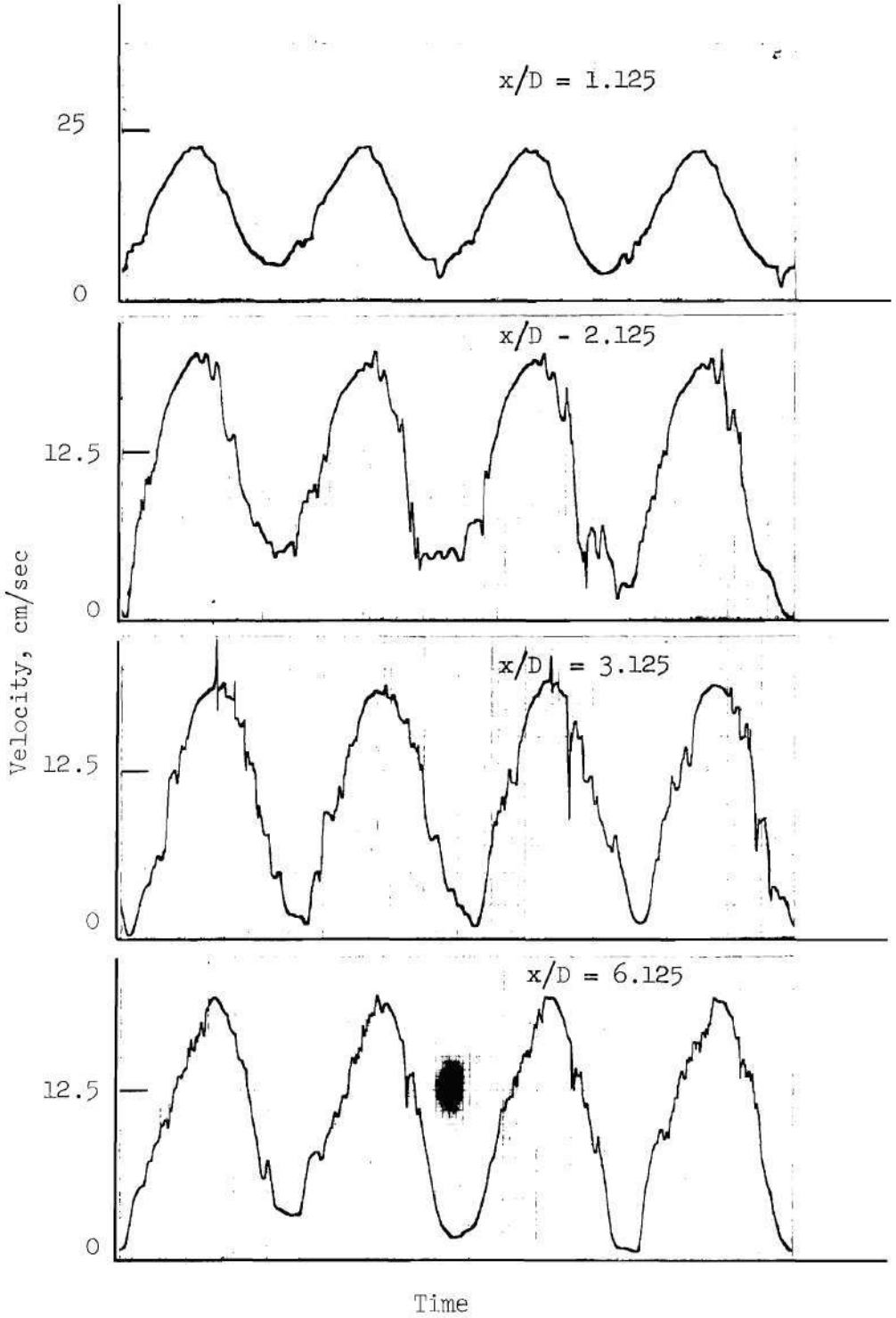

Figure 136. Axial Position Variation of Velocity Waveform for 25 % Sharp Occlusion, r = 0

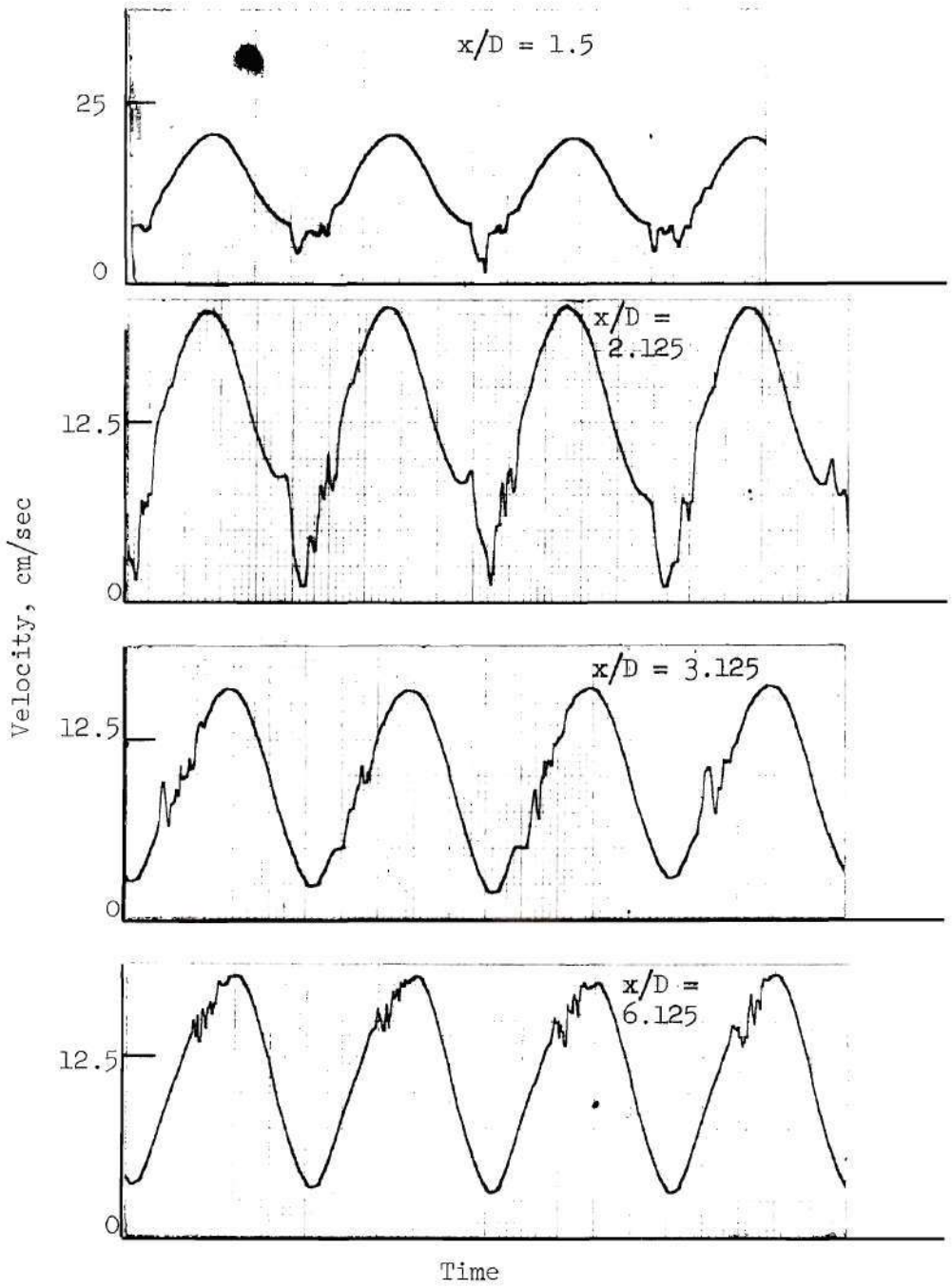

Figure 137. Axial Position Variation of Velocity Waveform for 25% Contoured Occlusion, r = 0

CHAPTER VIII

PULSATILE FLOW ENERGY SPECTRA RESULTS AND DISCUSSION, $\alpha = 15$, $R_{e_{pD}} = 2540$

This chapter presents the energy spectral distributions for pulsatile flow through the occlusions in a manner which is similar to presentation in Chapter VII for the steady flow results. It should be recalled that the spectral distributions were obtained by analyzing the entire waveform.

8.1 Energy Spectral Distributions for the 25 Percent Occlusions

The energy spectral distributions are summarized in Figures 138 through 142 for the 25 percent sharp occlusions and in Figures 143 through 146 for the 25 percent contoured occlusions. The energy levels for all axial and radial positions are considerably above those obtained with no occlusion present. The spectra for the sharp-edged occlusion at $x/D = 3.125$ (Figure 141) have a somewhat higher intensity than the other axial locations. The spectra obtained in the near wall radial location ($r = 12$ mm) show a slightly higher overall energy intensity than those obtained closer to the centerline at all axial positions with the sharp-edged occlusion. However, the near-wall locations with the contoured occlusion show a slight decrease in energy at the higher frequencies over the more centrally located spectra.

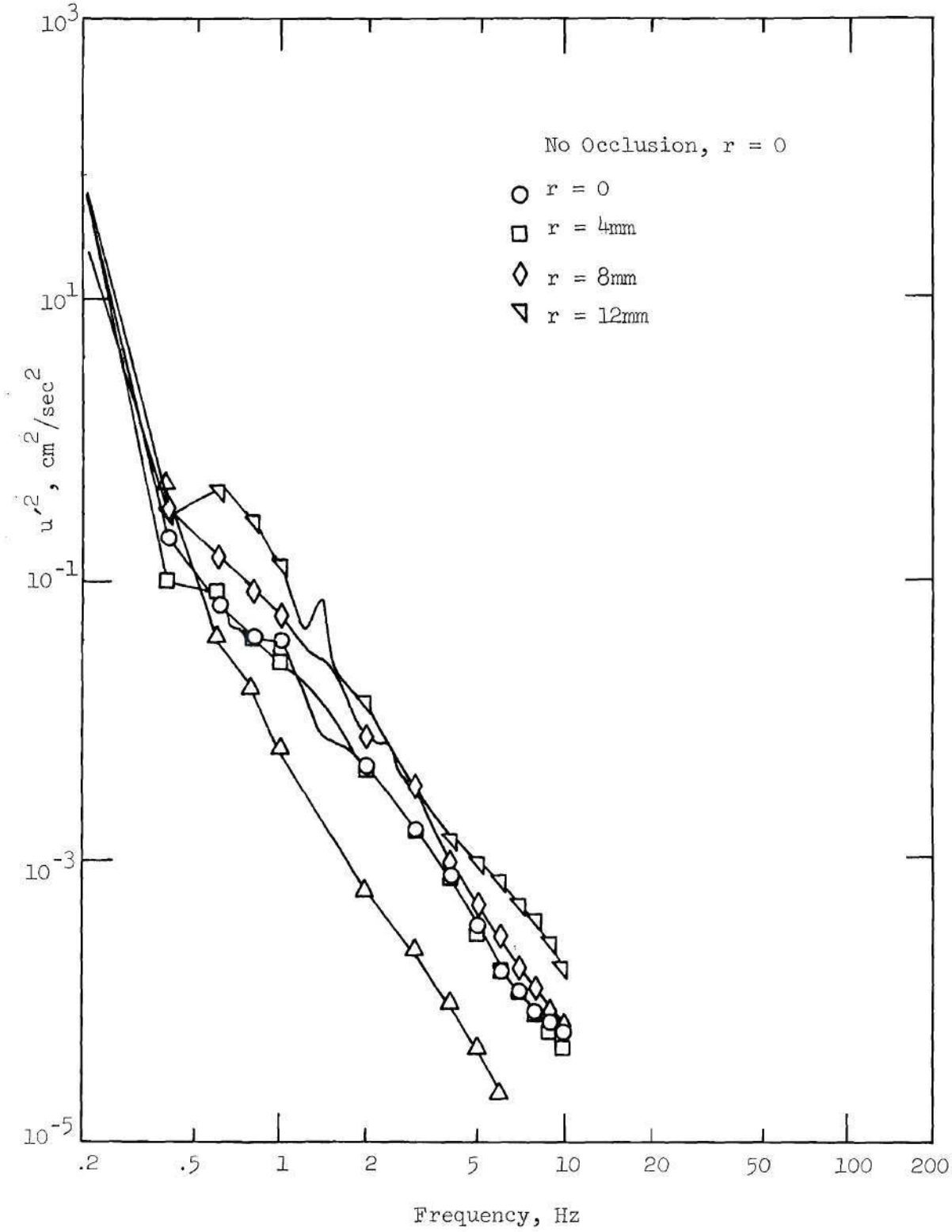

Figure 138. Energy Spectra for 25% Sharp-Edged Occlusion, $x/D = 0.5$, $\alpha = 15$, $R_{e_{DP}} = 2540$, F = 0.2 Hz.

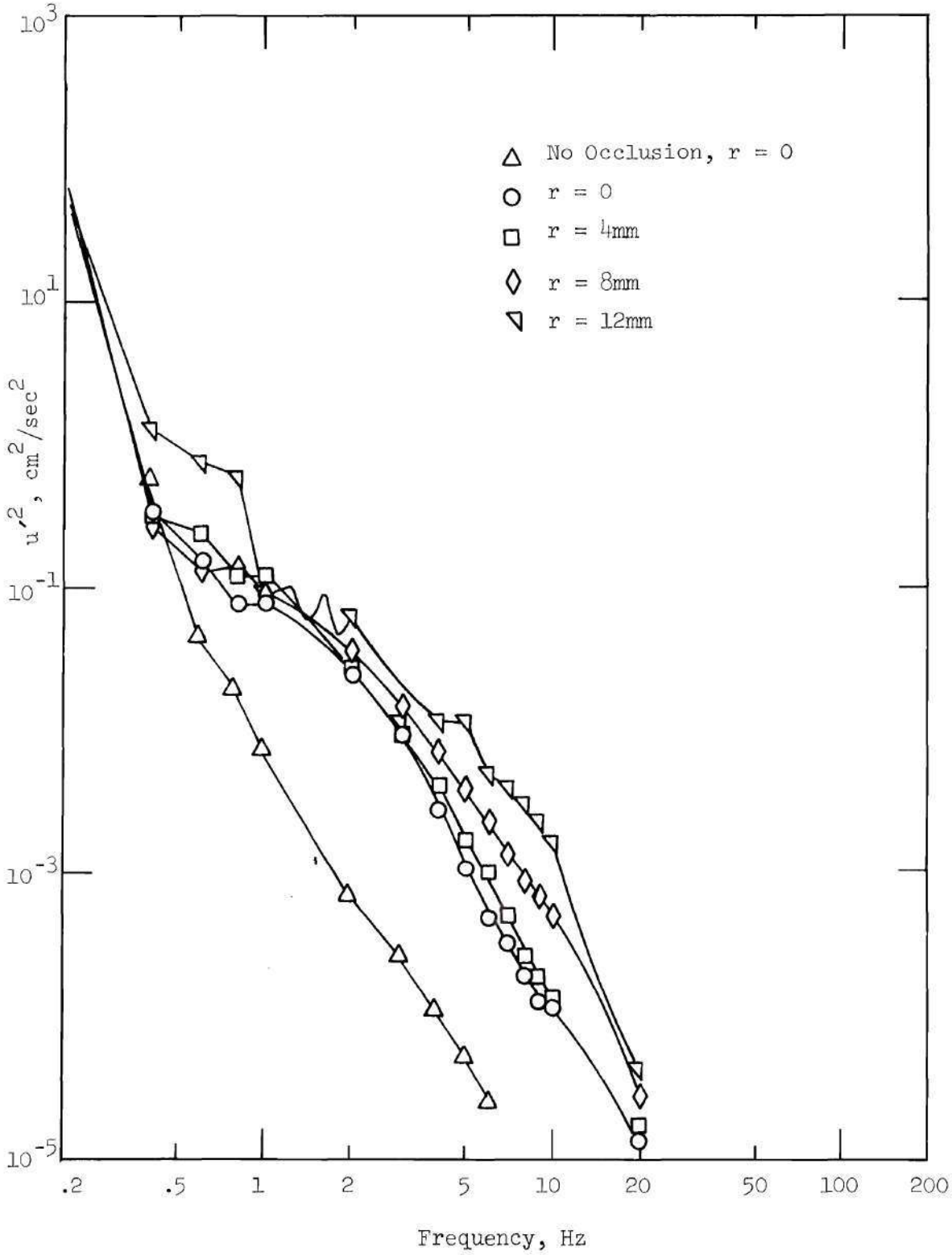

Figure 139. Energy Spectra for 25% Sharp-Edged Occlusion, x/D = 1.125, α = 15, $R_{e_{DP}}$ = 2540, F = 0.2 Hz.

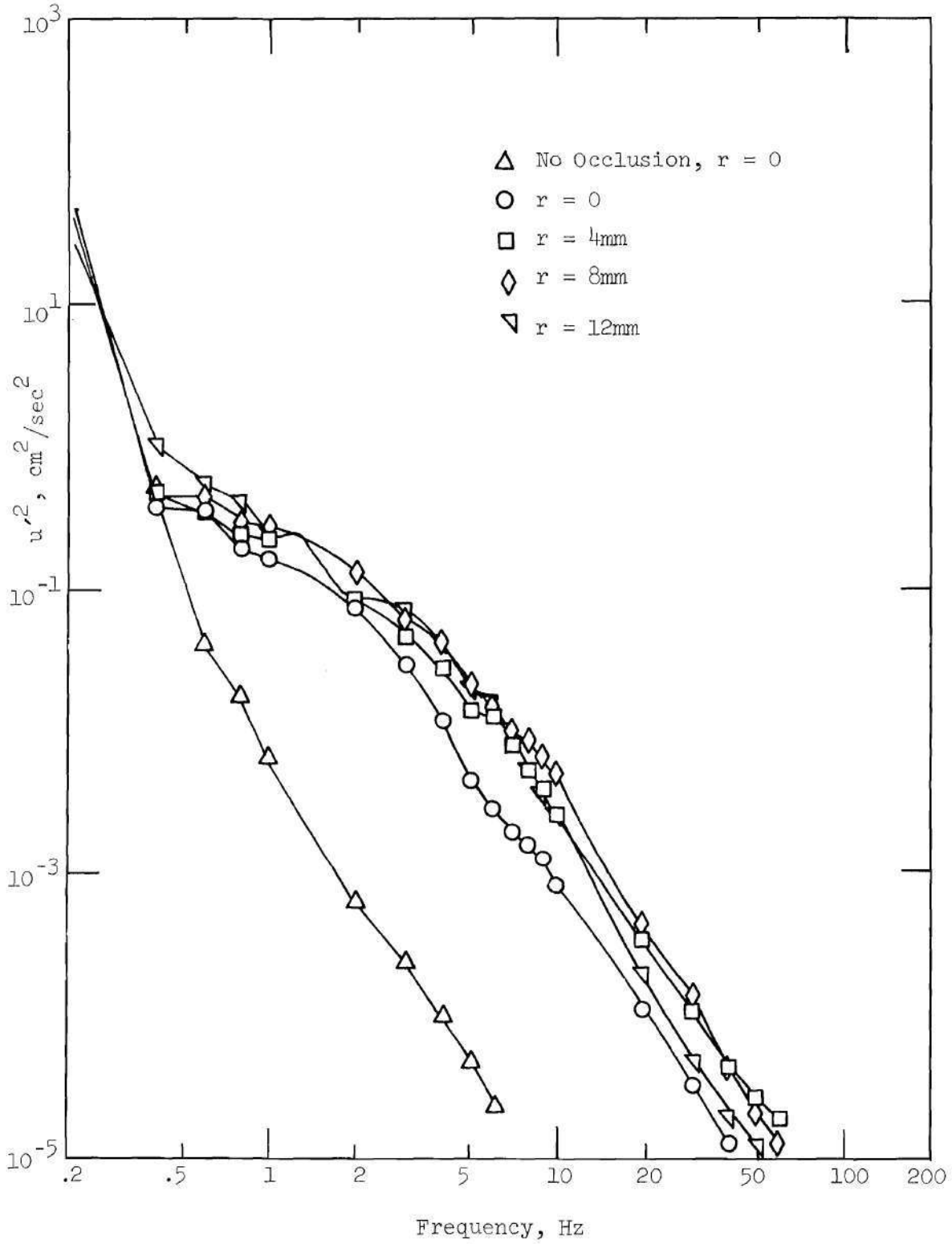

Figure 140. Energy Spectra for 25% Sharp-Edged Occlusion, x/D = 2.125, α = 15, $R_{e_{DP}}$ = 2540, F = 0.2 Hz.

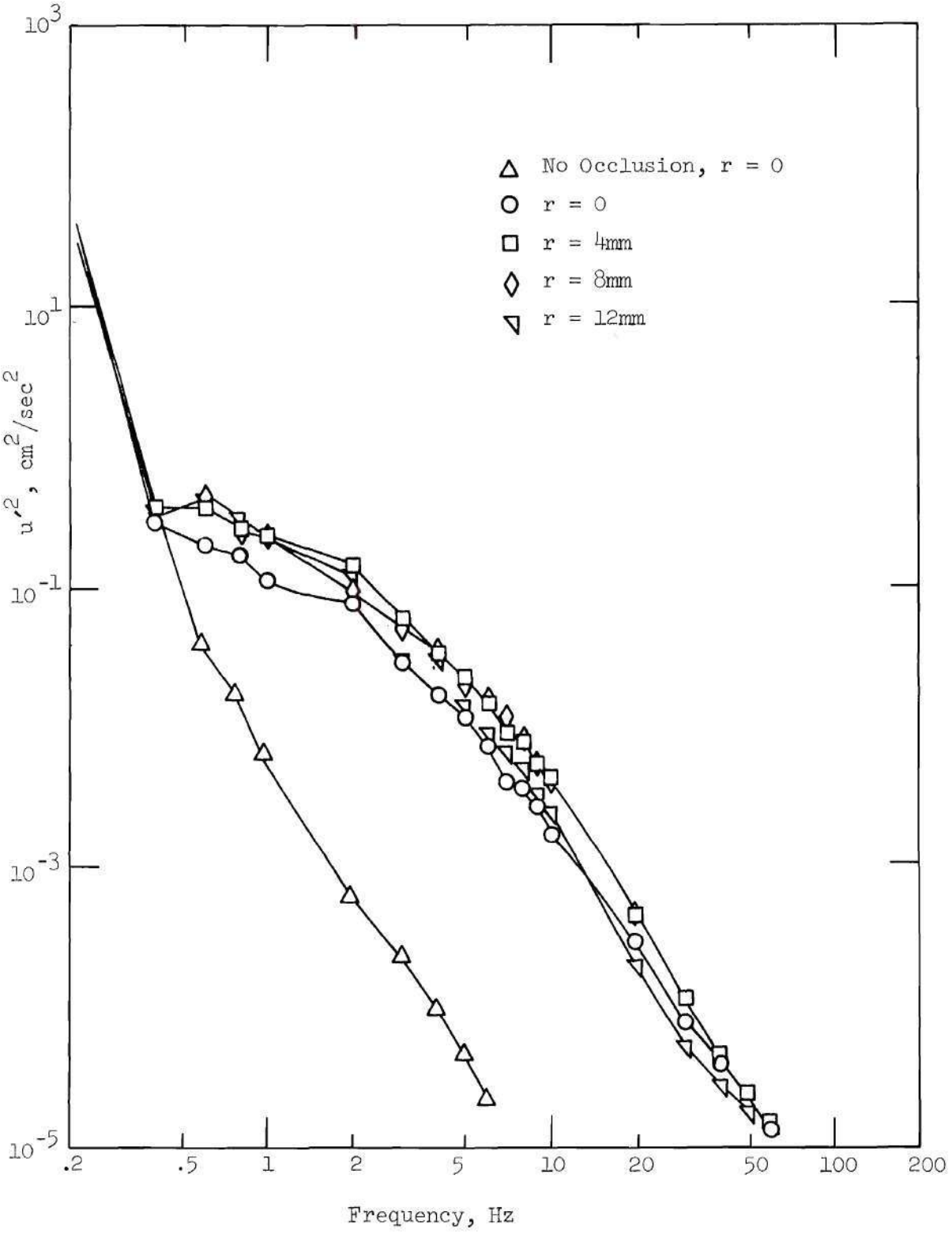

Figure 141. Energy Spectra for 25% Sharp-Edged Occlusion, $x/D = 3.125$, $\alpha = 15$, $R_{e_{DP}} = 2540$, $F = 0.2$ Hz.

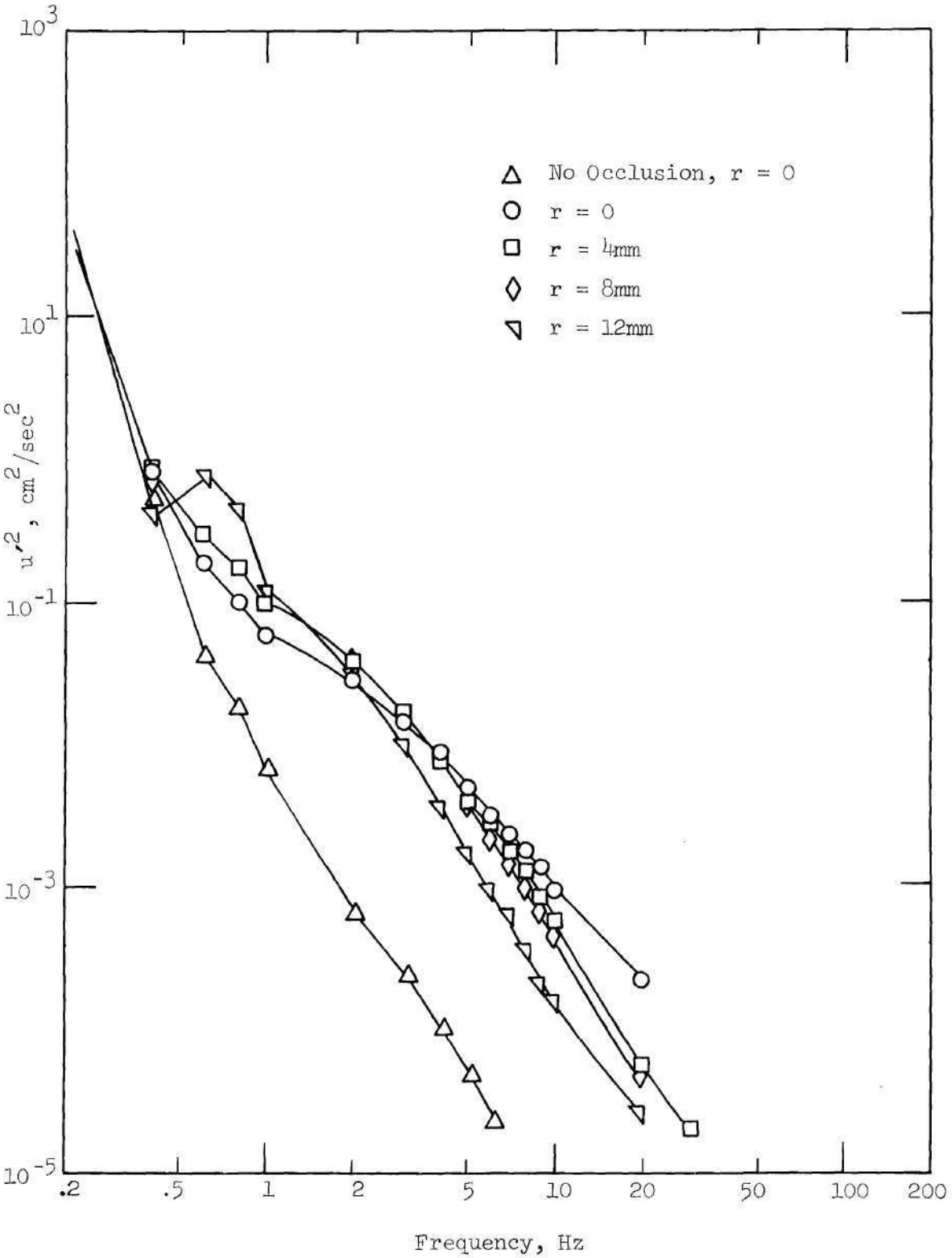

Figure 142. Energy Spectra for 25% Sharp-Edged Occlusion, x/D = 6.125, α = 15, R_{e_D} = 2540, F = 0.2 Hz

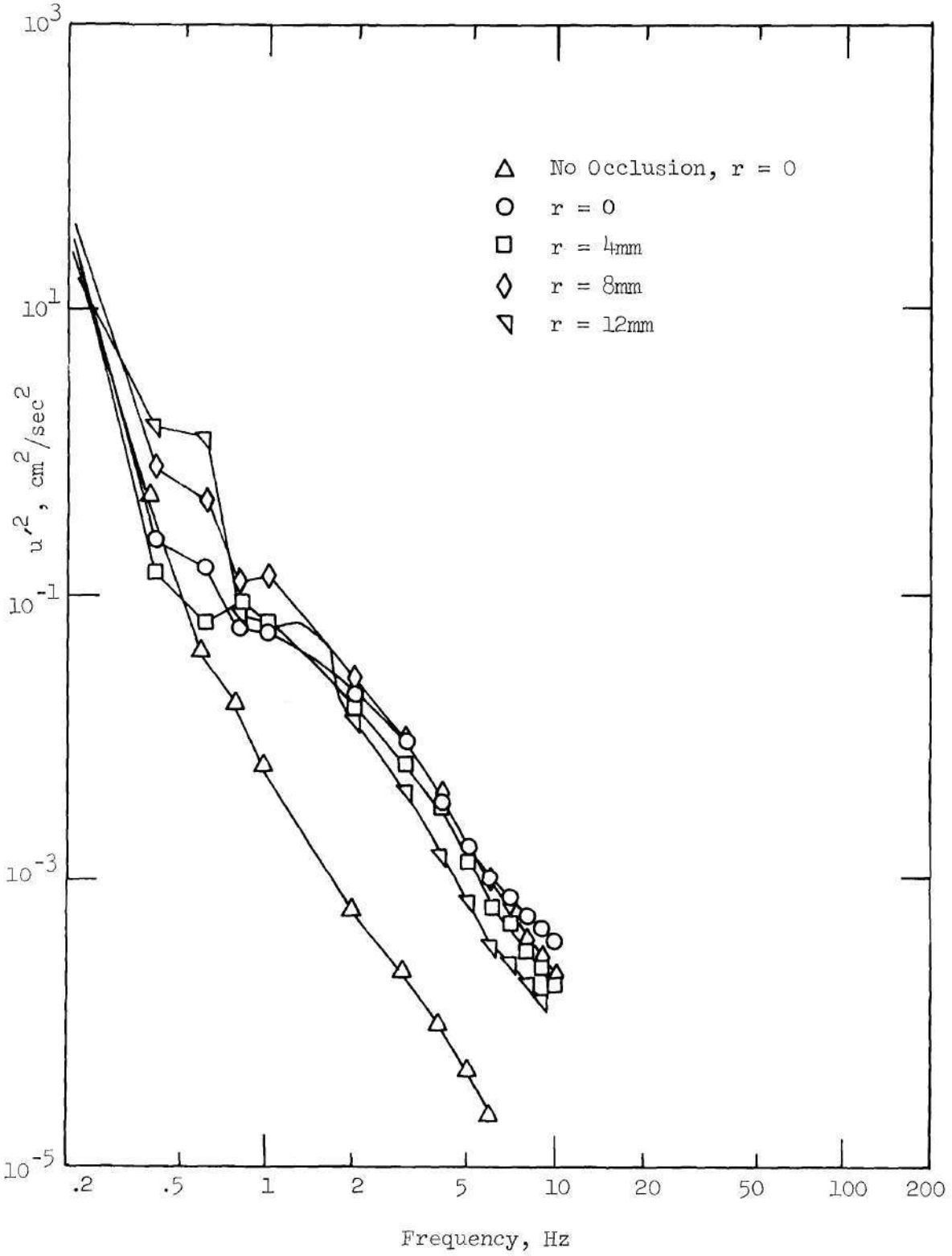

Figure 143. Energy Spectra for 25% Contoured Occlusion, x/D = 1.5, α = 15, $R_{e_{DP}}$ = 2540, F = 0.2 Hz.

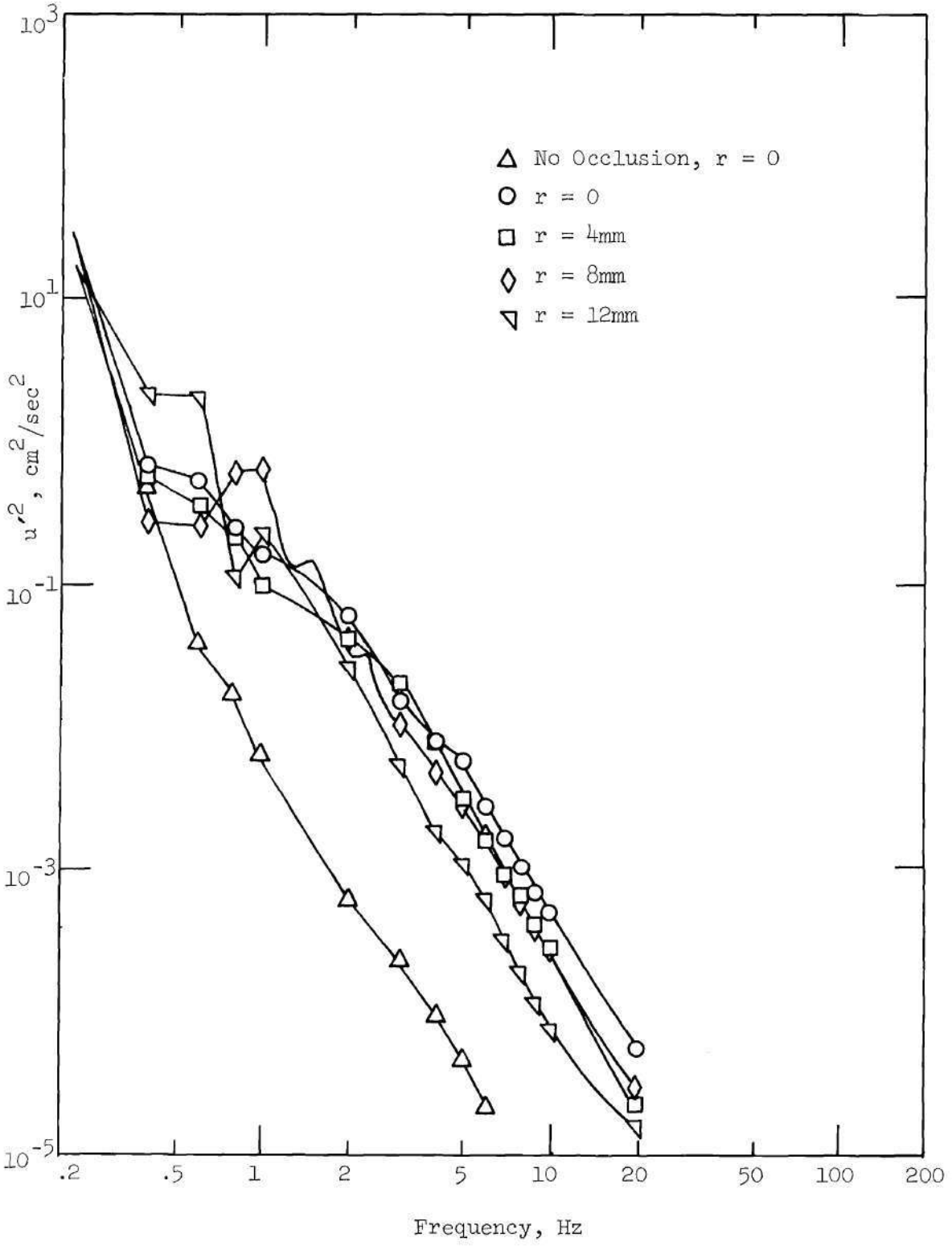

Figure 144. Energy Spectra for 25% Contoured Occlusion, x/D = 2.125, α = 15, $R_{e_{DP}}$ = 2540, F = 0.2 Hz.

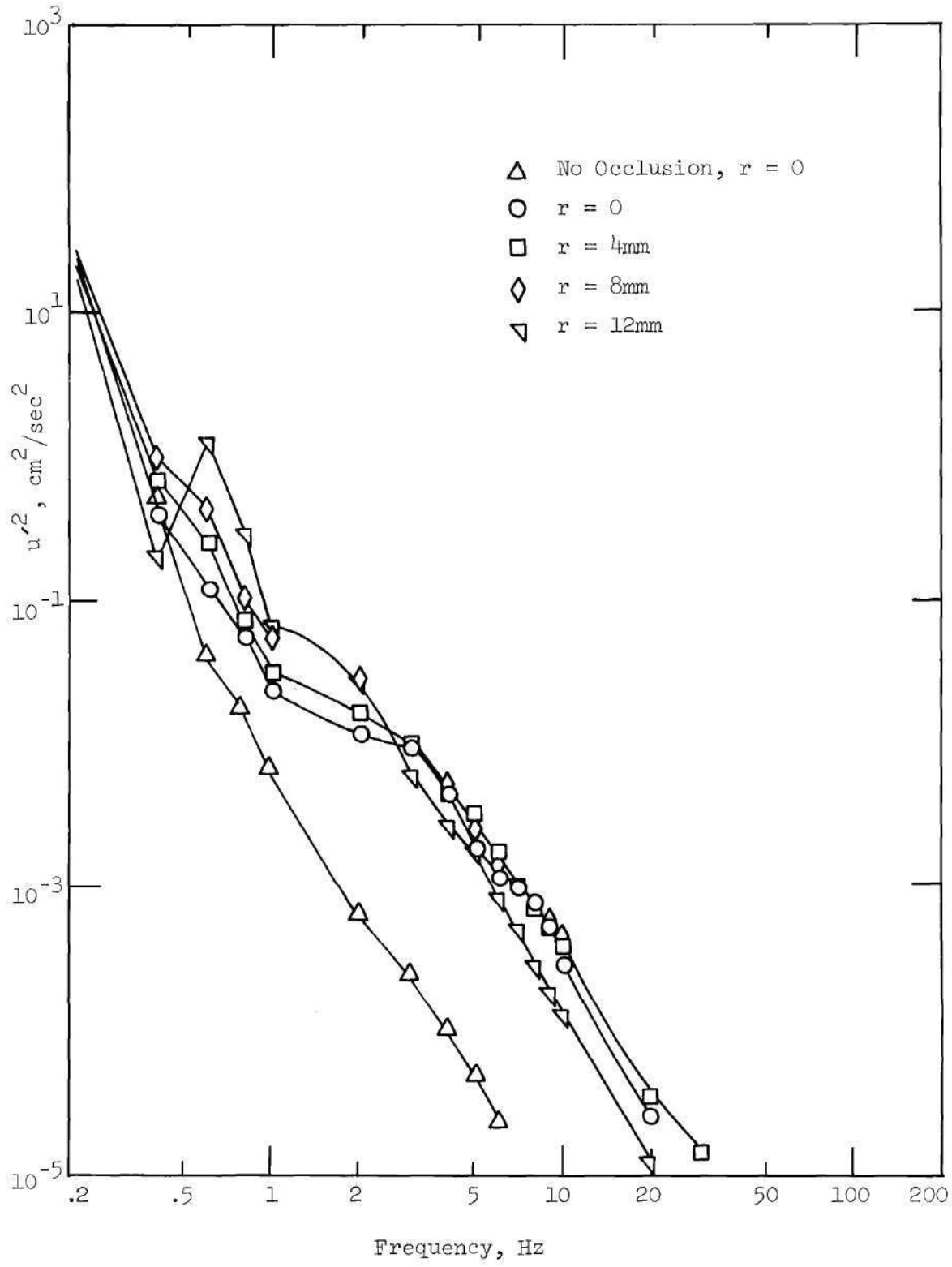

Figure 145. Energy Spectra for 25% Contoured Occlusion, $x/D = 3.125$, $\alpha = 15$, $R_{e_{DP}} = 2540$, $F = 0.2$ Hz.

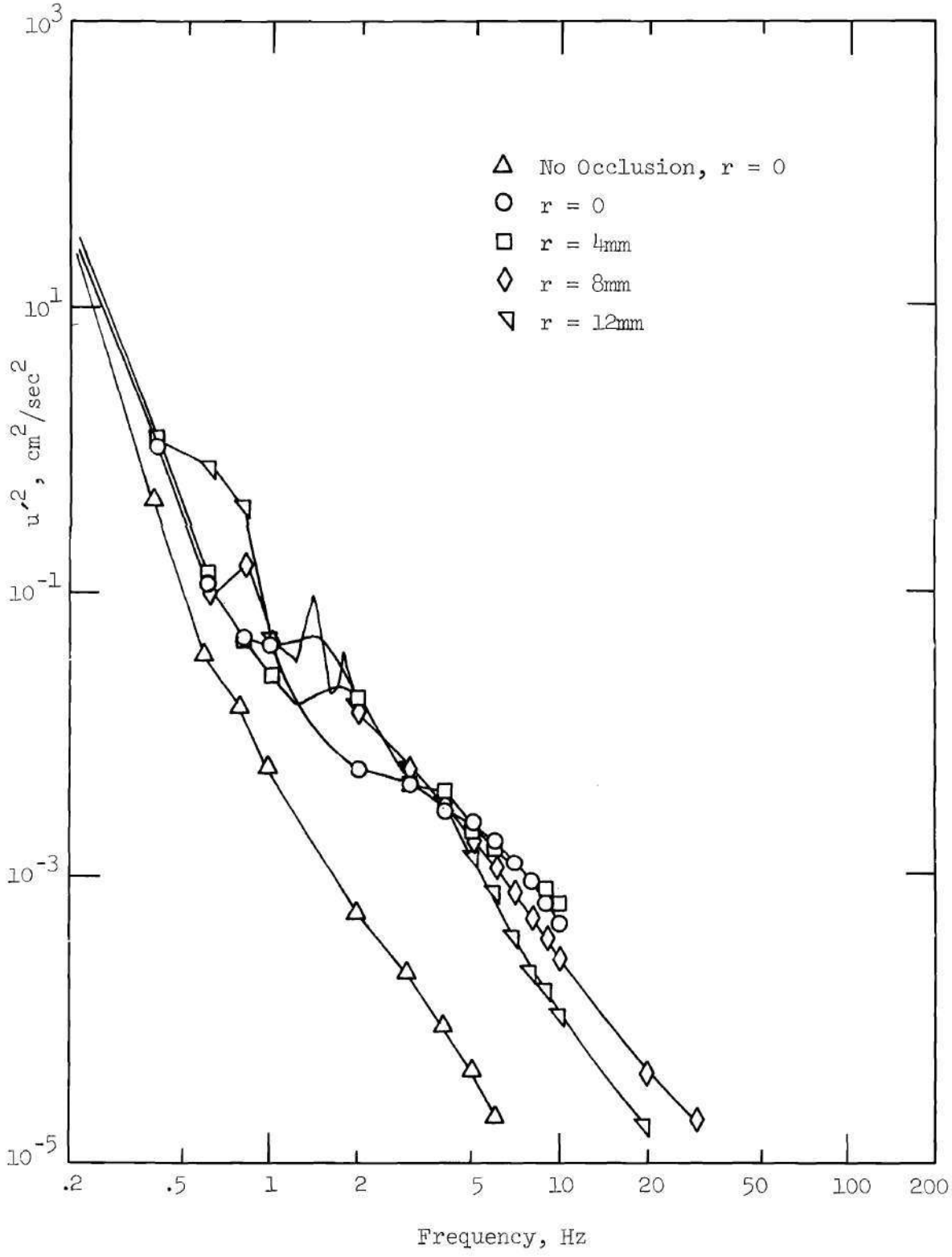

Fibure 146. Energy Spectra for 25% Contoured Occlusion, $x/D = 6.125$, $\alpha = 15$, $R_{e_{DP}} = 2540$, F = 0.2 Hz.

8.2 Energy Spectral Distributions for the 50 Percent Occlusions

The energy spectra for the 50 percent occlusions are shown in Figures 147 through 151 for the sharp-edged occlusions and in Figures 152 through 155 for the contoured occlusions. The spectra obtained at $x/D = 0.5$ with the sharp-edged occlusion show two distinct peaks at $4 = 8$mm and somewhat less intense peaks at $r = 4$ mm. Farther downstream at $x = 1.125$, the $r = 8$ mm energy levels are still more intense overall than the other radial positions. However, at $x/D = 3.125$ and 6.125 the energy levels are more nearly uniform for the entire cross-section.

The contoured occlusion spectra at $x/D = 1.5$ do not indicate any distinct peaks at the $r = 8$ mm position but the spectra do show a slight maximum at about 6 Hz. The energy level of the $r = 8$ mm spectra remains noticeably higher than the spectra at other radial positions until the $x/D = 3.125$ location where all radial positions yield about the same overall energy level. This uniform energy level is still in evidence at $x/D = 6.125$.

8.3 Energy Spectral Distributions for the 75 Percent Occlusions

The spectral distributions obtained downstream of the 75 percent occlusions indicate velocity fluctuation characteristics which are considerably different from those obtained with the lesser degrees of occlusion. The energy spectra obtained with the 75 percent sharp occlusion are shown in Figures 156 through 160. The near distal locations, $x/D = 0.5$ and 1.125 (Figures 156 and 157) produced spectra

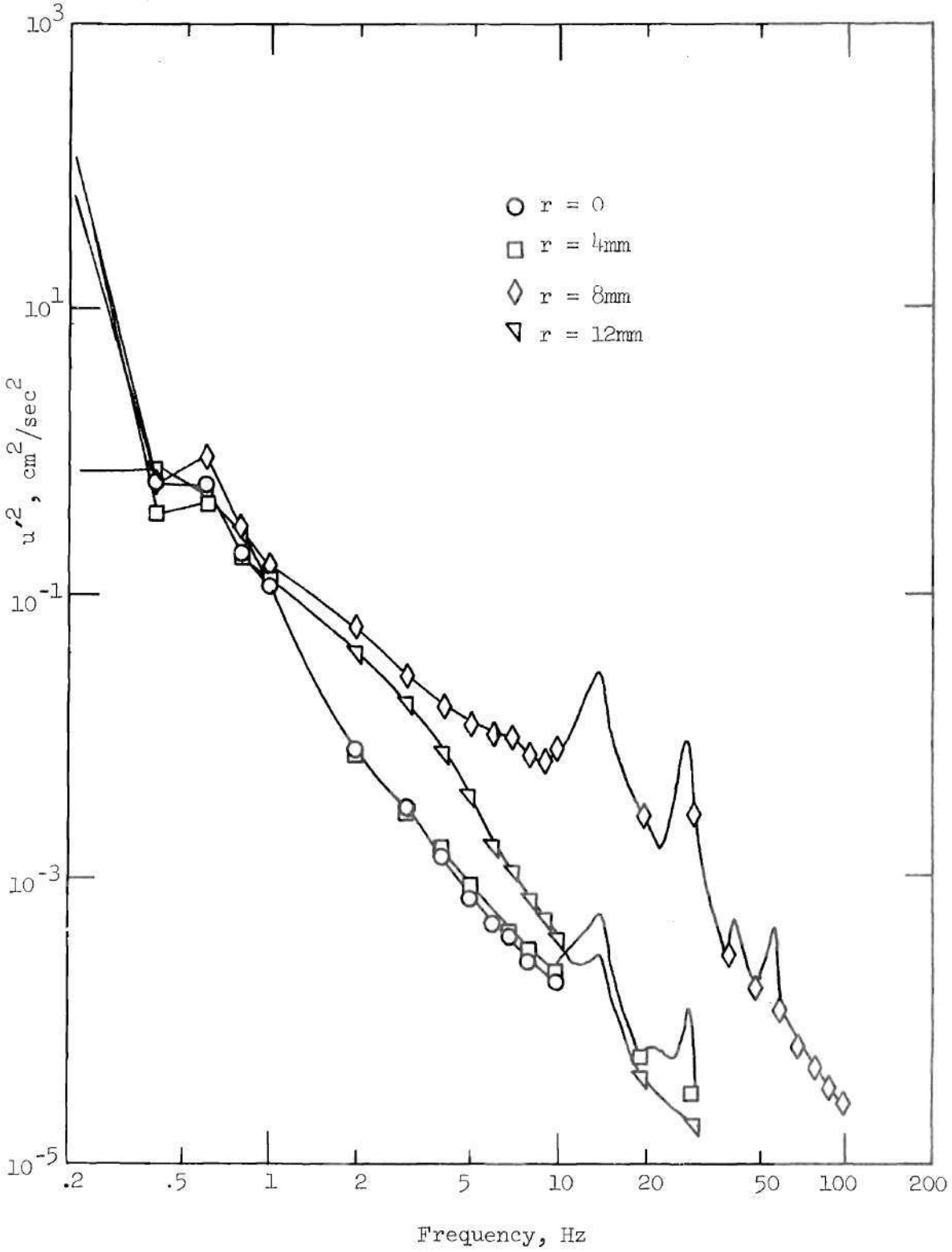

Figure 147. Energy Spectra for 50% Sharp-Edged Occlusion, x/D = 0.5, α = 15, $R_{e_{DP}}$ = 2540, F = 0.2 Hz.

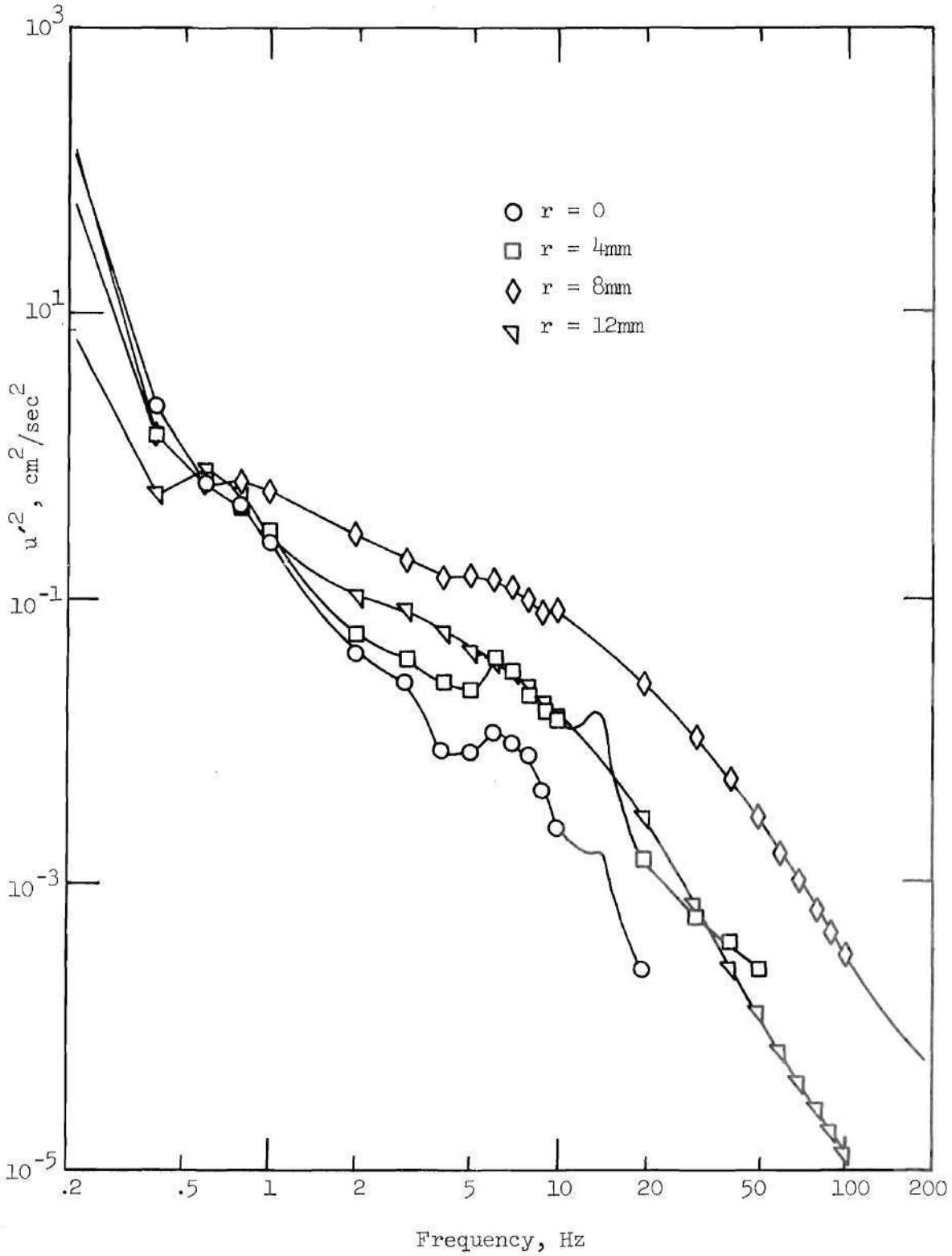

Figure 148. Energy Spectra for 50% Sharp-Edged Occlusion, $x/D = 1.125$, $\alpha = 15$, $R_{e_{DP}} = 2540$, $F = 0.2$ Hz.

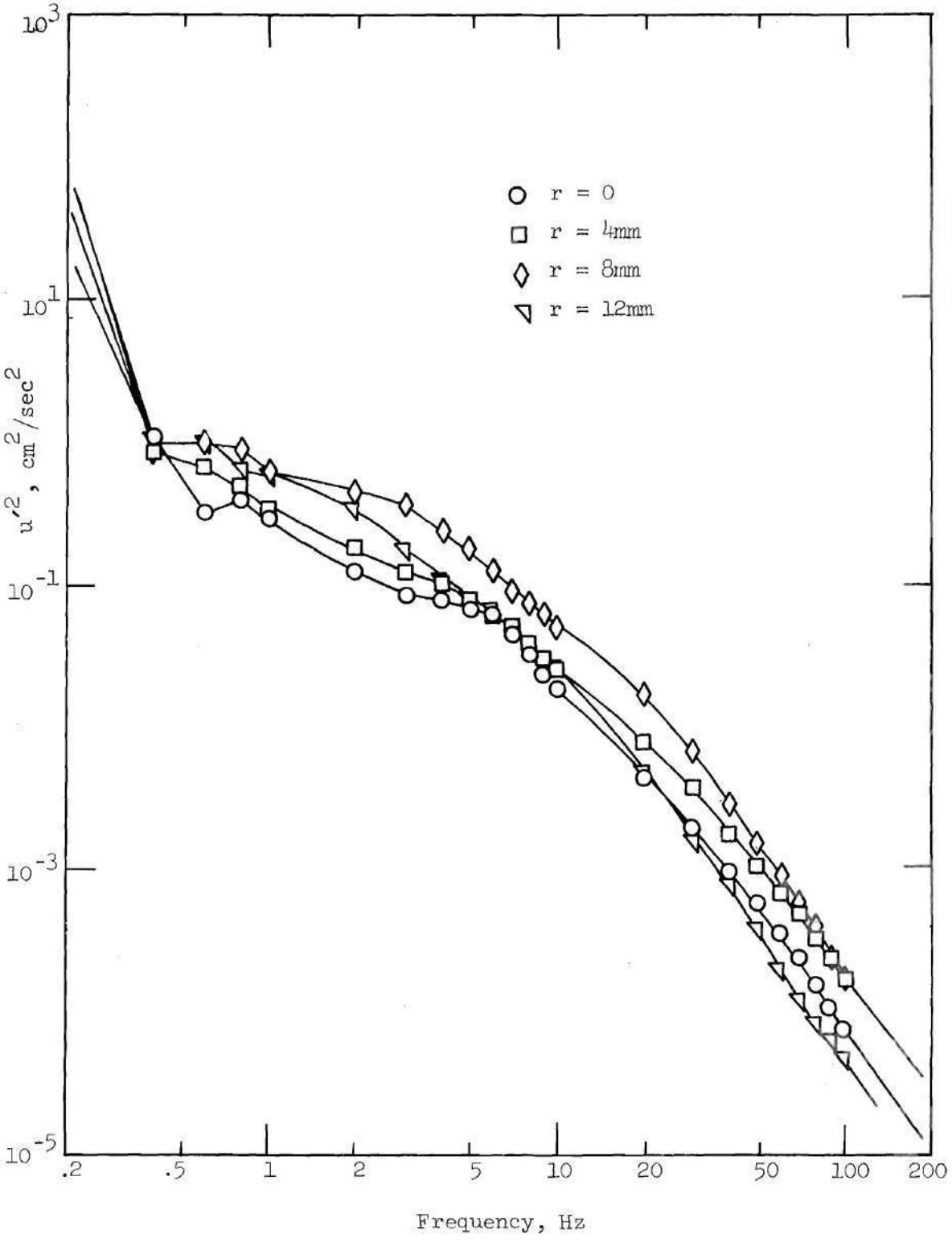

Figure 149. Energy Spectra for 50% Sharp-Edged Occlusion, x/d = 2.125, α = 15, $R_{e_{DP}}$ = 2540, F = 0.2 Hz.

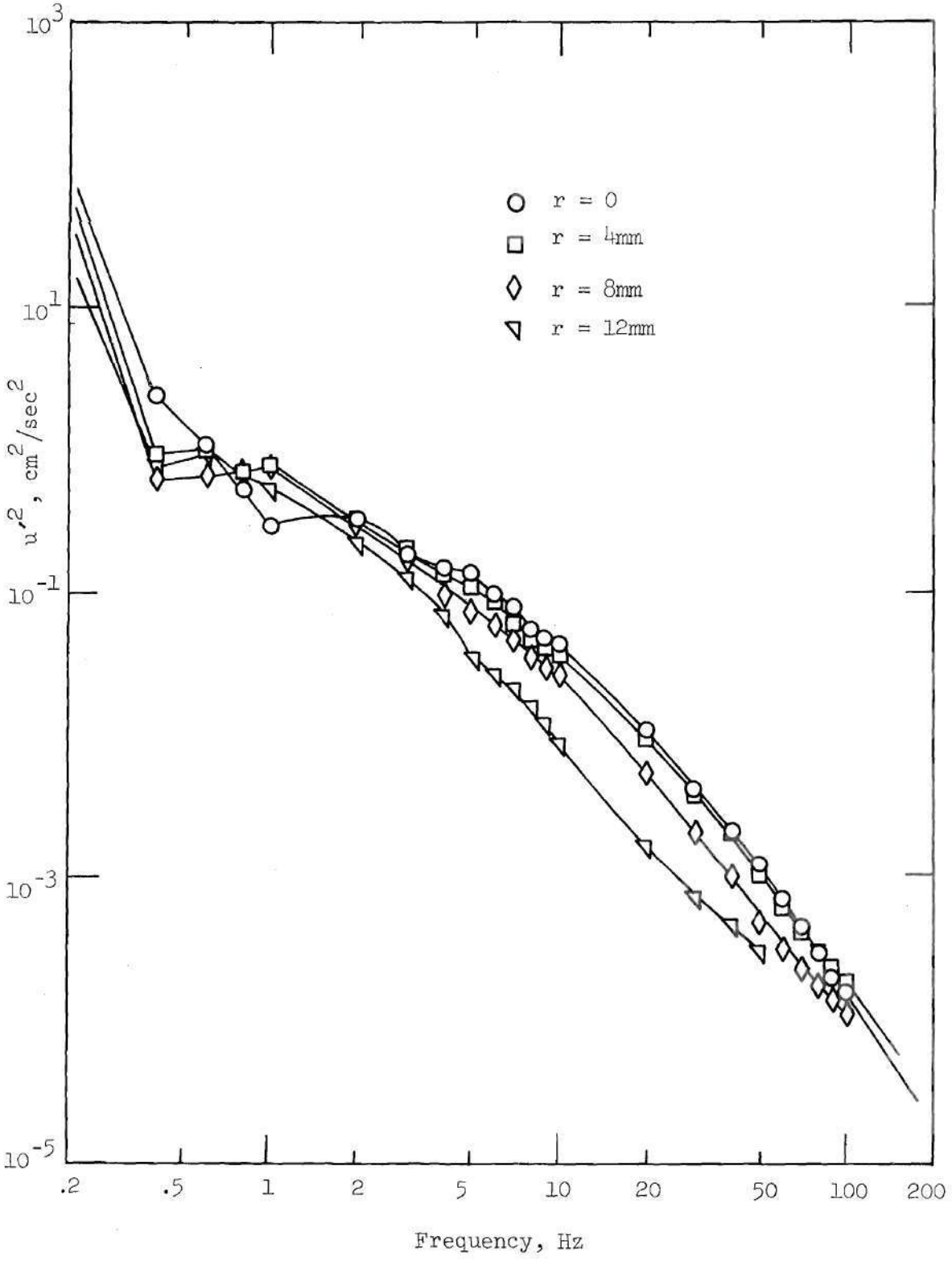

Figure 150. Energy Spectra for 50% Sharp-Edged Occlusion, x/D = 3.125, α = 15, $R_{e_{DP}}$ = 2540, F = 0.2 Hz.

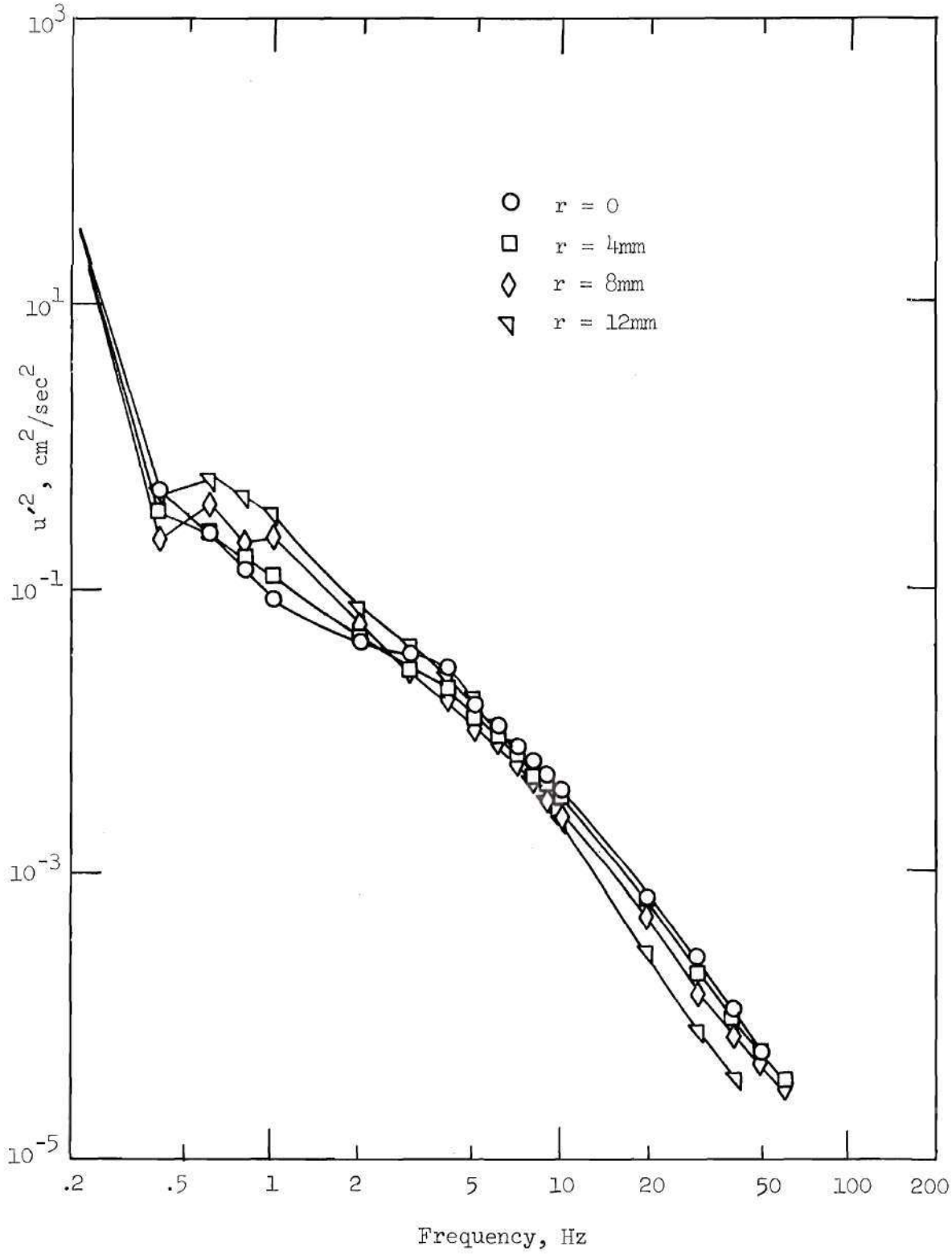

Figure 151. Energy Spectra for 50% Sharp-Edged Occlusion, x/D = 6.125, α = 15, $R_{e_{DP}}$ = 2540, F = 0.2 Hz.

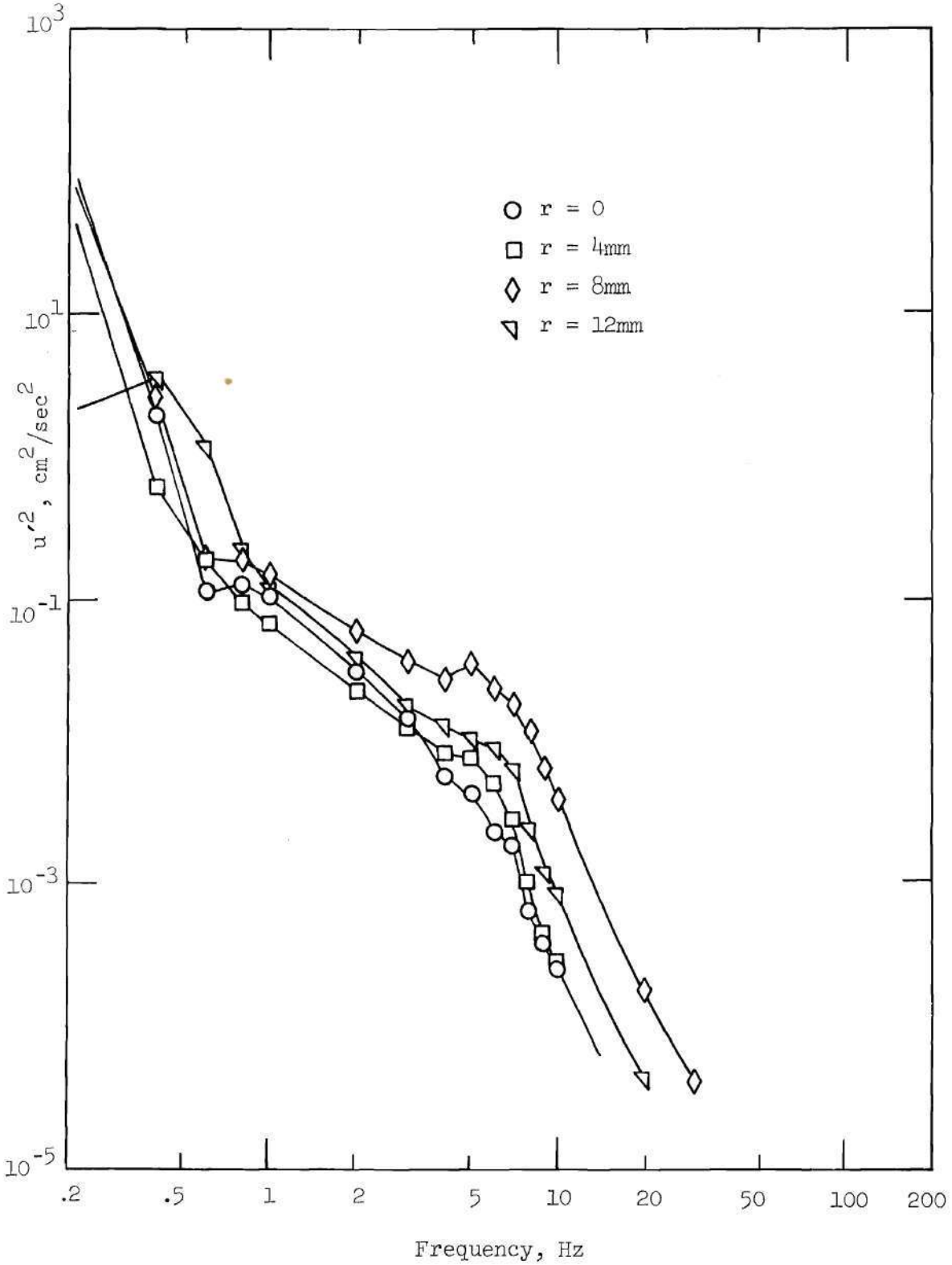

Figure 152. Energy Spectra for 50% Contoured Occlusion, x/D = 1.5, α = 15, $R_{e_{DP}}$ = 2540, F = 0.2 Hz.

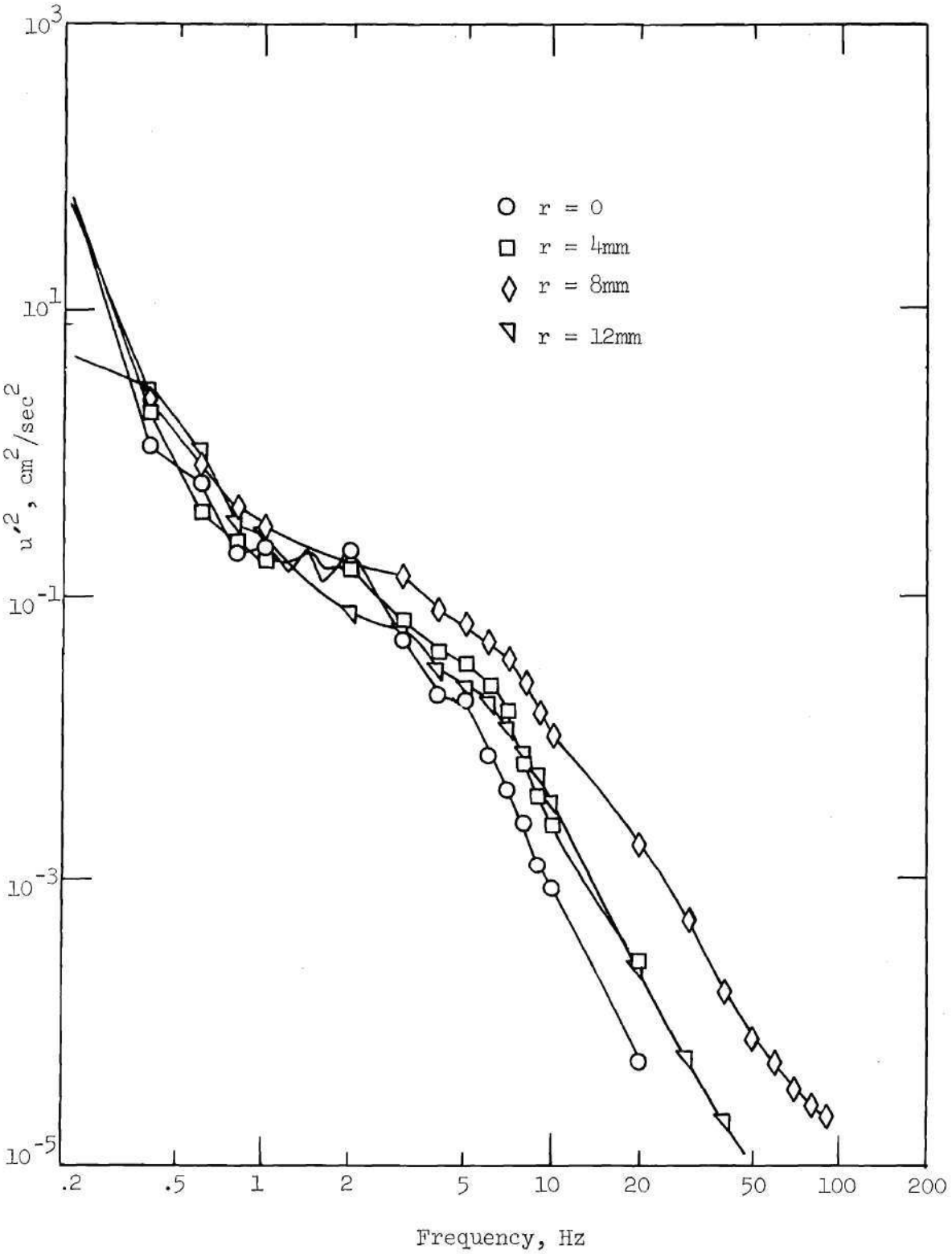

Figure 153. Energy Spectra for 50% Contoured Occlusion, x/D = 2.125, α = 15, $R_{e_{DP}}$ = 2540, F = 0.2 Hz.

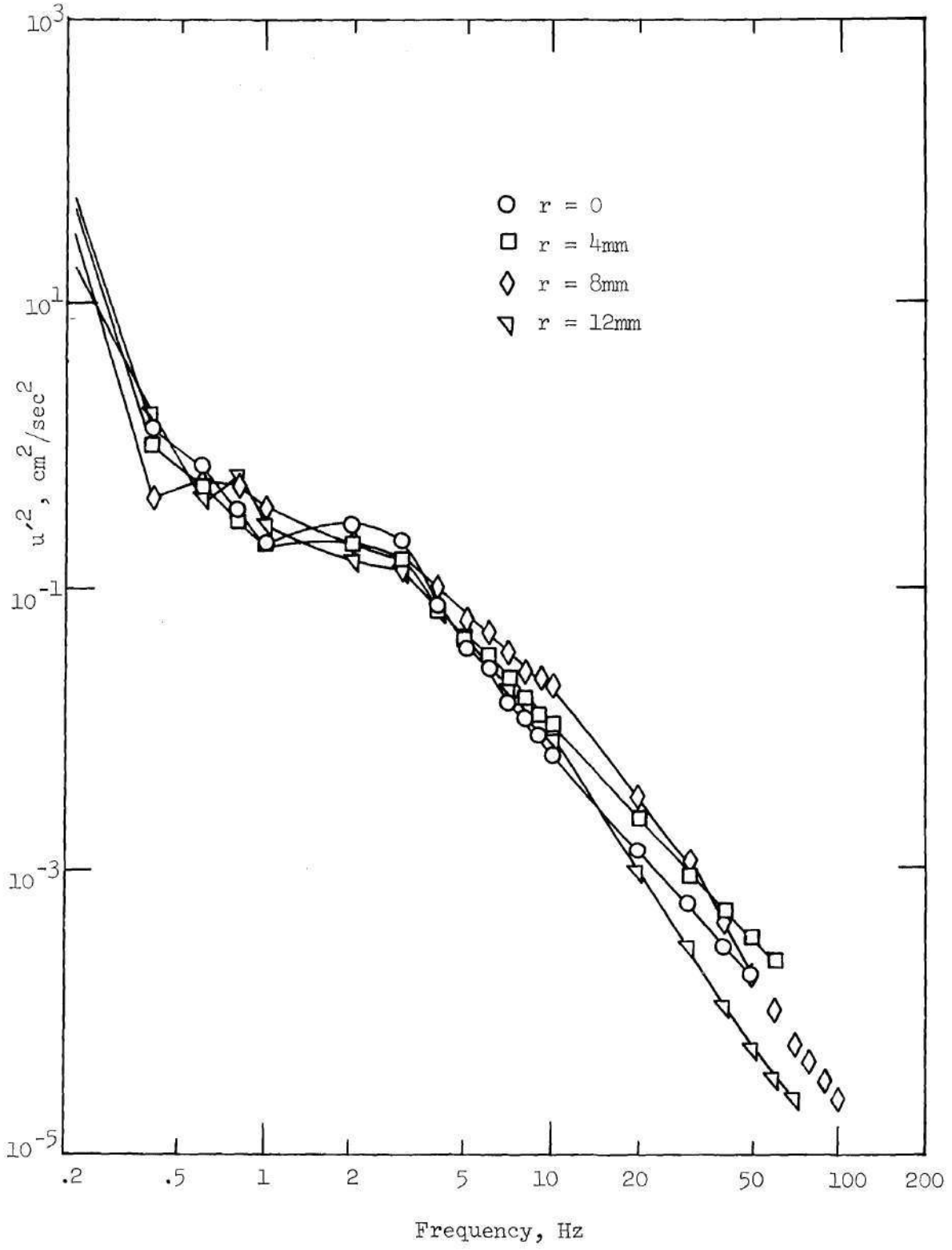

Figure 154. Energy Spectra for 50% Contoured Occlusion, x/D = 3.125, α = 15, $R_{e_{DP}}$ = 2540, F = 0.2 Hz.

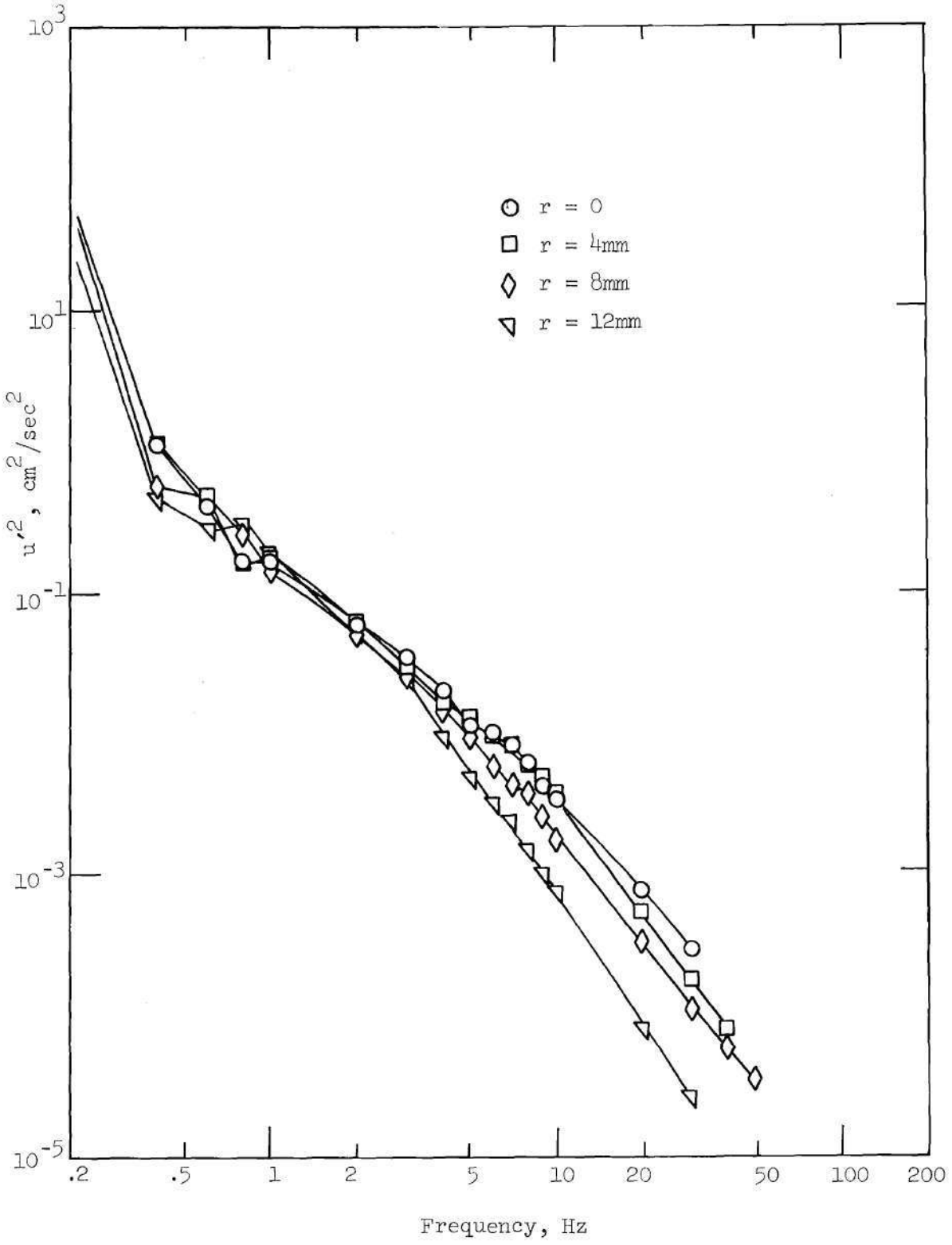

Figure 155. Energy Spectra for 50% Contoured Occlusion, x/D = 6.125, α = 15, $R_{e_{DP}}$ = 2540, F = 0.2 Hz.

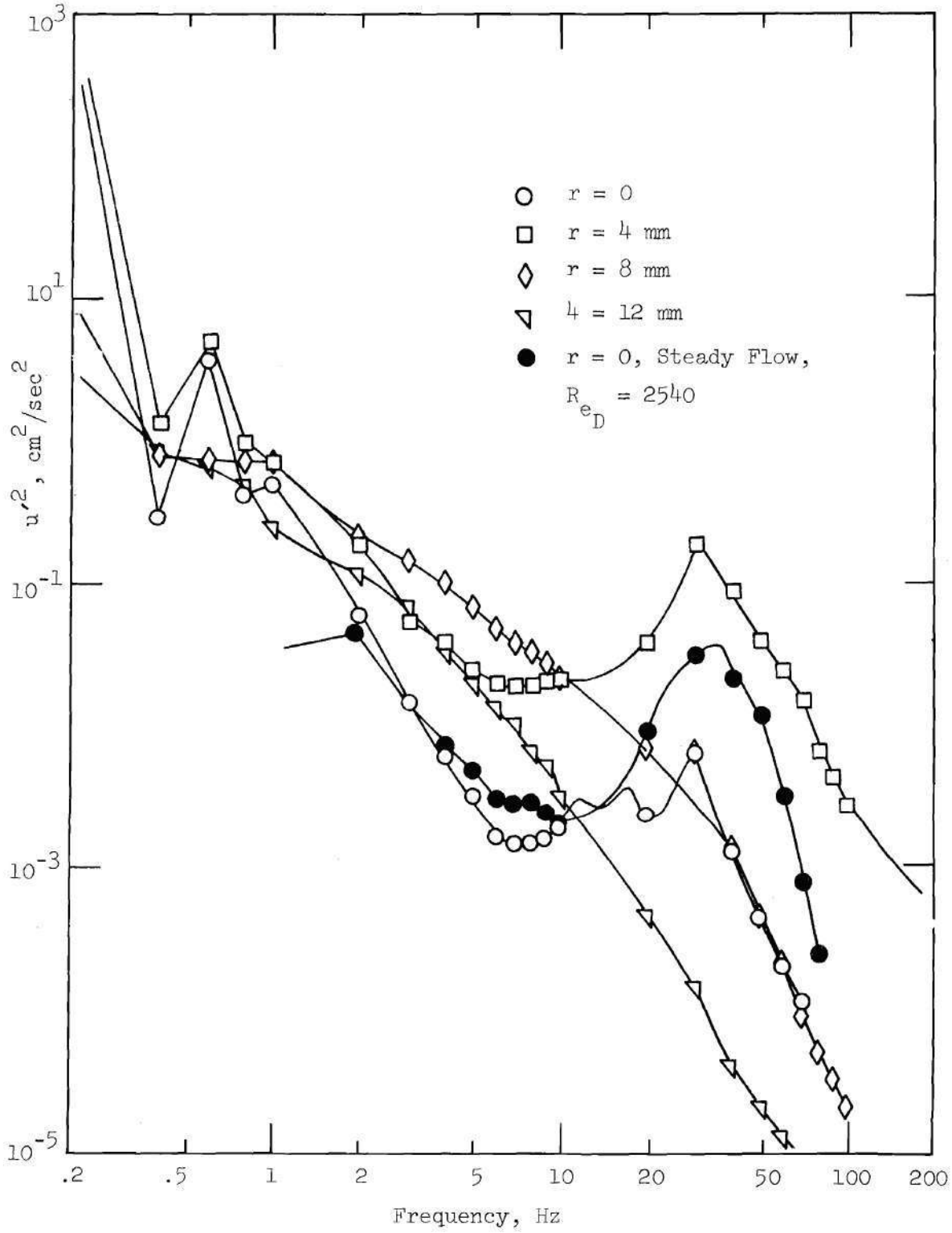

Figure 156. Energy Spectra for 75% Sharp-Edged Occlusion, x/D = 0.5, α = 15, $R_{e_{DP}}$ = 2540, F = 0.2 Hz

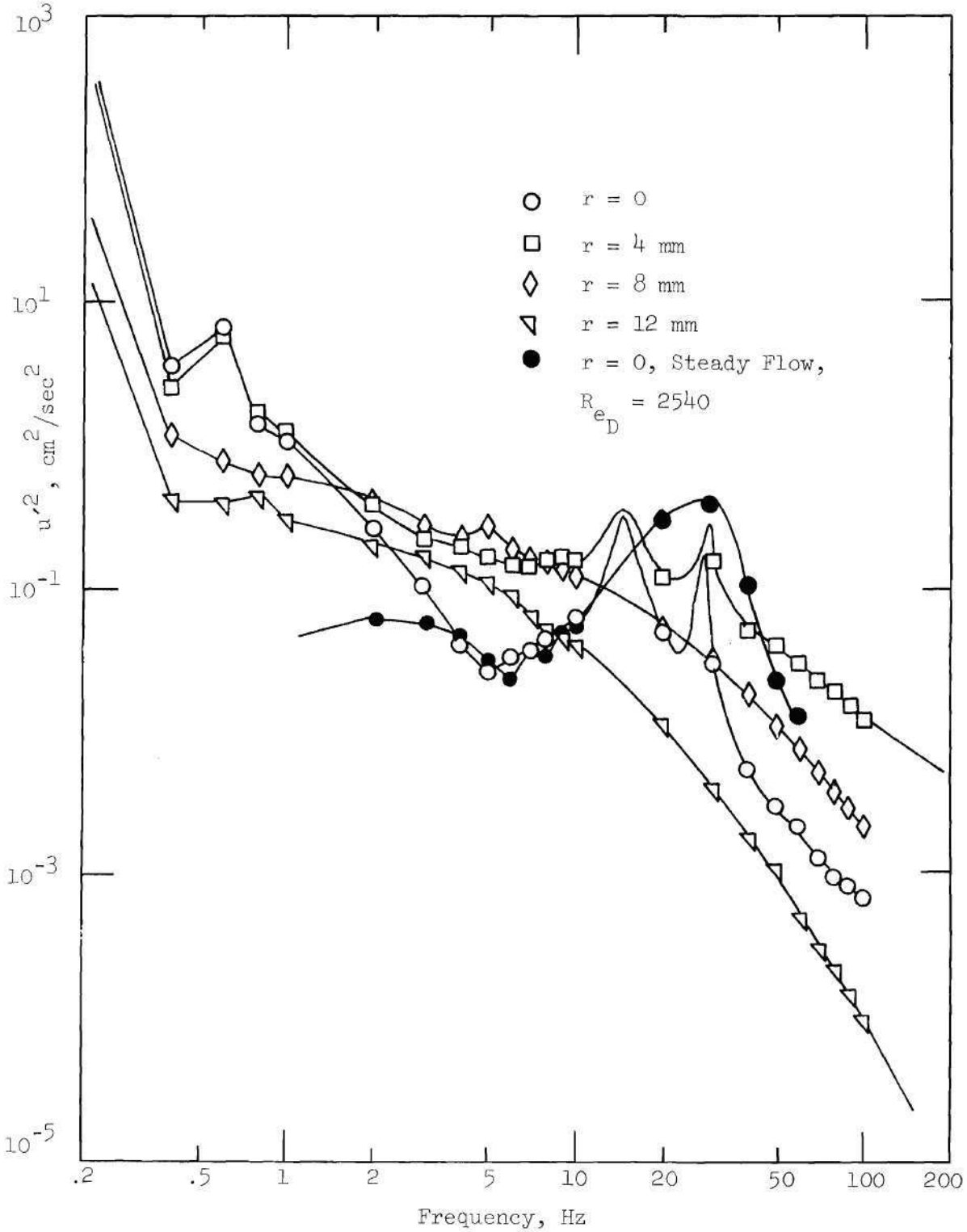

Figure 157. Energy Spectra for 75% Sharp-Edged Occlusion, x/D = 1.125, α = 15, $R_{e_{DP}}$ = 2540, F = 0.2 Hz

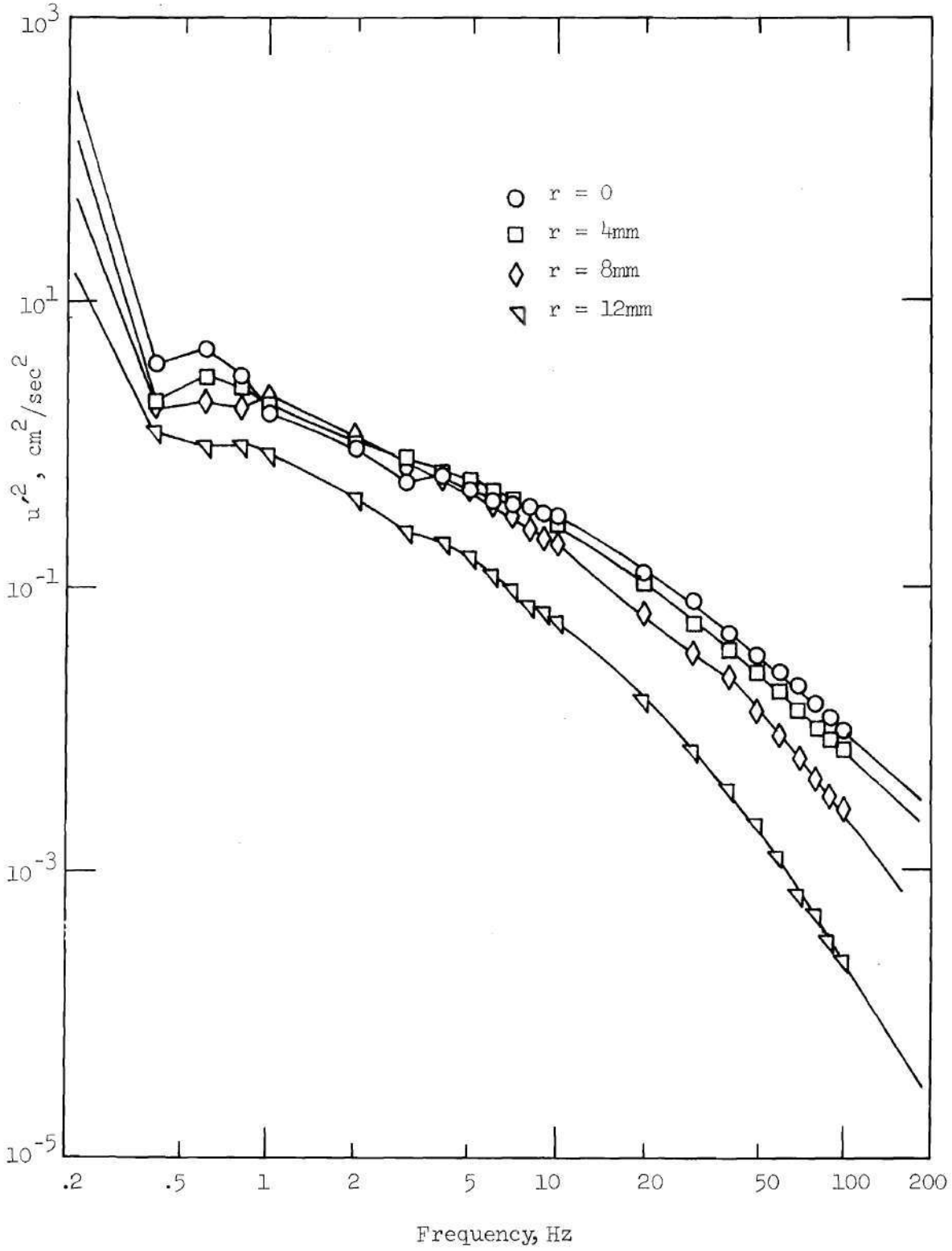

Figure 158. Energy Spectra for 75% Sharp-Edged Occlusion, $x/D = 2.125$, $\alpha = 15$, $R_{e_{DP}} = 2540$, $F = 0.2$ Hz.

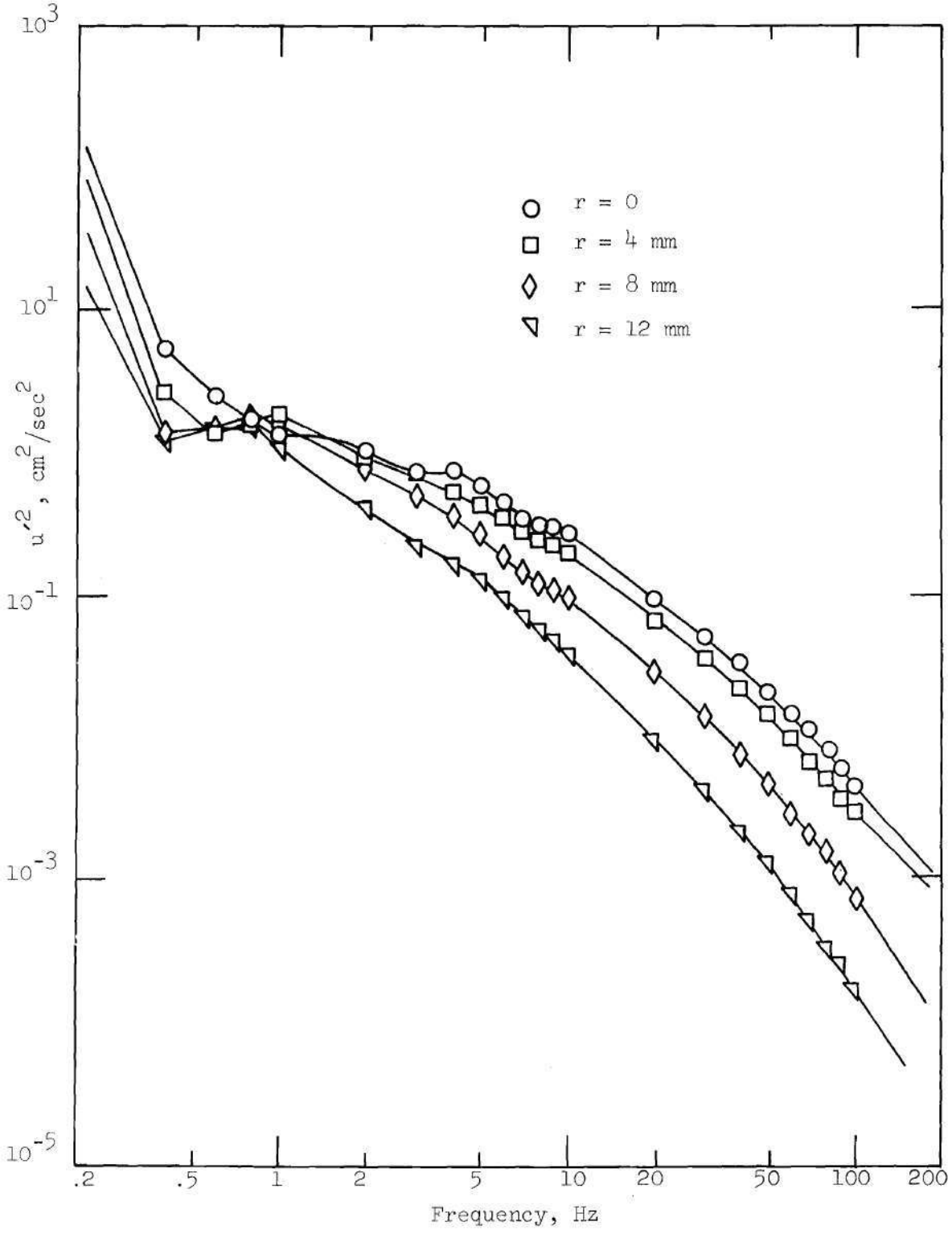

Figure 159. Energy Spectra for 75% Sharp-Edged Occlusion, x/D = 3.125, α = 15, $R_{e_{DP}}$ = 2540, F = 0.2 Hz

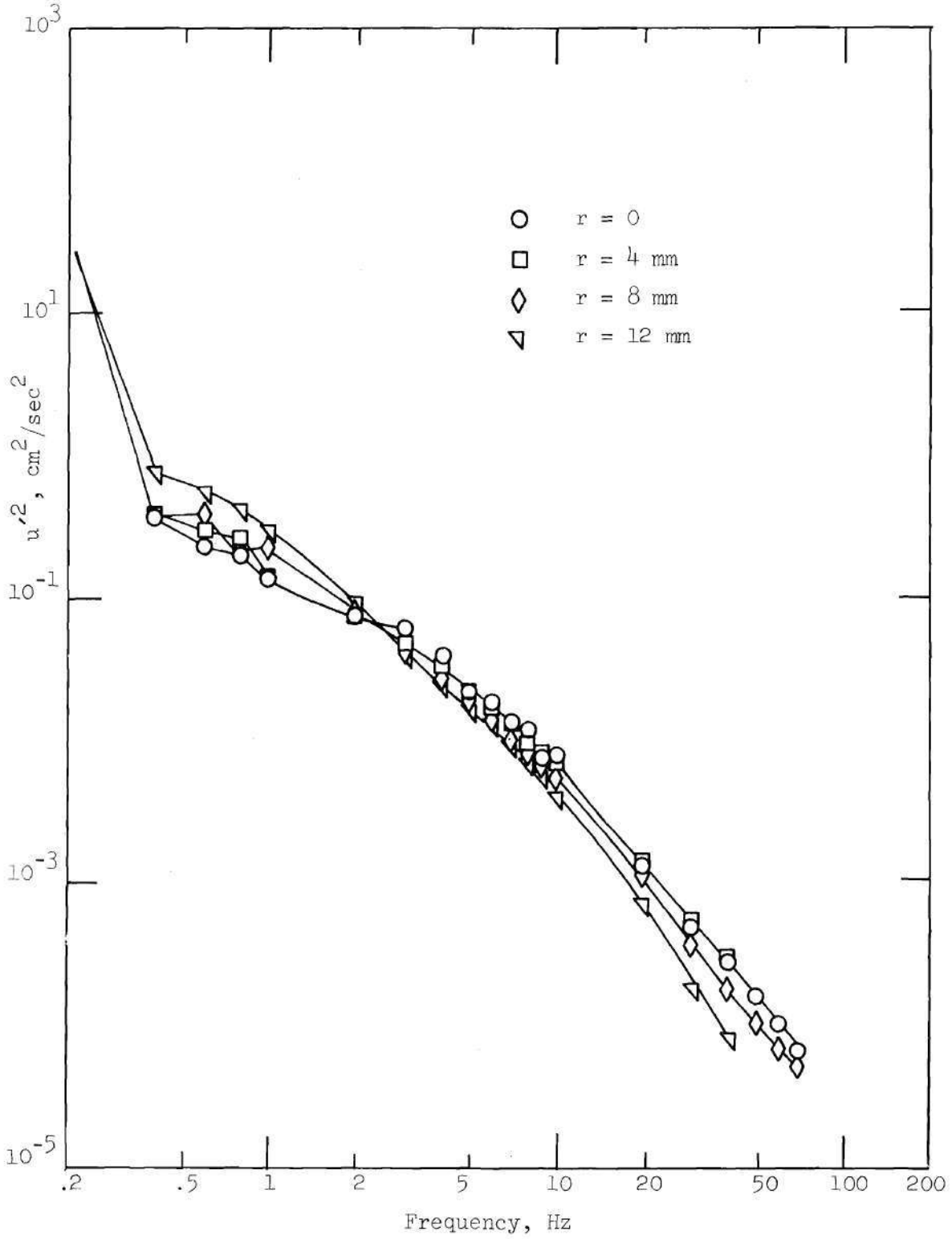

Figure 160. Energy Spectra for 75% Sharp-Edged Occlusion, $x/D = 6.125$, $\alpha = 15$, $R_{e_{DP}} = 2540$, $F = 0.2$ Hz

at r = 0 and 4 mm with distinct energy peaks. The x/D = 1.125 position actually shows two peaks; one peak at the same frequency of 28 Hz as seen at the x/D = 0.5 location and another peak at 14 Hz which appears to be a subharmonic. Also shown on these two figures is the energy spectra obtained in steady flow with the R_{eD} corresponding to the peak R_{eD} for this pulsatile data. The vortex shedding frequencies are the same for both the steady and pulsatile data at x/D = 0.5 which indicates that the vortex shedding occurring at the peak of the velocity pulse contributes to a large extent to the spectra averaged over the whole pulse. At x/D = 1.125, the steady flow shedding frequency corresponds to the higher frequency peak which indicates that the lower peak is a subharmonic. At these near distal axial locations, the spectra obtained closer to the wall, r = 8 and 12 mm, show a smooth energy decrease with increasing frequency. The near wall radial location produced energy intensities at most frequencies which are below those obtained away from the wall. The axial locations farther downstream, x/D = 2.125, 3.125 and 6.125 produced turbulent-like spectral distributions with no distinct peaks and the x/D = 6.125 spectra was radially homogeneous.

The 75 percent contoured occlusion also produced a peaked spectra in the near distal field at x/D = 1.5 and 2.125 (Figures 161 and 162) at x/D = 1.5 (Figure 161) the peak occurs at about 14 Hz and at x/D = 2.125 the 14 Hz peak can still be observed along with a subharmonic peak at 7 Hz. These peak frequencies correspond to the frequencies observed in the steady flow at the same R_{eD}. However, these frequencies are lower that those with the sharp occlusion and only appear at the r = 0 location. The intensities of the peaks are also lower than the sharp

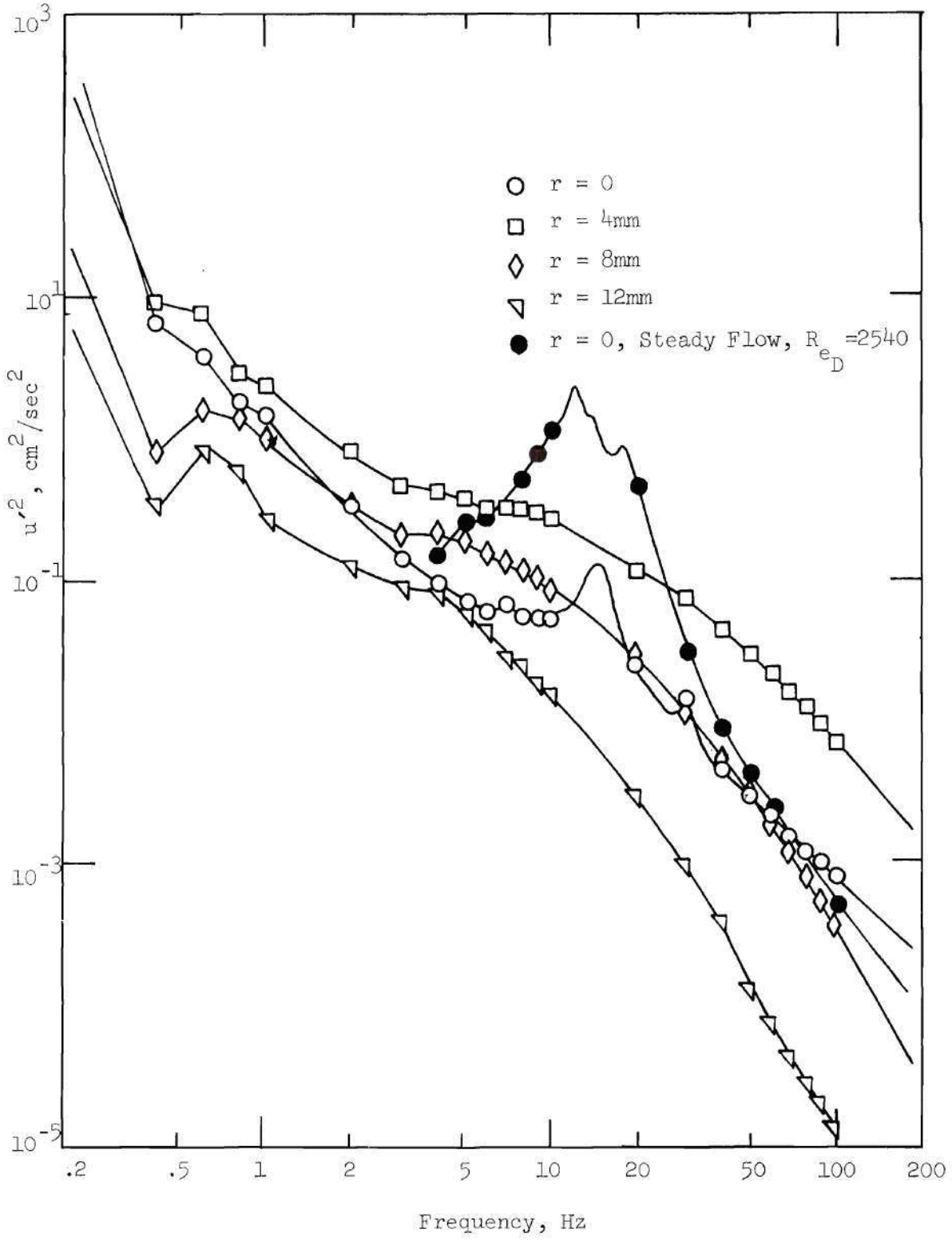

Figure 161. Energy Spectra for 75% Contoured Occlusion, x/D = 1.5, α = 15, $R_{e_{DP}}$ = 2540, F = 0.2 Hz.

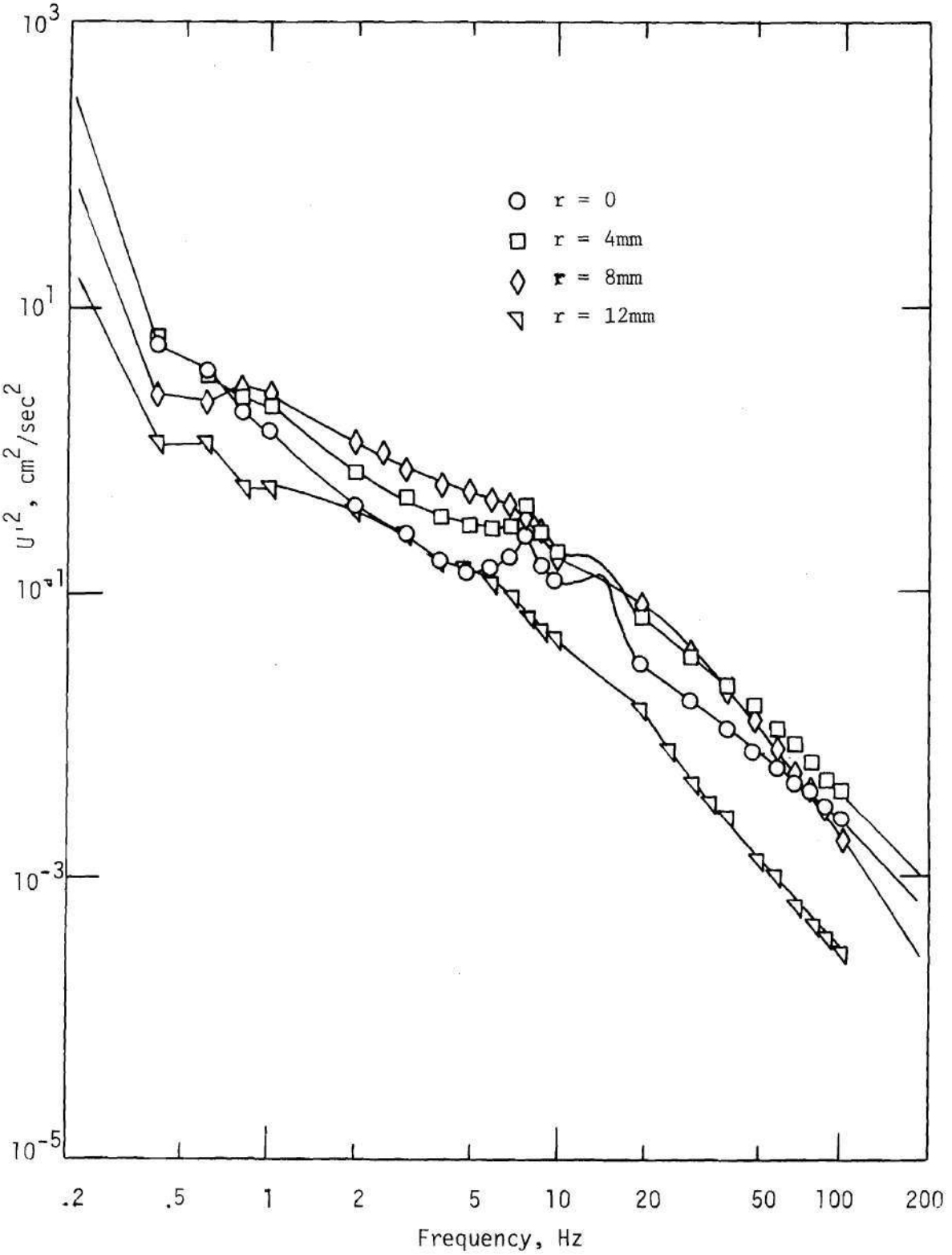

Figure 162. Energy Spectra for 75% Contoured Occlusion, x/D = 2.125, α = 15, Re_{DP} = 2540, F = 0.2 Hz.

occlusion peaks. The steady flow centerline spectra is also indicated for these two x/D locations which show that, like the sharp-edged occlusion data in Figures 155 and 156, the pulsatile flow produces significant energy in the vortex rings which occur near the high velocity portion of the flow pulse. The x/D = 3.125 and 6.125 axial locations (Figures 163 and 164) produced spectra similar to those obtained with the sharp occlusion.

8.4 Pulsatile Flow Energy Spectra Data Summary

The general trends in the energy spectra data obtained at $\alpha = 15$, $R_{eDP} = 2540$ have been discussed in the foregoing sections of this chapter and are summarized in the following statements.

1. The overall energy intensity increases and then decreases as x/D increases which indicates a region of maximum turbulence intensity for a given occlusion. This maximum occurs between 2D and 3D from the occlusion for all occlusions. The movies of the pulsatile flow showed that reattachment of the flow during the high velocity portion of the pulse occurred at approximately this same axial position. This flow reattachment, along with the break-up of the vortex ring structure results in a highly turbulent flow at this axial location.

2. For the low degrees of occlusion, i.e., 25 percent and 50 percent, the turbulence is distributed throughout the tube at all x/D positions. However, near the constriction, the energy tends to be slightly higher near the wall than at the centerline, whereas the reverse is true at large x/D.

3. For the 75 percent occlusions, there is a very uneven dis-

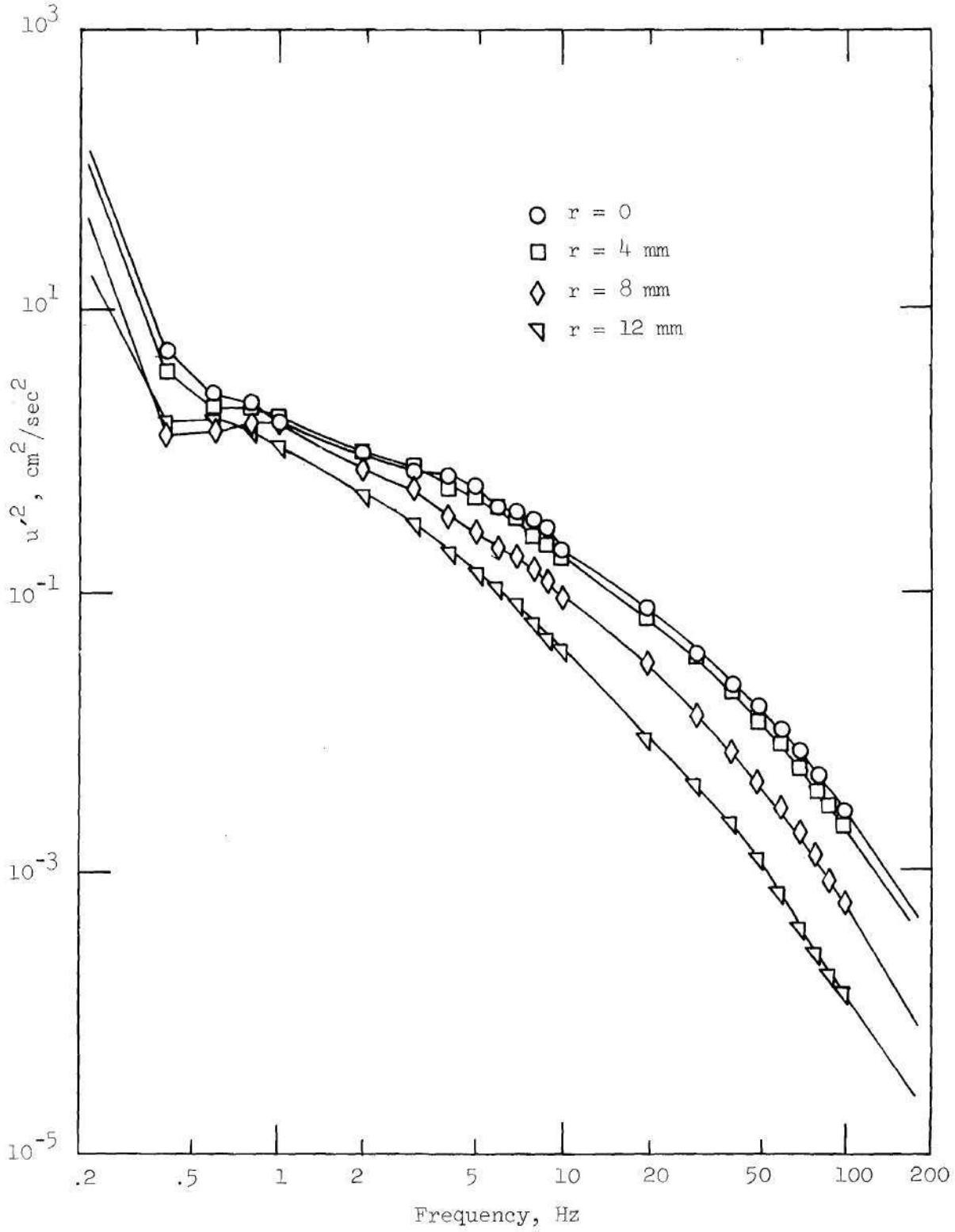

Figure 163. Energy Spectra for 75% Contoured Occlusion, x/D = 3.125, α = 15, $R_{e_{DP}}$ = 2540, F = 0.2 Hz

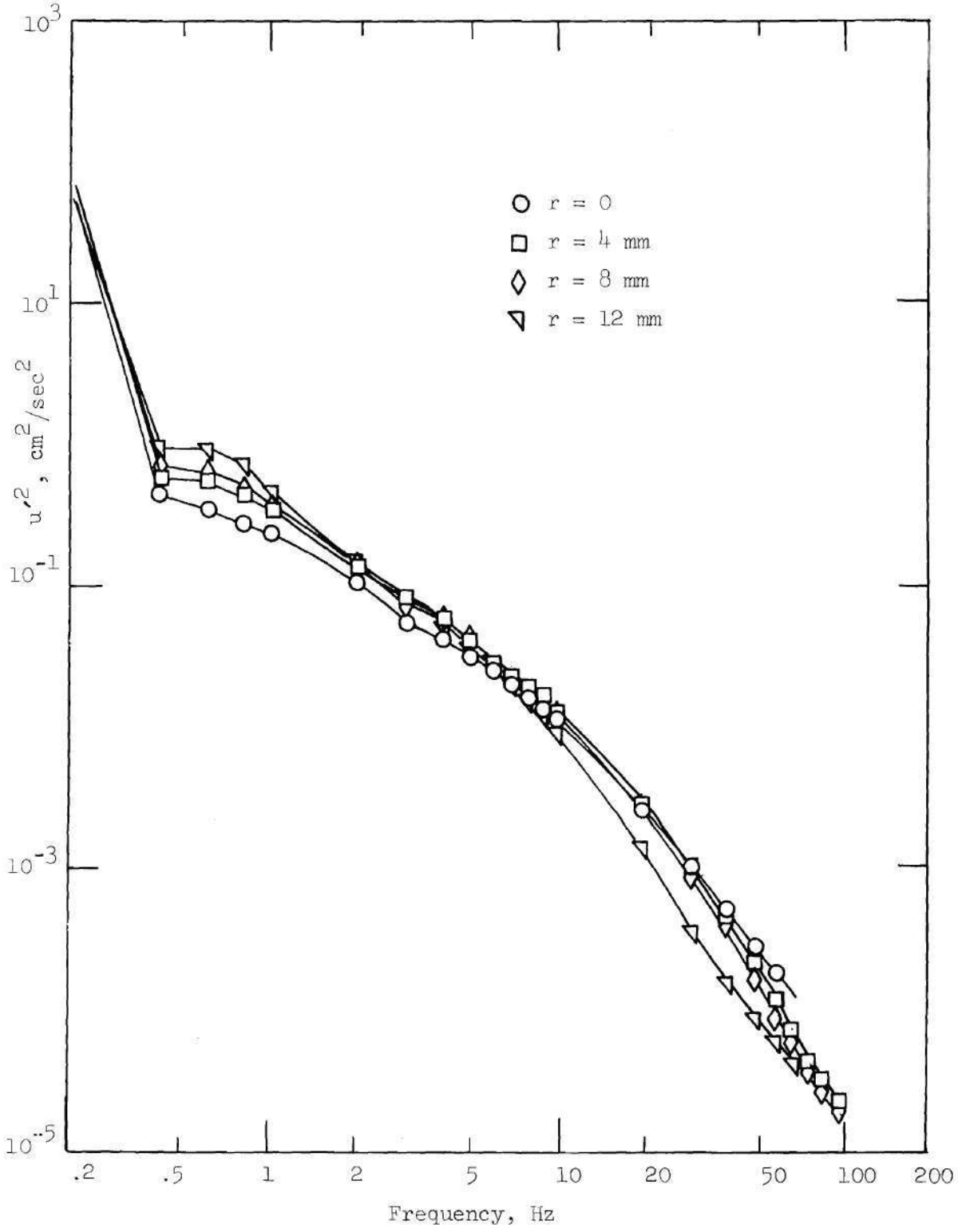

Figure 164. Energy Spectra for 75% Contoured Occlusion, x/D = 6.125, α = 15, $R_{e_{DP}}$ = 2540, F = 0.2 Hz

tribution of energy at low x/D with the near-centerline spectra showing a peaked distribution. The turbulence is more evenly distributed at x/D = 6.125.

4. For the low degrees of occlusion, i.e., 25 percent and 50 percent, the sharp-edged occlusion produced greater intensities than the contoured occlusion. For the high degree of occlusion, 75 percent, both occlusion shapes produced about the same turbulent energy distribution at x/D greater than 2.

5. The spectra obtained with the 75 percent occlusions indicate vortex shedding frequencies which correspond to those obtained in steady flow for $R_{eD} = 2540$.

8.5 Correlation with Nondimensional Energy, u'^2/U_o^2, and Strouhal Number, fd/U_o

Correlation of the flow phenomena, such as vortex shedding, associated with steady flow through constrictions in tubes has received attention in the literature; and these previous correlations with the Strouhal and Reynolds numbers based on orifice conditions give a motivation for presenting the energy spectra correlations in Chapter VI. No such guidance or justification is available for pulsatile flow. However, the most logical physical variables in the pulsatile case which influence the development of the flow patterns are constriction geometry, degree of constriction, velocity at the minimum constriction area and the velocity pulse waveform as defined by the peak velocity, fundamental pulse rate and pulse frequency content (see also Chapter II). For a given pulse waveform, then, it would appear that the nondimensional

correlations most analogous to the steady flow correlation would again be the Strouhal number based on the "orifice" conditions, fd/U_o and nondimensional energy, u'^2/U_o^2. For the pulsatile case, however, the velocity U_o is chosen to be the peak pulse velocity at the constriction minimum area. This velocity is believed to be appropriate since the most intense velocity fluctuations would be expected to occur during the higher velocity portion of the pulse and would thus exert considerable influence on the average energy spectra. This velocity, U_{op}, along with the fundamental pulse rate of the waveform also gives an indication of the acceleration and deceleration in the flow.

The above correlation is shown in Figures 165 through 168 for the sharp-edged occlusions and in Figures 169 through 172 for the contoured shapes. The centerline spectral data for all three occlusions and no occlusion data are shown on each plot for the same x/D axial position. The spectral peaks obtained in the near distal flow field of the 75 percent sharp occlusion (Figure 165) align with Strouhal numbers of about 0.5 and 0.9 which are in the same range of values obtained with the steady flow results in Chapter VI. At the more downstream locations, x/D = 2.125 and 3.125 (Figures 166 and 167), the spectra for the three occlusions appear to correlate reasonably well, with the 50 percent and 75 percent indicating better correlation than the 25 percent spectra. At x/D = 6.125 (Figure 168) the spectra do not correlate at all since this position is far removed from the direct influence of the occlusive jet flow.

The 75 percent contoured occlusion correlation shown in Figure

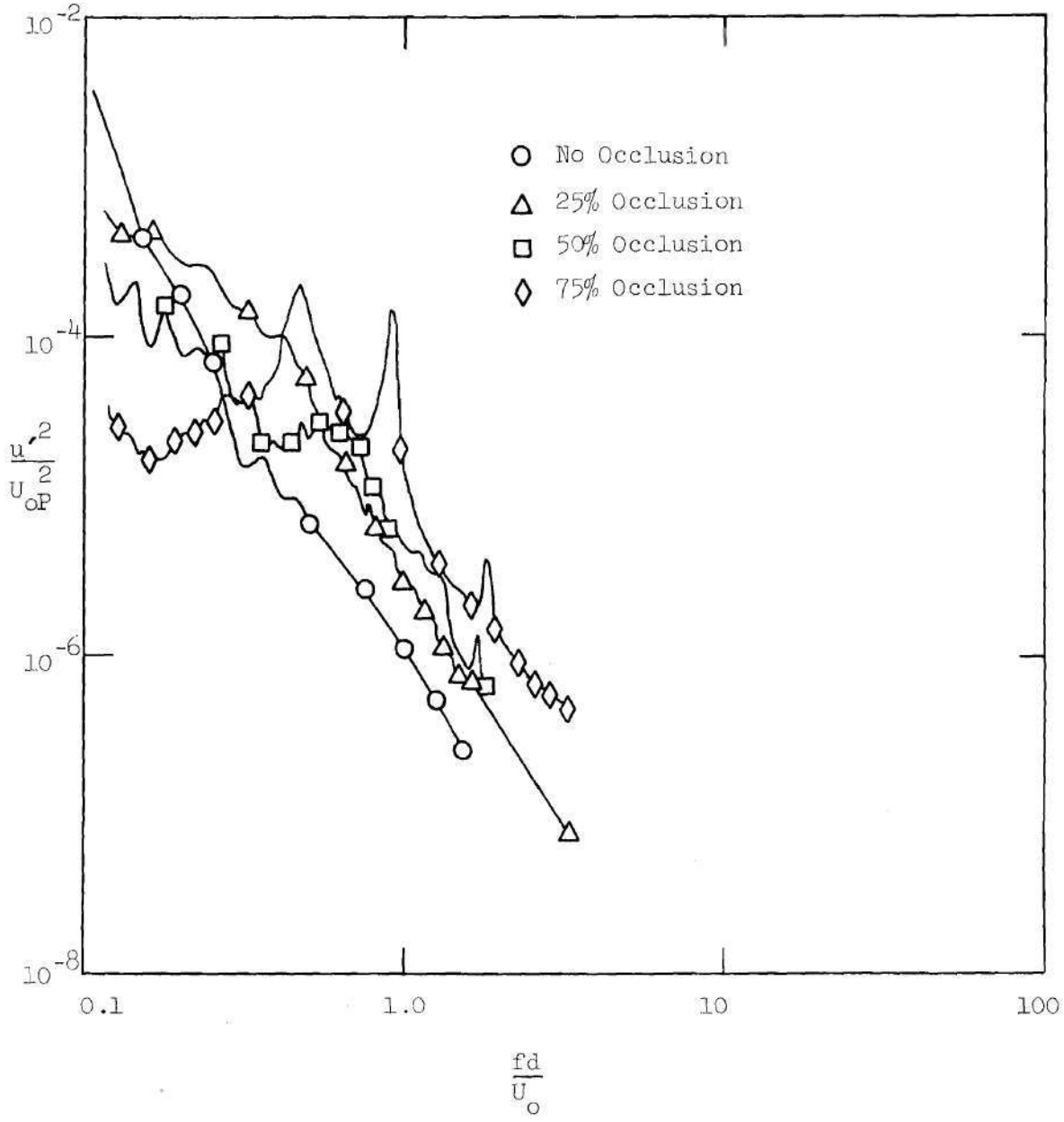

Figure 165. Strouhal Number Correlation at $\frac{x}{D} = 1.125$, $\alpha = 15$, $R_{e_{DP}} = 2540$ for Sharp-Edged Occlusions.

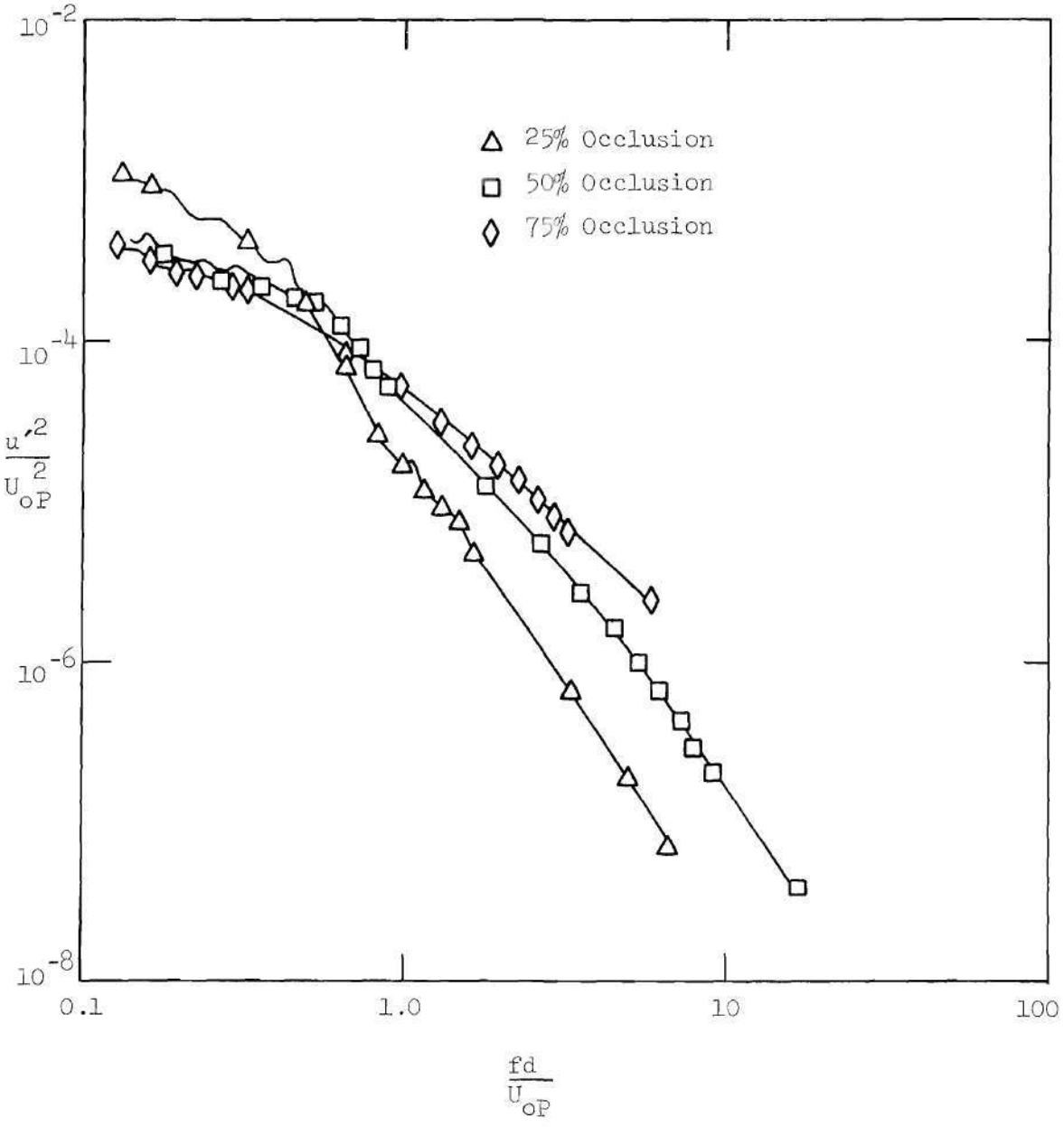

Figure 166. Strouhal Number Correlation at x/D = 2.125, α = 15, $R_{e_{DP}}$ = 2540 for Sharp-Edged Occlusions.

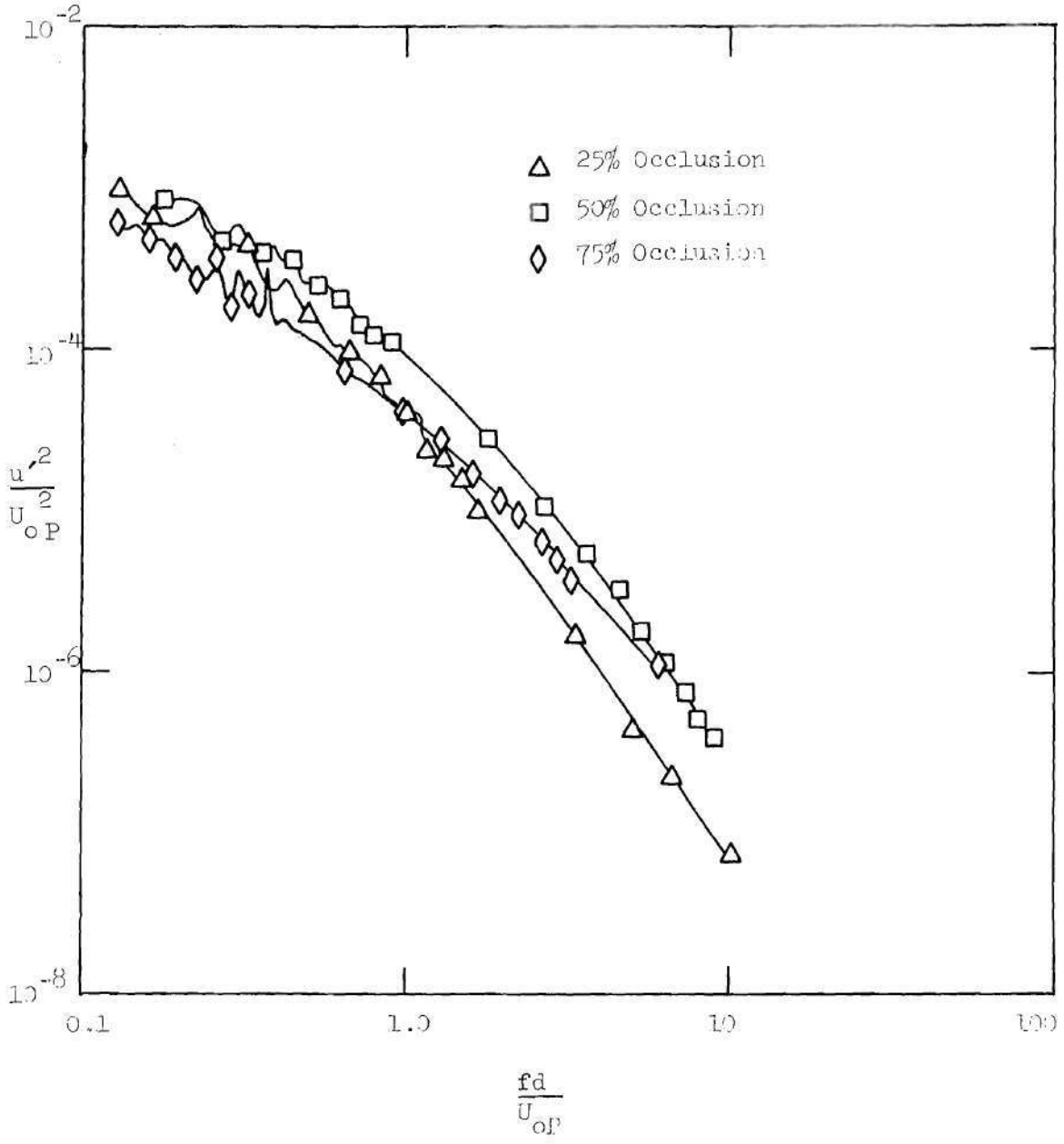

Figure 167. Strouhal Number Correlation at x/D = 3.125, α = 15, $R_{e_{DP}}$ = 2540, for Sharp-Edged Occlusions.

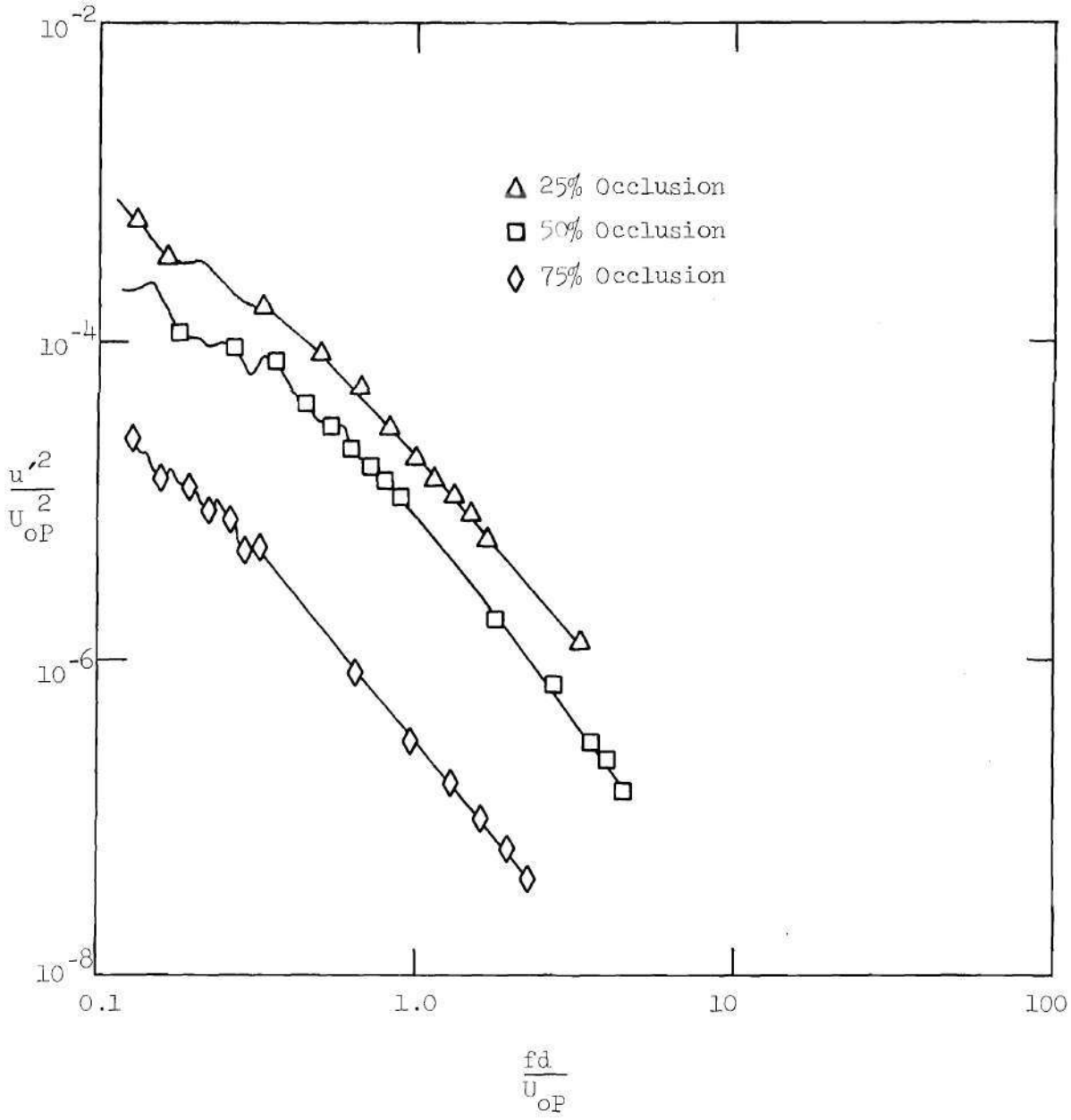

Figure 168. Strcuhal Number Correlation at x/D = 6.125, α = 15, $R_{e_{DP}}$ = 2540 for Sharp-Edged Occlusions.

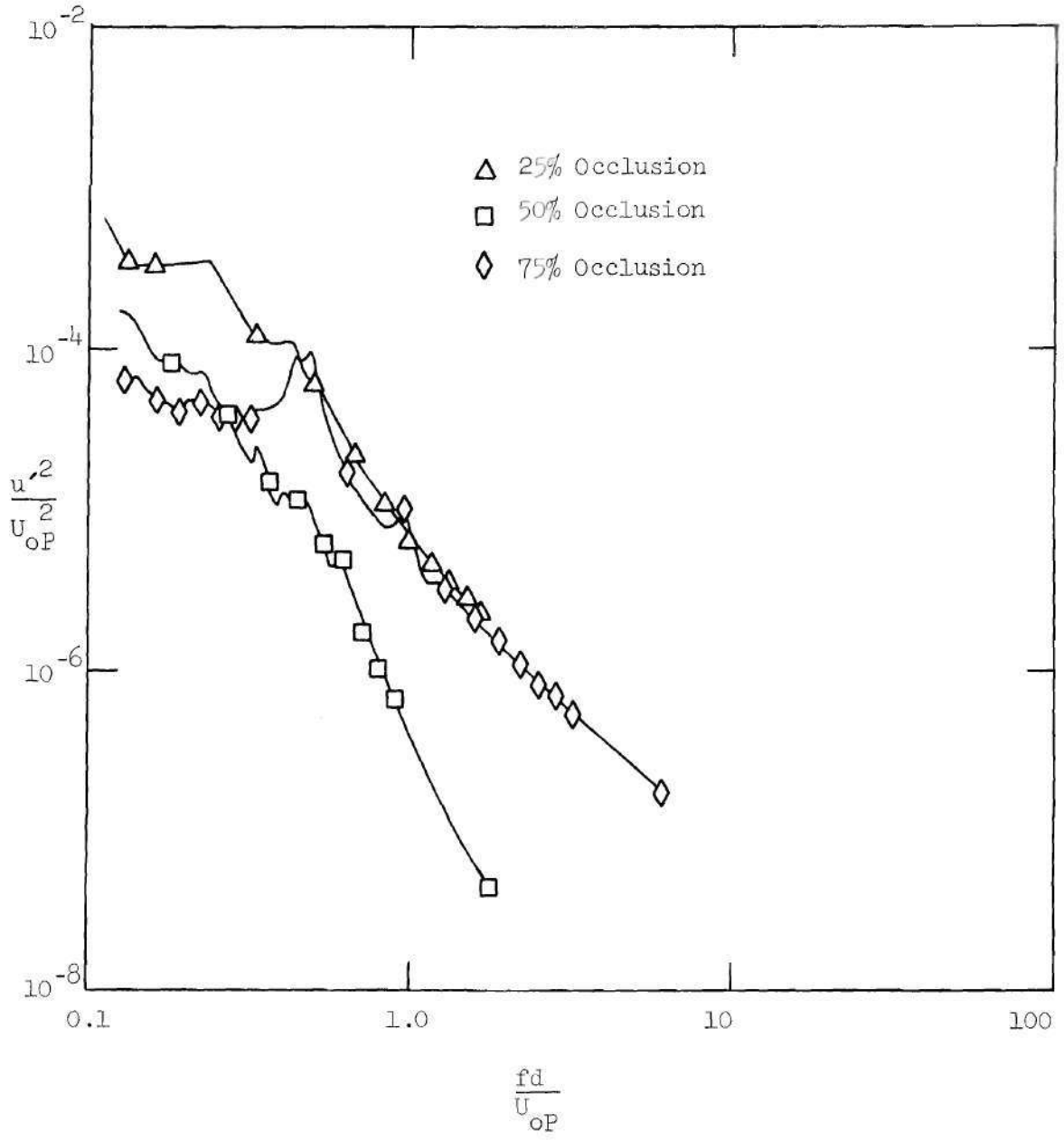

Figure 169. Strouhal Number Correlation at x/D = 1.5, α = 15, $R_{e_{DP}}$ = 2540 for Contoured Occlusions.

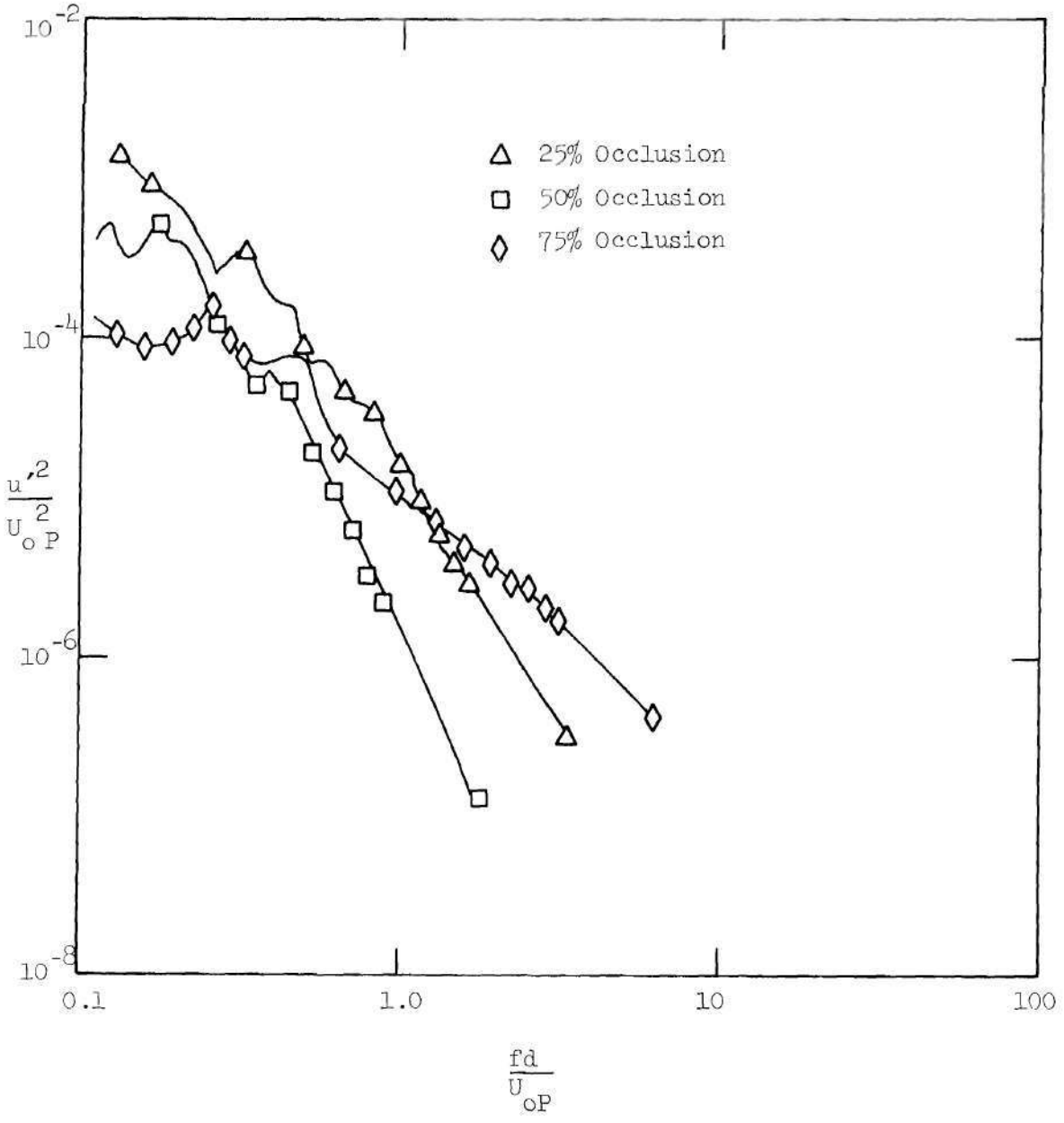

Figure 170. Strouhal Number Correlation at x/D = 2.125, α = 15, $R_{e_{DP}}$ = 2540 for Contoured Occlusions.

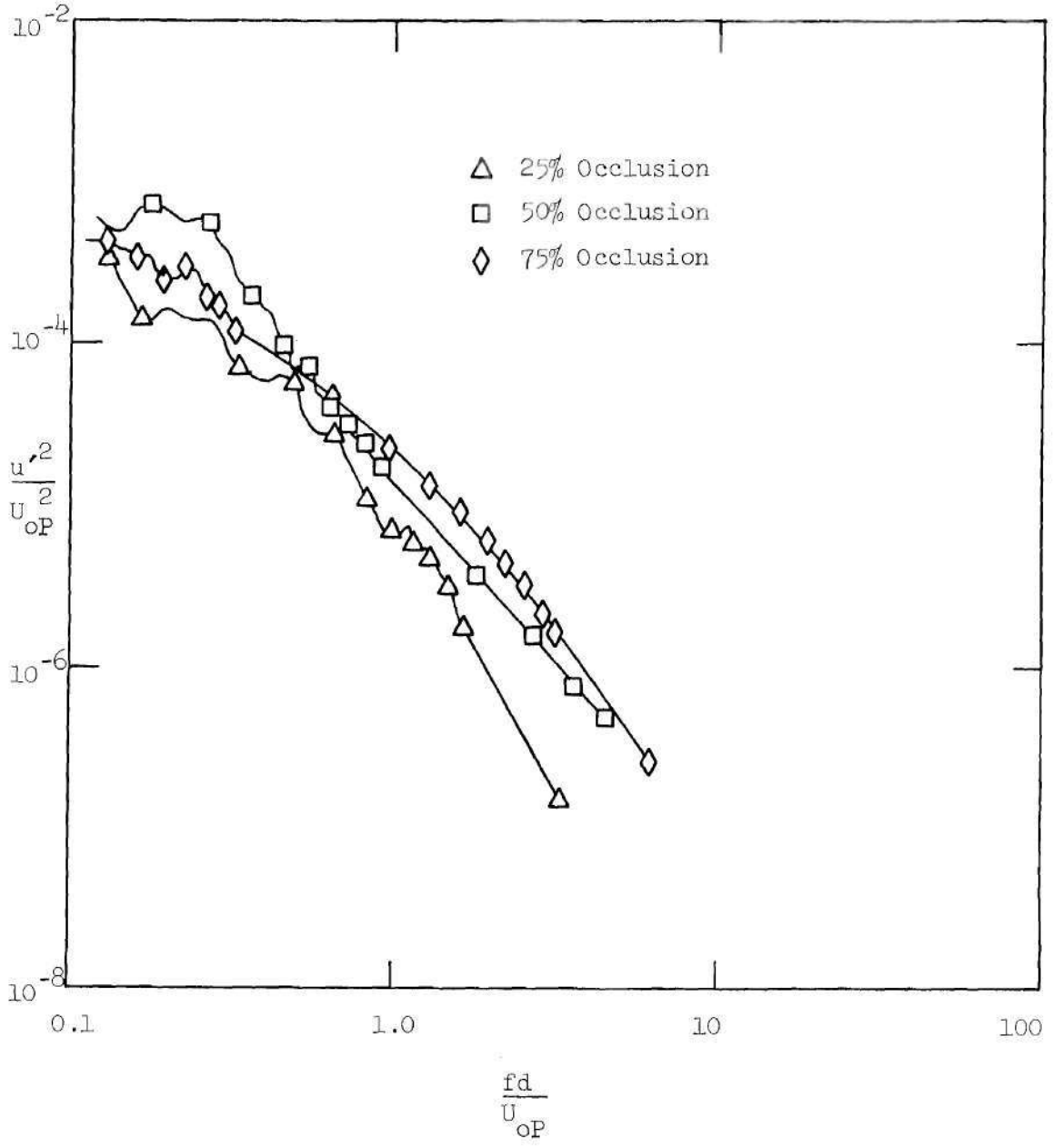

Figure 171. Strouhal Number Correlation at x/D = 3.125, α = 15, $R_{e_{DP}}$ = 2540 for Contoured Occlusions

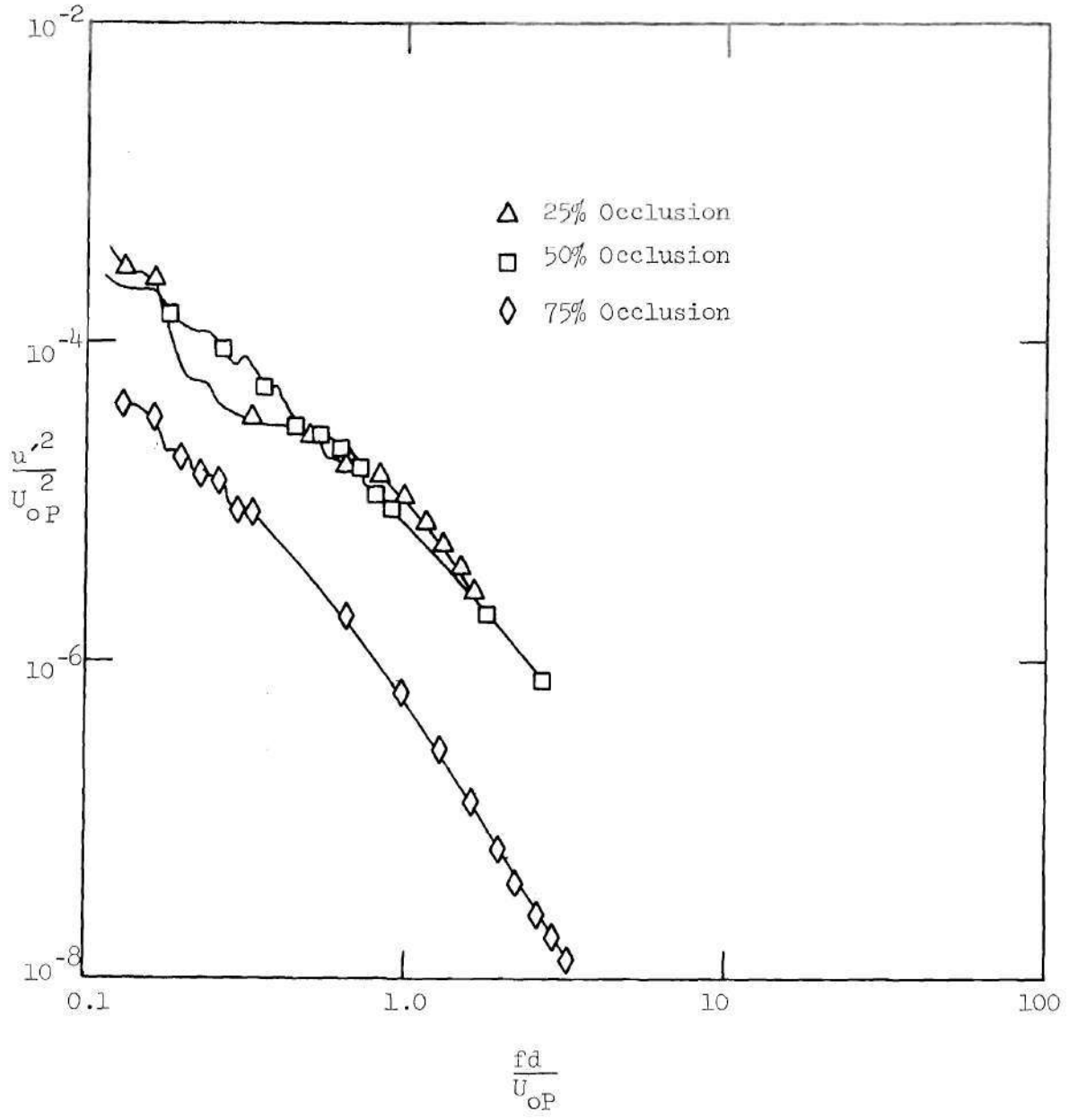

Figure 172. Strouhal Number Correlation at $x/D = 6.125$, $\alpha = 15$, $R_{e_{DP}} = 2540$ for Contoured Occlusions

169 for the x/D = 1.5 position also indicates that the Strouhal number of the spectral peak is near 0.5. In general, the correlation of the three occlusion sizes is not good at any of the axial positions. The correlation at x/D = 3.125 (Figure 171) appears to be reasonably good but when this result is considered in context with the poor data correlations at the other locations, it must be concluded that the overall correlation of the contoured occlusion results is poor with these parameters.

8.6 Correlation with Nondimensional Energy, $u'^2/\bar{U}_{PL}^2$, and "Local" Strouhal Number, $fD/\bar{U}_{PL}$

The Strouhal number correlations based on the orifice conditions which were presented in Section 6.5 for steady flow and in Section 8.5 for pulsatile flow have demonstrated that this type of correlation is suitable in the flow region dominated by the orifice flow. Also shown in Section 6.5 for steady flow was that a "local" Strouhal number based on the local mean velocity, $\bar{U}_L$, an effective streamtube diameter $\mathfrak{D}$, removed, to a certain extent, the dependence of the vortex shedding Strouhal number on axial distance. This correlation is expected to yield the best results in cases where the flow is progressing from laminar flow at the orifice, to discrete vortex shedding and then to fully developed turbulence. This is the situation for the sharp-edged occlusions ar R_{eD} = 2540 in steady flow.

The "local" Strouhal number correlation is applied to the pulsatile flow data by using the local mean peak cneterline velocity and the local effective jet streamtube diameter for nondimensionalization. The

effective streamtube diameter is calculated by assuming that the effective local flow area is inversely proportional to the square root of the local mean peak centerline velocity and using the unoccluded diameter and unoccluded peak centerline velocity, $U_{\infty p}$, as a reference. Therefore,

$$\mathcal{D} = D \left(\frac{U_{\infty p}}{\bar{U}_{LP}} \right)^{\frac{1}{2}}$$

Figure 173 shows the local correlation for the sharp-edged occlusions for the data obtained at axial positions which were dominated by the fully developed turbulent flow. These nondimensional parameters scale the data reasonably well for the positions shown. The data for the contoured occlusions shown in Figure 174 do not correlate as well. This lack of correlation is attributed to the fact that the contoured shape produces less of a flow disturbance and hence, the resulting fluctuations are not of a self-preserving nature.

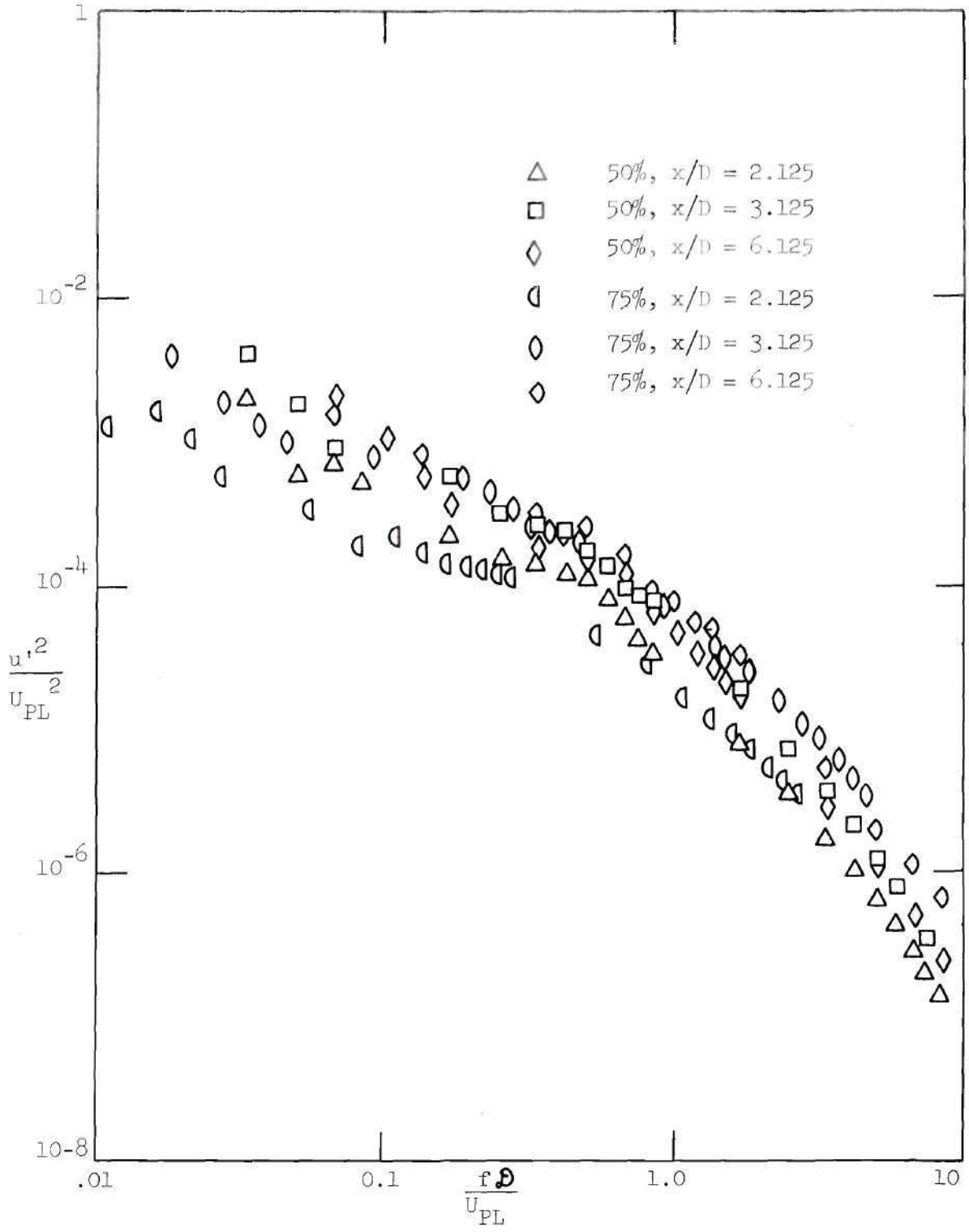

Figure 173. Local Strouhal Number Correlation for Sharp-Edged Occlusions, α = 15, F = 0.2 Hz, $R_{e_{D_P}}$ = 2540

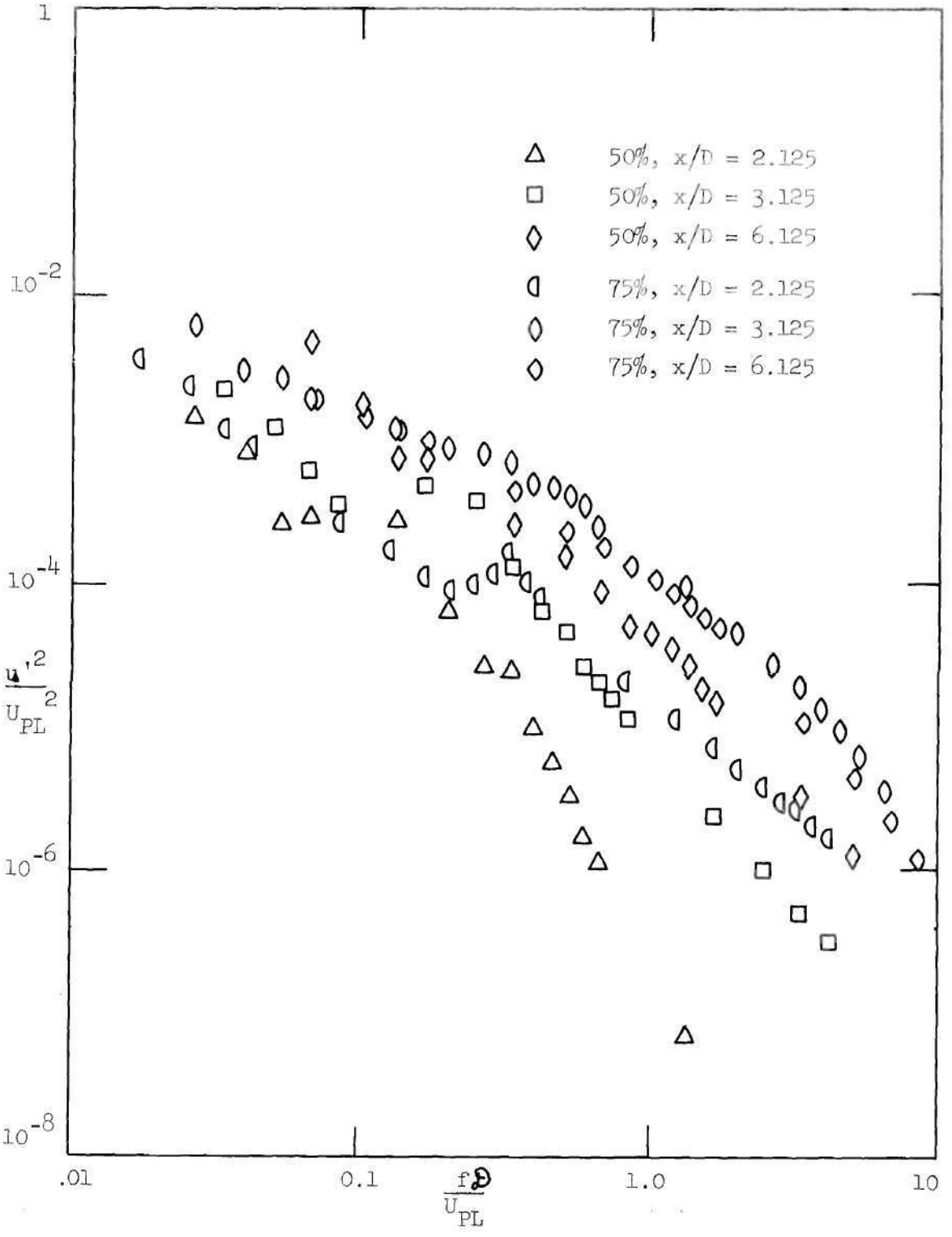

Figure 174. Local Strouhal Number Correlation for Contoured Occlusions, α = 15, F = 0.2 Hz, $R_{e_{D_P}}$ = 2.540

CHAPTER IX

PULSATILE FLOW ENERGY SPECTRA RESULTS AND DISCUSSION, α = 31.8 AND α = 45

This chapter presents the results of the measurement of the energy spectra downstream of the occlusions in pulsatile flow whose pulse rate and peak Reynolds numbers are considerably higher than those results discussed in Chapter VIII. Three different pulse rate conditions were used in these measurements, namely: (1) α = 31.8, R_{eDP} = 5,080, F = 1, (2) α = 45, R_{eDP} = 5,080, F = 2, and (3) α = 45, R_{eDP} = 15,200, F = 2. The flow conditions are considerably above those that would be expected for physiologically normal conditions. However, these higher frequency parameter and higher Reynolds number conditions are interesting from the standpoint that the development of turbulence should be substantially enhanced and, thus, more readily separated from the behavior of the transitional instabilities.

9.1 Velocity Waveforms for α = 31.4, R_{eDP} = 5,080 and α = 45, R_{eDP} = 15,200

The proximal waveforms for the two different flow conditions are shown in Figures 175, 176 and 177. The waveforms indicate a more complex shape than did the α = 15, R_{eDP} = 2540 results which were discussed in Chapter VIII. The waveforms for the α = 31.8, R_{eDP} = 5,080 case shown in Figure 177 indicate that the proximal waveform was slightly different

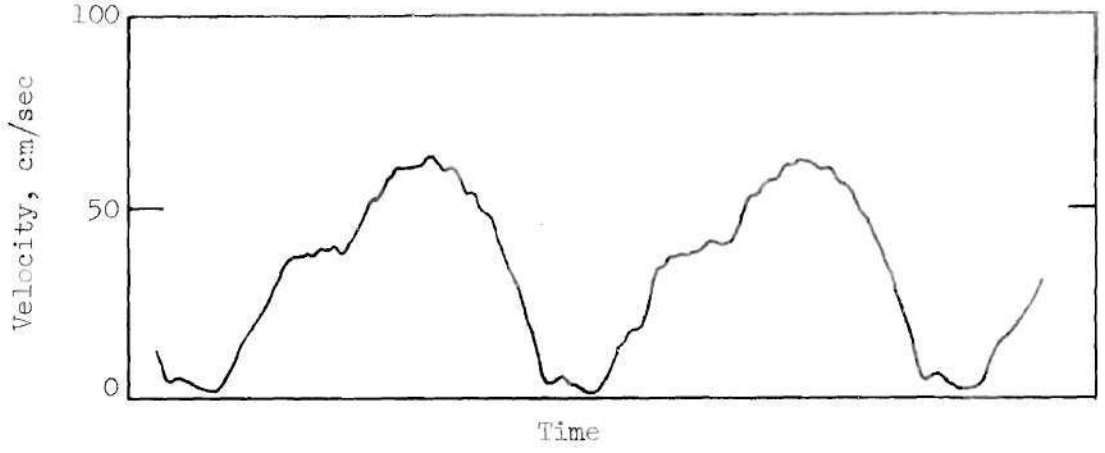

Figure 175 Proximal Velocity Waveform, U_p = 60 cm/sec, F= 2Hz

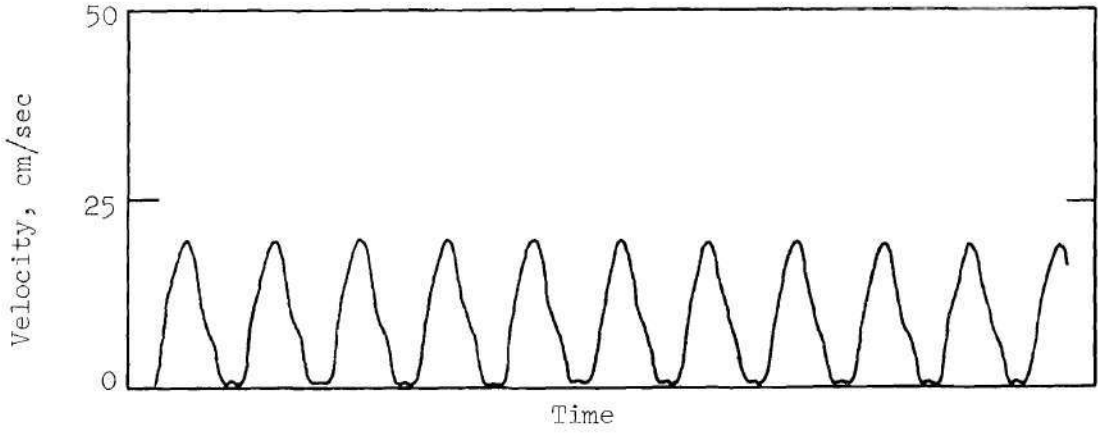

Figure 176 Proximal Velocity Waveform, U_p = 20 cm/sec, F = 2Hz

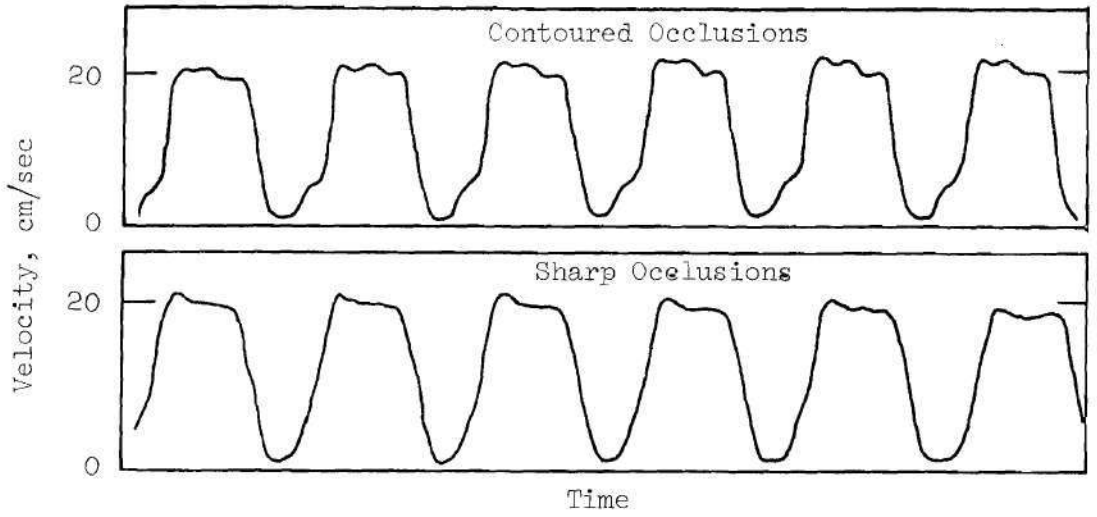

Figure 177 Proximal Velocity Waveform, U_p = 20 cm/sec, F = 1Hz

for the data obtained with the two occlusion geometries. It is believed that these differences do not significantly affect the energy spectra data.

9.2 Energy Spectra Results for $\alpha = 31.8$, $R_{eDP} = 5,080$

Figures 178 and 179 illustrate the effect of increasing the degree of constriction for the contoured and sharp-edged occlusions for a fixed axial position. The relative increase in the energy content at higher frequencies is apparent as the occlusion sizes increase from 0 to 75 percent area reduction for both occlusion shapes. The spectra for the 75 percent sharp-edged occlusion shows relatively intense harmonic peaks at 3, 5 and 7 Hz, whereas the lesser degrees of occlusion do not. None of the contoured occlusion spectra show this characteristic.

The variation of the energy spectra for the 75 percent occlusion as a function of axial position is shown in Figures 180 and 181 for the two constriction shapes. The decrease in the energy intensity as the probe is moved downstream is indicative of the spreading of the turbulent jet formed by the partial occlusion and of interaction of the jet with the tube wall.

9.3 Energy Spectra Results for $\alpha = 45$, $R_{eDP} = 5,080$

The comparisons of the energy spectra with increasing degree of constriction and with increasing downstream axial location are shown in Figures 182 through 185. The trends in the energy spectra for the sharp occlusions (Figures 181 and 182) are similar to these found at the lower α flow conditions; i.e., the overall energy intensity increases

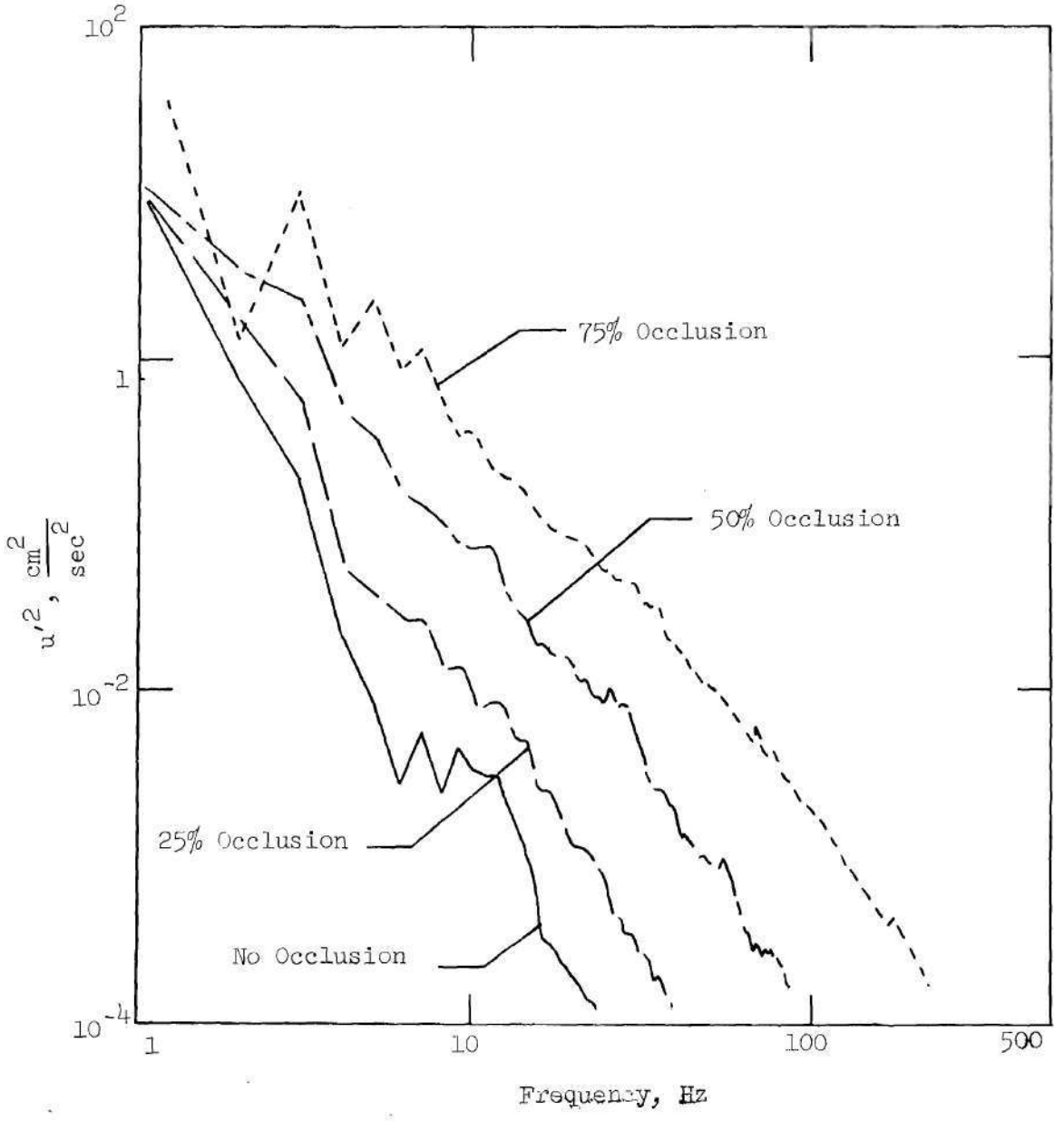

Figure 178. Effect of Area Reduction on Turbulent Energy Spectra, Sharp-Edged Occlusion, x/D = 1, F = 1 Hz, U_p = 20 cm/sec, $R_{e_{DP}}$ = 5,080, α = 31.8

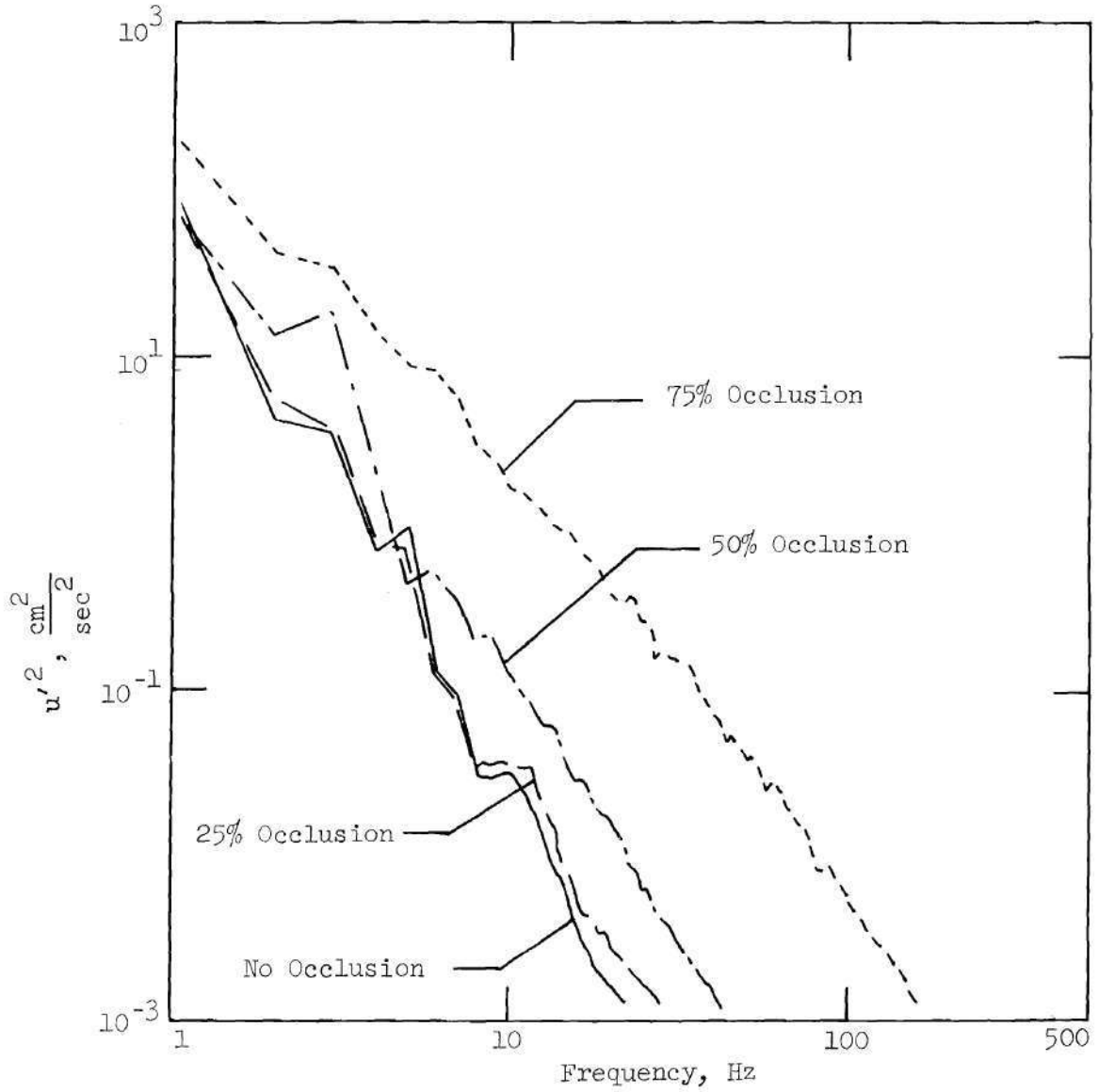

Figure 179. Effect of Area Reduction on Turbulent Energy Spectra, Contoured Occlusion, x/D = 2, F = 1 Hz, U_p = 20 cm/sec, $R_{e_{DP}}$ = 5.080, α = 31.8

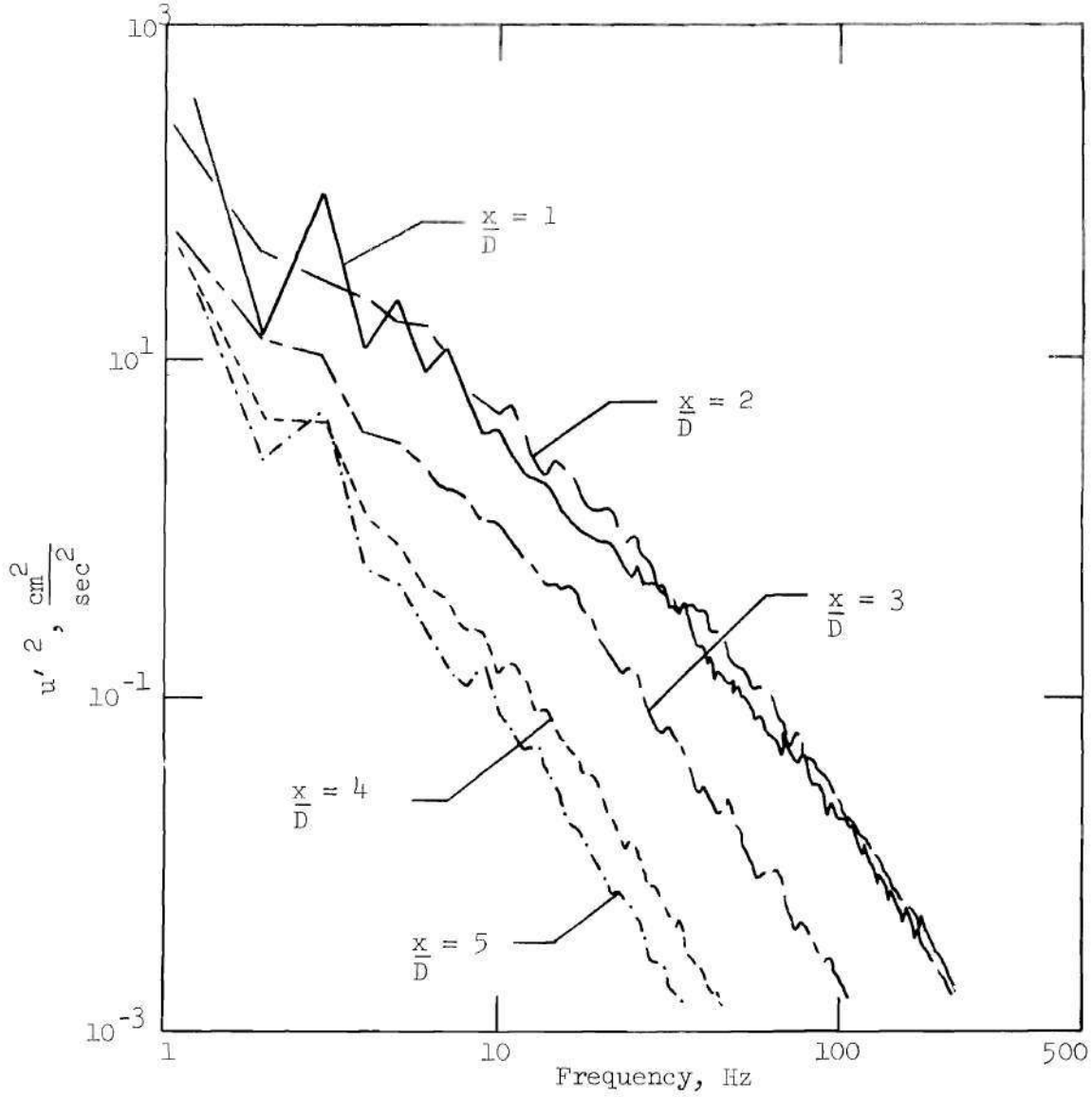

Figure 180. Effect of Axial Location Upon Turbulent Energy Spectra, 75% Sharp-Edged Occlusion, F = 1
U_p = 20 cm/sec, Re = 5,080, α = 31.8

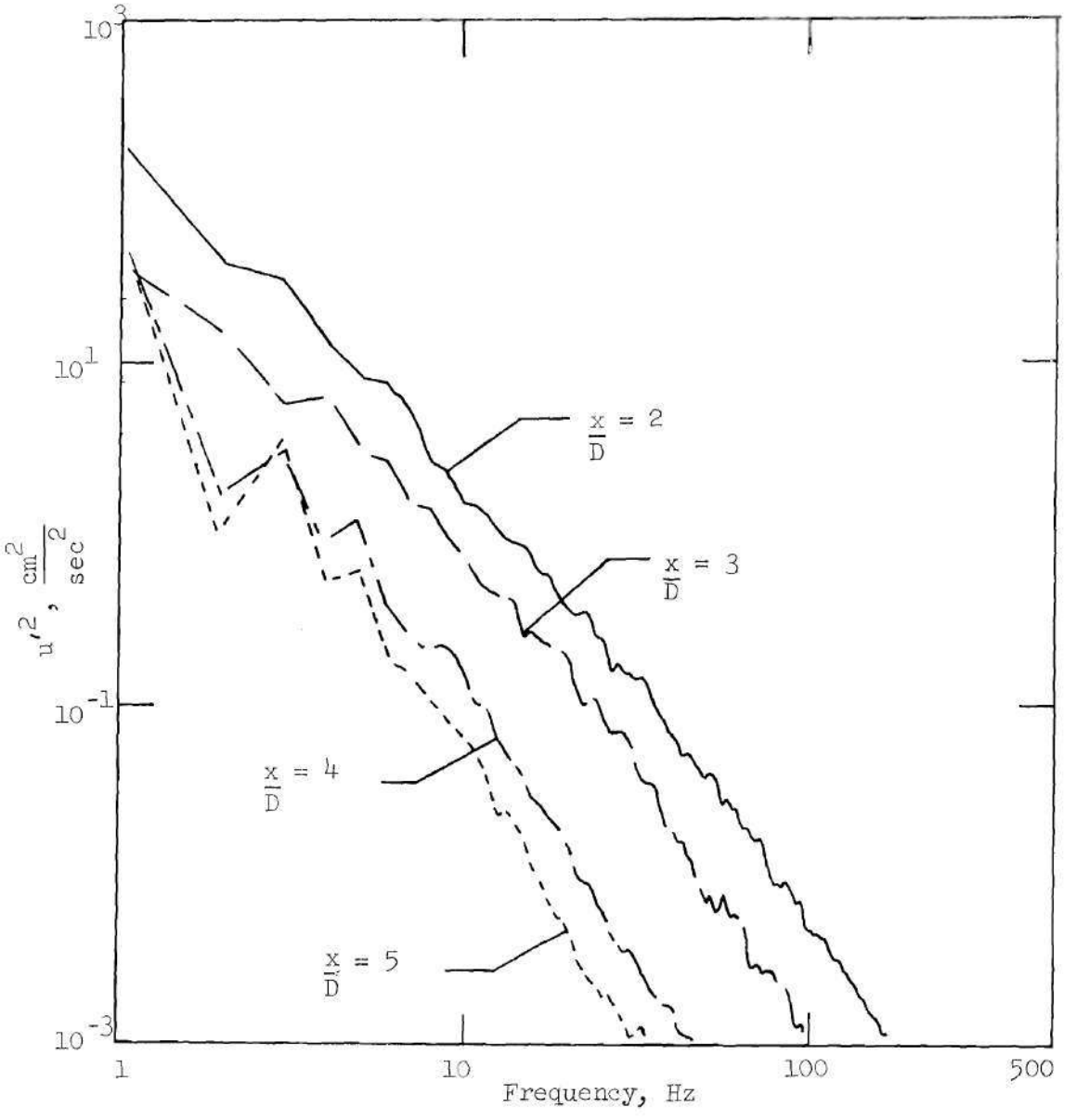

Figure 181. Effect of Axial Location Upon Turbulent Energy Spectra, 75% Contoured Occlusion, F = 1 Hz U_p = 20 cm/sec, Re = 5,080, α = 31.8

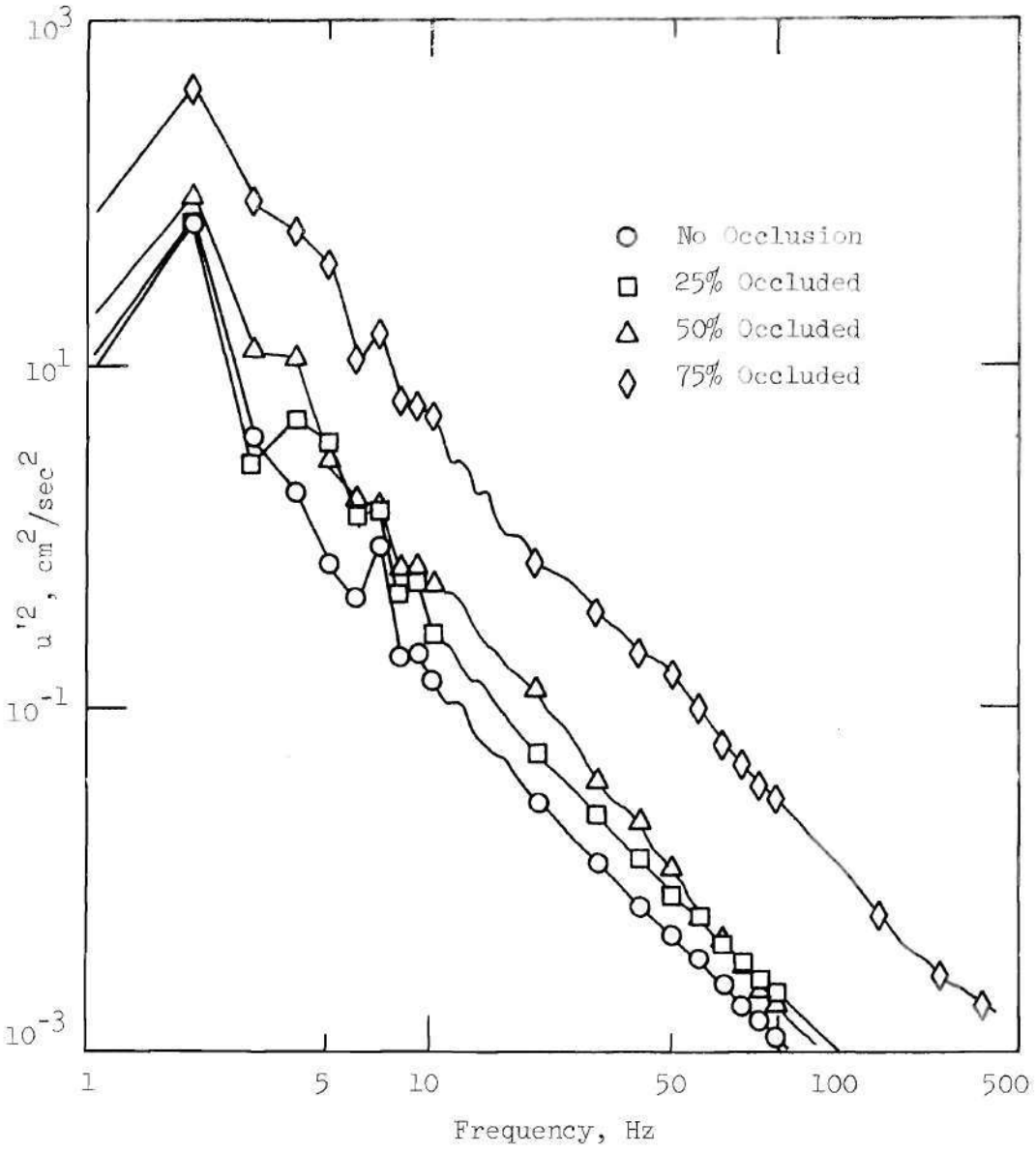

Figure 182. Effect of Area Reduction on Turbulent Energy Spectra, Sharp-Edged Occlusion, x/D = 1.0, F = 2 Hz, U_p = 20 cm/sec, $R_{e_{DP}}$ = 5,080, α = 45

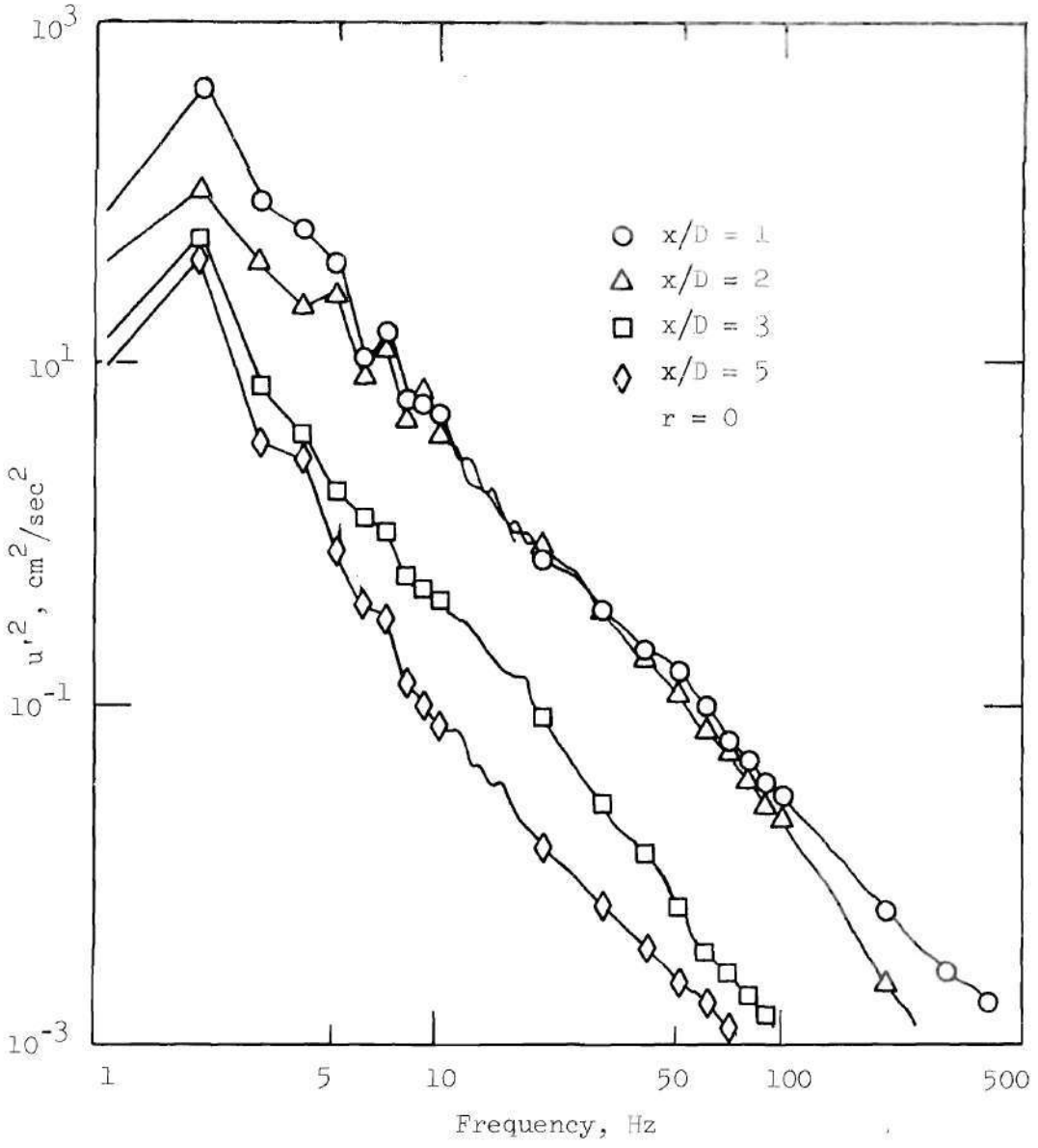

Figure 183. Effect of Axial Location Upon Turbulent Energy Spectra, 75% Sharp-Edged Occlusion, F = 2 Hz, U_p = 20 cm/sec, $R_{e_{DP}}$ = 5,080, α = 45

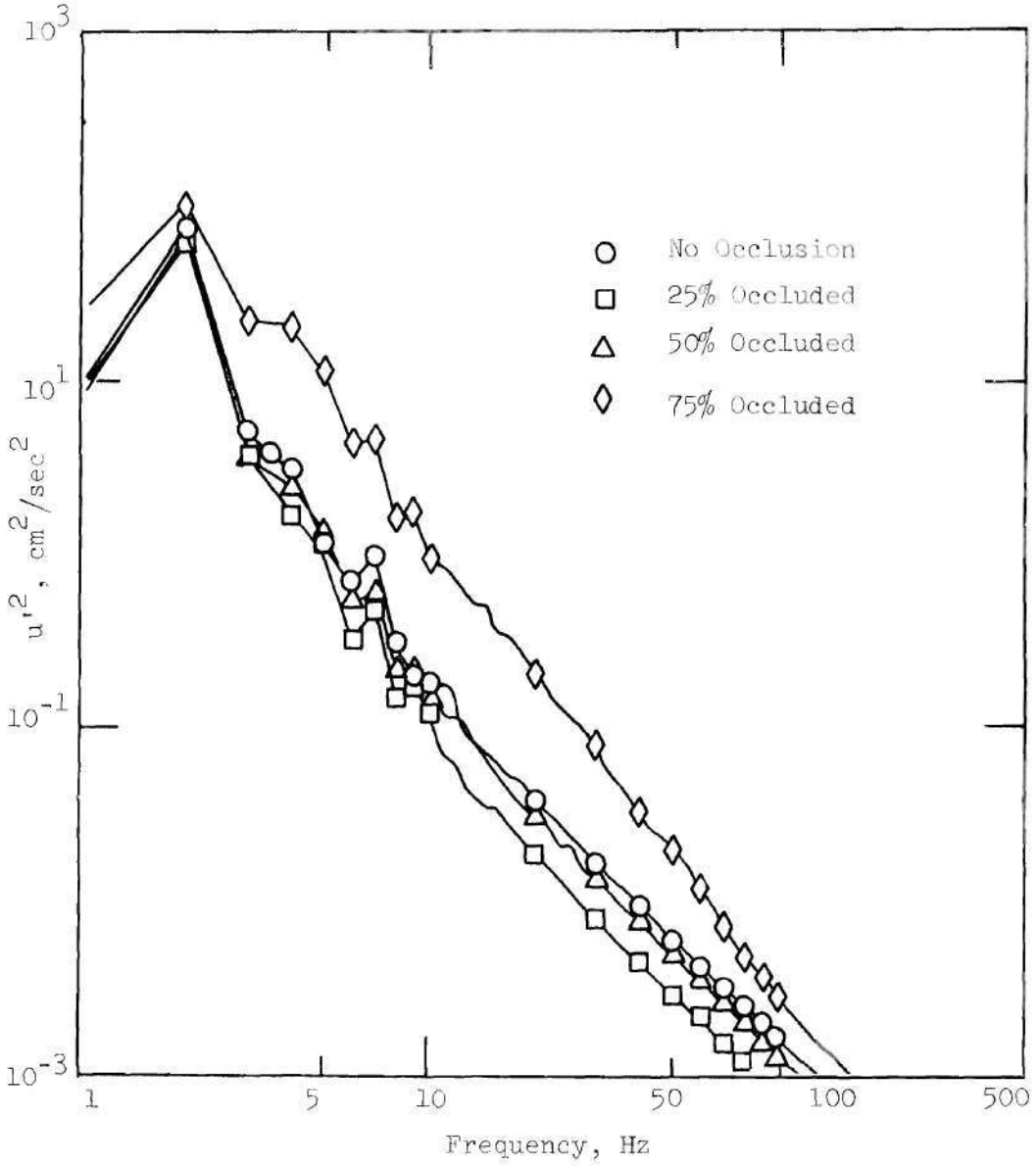

Figure 184. Effect of Area Reduction on Turbulent Energy Spectra, Contoured Occlusions, x/D = 2, F = 2 Hz, U_p = 20 cm/sec, $R_{e_{DP}}$ = 5,080, α = 45

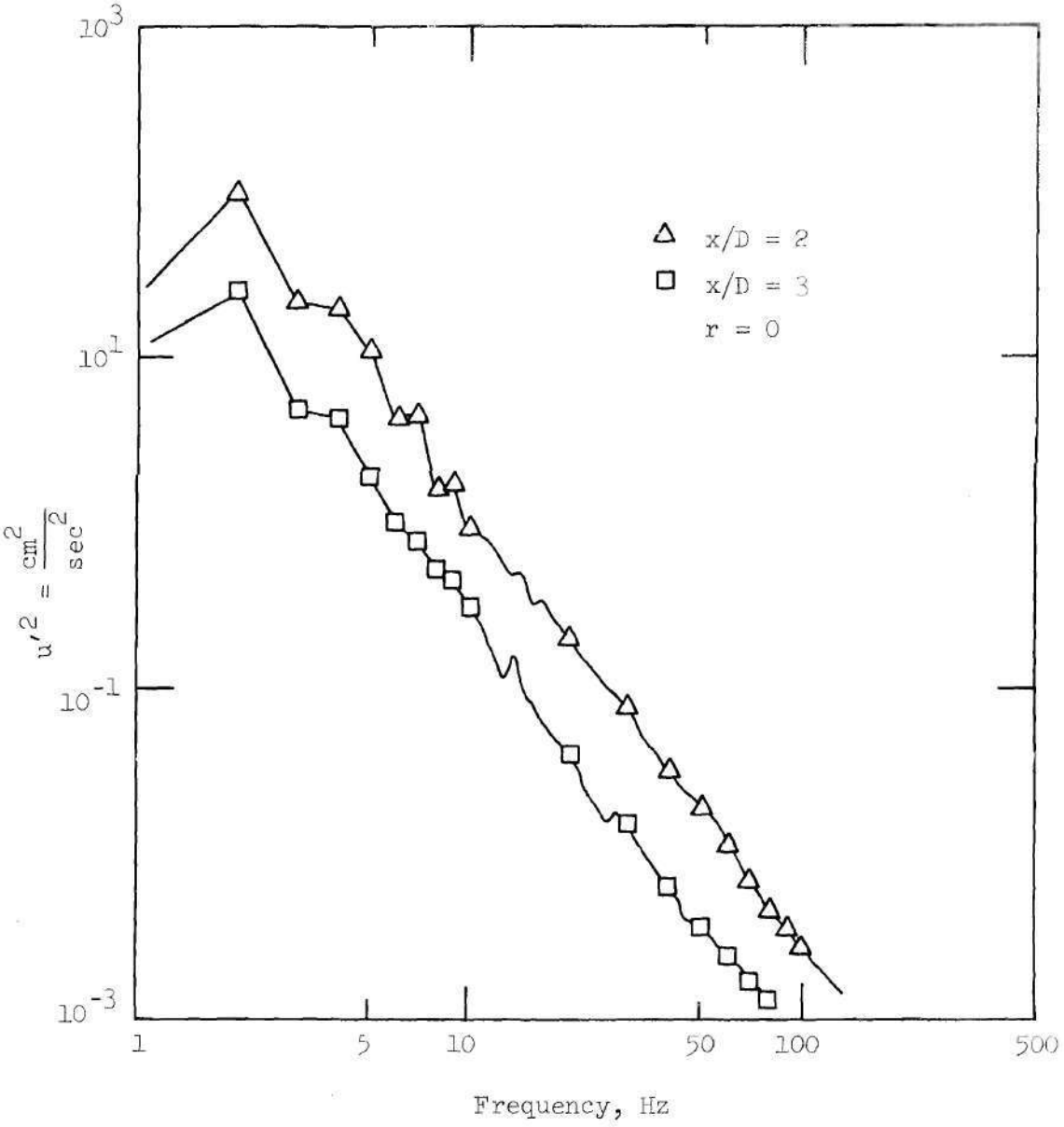

Figure 185. Effect of Axial Location Upon Turbulent Energy Spectra, 75% Contoured Occlusion, F = 2 Hz, U_P = 20 cm/sec, $R_{e_{DP}}$ = 5,080, α = 45

with the larger degrees of occlusion and decreases as the measurement point moves downstream from the constriction site. It should also be noted that the axial positions nearest to the occlusion, x/D = 1 and 2 in Figure 183, do not show an appreciable decrease in intensity.

The contoured occlusion results show a somewhat different trend with increasing degree of occlusion; this is indicated in Figure 184. The 25 percent and 50 percent occlusion energy spectra data actually show a slight decrease in intensity as compared with the no occlusion spectra. These smaller degrees of contoured occlusion appear to have damped the flucuations which were originally present in the unoccluded pulse. The 75 percent occlusion did result in an overall increase in energy intensity. The axial variation of the energy intensity for the 75 percent occlusion in Figure 185 indicates a similar trend as was found before with the sharp occlusion; however, the energy levels at these axial locations are noticeably lower than those obtained with the sharp occlusions.

9.4 Energy Spectra Results for $\alpha = 45$, $R_{eDP} = 15{,}200$

The resulting trends in the energy spectra for these flow conditions are summarized in Figures 186 and 187. As the degree of constriction is increased from 0 to 75 percent with the contoured constrictions, the overall intensity increases noticeably as demonstrated in Figure 186. The axial variation of the energy spectra is presented in Figure 187 for the 75 percent contoured occlusion. The overall energy intensity remains essentially the same downstream of the occlusion to about x/D = 4 and then shows a noticeable decrease at x/D = 6.

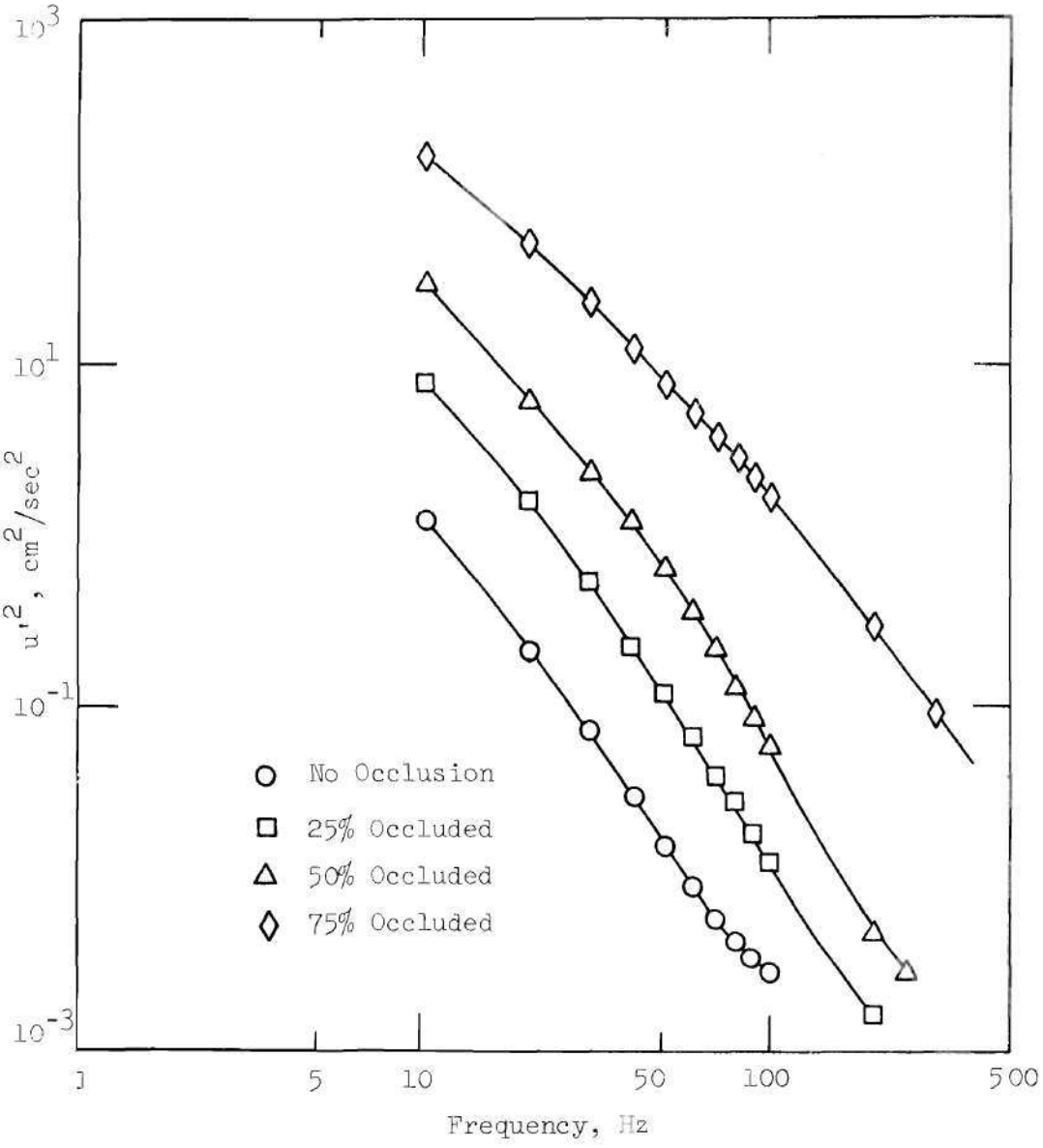

Figure 186. Effect of Area Reduction on Turbulent Energy Spectra, 75% Contoured Occlusion, x/D = 2, F = 2 Hz, U_p = 60 cm/sec, $R_{e_{DP}}$ = 15,200, α = 45

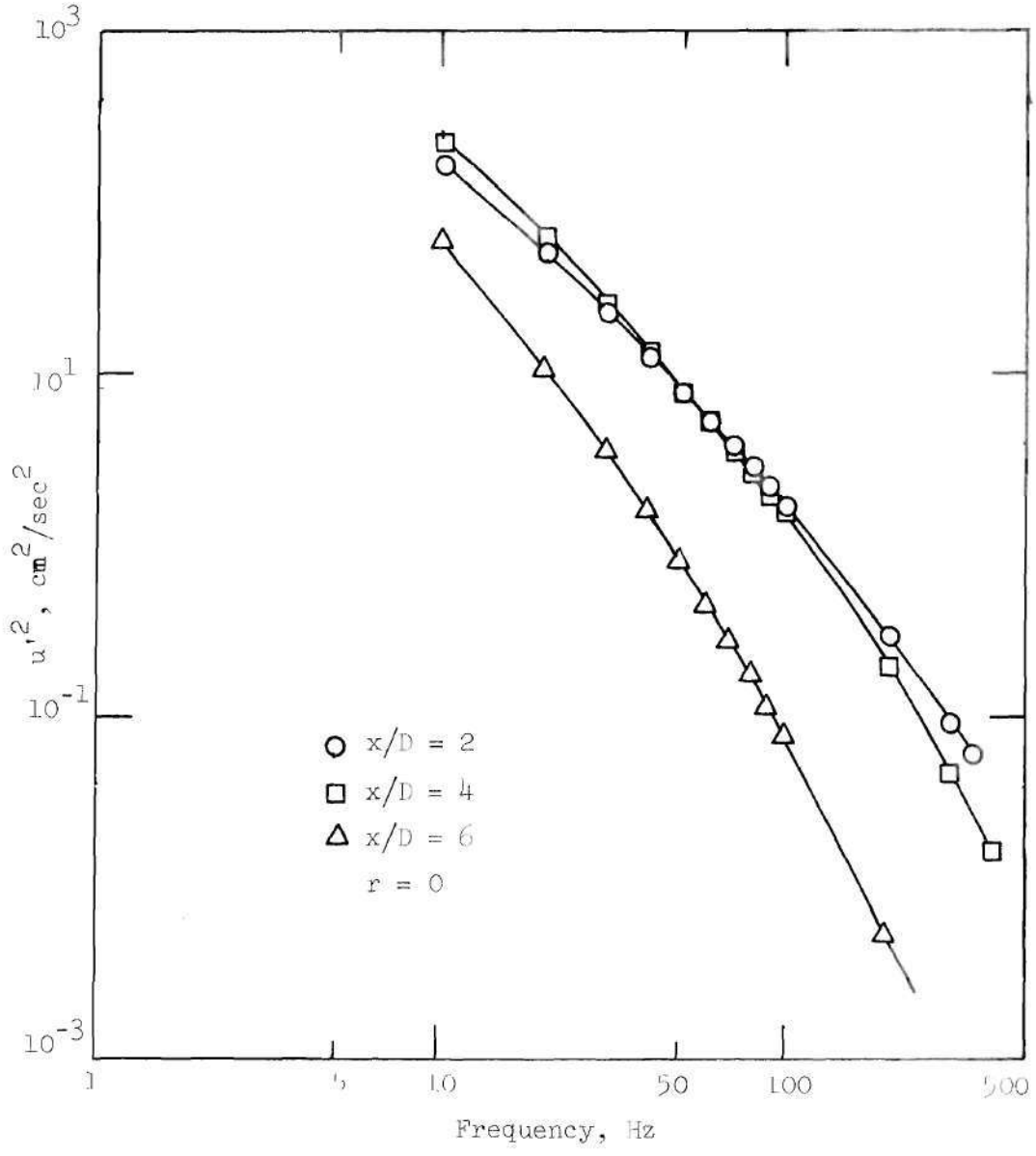

Figure 187. Effect of Axial Location on Turbulent Energy Spectra, 75% Contoured Occlusion, F = 2 Hz, U_p = 60 cm/sec, $R_{e_{DP}}$ = 15,200, α = 45

9.5 Correlation of the Energy Spectra with Strouhal Number

In the region within approximately one pulse length from the minimum area, the flow characteristics are dominated by the jet emerging from the constriction in the tube. It can be observed in the energy spectral data obtained for this particular case, $\alpha = 45$, $R_{eDP} = 15{,}200$, that the velocity fluctuations, u'^2, can be correlated with the Strouhal number, fd/U_o. This observation is different from the data obtained at $\alpha = 15$, $R_{eDP} = 2540$ (Section 8.6) where correlation with a "local" Strouhal number and $u'^2/\bar{U}^2_{LP}$ was shown.

In this region, if the data are plotted against Strouhal number, fd/U_o, for differing degrees of occlusion at the same axial location, the spectra appear to correspond. As illustrated in Figures 188 through 191, the spectra for both sharp-edged and well-rounded occlusions exhibit very little difference when plotted in this manner. Spectra which have been measured outside the region of direct jet influence do not show the correspondence presumably since the results would also be influenced by the turbulent field interacting with the tube wall. This is shown in Figures 192 and 193. Figure 192 illustrates this effect at $x = 6D$ whereas the data obtained at $x = 2D$ (Figure 190) and $x = 4D$ (Figure 191) did correlate with Strouhal number. Figure 193 shows data obtained at $x = 2D$ for a larger fundamental pulse rate of 2 Hz ($\alpha = 45$) which does not correlate with Strouhal number whereas the data at a lower pulse rate of 1 Hz ($\alpha = 31.8$, Figure 188) does correlate reasonably well.

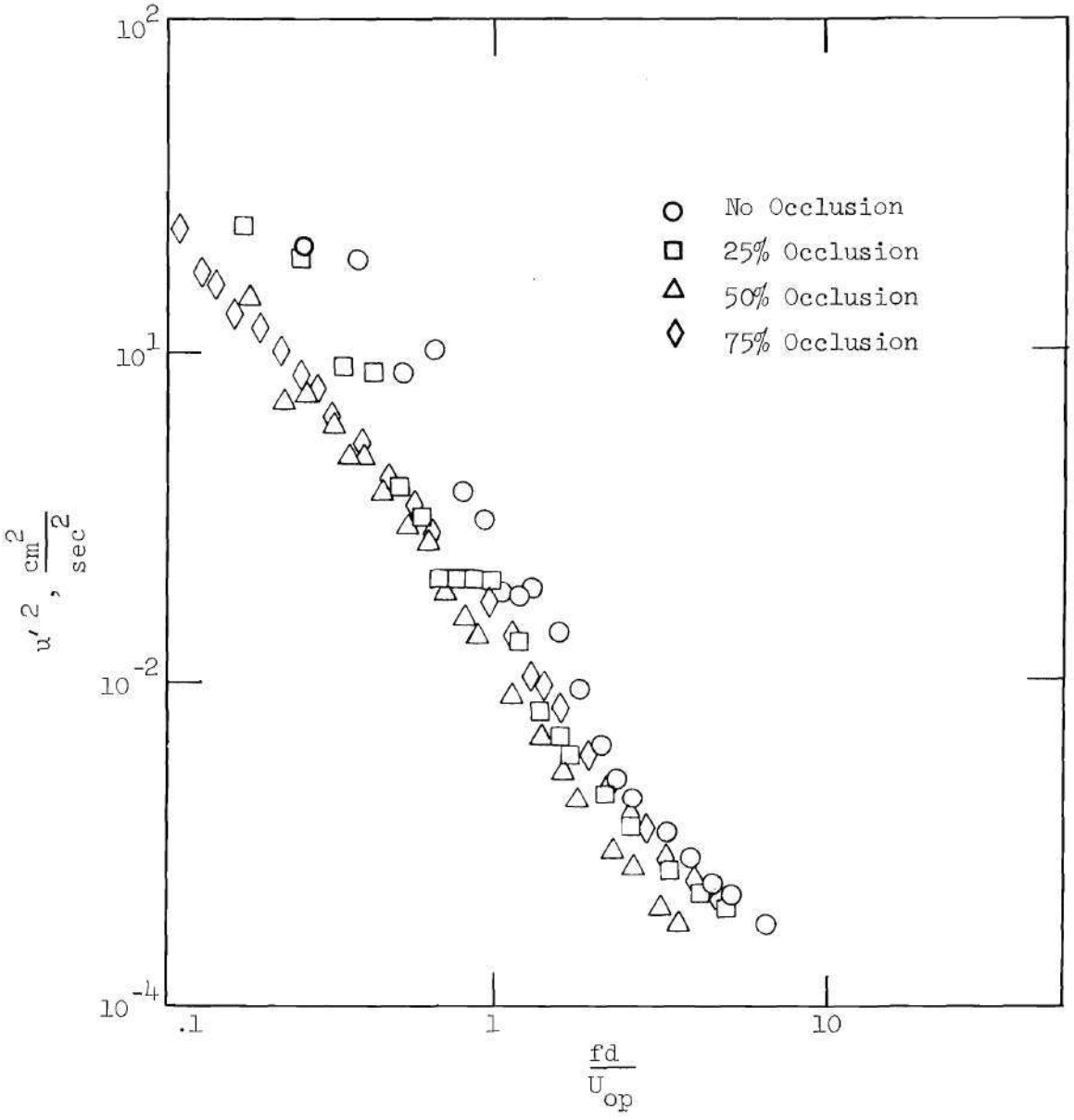

Figure 188. Strouhal Number Correlation, x = 2D, Contoured Occlusion, F = 1 Hz , U_p = 20 cm/sec, Re = 5,080, α = 31.8

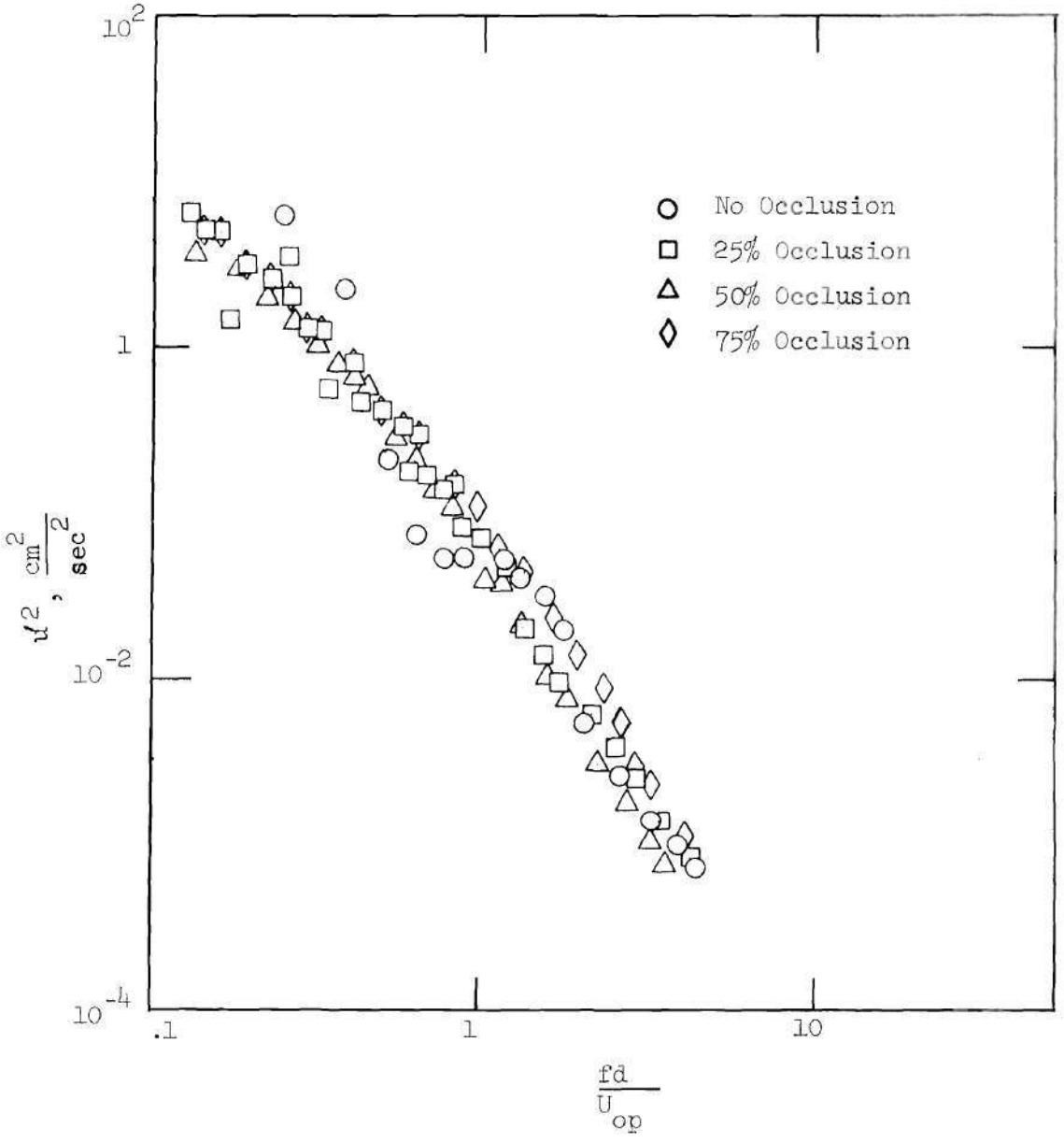

Figure 189. Strouhal Number Correlation, x/D=2, Sharp-Edged Occlusion, F = 1 Hz, U_p = 20 cm/sec, Re = 5,080, α = 31.8

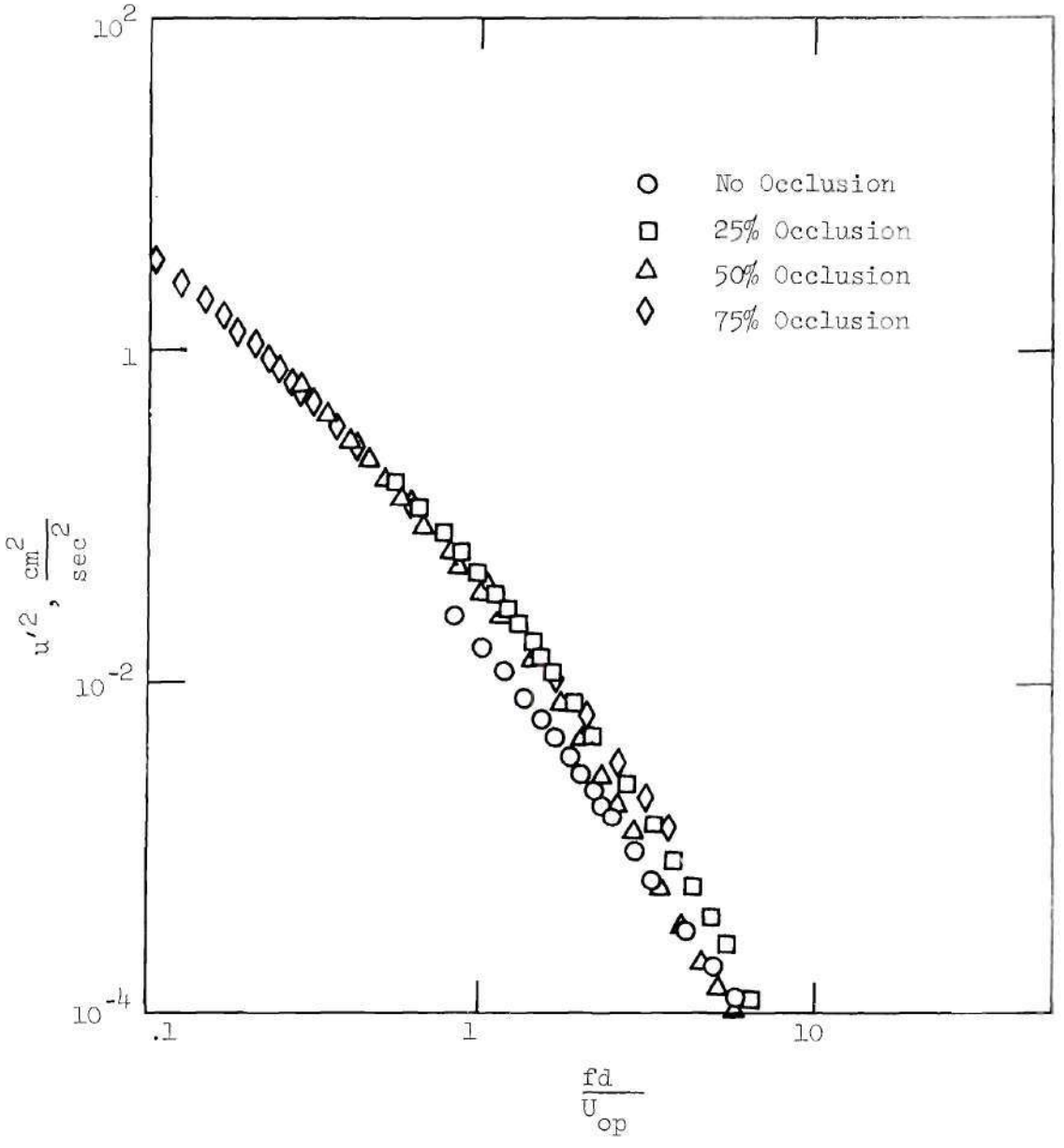

Figure 190. Strouhal Number Correlation, x/D=2, Contoured Occlusion, F = 2 Hz, U_p = 60 cm/sec, Re = 15,200, α = 45

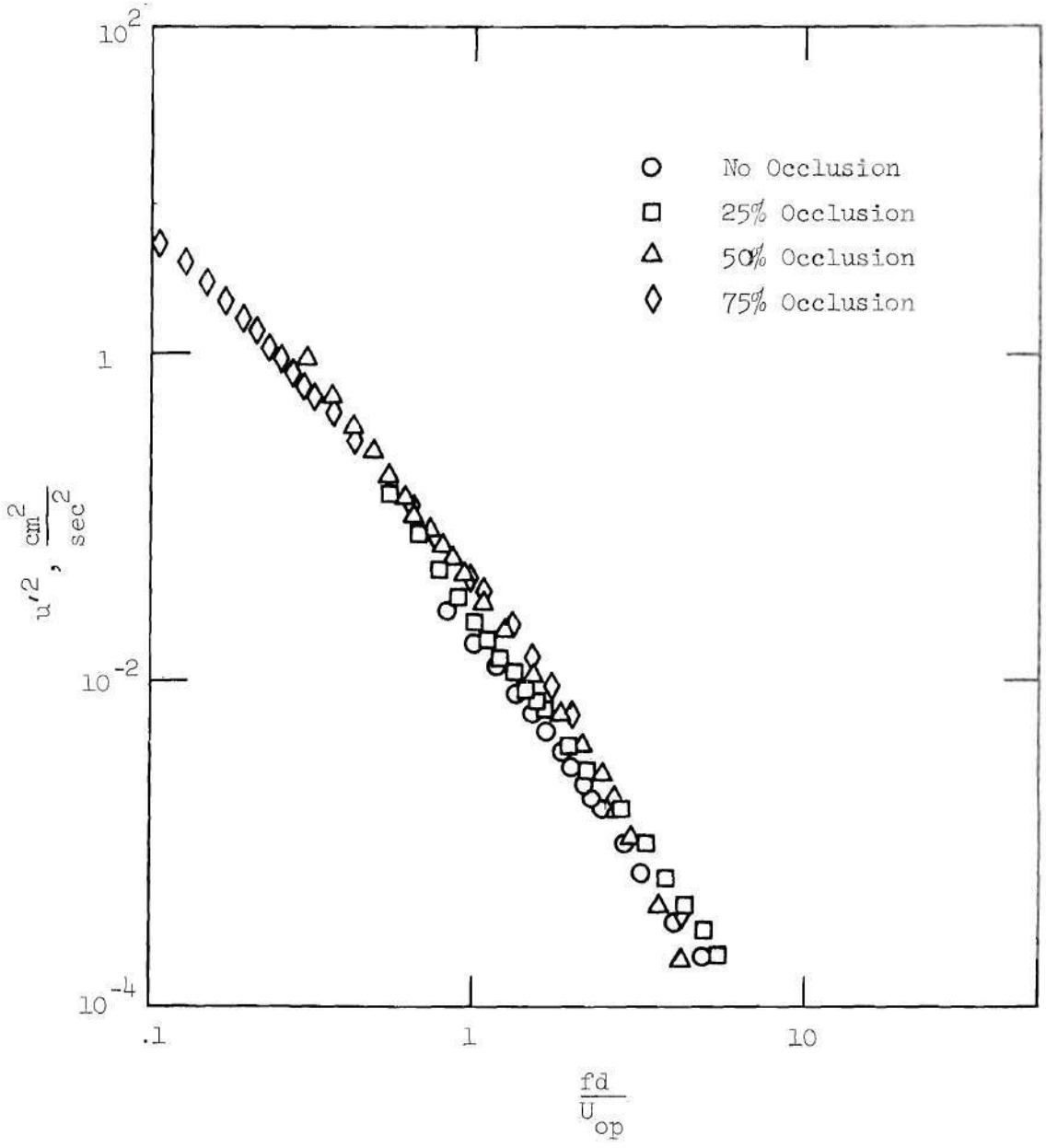

Figure 191. Strouhal Number Correlation, x/D=4, Contoured Occlusion, F = 2 Hz, U_p = 60 cm/sec, Re = 15,200, α = 45

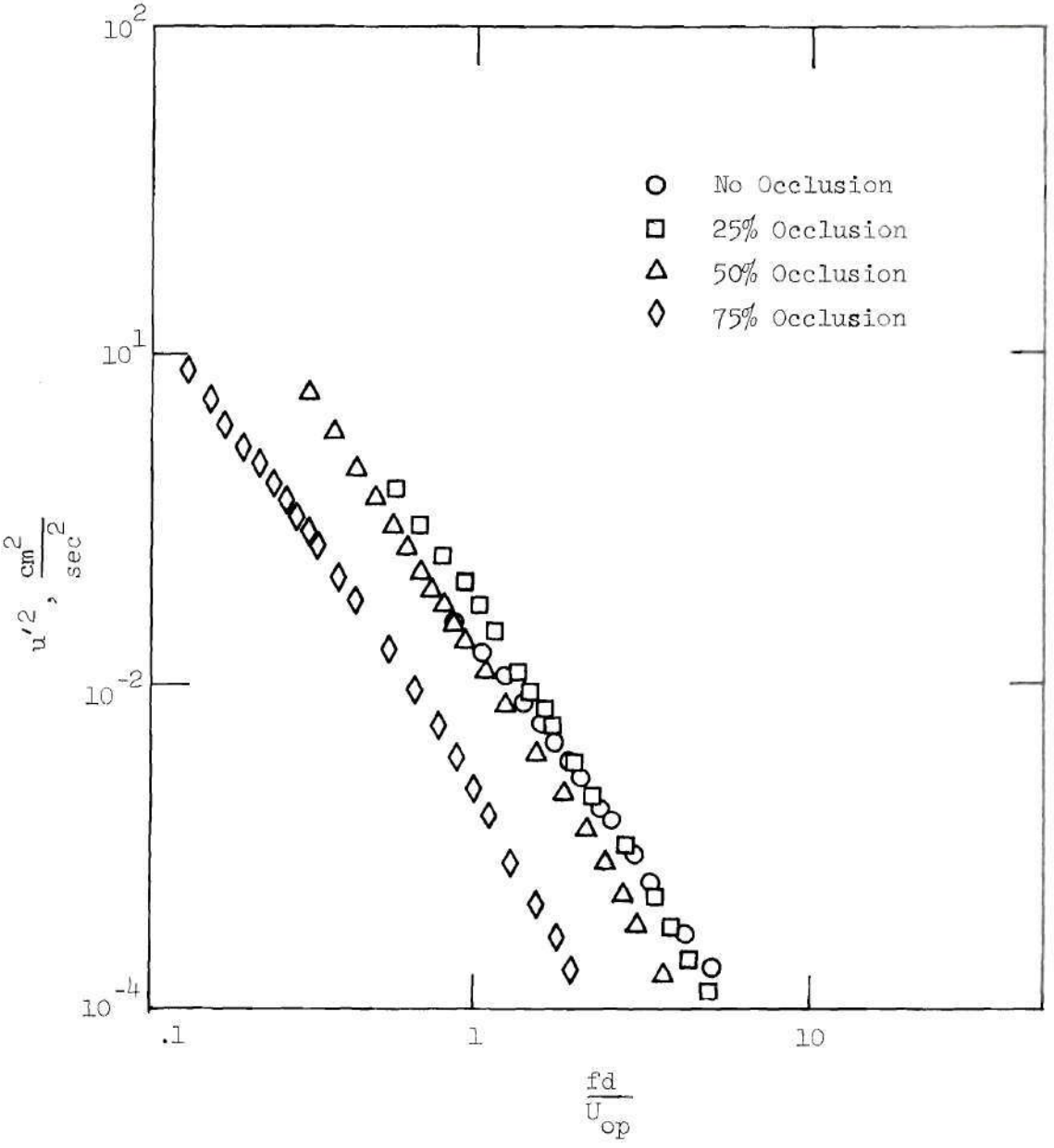

Figure 192. Strouhal Number Correlation, $\frac{x}{D} = 6$, Contoured Occlusion, F = 2 Hz, U_p = 60 cm/sec, Re = 15,200, α = 45

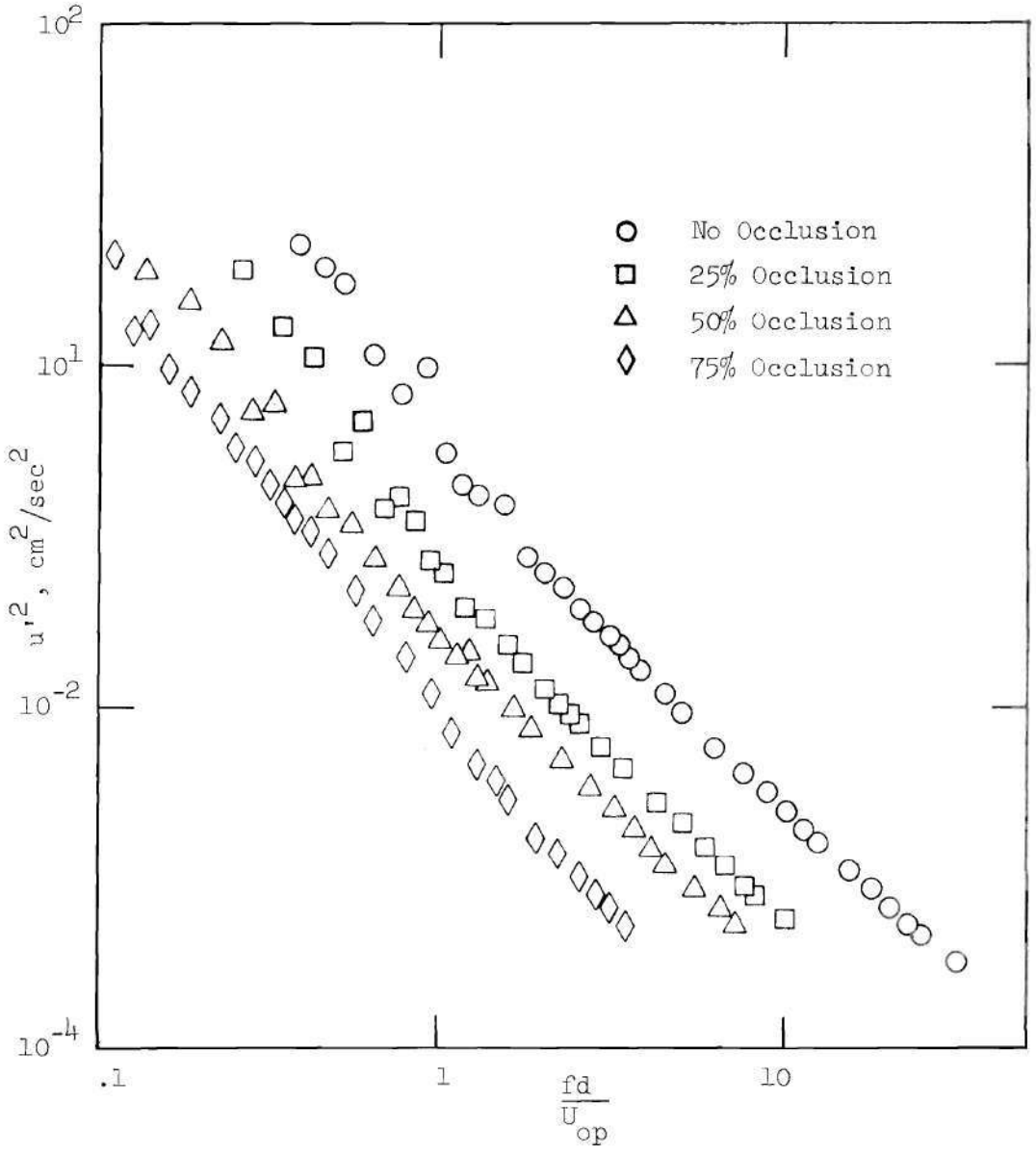

Figure 193. Strouhal Number Correlation, x/D = 2, Contoured Occlusion, F = 2 Hz, U_p = 20 cm/sec, Re = 5,080, α = 45

CHAPTER X

CONCLUSIONS AND RECOMMENDATIONS

The flow fields downstream of axisymmetric constrictions in rigid tubes have been investigated for steady and pulsatile flows with the goal of studying the flow instabilities and turbulence which occur in this region. In general, the turbulent energy spectra obtained in both steady and pulsatile flows show an increase in the overall energy level and a relative increase in the high frequency content of the velocity flucuations as the constriction blockage increases for the same proximal flow conditions. Other more specific conclusions and implications are noted in the following sections.

10.1 Steady Flow

The results of the steady flow inevstigations may be summarized in the following conclusions:

1. As noted in previous investigations, the flow visualization indicated that the separation and reattachment of the flow distal to the constrictions are dependent on the Reynolds number and the occlusion geometry.

2. In the region immediately downstream of the constriction a vortex ring pattern forms which produces velocity fluctuations in a narrow frequency band. The velocity fluctuation frequency decreases with increasing downstream axial distance but the intensity of these fluctuations grows as the vortex rings move downstream until the pattern

dissipates into a more randomly distributed frequency spectrum. The "orifice" Strouhal number, fd/U_o, of the vortex shedding frequency corresponding to the most intense velocity fluctuation is about 0.6 for the sharp-edged occlusions and about 0.4 for the contoured occlusions. The "orifice" Strouhal number of the vortices decreased with increasing axial distance but the "local" Strouhal number did not show as great a dependence on axial distance.

3. The energy spectra obtained along the centerline at the same R_{ed} and x/d in the jet dominated, near-distal region of the 75 percent and 90 percent sharp-edged occlusions scales by forming the nondimensional velocity fluctuation energy ratio, u'^2/U_o^2, and the nondimensional frequency ratio or Strouhal number, fd/U_o.

4. For the same R_{ed} and degree of constriction, the sharp-edged occlusions produced more intense velocity fluctuations at all axial locations than did the contoured occlusions.

10.2 Pulsatile Flow

The results of the pulsatile flow investigations may be summarized in the following statements:

1. In general, the pulsatile energy spectra show more radial homogeneity than did the steady flow spectra obtained in the same R_{ed} range. This homogeneity is caused in part by a large low frequency vortex which swirls into the near-wall region immediately distal to the constriction during the initial phase of the velocity pulse. This same region is occupied by low energy recirculatory flow in the steady flow case. Also contributing to the homogeneity is the diffusion of

turbulence during the deceleration phase of the velocity pulse. For the more severe degrees of occlusion, the diffusion is predominately from the central portion of the flow toward the wall. For slight degrees of occlusion the turbulence is generated at or near the wall principally during the deceleration phase and quickly diffuses toward the centerline of the flow during the lowest velocity phase of the fundamental pulse. Therefore, the pulsatile flow through occlusions is characterized by the lack of a continuous and distinct recirculation zone.

2. *At the lower pulse rate tested,* $\alpha = 15$, $R_{eDP} = 2540$, with the sinusoidal shaped proximal waveform, no clear energy spectra correlation with a nondimensional energy or Strouhal number based on the orifice flow conditions could be seen. However, by using a nondimensional fluctuation energy and Strouhal number based on the local flow conditions, the spectra obtained with the 50 percent and 75 percent sharp-edged occlusions correlated reasonably well in the region of fully developed turbulent flow.

3. The higher frequency parameter and higher Reynolds number data obtained with a complex proximal waveform indicated that in the region dominated by the occlusive jet flow, the velocity fluctuations could be correlated with the degree of the constriction by using the nondimensional Strouhal number, fd/U_o.

10.3 Implications of the Present Results to Stenotic Flows

Previous investigators of vessel wall damage in cardiovascular diseases have furnished a limited amount of evidence on the interplay

of hemodynamics and the formation of atherosclerotic plaques. It has been suggested that a large recirculatory zone distal to stenoses prevents the transfer of nutrients to the vessel wall and contributes to further degeneration of vessel tissues.[34] The present study suggests that a large continuous stagnant recirculatory zone does not exist in pulsatile flow through stenosis. Turbulence in the frequency range of 20 to 50 Hz distal to occlusions has been suggested as a factor in poststenotic dilation[7]. The turbulent spectra reported here indicate that highly energetic turbulent fluctuations do indeed exist throughout the vessel cross-section in the near distal field of the simulated stenosis. The turbulence is most intense in the distal region approximately 2D to 3D from the constriction site which indicates that vessel wall damage would be most likely in this region.

The present results indicate that very slight obstructions can produce significant turbulence in pulsatile flow. This fact suggests that fluid mechanical aspects may influence the development of the occlusion shape after the initial formation of the plaque begins. The presence of detectable turbulence for slight obstructions indicates that if sensitive, noninvasive techniques such as an ultrasonic doppler velocimeter, could be used in clinical diagnoses, the initial formation of occlusions could be detected long before the constriction increased to the point of producing audible turbulence.

10.4 Recommendations for Future Research

This investigation has considered a flow field which is somewhat simpler than that which would occur in a physiologically realistic

situation. The following additional parameters should be included in future systematic studies to develop a better understanding of the interactions of the fluid with the vessel wall.

1. Elastic tubes and stenoses should be used to determine the feedback and/or damping effects of the tube wall on the fluid fluctuations. Several different elasticities whose values correspond to those found in healthy and diseased arteries should be included.

2. Asymmetric and irregularly shaped stenoses should be used since most, if not all, of cardiovascular occlusions are in this category.

3. The effects of pulse waveform, as defined by the frequency parameter and harmonic content, on the development of instabilities and turbulence should be determined.

4. Experiments should be conducted using pulsed free jets to examine the effect of wall proximity on the formation of large and small scale turbulence.

APPENDIX

HOT FILM ANEMOMETER

This appendix gives a detailed description of the principle of operation, manufacturer's model numbers, calibration techniques and operating procedures for the hot film anemometer system.

Principle of Operation

The measurement of fluid velocity by use of hot film (or hot wire) anemometry is based on the convective heat loss from a heated sensing surface to the surrounding fluid. In general, the heat loss depends on the temperature, geometrical shape, and dimensions of the sensor, and on velocity and thermodynamic properties of the fluid being studied.[37,38] For a given sensor and fluid, the heat loss then becomes a measure of the fluid velocity if the sensor and fluid temperatures are known. A more generalized discussion of the commonly used probe configurations, applications and particular characteristics can be found in the references.[37,38] This discussion will concentrate on the conical hot film probe which is used in these experiments and shown in Figure 194.

The conical hot film probe was employed because: (1) this probe configuration has been used extensively in related *in vivo* experiments and will permit a comparison of *in vivo* and *in vitro* results without probe characteristic biasing, (2) this geometry is less prone to

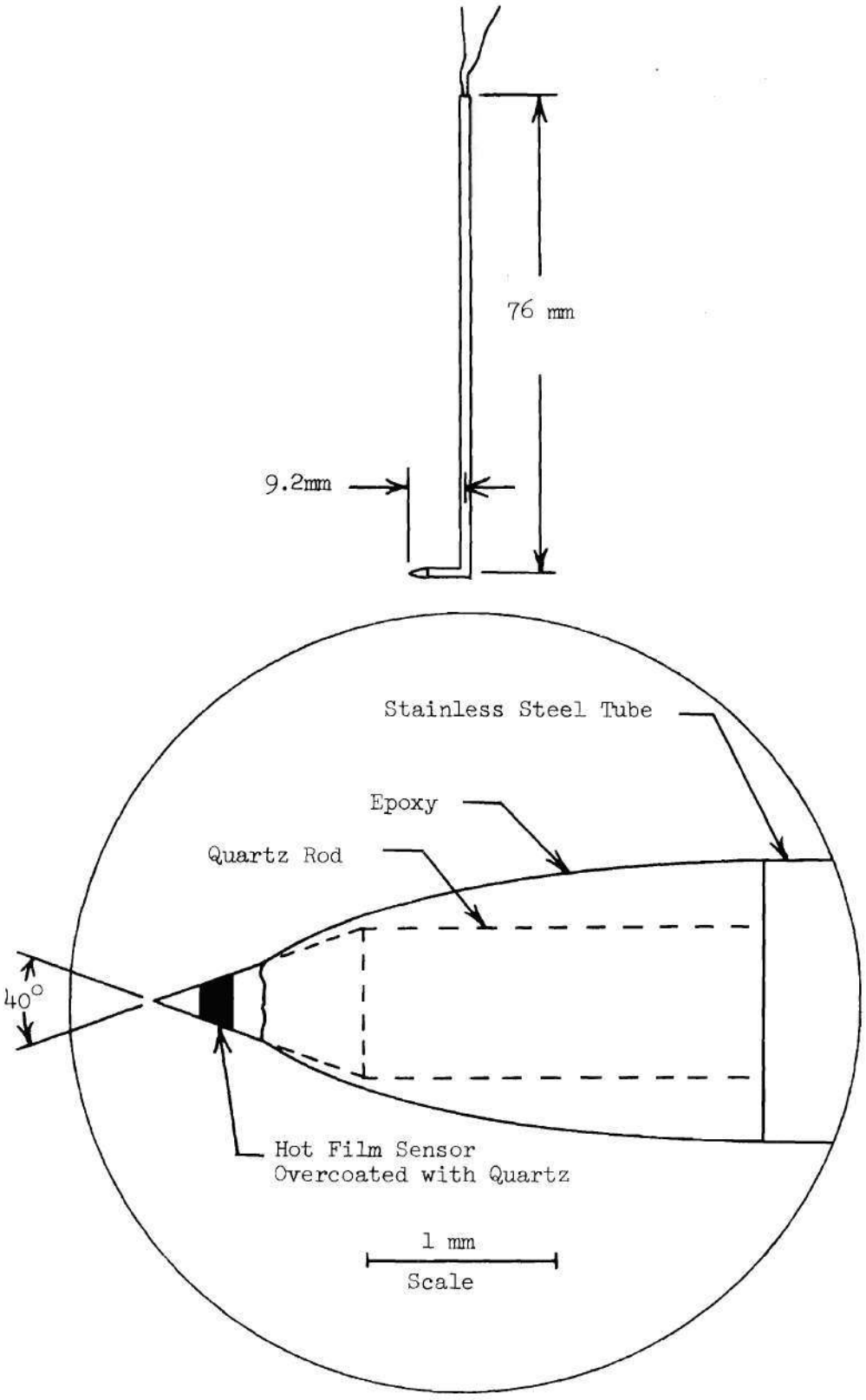

Figure 194. Conical Hot Film Probe

contamination, and (3) the configuration allows easy insertion through the tube walls. The flow sensor is a vacuum-sputtered film of either nickel or platinum deposited on the conically shaped end of a quartz rod. The film thickness is only a few thousand angstroms to minimize thermal inertia. Electrical insulation from the surrounding fluid medium is achieved by overcoating the film with a 1 or 2 micron thick layer of quartz. This thickness of quartz is sufficiently thin so that damping of the dynamic heat transfer is not a factor in the frequency response of the sensor. Probes manufactured commercially by Thermo Systems Incorporated (TSI) and DISA Electronics (DISA) were used in these experiments and have similar configurations and characteristics. The TSI probe is designated Model 1264W and the DISA probe was a blood flow probe which was also used extensively in the in vivo experiments described in Reference 9.

The sensor element is heated to the desired temperature by current supplied from an anemometer, basically consisting of a Wheatstone bridge in which the sensor forms part of one bridge arm and an amplifier. The current flowing through the bridge heats the sensor, and the amplifier output voltage is a measure of the heat loss from the sensor. The system can be operated either in a constant current mode or a constant temperature mode. In the constant current mode, the heating current to the sensor is held constant and the probe temperature is allowed to vary with the flow velocity. In the constant temperature mode, the probe temperature, of probe resistance in the bridge, is held constant. The bridge voltage necessary to maintain this constant

resistance is a measure of the heat transfer and hence, also the fluid velocity. Of the two modes, the constant temperature system has inerenetly better frequency response, greater sensitivity and less chance of probe burn-out. All data reported here were obtained with a constant temperature system.

The most desirable sensor operating temperature is chosen by consideration of several factors: (1) the sensitivity required, (2) fluid temperature, and (3) in the case of liquids, the temperature at which bubbles tend to form. The overheat ratio is defined as:

$$\frac{R_H}{R_c} = 1 + \alpha\,(T_s - T_f)$$

where R_H = operating resistance of sensor

R_c = resistance of sensor at fluid temperature

α = temperature coefficient of resistance of sensor at the fluid temperature

T_s = sensor temperature

T_f = fluid temperature

Of great importance in preserving probe sensitivity and calibration repeatability is the use of the same overheat, R_H/R_c, in the calibration and use of the probe. For use in water, an overheat ratio of 1.01 is a good compromise.

In general, the bridge voltage output is related to the fluid velocity by the relation:

$$V^2 = V_o^2 + KU^n$$

where U = fluid velocity

V = bridge voltage at velocity U

V_o = bridge voltage for $U = 0$

K and n = constants which depend on the thermodynamic properties of the fluid, probe geometry and the overheat ratio.

This nonlinear relationship can create additional complexity during data analysis. For this reason, a linearizer circuit is employed to transform the nonlinear anemometer output voltage into a voltage which can be related directly to the fluid velocity.

Two different anemometer-linearizer systems were used in the course of the experiments: (1) a DISA Model 55D01 anemometer and Model 55D10 linearizer, and (2) a TSI Model 1050 anemometer and Model 1052 linearizer. Both of the linearizers could be adjusted to linearize a particular calibration curve to within ± 5 percent or better in a one decade velocity range.

Hot Film Probe Calibration

The relationship between the anemometer bridge voltage and the fluid velocity was determined for each probe by calibration in a water flow whose velocity was accurately known. The probes were calibrated with the aid of the calibration table shown in Figure 195. The apparatus consists of a circular channel machined in a 1 inch thick plexiglas disc

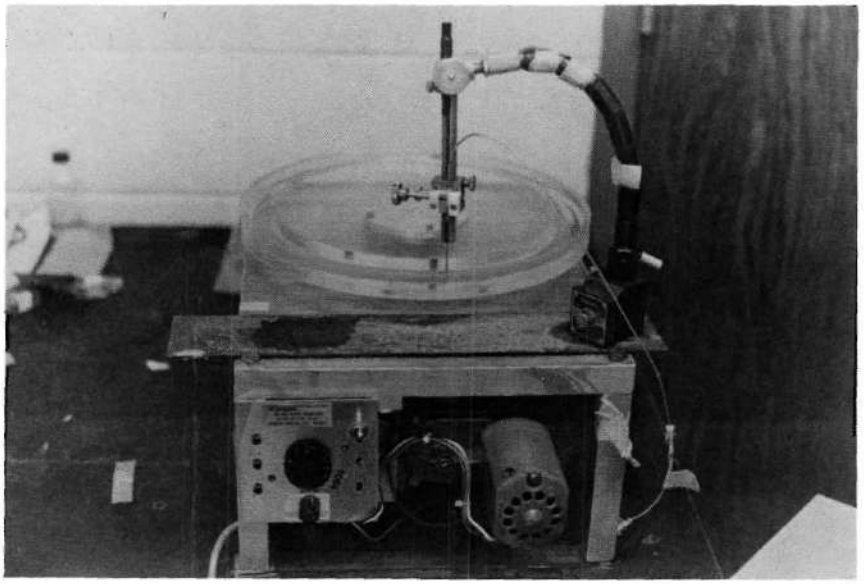

Figure 195. Hot Film Probe Calibration Table

which in turn is rotated by a system of stepped pulleys and a variable speed motor. The channel design allows calibration with as little as 200 cc of fluid. This small volume requirement is particularly advantageous when a blood calibration is required. The system could be controlled to produce velocities up to 120 cm/sec in the channel fluid. The probe was inserted into the calibration fluid and rigidly held in place with the same goose-neck micrometer apparatus that was used in the experiments (see Appendix I). It was determined experimentally that the wake behind the probe did not wrap around the channel and perturb the flow over the probe. The rotational speed, and therefore the fluid velocity at a known radius, was measured with a timing mark on the disk and a manual timer accurate to 0.1 sec. The rotational speed was determined by timing ten revolutions. A typical probe calibration using the TSI probe and anemometer is shown in Figure 196.

Operating Procedures and Comments

Of utmost importance for accurate velocity measurements is to maintain the same probe overheat in the application of the probe as was used in the calibration. The temperature of the water in the flow system could change as much as $2^{\circ}C$ during the course of a day's experiment due to the water being colder than room temperature when the experiment began. This temperature change was minimized by allowing the water to sit overnight in containers and by circulating the water several hours in the system before data were taken. Even with these precautions, the water temperature would change several tenths of a degree during a day's run. This variation in water temperature has a

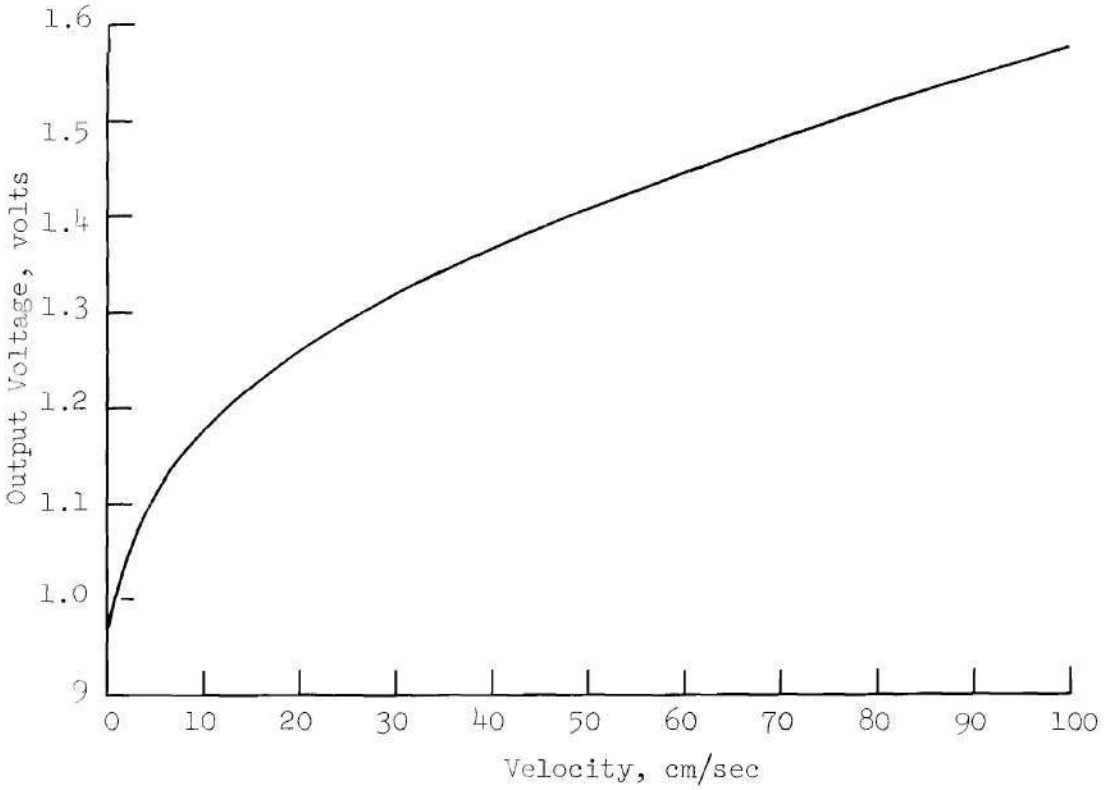

Figure 196. Typical Conical Hot Film Probe Calibration with TSI Anemometer

noticeable effect on probe sensitivity if the probe operating resistance is not adjusted to yield the correct overheat ratio. For this reason the probe cold resistance was checked often and the probe hot resistance adjusted if necessary.

Another factor in calibration repeatability is the deposition of contaminants on the sensor surface. Even though the water was filtered before use, room dust eventually contaminated the water during the course of draining and refilling for occlusion or probe position changes. If a contaminant, such as a dust filament, should adhere to the surface the probe sensitivity is noticeably reduced. This response is easily seen as a sudden decrease in anemometer output and the probe must be clenaed and the calibration checked.

Bubbles occasionally formed on the sensor surface, even for the low 1 percent overheat. However, from the experience gained by using numerous probes from both manufacturers, it is the opinion of the author that bubble formation only occurs when the quartz overcoating or the epoxy sealer on the lead elements does not completely insulate the sensor or leads from the conducting fluid. The water was not distilled or demineralized and would have significant conductivity to enhance bubble formation from electrolytic action. Once bubbles begin forming at frequent intervals, the probe claibration is unreliable and seldom repeats.

BIBLIOGRAPHY

1. Cardiovascular Diseases in the U. S., Facts and Figures, The American Heart Association, 1965.

2. Heart Facts, The American Heart Association, 1974.

3. R. F. Rushmer, Cardiovascular Dynamics, 3rd Edition, W. B. Saunders Co., 1970, 293-313.

4. N. S. Lees and C. F. Dewey, Jr., "Phonoangiography: A New Noninvasive Diagnostic Method for Studying Arterial Disease," Nat'l. Acad. Sci., 67, 935-942, October, 1970.

5. A. H. Sacks, E. G. Tickner, and I. B. Macdonald, "Criteria for the Onset of Vascular Murmurs," Circulation Research, XXIX, 249-256, Sept., 1971.

6. E. L. Yellin, "Hydraulic Noise in Submerged and Bounded Liquid Sets," in Biomedical Fluid Mechanics Symposium, Denver, 1966, 209-221.

7. Roach, M. R., 1972, "Poststenotic Dilatation in Arteries," Cardiovascular Fluid Dynamics, Vol. 2, ed. by D. Bergel, Academic Press, London.

8. Kim, B. M. and Corcoran, W. H., "Experimental Measurements of Turbulence Spectra Distal to Stenosis," J. Biomechanics, 7, 335-342, 1974.

9. D. P. Giddens, R. F. Mabon, R. A. Cassanova, R. K. Menon, and J. Chandler, "Experimental Observations of the Velocity Field Distal to Partial Occlusions in Arteries," Paper presented at 10th S.E.S. Meeting, Raleigh, N. C., Nov., 1973.

10. Johansen, F. C., "Flow Through Pipe Orifices at Low Reynolds Numbers," Proc. Roy. Soc., A126, 231-243, 1929.

11. Anderson, A. B. C., "Structure and Velocity of Periodic Vortex-Ring Flow Pattern of a Primary Pfeifenton (Pipe Tone) Jet," J. Acoustical Soc. Amer., 27, 1048-1053, 1955.

12. Anderson, A. B. C., "Vortex-Ring Structure-Transition in a Jet Emitting Discrete Acoustic Frequencies," J. Acoustical Soc. Amer., 28, 914-721, 1956.

13. Becker, H. A. and Massaro, T. A., "Vortex Evolution in a Round Jet," J. Fluid Mech., 31, 435-448, 1968.

14. Crow, S. C. and Champagne, F. H., "Orderly Structure in Jet Turbulence," J. Fluid Mech., 48, 547-591, 1971.

15. Chan, Y. Y., "Spatial Waves in Turbulent Jets," Phys. of Fluids, 17, 46-53, 1974.

16. Iribarne, A., Frantisak, F., Hummel, R. L. and Smith, J. W., "An Experimental Study of Instabilities and Other Flow Properties of a Laminar Pipe Jet," AIChE Journal, 18, 689-698, 1972.

17. Beavers, G. S. and Wilson, T. A., "Vortex Growth in Jets," J. Fluid Mech., 44, 97-112, 1970.

18. Ko, N. W. M. and Davies, P. O. A. L., "The Near Field Within the Potential Cone of Subsonic Cold Jets," J. Fluid Mech., 50, 49-78, 1971.

19. Teyssandier, R. G. and Wilson, M. F., "An Analysis of Flow Through Sudden Enlargements in Pipes", J. Fluid Mech., 64, 85-95, 1974.

20. Chaturvedi, M. C., "Flow Characteristics of Axisymmetric Expansions," J. Hydraul. Div. A.S.C.E., 89 (HY3), 61-92, 1963.

21. Fry, D. L., "Responses of the Arterial Wall to Certain Physical Factors," in Atherogenesis: Initiating Factors, A Ciba Foundation Symposium 12 (New Series), pp. 93-125, Elsevier. Excerpta Medica. North Holland, Amsterdam, 1973.

22. Caro, C. G., "Transport of Material Between Blood and Wall in Arteries," in Atherogenesis: Initiating Factors, A Ciba Foundation Symposium 12 (New Series), pp. 127-164, Elsevier. Excerpta Medica. New Holland, Amsterdam, 1973.

23. Forrester, J. H. and Young, D. F., "Flow Through a Converging-Diverging Tube and Its Implications in Occlusive Vascular Disease - I," J. Biomechanics, 3, 297-305, 1970.

24. Forrester, J. H. and Young, D. F., "Flow Through a Converging-Diverging Tube and Its Implication in Occlusive Vascular Disease - II," J. Biomechanics, 3, 307-316, 1970.

25. Young, D. F. and Tsai, F. Y., "Flow Characteristics in Models of Arterial Stenoses - I. Steady Flow," J. Biomechanics, 6, 395-410, 1973.

26. Young, D. F. and Tsai, F. Y., "Flow Characteristics in Models of Arterial Stenoses - II. Unsteady Flow," J. Biomechanics, 6, 547-559, 1973.

27. Tsai, F. Y. and Young, D. F., "Some Turbulence Measurements in an Arterial Stenosis," Proc. 10th Annual Rocky Mtn. Bioengr. Sym., May 7-9, 1973.

28. Rudinger, G., 1966, "Review of Current Mathematical Methods for the Analysis of Blood Flow," Biomedical Fluid Mechanics Symposium, Denver, 1-33.

29. Fich, S., Welkowitz, W. and Hilton, R., 1966, "Pulsatile Blood Flow in the Aorta," in Biomedical Fluid Mechanics Symposium, Denver, 34-44.

30. Bergel, D. H., Clark, C., Schultz, D. L. and Pedoe, D. S. T., 1970, "The Measurement of Instantaneous Blood Velocity and a Calculation of Total Mechanical Energy Expenditure in Ventricular Pumping," Specialists Meeting on Fluid Dynamics of Blood Circulation and Respiratory Flow, AGARD Conference Proceedings # 65.

31. J. R. Womersley, "Method for the Calculation of Velocity, Rate of Flow and Viscous Drag in Arteries When the Pressure Gradient is Known," J. Physiol., 127, 553-563.

32. D. A. McDonald, Blood Flow In Arteries, Edward Arnold (Publishers) Ltd., London, 1960.

33. W. G. Fraser, "What Is Known About the Physiology of Larger Blood Vessels," In Biomechanics, ed. by Y. C. Fung, ASME, 1966, pp. 1-19.

34. R. Skalak, "Wave Propagation in Blood Flow," In Biomechanics, ed. by Y. C. Fung, ASME, 1966, pp. 20-46.

35. R. M. Nerem, W. A. Seed, and N. B. Wood, "An Experimental Study of the Velocity Distribution and Transition to Turbulence in the Aorta," J. Fluid Mech., 52, 137-160, 1972.

36. Caro, C. G., Fitz-Gerald, J. M. and Schroter, R. C., "Atheroma and Arterial Wall Shear: Observation Correlation and Proposal of a Shear Dependent Mass Transfer Mechanism of Atherogenesis," Proc. Roy. Soc. Lod. B, 177, pp. 109-159, 1971.

37. DISA Probe Manual, DISA Electronic A/S, DK 2730 Herlev, Denmark.

38. TSI Anemometry, Thermo-Systems Inc., 2500 Cleveland Ave., St. Paul, Minnesota, 55113.

VITA

Robert Anthony Cassanova was born in Columbia, South Carolina on April 12, 1942. He attended elementary schools in Columbia and high schools in Columbia and Charlotte, North Carolina. He was graduated from Myers Park High School in June, 1960. In September, 1960, Mr. Cassanova entered North Carolina State University in Raleigh, North Carolina, where he received the degree of Bachelor of Science in Mechanical Engineering with an Aerospace Option in June 1964. He is a member of the Theta Tau engineering fraternity.

Mr. Cassanova was employed by ARO, Inc. in Tullahoma, Tennessee as a project engineer and research engineer from June 1964 until December, 1967. While working at ARO, Inc., Mr. Cassanova attended graduate school at the University of Tennessee Space Institute and received the degree of Master of Science in Aerospace Engineering in June 1967.

Since December, 1967, Mr. Cassanova has been a research engineer on the faculty of the School of Aerospace Engineering at Georgia Tech where he also studied in the doctoral program.

On August 1, 1964, Mr. Cassanova was married to the former Alice Marie Benson of Battleboro, North Carolina. They have two sons, William Anthony and Jeffrey Patrick.